



**Politecnico
di Torino**



**University
of Windsor**

Politecnico di Torino and University of Windsor

MSc Double Degree in Automotive Engineering

Academic year 2023/2024

Graduation Session October 2024

Material dependence of the internal stresses developed during lithiation of battery electrodes in Li-ion batteries



Academic Supervisors:

Dr. Reza Riahi

Dr. Giuseppe Elia

Dr. Claudio Gerbaldi

Company Supervisors:

Dr. Antonio Giuliano

Dr. Saytam Panchal

Candidate:

Filippo D'Ugo

Material dependence of the internal stresses developed during lithiation of battery electrodes in Li-ion batteries

By

Filippo D'Ugo

A Thesis

Submitted to the Faculty of Graduate Studies
through the Department of Mechanical, Automotive and Materials Engineering
in Partial Fulfillment of the Requirements for
the Double Degree of Master of Applied Science
at the University of Windsor and Politecnico di Torino

Windsor, Ontario, Canada

2024

©2024 Filippo D'Ugo

Material dependence of the internal stresses
developed during lithiation of battery electrodes
in Li-ion batteries

by

Filippo D'Ugo

APPROVED BY:

M.Mirhassani

Department of Electrical and Computer Engineering

A.Edrisy

Department of Mechanical, Automotive and Materials Engineering

R.Riahi, Advisor

Department of Mechanical, Automotive and Materials Engineering

August 16, 2024

Declaration of Originality

I hereby certify that I am the sole author of this thesis and that no part of this thesis has been published or submitted for publication.

I certify that, to the best of my knowledge, my thesis does not infringe upon anyone's copyright nor violate any proprietary rights and that any ideas, techniques, quotations, or any other material from the work of other people included in my thesis, published or otherwise, are fully acknowledged in accordance with the standard referencing practices. Furthermore, to the extent that I have included copyrighted material that surpasses the bounds of fair dealing within the meaning of the Canada Copyright Act, I certify that I have obtained a written permission from the copyright owner(s) to include such material(s) in my thesis and have included copies of such copyright clearances to my appendix.

I declare that this is a true copy of my thesis, including any final revisions, as approved by my thesis committee and the Graduate Studies office, and that this thesis has not been submitted for a higher degree to any other University or Institution.

Abstract

Lithium-ion batteries, due to the growing shift towards renewable energy sources, are becoming particularly promising, offering one of the highest energy densities among their competitors. Anyway, one of the primary issues related to them lies in the damage incurred through electric cycling. The damage, caused by the repeated insertion and extraction of lithium ions within the active materials induces mechanical stresses, called diffusion-induced stresses (DIS), leading to crack propagation, material degradation and subsequent decline in performance. The objective of this thesis is to develop a detailed electrochemical-mechanical model for battery cell using COMSOL Multiphysics. The model aims to accurately estimate the stresses within the battery anode during the lithiation process. Through this model, different anode materials such as graphite and silicon will be separately investigated to understand their influence on stress development. Furthermore, the study will delve into key parameters such as active anode particle size, anode thickness and charging rate to comprehend their effects on stress development within the anode.

The results show that, the developed electrochemical-mechanical battery model is able to accurately reproduce the experimental cell behavior. Specifically, the voltage vs. time curve is reproduced within an error margin of 3% for the graphite anode cell and 2% for the silicon one. Regarding the mechanical model, it precisely replicates the experimental results, staying within an error margin below 2% for the graphite anode and 5% for the silicon. The maximum stress for graphite is 53.69 MPa, while for silicon it is 1.5 GPa. While, at the end of the cycle, the residual stress is 8.33 MPa for graphite and 0.19 GPa for silicon. The stress increases over time during charging, but both materials exhibit a decrease in slope in the later phases, while during discharging a decrease is experienced. Experimental results show that these stresses did not cause fragmentation of the electrode but caused permanent deformation as some lithium ions remained trapped inside the anode. Considering the entire electrode thickness, a trend can be recognized, where during the charging phase the maximum stress is always at the electrolyte interface. However, during the last phase of discharging, it is inverted with the maximum stress at the current collector interface. The results of the parametric studies show that, for graphite, the most detrimental factor for increasing stress is a high charging rate, leading to a 69.7% increase, while the most beneficial is having a lower particle radius, inducing a 32.24% decrease. For silicon, the highest charging rate is the most dangerous, generating a 65.3% increase, while the lowest rate is the most beneficial, provoking a negative variation of 33.3%.

A nonna Lella e nonno Guido,
a voi che siete il mio tutto

Acknowledgment

Firstly, I would like to express my deep gratitude to my thesis supervisor at the University of Windsor, Dr. Reza Riahi, for his invaluable guidance and support throughout this research. I also extend my thanks to my supervisors at Politecnico di Torino, Dr. Giuseppe Elia and Dr. Claudio Gerbaldi, along with Dr. Mattia Giuliano and Dr. Saytam Panchal from STELLANTIS, whose insightful feedback and assistance were instrumental in the development of this thesis.

My sincere appreciation goes to my committee members, Dr. Afsaneh Edrisy and Dr. Mitra Mirhassani, for their critical evaluations and constructive comments that greatly contributed to the refinement of this work.

Additionally, I would like to express my gratitude to STELLANTIS, Politecnico di Torino, represented by Dr. Maria Pia Cavatorta and Dr. Vittorio Ravello, and the University of Windsor, represented by Dr. Ofelia Jianu. Their support made this project possible and enabled me to pursue this Double Degree in Automotive Engineering.

I also want to thank my mother for her unwavering support and for being a consistent source of inspiration in my life. You sacrificed everything for me and your guidance has made me immensely proud of the person you are. The person I have become is due to your endless encouragement.

My heartfelt thanks go to my father, whose steadfast support and pride in my achievements have always been a source of motivation. Your belief in me is deeply appreciated and being your son is a source of great honor for me, hoping that one day I will become the kind of father that you are.

To my grandmother Gabriella and my grandfather Guido, who raised me as their own and provided me with everything I needed, I am grateful every day. You are like parents to me, and the difficulty of being away from you is beyond words. Knowing that I make you proud is the greatest gift I could ask for.

To my sister Federica, who began this journey with me and has always been a constant presence in my life, I am thrilled to share these victories with you.

I am deeply grateful to my uncle Dante, who has played a pivotal role in my journey to adulthood. The countless hours we spent playing together as a child and the valuable lessons on driving are memories I will always cherish. Your guidance has significantly influenced who I am today. Thank

you for your unwavering support.

To my aunt Federica, who has been like a second mother. Your support and care have meant the world to me and your guidance throughout my childhood has helped me become a better person. You are a true source of inspiration and I am proud to be your nephew.

To my cousin Alessandra, who is like a sister to me, we have shared so much together and I look forward to celebrating all future victories with you, which I am confident will come.

To my grandmother Liliana, who always shows a great interest in my well-being and makes me feel at home every time I visit, without asking for anything in return, I am deeply grateful.

Finally, to Costanzo, who entered our family with great respect and has shown incredible interest and support in everything I do, establishing a strong bond that I cherish deeply.

Contents

Declaration of Originality	iv
Abstract	v
Dedication	vi
Acknowledgment	vii
List of Tables	xii
List of Figures	xxi
List of Abbreviations	xxii
1 Introduction on Li-ion batteries	1
1.1 Basics of Li-ion batteries	1
1.2 Electrodes for lithium-ion batteries	4
1.2.1 Anode materials	5
1.2.2 Cathode materials	6
1.2.3 Binders	9
1.3 Electrolytes for lithium-ion batteries	10
1.4 Separators for lithium-ion batteries	10
1.5 Causes of the stresses development in electrode materials from lithiation/delithiation	11
2 Literature Review	14
2.1 Characteristic of different electrode materials during lithiation or de-lithiation process	14
2.1.1 Characteristic of anode materials during lithiation/de-lithiation process . .	17
2.1.2 Characteristic of cathode materials during lithiation/de-lithiation process .	19
2.2 Effects of diffusion-induced stresses	21
2.3 Coupled electrochemical-mechanical model for Li-ion cell	23
2.3.1 Single-particle model	25
2.3.2 Pseudo-two-dimensional model	28
2.3.3 Two-dimensional model	32
2.3.4 Three-dimensional model	34
2.4 Influence of key parameters on stress development	35
2.5 Experimental determination of diffusion-induced stress in Li-ion cell	38

3	Methodology	42
3.1	Objective of the thesis	42
3.2	Software employed: COMSOL Multiphysics	42
3.3	Description of the implemented electrochemical-mechanical battery cell model	43
3.4	Model constraints and boundary conditions	46
3.5	Understanding COMSOL domains	47
3.5.1	Global definitions domain	47
3.5.2	Definitions domain	48
3.5.3	Geometry domain	49
3.5.4	Materials domain	49
3.5.5	Physics domain	58
3.5.5.1	Separator domain	60
3.5.5.2	Porous electrode domain along with diffusion-induced stresses evaluation	63
3.5.5.3	Electric ground, Electric current and Current conductor domains	75
3.5.5.4	No flux, Insulation and Initial values domains.	77
3.5.5.5	Electrode surface domain.	80
3.5.6	Mesh	83
3.5.7	Study domain	85
3.6	Optimization of the model parameters tuning using a MATLAB code to fit experimental results	86
3.7	Input data for simulations	87
3.7.1	Input data for simulation of graphite anode	88
3.7.2	Input data for simulation of silicon anode	94
4	Experiments conducted at the laboratory	100
4.1	Mixture preparation	100
4.2	Application of the anode mixture on the current collector	104
4.3	Experimental cell assembly	106
4.4	Evaluation of cell deflection and stress under charging-discharging cycle	109
5	Results and discussions	116
5.1	Graphite anode	116
5.1.1	Model validation	116
5.1.2	Extended model results	124
5.1.3	Parametric analyses	131
5.2	Silicon anode	135

5.2.1	Model validation	135
5.2.2	Extended model results	143
5.2.3	Parametric analyses	150
5.3	Comparison between graphite and silicon anodes	154
6	Conclusion and future works	159
	References	161
	Vita auctoris	171

List of Tables

1	Phases, crystal structures, lattice parameters and crystal volumes that form during progressive electrochemical lithiation (of anode) and de-lithiation (of cathode) of the various electrode materials for Li-ion batteries[1][2][3][4][5][6][7].	16
2	Li-ion cell electrochemical-mechanical model present in the literature.	25
3	Advantages and drawbacks of the single-particle model.	28
4	P2D and single-particle model governing equations [8].	31
5	Advantages and drawbacks of the P2D model.	31
6	Advantages and drawbacks of the 2D model.	33
7	Advantages and drawbacks of the 3D model.	35
8	Assumptions and boundary conditions for the developed electrochemical-mechanical model.	47
9	Copper input data taken from the COMSOL library and literature [9].	52
10	LiPF ₆ input data taken from the COMSOL library and literature [10] [11].	52
11	Lithium metal input data taken from the COMSOL library.	55
12	Graphite input data taken from the COMSOL library and literature [12] [13] [14] [15] [16].	55
13	Silicon input data taken from the COMSOL library [17] [18] [19] [20] [21] [22].	57
14	Required input data for the 'Lithium-ion battery' domain.	60
15	Required input data for the 'Separator' domain.	63
16	Required input data for the 'Porous electrode' domain.	74
17	Required input data for the 'Electric ground, Electrode current and Current conductor' domains.	77
18	Required input data for the 'No flux, Isolation and Initial conditions' domains.	79
19	Required input data for the 'Electrode surface' domain.	83
20	General data required for the simulation [23] [24] [25]. Input data graphite anode.	88
21	Graphite input data taken from the COMSOL library and literature [12] [13] [14] [15] [16]. Input data graphite anode.	89
22	Copper input data taken from the COMSOL library and literature [9]. Input data graphite anode.	91
23	LiPF ₆ input data taken from the COMSOL library and literature [10] [11]. Input data graphite anode.	91
24	Lithium metal input data taken from the COMSOL library. Input data graphite anode.	93
25	General data required for the simulation [23] [24] [21]. Input data silicon anode.	94

26	Silicon input data taken from the COMSOL library [17] [18] [19] [20] [21] [22]. Input data silicon anode.	95
27	Copper input data taken from the COMSOL library and literature [9]. Input data silicon anode.	96
28	LiPF ₆ input data taken from the COMSOL library and literature [10] [11]. Input data silicon anode.	96
29	Lithium metal input data taken from the COMSOL library. Input data silicon anode.	99
30	Mixture composition for graphite anode.	101
31	Mixture composition for silicon anode.	102
32	Thickness employed for graphite anode and for its current collector.	104
33	Thickness employed for silicon anode and for its current collector.	104

List of Figures

1	(a) Plot comparing the specific energies (x-axis) and energy densities (y-axis). (b) Plot comparing the energy densities (x-axis) and power densities (y-axis) [26].	3
2	Reaction taking place in a Li-ion cell during charging on the left and discharging on the right [27].	3
3	Typical electrode architectures for the more common ‘porous composite electrode’ and the thin film electrode [26].	5
4	Schematic drawing of layered structure (LiCoO ₂ , NMC, NCA LiNiO ₂ and LiMn ₂ O ₄) which shows the lithium ions between the transition-metal oxide/sulphide sheets [28].	8
5	Structures of orthorhombic LiFePO ₄ [29].	9
6	Illustration of a small part of an electrode, focusing on binder [30].	9
7	Schematic illustrations of (a) constraining effects of neighboring active particles, inactive matrix and current collector/substrate on the expanding active particles upon lithiation of ‘porous composite electrode’; (b) stress generated at inter-particle contact between expanding electrode particles upon lithiation; (c) constraining of the in-plane dilation of thin film electrodes, upon lithiation, by the inactive current collector/substrate; (d) Li-concentration gradient between lithiated and unlithiated portions of a particle, resulting in the development of stress discontinuities. The same is true for adjacent regions possessing different crystal structures/phases [26].	13
8	Typical potential (against Li/Li ₊) vs. degree of lithiation/delithiation for graphite [26].	18
9	(a) Volumetric and gravimetric capacities of the various anode materials, showing the metallic anode materials possessing considerably superior capacities, compared to carbon. (b) Variation of % volume change per Si atom and longitudinal elastic modulus with degree of lithiation. Note the significant increase in volume, along with softening, with progress of lithiation [1][31].	18
10	(a) Variation of potential (vs.Li/Li ⁺) with respect to degree of lithiation (discharge) and de-lithiation (charge) for Li _x Mn ₂ O ₄ , even during lithiating beyond x = 1. (b) Variation of lattice parameter for both the cubic phases of Li _x Mn ₂ O ₄ with degree of lithiation (between x = 0.1 and 1) [32].	20
11	Internal crack distribution for Ni-rich Li[Ni _x Co _y Mn _{1-x-y}]O ₂ cathode particle [33].	22
12	Variation of specific capacities for different electrode materials in function of the number of electrochemical cycles [34][35].	23
13	Single-particle model of a Li-ion cell [36].	28
14	P2D model of a Li-ion cell [37].	32

15	Example of a 2D model for a Li-ion cell [38].	33
16	Example of a 3D model for a Li-ion cell [39].	35
17	Von Mises stress at the surface of the particles along the thickness of the anode for different rates of discharge [40].	37
18	Von Mises stress at the surface of the particles along the thickness of the anode for various particle sizes [40].	37
19	Von Mises stress at the surface of the particles along the thickness of the anode for various porosity values [40].	38
20	Schematic of the in situ measurement system, which consists of an electrochemical cell, CCD camera and a computer [41].	40
21	Curvature evolution of composite graphite electrodes in 8 cycles [41].	40
22	The evolution of stress in the active layer in the thickness of 90 μm [41].	41
23	Electrochemical-mechanical model implemented.	45
24	Comsol domains for the implemented model.	47
25	Global definition domain for the implemented model.	48
26	Definition domain for the implemented model.	49
27	Geometry domain for the implemented model.	49
28	Materials domain for the model with graphite anode.	52
29	Diffusion coefficient depending only on the lithium concentration, $D_c(c)$, for LiPF_6	53
30	Electrical conductivity depending only on the lithium concentration, $\sigma_c(c)$, for LiPF_6	53
31	Transport number depending only on the lithium concentration, $t_{+c}(c)$, for LiPF_6	54
32	Activity dependence varying only with the lithium concentration, $\frac{\partial \ln(f)}{\partial \ln(c)}(c)$, for LiPF_6	54
33	Equilibrium potential depending only on the normalized lithium concentration, $E_{eq,c}$, for graphite. $E_{eq,inv}$ which appears in Equation 25 is the inverse of the function depicted in the figure.	56
34	Derivative of the equilibrium potential with respect to the temperature depending only on the normalized lithium concentration, $\frac{dE_{eq}}{dT}_c$, for graphite.	56
35	Volume variation in function of the normalized concentration for graphite, $\frac{dvol}{dc}(\frac{c_s}{c_{s,max}})$	57
36	Equilibrium potential depending only on the normalized lithium concentration, $E_{eq,c}$, for silicon. $E_{eq,inv}$ which appears in Equation 25 is the inverse of the function depicted in the figure.	58
37	Volume variation in function of the normalized concentration for silicon, $\frac{dvol}{dc}(\frac{c_s}{c_{s,max}})$	58
38	Physics domain for the developed model.	60

39	Porous electrode configuration along with parameters for potentials and concentrations [28].	73
40	Volume variation in function of the normalized concentration for graphite, $\frac{dvol}{dc}(\frac{c_s}{c_{s,max}})$. (reproduction of Figure 35).	75
41	Volume variation in function of the normalized concentration for silicon, $\frac{dvol}{dc}(\frac{c_s}{c_{s,max}})$. (reproduction of Figure 37).	75
42	No mass flux condition across the blue boundaries for the developed model.	79
43	Electric insulation condition across the blue boundaries for the developed model.	79
44	Applied mesh for the developed model.	85
45	Portion of the MATLAB code implemented for the mechanical-model tuning optimization.	87
46	Equilibrium potential depending only on the normalized lithium concentration, $E_{eq,c}$, for graphite. $E_{eq,inv}$ which appears in Equation 25 is the inverse of the function depicted in the figure. Input data graphite anode.	89
47	Derivative of the equilibrium potential with respect to the temperature depending only on the normalized lithium concentration, $\frac{dE_{eq}}{dT}_c$, for graphite. Input data graphite anode.	90
48	Volume variation in function of the normalized concentration for graphite, $\frac{dvol}{dc}(\frac{c_s}{c_{s,max}})$. Input data graphite anode.	90
49	Diffusion coefficient depending only on the lithium concentration, $D_c(c)$, for LiPF ₆ . Input data graphite anode.	91
50	Electrical conductivity depending only on the lithium concentration, $\sigma_c(c)$, for LiPF ₆ . Input data graphite anode.	92
51	Transport number depending only on the lithium concentration, $t_{+c}(c)$, for LiPF ₆ . Input data graphite anode.	92
52	Activity dependence varying only with the lithium concentration, $\frac{\partial \ln(f)}{\partial \ln(c)}_c(c)$, for LiPF ₆ . Input data graphite anode.	93
53	Equilibrium potential depending only on the normalized lithium concentration, $E_{eq,c}$, for silicon. $E_{eq,inv}$ which appears in Equation 25 is the inverse of the function depicted in the figure. Input data silicon anode.	95
54	Volume variation in function of the normalized concentration for silicon, $\frac{dvol}{dc}(\frac{c_s}{c_{s,max}})$. Input data silicon anode.	96
55	Diffusion coefficient depending only on the lithium concentration, $D_c(c)$, for LiPF ₆ . Input data silicon anode.	97
56	Electrical conductivity depending only on the lithium concentration, $\sigma_c(c)$, for LiPF ₆ . Input data silicon anode.	97

57	Transport number depending only on the lithium concentration, $t_{+c}(c)$, for LiPF_6 . Input data silicon anode.	98
58	Activity dependence varying only with the lithium concentration, $\frac{\partial \ln(f)}{\partial \ln(c)}(c)$, for LiPF_6 . Input data silicon anode.	98
59	FOUR E'S scientific vortex mixer.	102
60	Thermo scientific CIMAREC hot plate.	103
61	Electronic balance SLSC series.	103
62	Base used for the application of anode mixture on the current collector.	105
63	Four paths precision film applicator used for choosing the anode thickness.	105
64	Vacuum drying oven DZF-6020.	106
65	CATIA CAD model of the Teflon box containing the cell.	107
66	CATIA CAD model of the Ultra-high molecular weight polyethylene insert used to fix the cell, contained within the Teflon box.	108
67	CNC milling machine.	108
68	Glovebox.	109
69	Description of the built experimental-cell.	109
70	Deflection evaluation setup equipped with a digital microscope.	110
71	Eight channel battery analyzer.	111
72	Charging-discharging cycle applied to the graphite anode using the LANDT Bat- tery Analyzer program.	111
73	Charging-discharging cycle applied to the silicon anode using the LANDT Battery Analyzer program.	112
74	Deflection of the cantilever anode during lithiation, in blue, and delithiation, in green.	114
75	Selection of anode active particle position for the model intra-particle results.	114
76	Convention utilized for the experimental stress evaluation. (a) indicates the initial state of the anode, while (b) a deformed state with lithium ions insertion. For the extraction of lithium ions the convention is still the same, but the deflection obviously decreases [41].	115
77	Voltage-time profile of the graphite anode cell during the charging-discharging cycle.	117
78	Selection of active particle position for intra-particle results, graphite anode.	118
79	Normalized lithium ions concentration variation in the selected active particle dur- ing the charging phase of the cycle, graphite anode.	119
80	Normalized lithium ions concentration variation in the selected active particle dur- ing the discharging phase of the cycle, graphite anode.	119
81	Deflection of graphite cantilever anode during the charging-discharging cycle.	120

82 Images taken by the digital microscope capturing the graphite anode deflection, throughout the experiments, for different SOC's during the cycle, focusing on the charging phase. **(a)**, **(b)** and **(c)** represent the deflection at SOC equal to 0%, 63% and 100%, respectively. 121

83 Surface Von Mises stress comparison between experimental and model data during the charging-discharging cycle for the selected active particle, graphite anode. . . . 123

84 Relative error of the surface Von Mises stress between experimental and model data during the charging-discharging cycle for the selected active particle, graphite anode. 123

85 Radial stress in the selected active particle during the charging phase of the cycle, graphite anode. 124

86 Radial stress in the selected active particle during the discharging phase of the cycle, graphite anode. 124

87 Tangential stress in the selected active particle during the charging phase of the cycle, graphite anode. 126

88 Tangential stress in the selected active particle during the discharging phase of the cycle, graphite anode. 126

89 Hydrostatic stress in the selected active particle during the charging phase of the cycle, graphite anode. 127

90 Hydrostatic stress in the selected active particle during the discharging phase of the cycle, graphite anode. 127

91 Von Mises stress in the selected active particle during the charging phase of the cycle, graphite anode. 128

92 Von Mises stress in the selected active particle during the discharging phase of the cycle, graphite anode. 128

93 Surface Von Mises stress evolution across the graphite anode thickness, highlighting the anode in color, throughout the charging-discharging cycle at various SOC's. The charging phase is represented by the SOC text in blue (**(a)**, **(b)**, **(c)**, **(d)**, **(e)** and **(f)**), while the discharging phase is indicated in green (**(g)**, **(h)**, **(i)**, **(j)** and **(k)**). . . . 131

94 Impact of the active particle radius on surface Von Mises stress during the charging phase of the cycle for the selected active particle, graphite anode. 132

95 Impact of the graphite anode thickness on surface Von Mises stress during the charging phase of the cycle for the selected active particle. 133

96 Impact of the charging rate on surface Von Mises stress during the charging phase of the cycle for the selected active particle, graphite anode. 134

97	Comparison of different surface Von Mises stress variations at 100% SOC for the parametric studies performed. On the x-axis, the number 1 refers to the active particle radius sweep, the number 2 to the anode thickness sweep and the number 3 to the charging rate sweep. Graphite anode.	135
98	Voltage-time profile of the silicon anode cell during the charging-discharging cycle.	136
99	Selection of active particle position for intra-particle results, silicon anode.	138
100	Normalized lithium ions concentration variation in the selected active particle during the charging phase of the cycle, silicon anode.	138
101	Normalized lithium ions concentration variation in the selected active particle during the discharging phase of the cycle, silicon anode.	138
102	Deflection of silicon cantilever anode during the charging-discharging cycle.	139
103	Images taken by the digital microscope capturing the silicon anode deflection, throughout the experiments, for different SOC during the cycle, focusing on the charging phase. (a) , (b) and (c) represent the deflection at SOC equal to 0%, 61% and 100%, respectively.	141
104	Surface Von Mises stress comparison between experimental and model data during the charging-discharging cycle for the selected active particle, silicon anode.	142
105	Relative error of the surface Von Mises stress between experimental and model data during the charging-discharging cycle for the selected active particle, silicon anode.	143
106	Radial stress in the selected active particle during the charging phase of the cycle, silicon anode.	144
107	Radial stress in the selected active particle during the discharging phase of the cycle, silicon anode.	144
108	Tangential stress in the selected active particle during the charging phase of the cycle, silicon anode.	145
109	Tangential stress in the selected active particle during the discharging phase of the cycle, silicon anode.	145
110	Hydrostatic stress in the selected active particle during the charging phase of the cycle, silicon anode.	146
111	Hydrostatic stress in the selected active particle during the discharging phase of the cycle, silicon anode.	146
112	Von Mises stress in the selected active particle during the charging phase of the cycle, silicon anode.	147
113	Von Mises stress in the selected active particle during the discharging phase of the cycle, silicon anode.	147

114	Surface Von Mises stress evolution across the entire silicon anode thickness, highlighting in color, throughout the charging-discharging cycle at various SOCs. The charging phase is represented by the SOC text in blue ((a), (b), (c), (d), (e) and (f)), while the discharging phase is indicated in green ((g), (h), (i), (j) and (k)).	150
115	Impact of the active particle radius on surface Von Mises stress during the charging phase of the cycle for the selected active particle, silicon anode.	151
116	Impact of the silicon anode thickness on surface Von Mises stress during the charging phase of the cycle for the selected active particle.	152
117	Impact of the intensity of the charging rate on surface Von Mises stress during the charging phase of the cycle for the selected active particle, silicon anode.	153
118	Comparison of different surface Von Mises stress variations at 100% SOC for the parametric studies performed. On the x-axis, the number 1 refers to the active particle radius sweep, the number 2 to the anode thickness sweep and the number 3 to the charging rate sweep. Silicon anode.	154
119	Deflection of graphite cantilever anode during the charging-discharging cycle. It is a reproduction of Figure 81	155
120	Deflection of silicon cantilever anode during the charging-discharging cycle. It is a reproduction of Figure 102	155
121	Surface Von Mises stress comparison between experimental and model data during the charging-discharging cycle for the selected active particle, graphite anode. It is a reproduction of Figure 83	156
122	Surface Von Mises stress comparison between experimental and model data during the charging-discharging cycle for the selected active particle, silicon anode. It is a reproduction of Figure 104	156
123	Relative error of the surface Von Mises stress between experimental and model data during the charging-discharging cycle for the selected active particle, graphite anode. It is a reproduction of Figure 84	156
124	Relative error of the surface Von Mises stress between experimental and model data during the charging-discharging cycle for the selected active particle, silicon anode. It is a reproduction of Figure 105	156
125	Surface Von Mises stress evolution across the entire thickness of the graphite anode at 83% SOC during charging, highlighting the maximum difference in stress values between the side close to electrolyte and the one close to current collector.	157
126	Surface Von Mises stress evolution across the entire thickness of the silicon anode at 77% SOC during discharging, highlighting the maximum difference in stress values between the side close to electrolyte and the one close to current collector.	157

- 127 Comparison of different surface Von Mises stress variations at 100% SOC for the parametric studies performed. On the x-axis, the number 1 refers to the active particle radius sweep, the number 2 to the anode thickness sweep and the number 3 to the charging rate sweep. Graphite anode. It is a reproduction of **Figure 97**. . . 158
- 128 Comparison of different surface Von Mises stress variations at 100% SOC for the parametric studies performed. On the x-axis, the number 1 refers to the active particle radius sweep, the number 2 to the anode thickness sweep and the number 3 to the charging rate sweep. Silicon anode. It is a reproduction of **Figure 118**. . . 158

List of Abbreviations

BEV	Battery electric vehicle
CCD	Charged-coupled device
CMC	Carboxymethyl cellulose
C-rate	Charging/discharging rate
DIS	Diffusion-induced stresses
DOD	Depth of discharge
GIC	Graphite intercalation compound
HEV	Hybrid electric vehicle
LMO	Lithium ion manganese oxide
NCA	Lithium nickel cobalt aluminum oxide
NMC	Lithium nickel manganese cobalt oxide
NMP	N-Methylpyrrolidone
ODE	Ordinary differential equations
PAA	Polyacrylic acid
PEO	Polyethylene oxide
PVDF	Polyvinylidene fluoride
P2D	Pseudo-two-dimensional
SBR	Styrene-butadiene rubber
SEI	Solid electrolyte interface
SOC	State of charge
SP	Single-particle
RVE	Representative volume element
1D	One-dimensional
2D	Two-dimensional
3D	Three-dimensional

1 Introduction on Li-ion batteries

1.1 Basics of Li-ion batteries

Li-ion batteries serve as the predominant power source for a multitude of portable electronic devices, including cell phones, digital cameras and laptops. Their significance extends to heavy-duty applications, such as automobiles, as a means to address challenges associated with non-renewable energy sources. Li-ion batteries boast the highest energy densities among rechargeable batteries, coupled with commendable power density values. Energy density elucidates the amount of energy storable in a unit volume, a critical factor for Battery Electric Vehicles (BEVs) or Hybrid Electric Vehicles (HEVs) aiming to increase their electric range. On the other hand, power density relates to the ability to store power in a unit volume, which is crucial for meeting the dynamic requirements of a vehicle, including rapid acceleration. While these trends are typically opposing, as illustrated in **Figure 1**, Li-ion batteries manage to strike a favorable compromise. Moreover, they exhibit a low self-discharge rate¹ of approximately 5% per month, a significant improvement compared to the > 30% per month and 20% per month for Ni-metal hydride and Ni-Cd batteries, respectively. Additionally, Li-ion batteries are devoid of memory effects², environmentally friendly compared to other batteries and capable of operating within a wider temperature range, spanning from -25°C to 50°C [26][42][43].

The battery is composed of multiple cells connected in series or parallel, where Redox reactions occur. Through the utilization of Li-ions as charge carriers, these reactions generate the electric current. The primary components of a typical Li-ion cell include:

- Two electrodes (cathode and anode): comprising active materials connected to an external circuit via metallic collectors. These active materials, which can reversibly intercalate/de-intercalate³ Li-ions in response to voltage, define the performance characteristics.
- Electrolyte: serving as an ionic conductor and electronic separator, it facilitates the conduction of Li-ions between the cathode and anode.
- Separator: permeable to the flow of Li-ions, allowing the necessary ion transport.

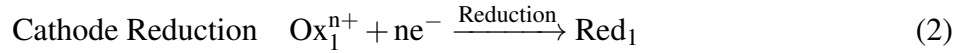
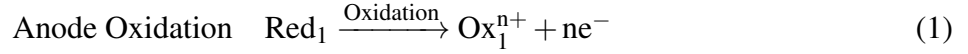
To comprehend the internal dynamics of a battery and the genesis of the current, it is possible to start by examining the discharging process. During discharge, Li-ions are released from the anode as positive ions, flowing through the electrolyte via the separator and being received by the cathode,

¹Process that causes battery discharge even if no electrical consumers are connected.

²Gradually loosening the ability to deliver energy different from its regular usage pattern.

³Addition/Subtraction of lithium ions into a host material without significantly changing the host structure. For a better explanation of these terms, please refer to **Section 1.5**.

where reduction occurs. Simultaneously, electronic current flows through the external circuit from the anode to the cathode, facilitated by the respective current collectors. In terms of definition, the anode is the electrode where oxidation occurs, leading to the loss of electrons by the relevant chemical species. Conversely, in the cathode, reduction takes place and the chemical species gains electrons. [44]



These definitions for anode and cathode remain fixed, whether discussing charging or discharging. The only variables lie in the direction of the electrode flux and the sign of the electrode, as illustrated in **Figure 2**.

After introducing the fundamental working principles of Li-ion batteries in the preceding subchapter, the subsequent sections delve deeper into the components that constitute them. This includes a detailed exploration of the various materials that can be utilized in Li-ion batteries. The culmination of this discussion will center on the stress development encountered by Li-ion batteries during the lithiation process because the primary objective of this thesis work is to comprehend the reasons behind this stress occurrence and quantify its extent.

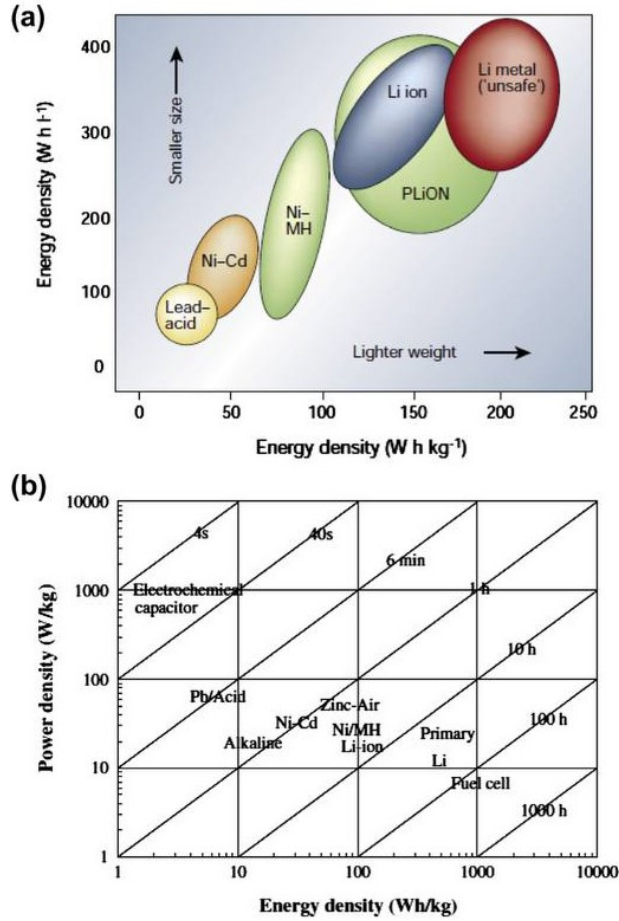


Figure 1: (a) Plot comparing the specific energies (x-axis) and energy densities (y-axis). (b) Plot comparing the energy densities (x-axis) and power densities (y-axis) [26].

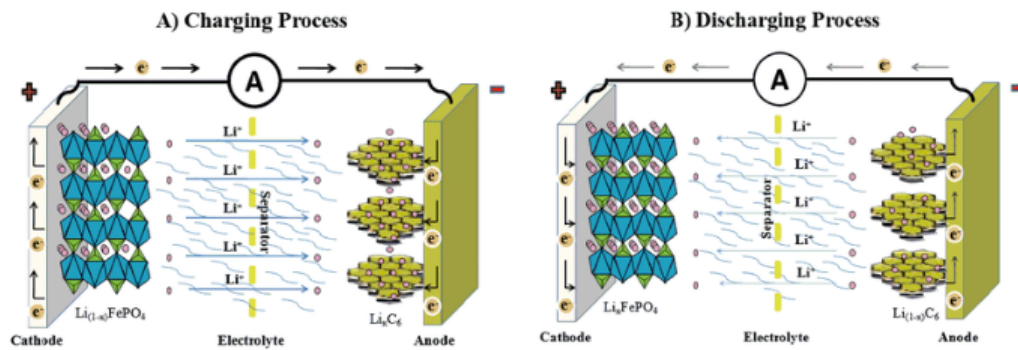


Figure 2: Reaction taking place in a Li-ion cell during charging on the left and discharging on the right [27].

1.2 Electrodes for lithium-ion batteries

The typical electrode architectures exhibit a twofold nature, as illustrated in **Figure 3**. In one approach particles of active materials, Li-hosts, are blended with binders, typically PVDF, and conductive carbon additives, usually carbon black, to form electrodes, which are widely utilized in commercial batteries. Another electrode type, known as thin film electrode, **Figure 3**, consists of active material films ranging from nanometers to microns in thickness. These electrodes, commonly employed in miniature batteries, possess simpler geometries and lack inactive components such as binders and carbon black, making them more suitable for scientific investigations [45].

Ongoing research explores novel electrode architectures like nano-rods and islands, aiming to enhance performance. In all cases, the active electrode components are positioned on metallic current collectors, typically Cu or Ni for anodes and Al or Pt for cathodes, connected to the external circuit. Regarding active electrode components, the current generation of Li-ion batteries employs graphite carbon for the anode electrode and layered transition metal oxide LiCoO_2 , phosphates LiFePO_4 or mixed metal oxides NMC or NCA for the cathode electrode. This configuration yields a net energy density ranging between 100-150 Wh/kg, with a cell capacity of approximately 70 mAh/g [46]. This energy density surpasses that of any other electrochemical energy storage system, as depicted in **Figure 1**. Precisely, a high cell capacity is crucial for batteries, especially those used in automobile applications. It directly influences the total energy stored during charging, contributing to an extended battery life and an obvious increase in vehicle range. Furthermore, the cycle lives of current Li-ion batteries typically fall between 500-1500 cycles, a commendable number compared to market competitors.

Research efforts have also explored metallic anode materials such as Si, Sn and Al, possessing Li-capacities exceeding that of graphitic carbon by factors of $\sim 3-10$. However, as highlighted in this work, the development of metallic anodes has been impeded by severe degradation, including capacity fade and huge stress development, usually limiting their cycle lives to less than 50 cycles [47].

Speaking about drawbacks, Li-ion batteries exhibit a lower power density compared to other technologies in the market. The ability to charging/discharging at high rates is not as widespread, and high charging/discharging rates typically reduce cycle lives. This hints at a correlation between mechanisms responsible for capacity fade and poor rate capabilities. Due to these considerations, the choice of electrode materials is crucial for battery performance. In the last decades, there has been significant research effort to develop new electrode materials/compositions to enhance battery performance.

Given the material's importance, the next chapter will provide a deeper analysis of various materials and their characteristics that are suitable for components in Li-ion batteries.

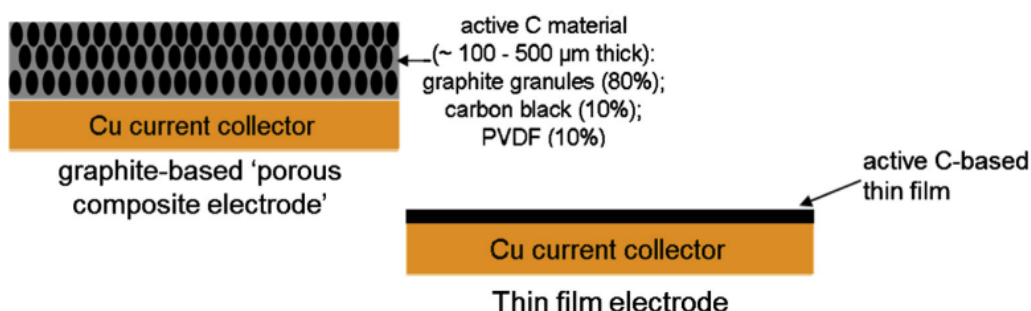


Figure 3: Typical electrode architectures for the more common ‘porous composite electrode’ and the thin film electrode [26].

1.2.1 Anode materials

In the past, lithium metal was a commonly used anode material but is no longer favored due to several reasons. One major concern is the formation of dendritic structures, often referred to as ‘dead lithium,’ during discharging. This phenomenon consumes the material significantly, leading to a decrease in cell life. Another issue is related to the formation of a solid electrolyte interface, a thin layer that develops on the electrode surface, resulting in capacity loss, poor cyclability and self-discharge [48].

Recognizing the limitations of lithium, the quest is now focused on identifying a suitable alternative material. An ideal candidate should possess the following characteristics:

- High specific capacity.
- Good compatibility with the electrolyte.
- Good charging-discharging cycle life and reversibility.
- More eco-friendly and safer.
- Easy manufacturing process and low prices.

While no unique material meets all these requirements, graphitic carbon is one of the most commonly used anode materials due to its low cost, good reliability and non-toxicity [42]. Carbonaceous materials, such as soft carbon, hard carbon and graphite, are extensively used nowadays. These materials, in addition to the mentioned characteristics, exhibit a low Li-ion insertion potential⁴, good cycling stability even after 500 charging-discharging cycles and high specific charge compared to other solutions on the market like transition metal oxides, which will be explained

⁴Measure of the energy needed to insert lithium ions into the electrode material during the charging process of a Li-ion battery.

later. Delving deeper, having a low Li-ion insertion potential is crucial as it reduces the energy required during charging, enables faster charging rates and lowers stresses in the battery due to the lithiation process. Staying on the topic of carbonaceous materials, it is worth mentioning that graphene is also becoming widespread.

Moving forward, other types of materials that can be used for Li-ion batteries include lithium-metal alloys and transition metal oxides. The former is characterized by fast electrode decay due to a significant volume change (on the order of 310%, 255% and 130%) during the lithiation process [49]. Meanwhile, the latter is gaining attention due to high values of reversible capacities, reaching up to 700 mAhg^{-1} , almost three times larger than that of graphite-based anode electrodes currently used in commercial rechargeable lithium-ion batteries [28]. To better understand the aforementioned quantities, it is essential to differentiate between reversible capacity and total capacity. Reversible capacity is the stable capacity delivered by the electrode after completing the formation cycles, while total capacity of a battery includes both the energy related to the reversible process and the one related to the irreversible one [50].

Another material that can be used is silicon, which exhibits a remarkably high capacity of up to 4600 mAhg^{-1} , ten times higher than that of conventional graphite. Additionally, silicon is abundantly available in nature as the second most abundant element in the Earth's crust, it is also non-toxic and eco-friendly. However, a significant challenge associated with silicon is its high volume expansion, up to 400% upon full lithiation, resulting in considerable stress development [51].

1.2.2 Cathode materials

The lithium-based metal oxides are generally used as cathode materials in the lithium batteries. But, in the recent years, new low-cost solutions are developing, like LiMn_2O_4 , LiFePO_4 and other higher capacity materials such as $\text{LiNi}_{1-x}\text{Co}_x\text{O}_2$.

When considering materials, there are several options available, each with its own set of characteristics. However, when considering an ideal candidate, it should possess the following attributes:

- Readily-reducible ions, like a transition metal.
- Good conductivity.
- Rapid reaction with lithium in both intercalation and de-intercalation.
- It should react with lithium with high free energy of reaction, meaning that the reaction is thermodynamically favorable and once started it can proceed spontaneously.
- High capacity and high voltage, preferably 4 V.
- It should not change the host structure when lithium is added.

- Low cost of analysis and easy to handle.
- Environmental benign.
- It should be stable, so it has not to change structure or degrade when is overcharged or over-discharged.

At present, most of the cathode material studied and used can be divided into two big groups, both having a really good ability to reversibly intercalate lithium ions during charging and discharging cycles and for this reason they are very used in the application: Layered compounds and olivine materials.

The first consists of layered compounds, as the name suggests, with an anion close-packed or almost close-packed lattice in which the alternate layers between the anion sheets are occupied by a redox-active transition metal. Lithium then inserts itself into the empty strata, as shown in **Figure 4**. The most used in this group are LiCoO_2 , NMC, NCA, LiNiO_2 and LiMn_2O_4 . LiCoO_2 is largely employed, characterized by a voltage of 3.9 V and a theoretical capacity of about 274 mAhg^{-1} . Despite of that at most only half of lithium can be reversibly extracted and inserted due to structural restriction. For this reason most of the time the voltage is increased up to 4.2-4.25 V, regardless a small decrease in the total capacity of about 70 units, because the battery can be cycled over 1000 charging/discharging cycles.

NMC, specifically $\text{LiNi}_x\text{Mn}_y\text{Co}_z\text{O}_2$, stands out as the most utilized cathode material in current applications. Its composition of nickel, manganese and cobalt offers high specific capacity, low internal resistance and excellent stability. Variants like NMC111, NMC442, NMC523, NMC622 and NMC811 exist, differing in the ratios of nickel, manganese and cobalt. In recent years, there is a growing trend towards NMC-type cathodes with reduced cobalt content, aiming to address sustainability and cost concerns linked to cobalt limited supply. In addition to the benefits related to decreasing cobalt concentration, the increased nickel concentration enhances capacity, with NMC811 showing an improved specific capacity of 200 mAhg^{-1} when compared to NMC111 (160 mAhg^{-1} , both 4.3 V vs Li^+/Li). However, higher nickel concentrations heighten cathode reactivity with the electrolyte, necessitating additional measures like electrode coatings or advanced particle designs. Strategies such as core-shell and concentration gradient particles help maintain desirable electrochemical performance by incorporating nickel-rich NMC in the core for capacity and less reactive manganese-rich NMC on the surface for improved stability against electrolyte interaction.

NCA cathodes, $\text{LiNi}_{1-x-y}\text{Co}_x\text{Al}_y\text{O}_2$, join NMC-type cathodes as front runners within the automobile industry. They show a comparable specific capacity to NMC811, but the value of the latter is higher, while the incorporation of aluminum ions provides enhanced thermal stability. For these reasons NCA is often the choice for “long-range” EVs, such as the ones provided by Tesla, which boast ranges $> 500 \text{ km}$ [52].

Speaking about different solutions , LiNiO_2 is not extensively employed despite its favorable capacity values and the higher natural abundance of nickel compared to cobalt. Its limited usage can be attributed to the absence of a well-defined stoichiometric representation and its susceptibility to thermal instability [53].

The alternative is LiMn_2O_4 . The latter is the last on the list because, despite its low toxicity and abundant raw material sources, it registers a great volume change of 6.5% during lithiation process. This leads to a structure degradation, properties deterioration and low cycle life [54].

The other group belong to olivine materials, depicted in **Figure 5**. The most used between them is LiFePO_4 since its low cost, abundance in nature and environmentally friendly being. Furthermore its olivine structure guarantees a usage at around 100% of the theoretical capacity. The problem related to this material is a low conductivity and most of the time a carbonaceous coating is present to overcome it.

For the sake of completeness it is worth mentioning another material that is now currently under investigation: Vanadium Oxide. Lots of attention is around it due to its high energy density, however low discharge voltage limit its adoption.

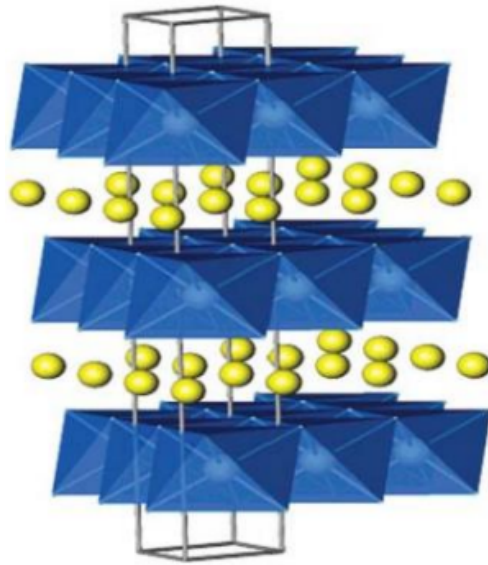


Figure 4: Schematic drawing of layered structure (LiCoO_2 , NMC, NCA LiNiO_2 and LiMn_2O_4) which shows the lithium ions between the transition-metal oxide/sulphide sheets [28].

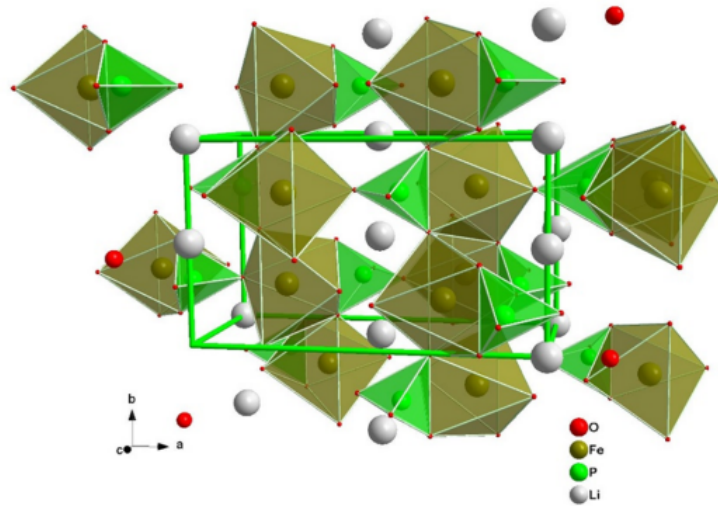


Figure 5: Structures of orthorhombic LiFePO_4 [29].

1.2.3 Binders

Binders are an important element of the electrode that can increase the battery performance due to their chemical and adhesive properties. Entering more into the details, the aim of the binder, as the word suggest, is to bind the active materials of the electrode, as shown in **Figure 6**. Usually a combination of polyvinylidene fluoride, PVDF, and N-methyl pyrrolidone, NMP, is used. However this type cannot be used when an ionic liquid based electrolyte is present because its mass tends to break away form the current collector in response to the PVDF swell due to the ionic liquids. The results of this process is a decline in the performance of the lithium-ion battery during charging-discharging, quick capacity loss and decrease battery serviceability.⁵ [55]

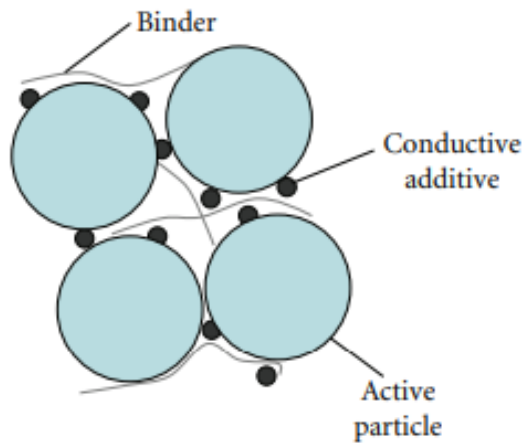


Figure 6: Illustration of a small part of an electrode, focusing on binder [30].

⁵Refers to the ease with which a battery can be maintained, repaired or serviced during its operational life.

1.3 Electrolytes for lithium-ion batteries

The electrolyte holds a crucial role in lithium-ion batteries, primarily responsible for ions transportation. A high-quality electrolyte should exhibit the following characteristics:

- Good ionic conductivity.
- High chemical stability that reduced the formation of not-desired product during undesired reactions.
- Ensuring electronic insulation.
- Safe to use.

Typically, the electrolyte comprises three components: conducting salts, additives and a solvent, with the additives dissolved in the latter. These components can exist in solid or liquid form, with polymer-based and liquid electrolytes being the most prevalent for these type of batteries [56].

Polymer-based electrolytes usually consist of a polymer matrix, conducting salts and solvents, such as Polyethylene Oxide, PEO. They are known for their high ion conductivity achieved through lithium-based salts or polymers and they can also fulfill the separator function.

Liquid electrolytes also exhibit high ion conductivity and utilize various solvents with specific dielectric and viscosity constants to meet the required criteria. The most used is LiPF_6 [57][58].

1.4 Separators for lithium-ion batteries

The separator assumes a crucial role in the functionality of lithium-ion batteries. Comprising a porous membrane positioned between the anode and cathode, its primary function is to prevent direct contact between the two electrodes, while facilitating the flow of ions in the presence of current within an electrochemical cell. Since the available solutions on the market are not highly diverse, the separator typically consists of a polymeric membrane, usually polyethylene designed with a microporous layer. A proficient separator should possess the following attributes:

- Sufficient strength to prevent damage during battery construction.
- Stability to minimize side effects on the battery during charge and discharge.
- Capability to contribute to the power cycle life and safety of the battery [30].

1.5 Causes of the stresses development in electrode materials from lithiation/delithiation

After a brief introduction about the Li-ion batteries and their main components this sub-chapter is crucial for the development of the work. The main objective of this thesis is to develop a model able to estimate the stresses in the anode during the lithiation/delithiation process, so understanding the main reasons for which these stresses are generated is a key factor to proceed ahead with the analysis.

As outlined in the previous section, the working principle of Li-ion batteries involves a continuous insertion/removal of Li-ions from the electrode materials during electrochemical cycling. The insertion/removal can result from different mechanism depending on the type of the active electrode materials. For instance, in graphite or layered oxides like LiCoO_2 occurs by intercalation and de-intercalation. The latter can be defined as the reversible insertion of guest species in-between crystallographic planes of the host crystal lattice without disturbing the arrangements of these planes [59][3]. On the other hand, metallic anode such as Si, Sn and Al allow intake and release of Li-ions via alloying and de-alloying, forming intermetallic compounds or solid solutions with lithium [60]. Therefore the word lithiation/de-lithiation is a more generic term referred as intercalation/de-intercalation or alloying/de-alloying.

In both cases Li-ions require temporary accommodation within the host lattice as they are repeatedly inserted and removed. Accommodating these guest species changes the spacing between crystallographic planes of the host structure, leading to dimensional changes. Such insertion/removal also leads to transformation and changes in crystal symmetries in many materials. The particles desire to expand or contract, but being unable due to certain constraints, some stresses, called diffusion-induced stresses (DIS), are generated inside them. These constraints can be summarized as follows:

- Physical constraints in the dimensional changes in active materials: the major structural changes occur in the lattice parameter variation [61] or in the formation of new crystalline or amorphous phases due to the insertion or removal of Li-ions [62][63]. The major effects of these phenomena are a overall volume changes that are usually constrained by the neighboring particles, by the substrate current collector or by the space constraints of the cell, as it is depicted in **Figure 7 (a) and (b)**. These constraints make it impossible for the particle to expand or contract, consequently leading to the development of stress. Typically, this can be defined as the predominant source of stresses in numerous electrode materials.
- Inter-particle contacts: as described in **Section 1.2** the most prevalent electrode architectures consist of particles of active materials, along with binders and conductive additives. As the

volume of the active particle increases during lithiation, it is possible for them to come in contact between each other and generate a high stress at the interface, as can be seen in **Figure 7 (b) and (c)**.

- Mismatch between crystalline phases and Li-concentration gradients: since the lithiation or delithiation occurs mainly due to the diffusion of the Li-ions through the bulk of the active materials, steep Li-concentration gradients can be formed in the active material itself. These differences, depending on transport limitations associated with Li-diffusivity and current density, are more substantial at higher electrochemical cycling rates [64][65][66][67]. These gradients lead to different volume changes from the surface to the core, which implies that adjacent regions with the same active materials may have different crystal phases and different volumes. Obviously the direct contact between these regions leads to an induced stress development.
- Surface reactions: while the previous points described the causes of stress development due to the actual process of lithiation or de-lithiation, this one described the interaction between the electrodes and the electrolyte. The latter contains Li-ions usually in the form of inorganic salts dissolved in organic solvents, different from the Li-ions that belong to the electrodes, using the electrolyte as a medium for transportation. In fact the ions belonging to the electrolyte have significantly larger sizes compared to the unsolvated Li-ions, related to the electrodes. Hence the incorporation of the solvated ones can lead to a tremendous increase in spacing between the graphite basal planes. The same happens for all the other electrode materials, leading to a significant stress development. Fortunately this effect is mitigated with the formation of solid electrolyte interface (SEI), that is a layer, which is always forming with commonly used solvent, having the characteristic of avoiding further contact between the electrodes and the electrolyte. However the formation of this layer is not totally beneficial because it leads to irreversible consumption of Li, which cannot be further used for additional electrochemical cycling. Furthermore it has been observed by the study of Mukhopadhyay et al. [68] that this layer leads also to a compressive stress over almost 18 electrochemical cycles [26].

It must be noticed that these stresses are repeated cycle over the cycle, entering the fatigue field. It is worth clarifying that this field is not the object of the thesis, which wants to evaluate the static stress developing inside the battery. This is a sufficient approximation because the static stresses are the highest, being the predominant stress-factor for performance degradation.

Continuing the discussion on stresses, their magnitude varies over several factors such as the particular electrode material, the electrode architecture, electrode composition, the mechanism of Li-ions

insertion/removal, the electrochemical cycling rate⁶ and the potential range under consideration⁷. In conclusion electric cycling is one of the major causes of damage in lithium-ion batteries and substantial efforts have been dedicated to understanding and mitigating this phenomenon. The damage is primarily linked to the insertion and extraction of lithium ions within the active materials. These processes induce diffusion-induced stresses, resulting in crack propagation, material loss, pulverization of the active materials and other factors discussed in **Section 2.2** [16].

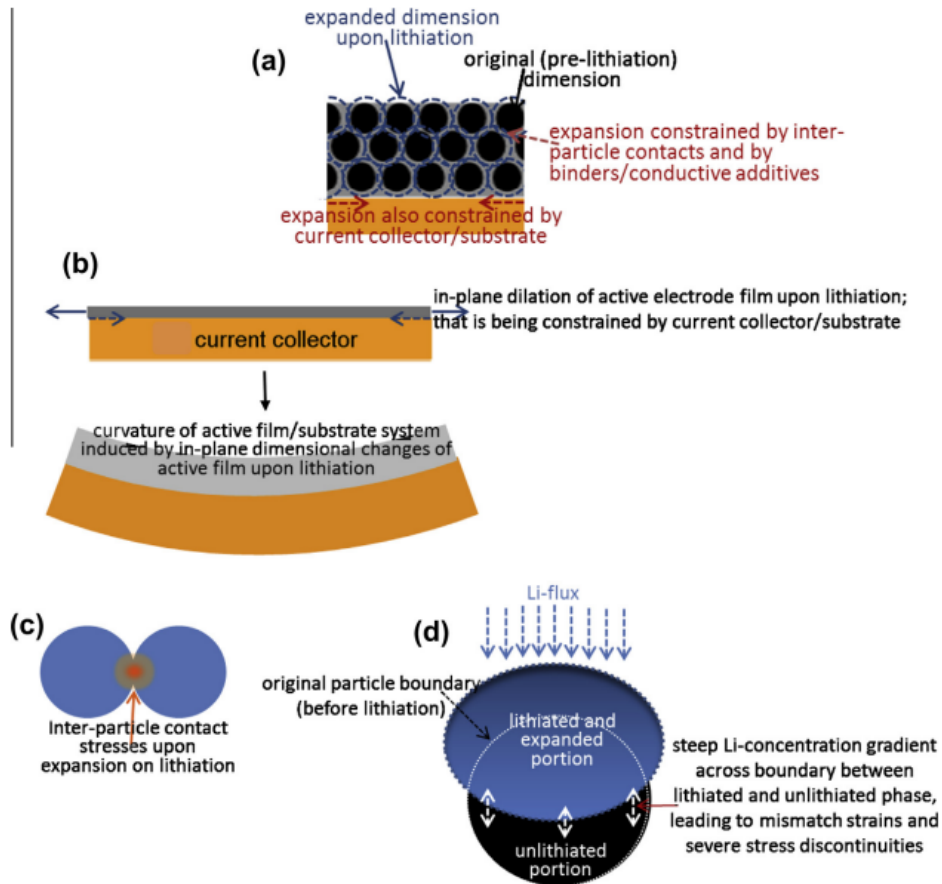


Figure 7: Schematic illustrations of (a) constraining effects of neighboring active particles, inactive matrix and current collector/substrate on the expanding active particles upon lithiation of ‘porous composite electrode’; (b) stress generated at inter-particle contact between expanding electrode particles upon lithiation; (c) constraining of the in-plane dilation of thin film electrodes, upon lithiation, by the inactive current collector/substrate; (d) Li-concentration gradient between lithiated and unlithiated portions of a particle, resulting in the development of stress discontinuities. The same is true for adjacent regions possessing different crystal structures/phases [26].

⁶Speed at which a battery or electrochemical cell can undergo charging and discharging cycles.

⁷Range of voltages between the battery fully charged state and its fully discharged state.

2 Literature Review

This chapter plays a crucial role in this work by presenting studies and considerations from previous research. Its main purpose is to provide a clear understanding of the current state of knowledge and discoveries related to the chosen topic. Through a detailed review of past research, this chapter offers insights into what has been learned so far. By summarizing previous findings, it sets the stage for the thesis contribution to the field and emphasizes the importance of the research, all avoiding replicating something already done in the past.

2.1 Characteristic of different electrode materials during lithiation or de-lithiation process

Understanding the characteristics of the materials used in Li-ion batteries is crucial for an optimal selection. It is important to consider all the features of a material before integrating it into a battery, in order to prevent undesirable behavior.

Several studies [1][2][3][4][5][6][7] have been conducted on this subject, all summarized in **Table 1**. In the latter are reported different aspects, experienced during lithiation and de-lithiation, for both anode and cathode active materials such as phases, crystal structures, lattice parameters, crystal volumes (also volume changes) and theoretical capacity.

Diving into the specifics of some of the reported characteristics that require clarification, the second column is referred to the different phases formed, depending on the degree of lithiation/de-lithiation, during the process. Furthermore the fifth column, referred as unit cell volume, indicates the volume of the cell structure, while the seventh column is referred to the volume per host atom and indicates the volume available in the structure for a foreign atom insertion. It is worth pointing out that all the data present are related to a charging process, in which lithiation involves the anode, which expand, and de-lithiation the cathode, which contracts, as shown in **Figure 2**. Obviously it will be the dual for discharging process.

Entering into details of anode materials behavior, comparing graphite and silicon is evident that the latter has a higher theoretical capacity in all the phases that can be formed, while the first evidence a lower volume expansion as a result of an intercalation process. Concerning the cathode materials, while there are notable differences in terms of volume expansion and theoretical capacity, the contrast is not as pronounced as observed with the anode materials. For instance, the theoretical capacity of LiCoO_2 surpasses that of LiMn_2O_4 and LiFePO_4 , while its volume expansion is more pronounced compared to the other two options. It is worth mentioning that NMC is not included in this table, even if it is one of the most used materials for cathode, but its behavior closely resembles that of LiCoO_2 because it can be considered as a solution of LiCoO_2 and $\text{LiNi}_{0.5}\text{Mn}_{0.5}\text{O}_2$ [69].

While this section provides a broad overview of the electrode materials response, it will be delved deeper into the details for both cathode and anode materials in **Section 2.1.1** and **Section 2.1.2**.

Table 1: Phases, crystal structures, lattice parameters and crystal volumes that form during progressive electrochemical lithiation (of anode) and de-lithiation (of cathode) of the various electrode materials for Li-ion batteries[1][2][3][4][5][6][7].

Electrode material	Phase	Space group (structure)	Unit cell parameter (Å)	Unit cell volume (Å ³)	% Increase in unit cell volume	Volume per host atom (Å ³)	% Volume increase per host atom	Theoretical Li-capacity (mAhg ⁻¹)
ANODE								
Graphite (C)	C	P6 ₃ /mmc (hexagonal)	a = 2.464 e ^b = 4.239 c = 6.711;d[0002] ^c = 3.302	V ^a = 51.38	0 (based on V)	-	-	-
	LiC ₁₈ (dilute stage II)	P6/mmm (hexagonal)	a = 2.47 e ^b = 4.254 c = 6.711;d[0002] = 3.469	V = 54.37	5.8 (based on V)	-	-	71
	LiC ₁₈ (stage III)	P6/mmm (hexagonal)	a = 4.288 e ^b = 4.255 c = 7.07;d[0002] = 3.395	V = 53.22	3.6 (based on V)	-	-	105
	LiC ₁₂ (stage II)	P6/mmm (hexagonal)	a = 4.288 e ^b = 4.262 c = 7.006;d[0002] = 3.417	V = 53.76	4.6 (based on V)	-	-	185
	LiC ₆ (stage I)	P6/mmm (hexagonal)	a = 4.305 √3 · a = 4.289 c = 3.706;d[0002] = 3.547	V = 56.51	10 (based on V)	-	-	372
Si	Si	Fd3̄m (cubic)	a = 5.472	V = 163.84	0	19.6	0	-
	LiSi	I41/a (tetragonal)	a = 9.357 b = 9.357 c = 5.746	V = 503.071		31.4	60	954
	Li ₁₂ Si ₇	Pnma (orthorhombic)	a = 8.532 b = 19.612 c = 14.302	V = 293.14	1360.66	43.5	122	1635
	Li ₁₃ Si ₄	Pbam (orthorhombic)	a = 7.914 b = 15.084 c = 4.429	V = 528.17	222.69	67.3	243	3100
	Li ₁₅ Si ₄ Li ₂₂ Si ₅	4I3̄d (cubic) F23 (cubic)	a = 10.595 a = 13.189	V = 2294.22	1300.28	76.4 82.4	290 320	3590 4200
CATHODE								
LiCoO ₂	LiCoO ₂	R3̄m (trigonal) (H1)	a = 2.817 c = 14.058	V = 96.75	0	-	-	270
	Li _{0.9} CoO ₂	R3̄m (trigonal) (H1)	a = 2.817 c = 14.08	V = 96.8	0	-	-	240
		R3̄m (trigonal) (H2)	a = 2.814 c = 14.19	V = 97.25	0.5 (based on initial H1)	-	-	
	Li _{0.78} CoO ₂	R3̄m (trigonal) (H2)	a = 2.812 c = 14.25	V = 97.75	1 (based on initial H1)	-	-	200
	Li _{0.51} CoO ₂	R3̄m (trigonal) (H2)	a = 2.812 c = 14.3	V = 98.0	1.3 (based on initial H1)	-	-	135
	Li _{0.5} CoO ₂	C2/m (monoclinic)	a = 2.813 c = 14.42	V = 98.6	1.9 (based on initial H1)	-	-	150
	Li _{0.45} CoO ₂	R3̄m (trigonal) (H2)	a = 2.809 c = 14.4	V = 98.3	-0.3 (based on Li _{0.5} CoO ₂)	-	-	120
	Li _{0.22} CoO ₂	R3̄m (trigonal) (H2)	a = 2.81 c = 14	V = 95.7	-2.9 (based on Li _{0.5} CoO ₂)	-	-	65
	CoO ₂	R3̄m (trigonal) (H2)	a = 2.822 c = 12.879	V = 88.8	-9.9 (based on Li _{0.5} CoO ₂)	-	-	-
LiMn ₂ O ₄	Li ₂ Mn ₂ O ₄	I4 ₁ /amd (tetragonal)	a = 5.646 c = 9.25	V = 294.86	-47.3 (based on LiMn ₂ O ₄)	-	-	240
	LiMn ₂ O ₄	Fd3m (cubic)	a = 8.242	V = 559.47	0	-	-	120
	Li _{0.5} Mn ₂ O ₄	Fd3m (cubic)	a = 8.15	V = 541.34	-3.2 (based on LiMn ₂ O ₄)	-	-	60
	Li _{0.4} Mn ₂ O ₄	Phase I: Fd3m (cubic) Phase II: Fd3m (cubic)	a = 8.124 (fraction: 0.7) a = 8.103 (fraction: 0.3)	V = 536.18 V = 532.03	-4.2 (based on LiMn ₂ O ₄) -4.9 (based on LiMn ₂ O ₄)	-	-	48
	Li _{0.3} Mn ₂ O ₄	Phase I: Fd3m (cubic) Phase II: Fd3m (cubic)	a = 8.108 (fraction: 0.41) a = 8.08 (fraction: 0.59)	V = 533.02 V = 527.51	-4.7 (based on LiMn ₂ O ₄) -5.7 (based on LiMn ₂ O ₄)	-	-	36
	Li _{0.15} Mn ₂ O ₄	Phase II: Fd3m (cubic)	a = 8.048	V = 521.27	-6.8 (based on LiMn ₂ O ₄)	-	-	18
	LiFePO ₄	LiFePO ₄	Pnma (orthorhombic)	a = 10.33 b = 6.01	V = 291.2	0	-	-

^a Average cell volume of the space defined by two neighboring C-planes.

^b Edge length of the rhombohedral cell with saturated Li in-plane density.

^c Average layer spacing of neighboring C planes.

2.1.1 Characteristic of anode materials during lithiation/de-lithiation process

As already announced, in this section the characteristics of anode materials will be treated with more attention. The first focus is on graphitic carbon that is one of the most used materials for the anode of Li-ion batteries. It can be visualized by consisting stacks of graphene sheets which in between the Li-ions are intercalated forming the so called Li-graphite intercalation compounds (Li-GICs). The composition corresponding to the maximum Li-intake has only one Li-ion in between every other basal plane of the graphite, for this reason the graphite can host only one Li-ion per six carbon atoms. The previous number is very important and it should be as larger as possible because is directly related to the gravimetric capacity. In fact in this case, being this number not so high, the maximum gravimetric capacity is $\sim 372 \text{ mAhg}^{-1}$, smaller with respect to other competitors on the market. Despite this value that is not one of the highest, the volume variation encountered upon full lithiation is $\sim 14\%$, a really low value and this time better than the competitors. As a consequence the diffusion-induced stress generated are much lower with respect to other solutions. Furthermore it has been estimated that the lithiation process also reduces the elastic modulus, by $\sim 12\%$ upon full lithiation in this case. Another important observation is that the graphite lithiation/de-lithiation process occurs only for potential in between ~ 0.3 and ~ 0.01 V. This behavior is depicted in **Figure 8**, in which the degree of lithiation, representing the ratio of the number of lithium ions incorporated into the material to the total number of lithium ions that the material can accommodate, is plotted on the x-axis. This ratio varies between 0 (no lithiation/fully de-lithiation) and 1 (full-lithiation/no de-lithiation). Meanwhile the y-axis denotes voltage, confirming the previously mentioned range. Even though graphitic carbon is still the most commonly used anode material, research efforts over the last decades have been directed towards metallic anode materials as Si, Sn and Al. For the latter alternatives the lithiation happens for alloying/de-alloying of Li-ions and their theoretical gravimetric capacity is higher, by almost an order of magnitude in some cases, with respect to graphite ones. Obviously also the number of lithium ions that can be hosted are higher by ~ 3 - 10 times [31]. Entering more into the details the Si has a theoretical gravimetric capacity of $\sim 4200 \text{ mAhg}^{-1}$ upon full lithiation, Sn has a theoretical gravimetric capacity of $\sim 1000 \text{ mAhg}^{-1}$, which is lower than the previous due to the higher atomic weight, and Al has a theoretical gravimetric capacity of $\sim 2200 \text{ mAhg}^{-1}$. Despite these benefits on the capacity, all these materials register a huge volume increase due to lithiation, which can arrive to value up to 400% for Si and make them really difficult to be used for the battery application. All of these features can be seen in **Figure 9 (a)**, while **Figure 9 (b)** illustrates the behavior specifically for the silicon phases formed during the process. It is clear that as the degree of lithiation increases, there is a significant rise in volume expansion, accompanied by a subsequent softening of the materials resulting in a decrease in the elastic modulus.

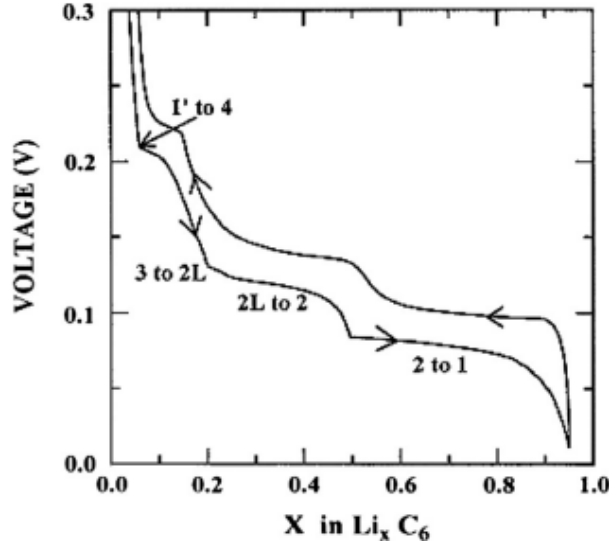


Figure 8: Typical potential (against Li/Li₊) vs. degree of lithiation/delithiation for graphite [26].

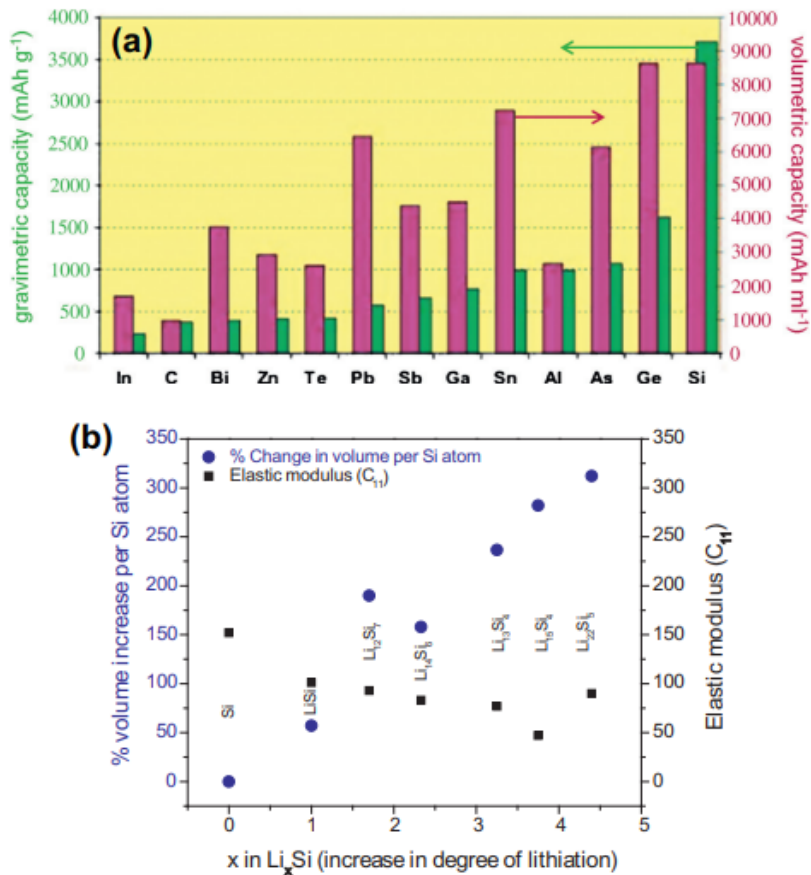


Figure 9: (a) Volumetric and gravimetric capacities of the various anode materials, showing the metallic anode materials possessing considerably superior capacities, compared to carbon. (b) Variation of % volume change per Si atom and longitudinal elastic modulus with degree of lithiation. Note the significant increase in volume, along with softening, with progress of lithiation [1][31].

2.1.2 Characteristic of cathode materials during lithiation/de-lithiation process

As already announced, in this section the characteristics of cathode materials will be treated with more attention. Looking at **Table 1** it can be noticed that the percentage of volume expansion, contraction in this case, is way less than the one experienced in anode materials, and in the development of this section will be understood why it happens.

The most widely used materials for cathode are transition metal oxides, such as LiCoO_2 , LiMn_2O , LiFePO_4 , NMC and NCA. LiCoO_2 is characterized by a net theoretical capacity of $\sim 270 \text{ mAhg}^{-1}$, only about half of which is presently usable. This corresponds to 50% of Li-ions extraction and to a voltage usage between 3.5-4.25 V against metallic Li, higher than the voltage window for the graphite shown in **Figure 8** [70][5]. Furthermore the decrease in unit cell volume is 3%. This value is really low with respect to the one experienced in anode metallic materials, which were two orders of magnitude greater. Nevertheless it is worth pointing out that a strain $> 0.1\%$ is considered severe for the brittle ceramic (oxide) cathode materials, so even a low number can cause problems to the battery.

Speaking about another solution, since Mn is cheaper and more environmentally friendly compared to Co, cathodes based on LiMn_2O_4 are also extensively used in Li-ion batteries [71]. One of its characteristics is that, during de-lithiation (charging), the Li-ions are extracted between $x = 1$ (full-delithiation) and $x = 0$ (no-delithiation) within the potential range of 3.0 and 3.5 V as shown in **Figure 10 (a)**. In this case the degree of delithiation can also go beyond the value of 1, this looks quite strange and is related to the movement of the Li-ions towards the vacant octahedral sites. Speaking about the volume contraction, as depicted in **Table 1**, it is in the order of 7.5% for both the situation in which a cubic phase is present. It is important to clarify that these two, stages I and II in **Figure 10 (a)**, are not co-existing but are two different phases that can be formed during lithiation depending on the degree of it. Going beyond 1 as the degree of lithiation a tetragonal phase is formed, stage III in **Figure 10 (a)**, leading to a huge volume contraction of $\sim 50\%$ that should be avoided. Instead **Figure 10 (b)** shows how the lattice parameter of both the cubic faces changes in function of the degree of lithiation. The trend is both upwards and really similar, with the exception that dimensional values belonging to phase I are higher.

Another interesting material that is currently under-investigation is LiFePO_4 , mainly due to its high actual gravimetric capacity, $\sim 170 \text{ mAhg}^{-1}$, environmental compatibility, improved safety and superior performance under adverse conditions. Furthermore it registers also good values of volumetric expansion, in the order of $\sim 6.8\%$ [6][72].

Regarding NMC, which is presently the most widely used cathode material, it is difficult to identify unique characteristics as they are related to the percentage of each element present. Nevertheless, it can generally be observed that during lithiation the voltage typically ranges between 4.3 and 3.4 V in most cases, with slight variations depending on the percentage of element involved. More-

over, during charging, nickel undergoes oxidation first, with the participation of cobalt only above approximately 4.3 V vs Li/Li⁺. Going into more detail of the different available solutions, recent attention has been focused on NMC compositions with higher nickel content, as this results in an increase in capacity. For example, the capacity of NMC 811 is about 190-200 mAhg⁻¹, higher than the one of NCM 422 that is equal to 160 mAhg⁻¹ [69].

Concerning automotive applications NCA stands out as a highly favored cathode material.

LiNi_{0.8}Co_{0.15}Al_{0.05}O₂, which is the most common NCA used, shows a high theoretical capacity up to 279 mAhg⁻¹ and an actual capacity of ~190 mAhg⁻¹, higher than the competitors such as LiCoO₂ which achieves ~148 mAhg⁻¹ and LiFePO₄ with ~170 mAhg⁻¹. Indeed NCA is characterized by a high energy and power density with an average voltage of 3.7 V, making it suitable for automotive applications [73].

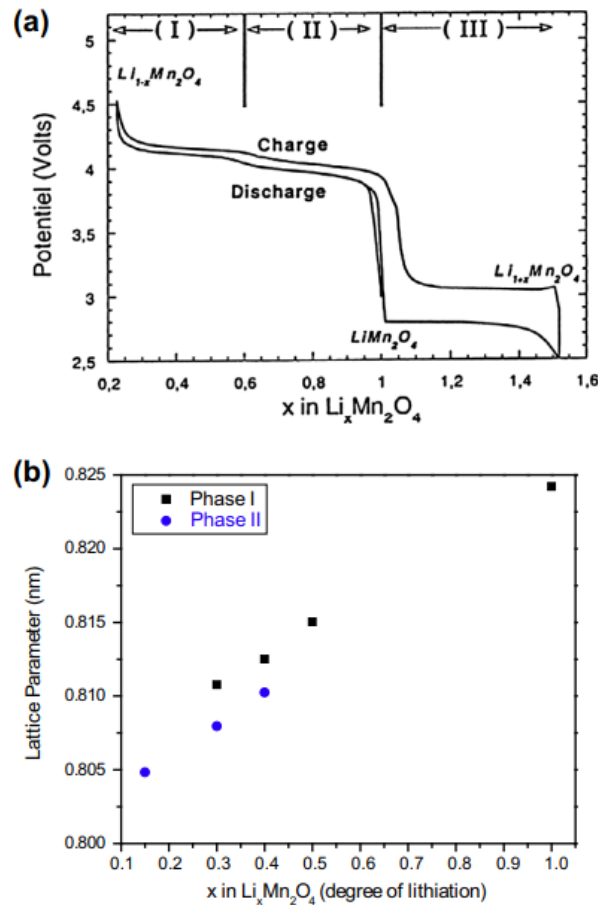


Figure 10: (a) Variation of potential (vs.Li/Li⁺) with respect to degree of lithiation (discharge) and de-lithiation (charge) for Li_xMn₂O₄, even during lithiating beyond x = 1. (b) Variation of lattice parameter for both the cubic phases of Li_xMn₂O₄ with degree of lithiation (between x = 0.1 and 1) [32].

2.2 Effects of diffusion-induced stresses

This chapter plays a crucial role in understanding the relationship between lithiation stresses and their effects, as identified in previous studies. Its aim is to provide a comprehensive overview of the current state of research on the subject. While the primary objective of the thesis is not to explore the effects of diffusion-induced stress, but rather to develop a predictive stress model, comprehending their consequences remains important. This underlines that the problem under investigation has an effective impact on the battery degradation. It serves as motivation for the research and push to find ways to minimize stress as much as possible.

The first effect is the mechanical degradation of the electrode materials, often manifested in fracture/disintegration of the electrode that is one of the main reasons for the eventual failure. It is important to note that 'failure' does not solely refer to the physical destruction of the battery; it signifies that the battery is no longer able to perform its function as effectively as before. Continuing speaking on mechanical degradation, under most circumstances the fractured portion loses contact with either the current collector or the rest of the active materials, leading to electrical isolation. Hence, progressive fracturing reduces the amount of the electrode materials and decreases the Li-capacity of the cell. Furthermore stress development also damages the binder and reduces the pore volume⁸[74][64][65][75][76][77]. To improve the comprehension of mechanical degradation, it is worth pointing out that it is directly related to cracks creation, distribution and propagation. To this purpose H.-H. Ryu et al. [33] study the crack propagation in charging and discharging process of a Ni-rich Li[Ni_xCo_yMn_{1-x-y}]O₂ cathode. As shown in **Figure 11** charging and discharging cycles make occur cracks propagation and bifurcation inside the material particle, leading to capacity and power loss.

Mechanical degradation, as also said before, leads to a capacity fade and reduces the energy density of the cells as electrochemical cycling continues. Capacity fades with electrochemical cycling, and so lithiation process, occurs in a severe way for all the metallic anodes that exhibit a huge volume change upon lithiation/de-lithiation, as shown in **Figure 12 (a)-(b)-(c)**. For graphitic anode, which exhibits a small volume increase compared to the metallic ones, capacity fade is not marked as before, **Figure 12 (b) and (d)** [78][79][63][80]. In addition to capacity fade, the fracture results in the creation of a fresh electrode surface. When this fresh surface comes into contact with the electrolyte, further electrolyte reduction takes place, leading to the formation of the SEI layer, resulting to the direct consequence of decreasing the capacity. Dimensional changes of the active materials also provoke fracture of the formed SEI, which results in a dynamic process involving the formation and reformation of SEI. This process leads to an increase of the overall stress inside the battery and also to a continuous irreversible consumption of Li from the system. It has also been observed that

⁸Total volume of void spaces or pores within a material.

this effect, regarding SEI layer formation, is more pronounced for metallic alloy materials due to their huge volume increase [81][82][68]. In addition to that, the stresses can reduce also the usable capacity to nearly half the theoretical one, as experienced for LiMn_2O_4 and LiCoO_2 [83][71].

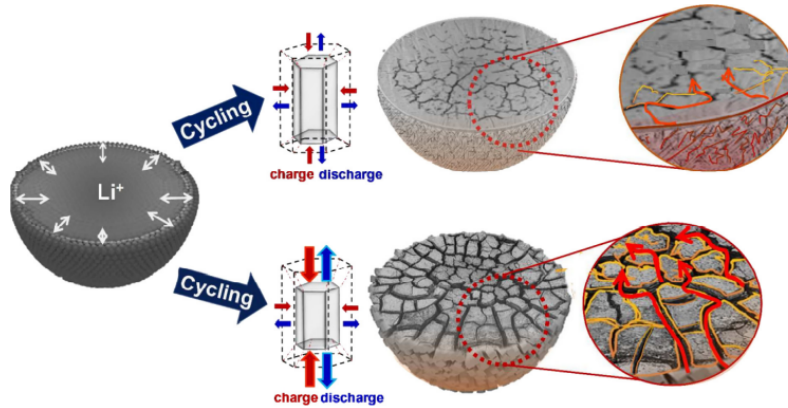


Figure 11: Internal crack distribution for Ni-rich $\text{Li}[\text{Ni}_x\text{Co}_y\text{Mn}_{1-x-y}]\text{O}_2$ cathode particle [33].

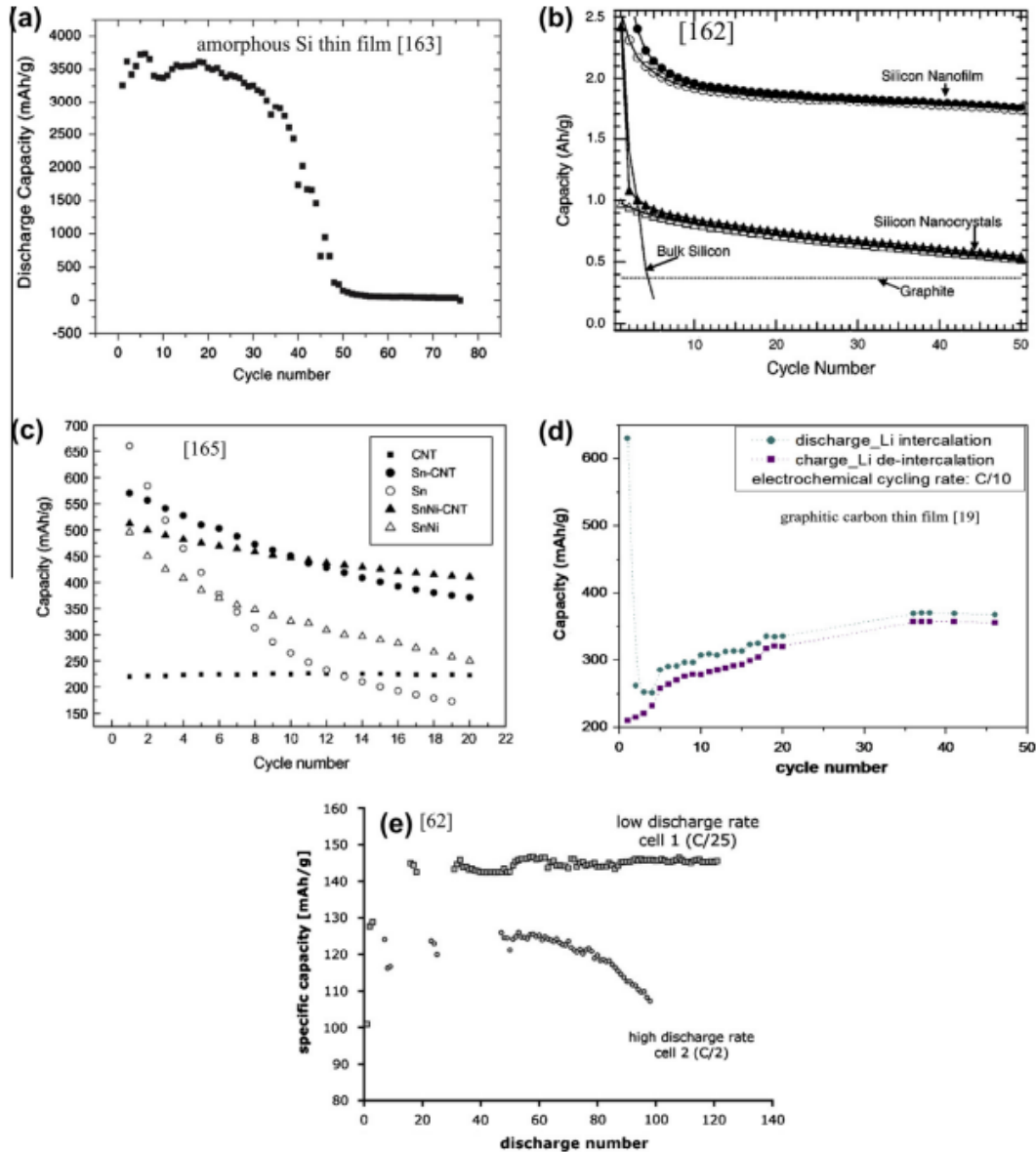


Figure 12: Variation of specific capacities for different electrode materials in function of the number of electrochemical cycles [34][35].

2.3 Coupled electrochemical-mechanical model for Li-ion cell

The main objective of this work is to develop an electrochemical-mechanical Li-ion cell model to predict the stresses inside battery cells. In the broadest sense, this type of model couples particle, electrode and battery level mechanism and electrochemistry. Within a battery, there are hundreds of layers of electrodes, and the inherent multiscale structure of electrode makes battery level computationally very expensive. Although the literature includes a case, done by P. Gupta and P. Gudmundson [84], where the battery level is also examined, this work will concentrate solely on the

first two levels, in an attempt to build a model that is both efficient and distinct from what is done in past studies. For the type of model developed in this thesis, the bases principle and the explanation of the choices made please make reference to **Section 3**. Continuing with the description, the model implemented should initially be a functional electrochemical model and subsequently integrate mechanics, for this reason the following lines will provide an explanation of these two aspects.

An electrochemical model can reflect the electrochemical reactions inside the lithium-ion battery through the utilization of the porous electrode theory principles formulated by Newman et al. [85]. Therefore, it is commonly used in the simulation research for life prediction and cell decay mechanism analysis of lithium-ion batteries [86]. The electrochemical mechanism model can not only describe the macroscopic physical quantities such as voltage and current, but also simulate the important microscopic physical quantities inside the battery strictly related to the lithium diffusion, as the lithium concentration inside each active particle or in the electrolyte.

But this type of model alone is not sufficient for the evaluation of the stresses, once constructed it is necessary to determine how to integrate it with the mechanical one. The coupling consists of utilizing data output from the electrochemical model, such as the lithium ions concentration within the active particle, active particle position, shape and geometry, Young modulus, Poisson ratio and volume expansion as functions of the degree of lithiation for the materials considered. If the electrochemical model provides accurate data as input, a well-built mechanical model will function effectively. These types of models are scarce in the literature, that is plenty of electrochemical ones but the coupling with mechanics is not so widespread. Anyway, to make a classification of the one present in the studies, they can be divided in different sub-classes depending on the geometry used for represent the lithium-ion cell. It is worth pointing out that this type of model integrates a microscopic scale with a macroscopic scale in the majority of the case, except for the single-particle model, that will be introduced later, which is characterized only by the microscopic one. The microscopic scale is the scale of the active particle and is usually represented by one dimension, the radius of the particle because most of the time they are assumed to be spherical. The macroscopic scale depicts the entire electrode level and depending on the situation can be represented by one dimension, which is the thickness of the electrode, or by two or three dimensions to closely approximate the actual form of a cell. Depending on the different scales and dimensions involved, the models present in the literature are divided in the following sub-classes: Single-particle SP, mono-dimensional 1D also called pseudo-two-dimensional P2D, two-dimensional 2D and three-dimensional 3D. It is important to observe that the designations given to classes related to dimensions, like 2D, are applied to the macroscopic dimensions, describing how the entire electrode is illustrated. Consequently, even though a single-particle model might depict a spherical particle in one, two, or three dimensions, all these cases are categorized within the same class. The models

described in the literature are outlined in **Table 2**, where the third column pertains to all studies associated with type that accounts for the effects of hydrostatic stress, meaning pressure stress spread all over the surface. Typically, most studies only consider radial and tangential stresses, assuming the particles to be spherical. However, more detailed models also take into account hydrostatic stress. For a more precise discussion of these stresses and their evaluation, please refer to **Section 3**

While in this sub-chapter the different models are only introduced in general, in the following ones, **Section 2.3.1 Section 2.3.2 Section 2.3.3 Section 2.3.4**, each of them will be described separately and in a more precisely.

Table 2: Li-ion cell electrochemical-mechanical model present in the literature.

Model Type	Studies	Hydrostatic stress considered	Hydrostatic stress not considered
Single-particle SP	[65] [16] [87] [88] [89] [90]	[16]	[65] [87] [88] [89] [90]
P2D	[40] [91] [66] [92] [93] [84]	-	[40] [91] [66] [92] [93] [84]
2D	[94] [95] [96]		[94] [95] [96]
3D	[39] [97] [98]		[39] [97] [98]

2.3.1 Single-particle model

In the initial section of this chapter, a brief explanation of the electrochemical single-particle model will be introduced to understand its fundamental operating principles. Following this introductory part, there will be a discussion of the studies performed on the electrochemical-mechanical models. This type of model originated as a simplification of the P2D one, which involves partial differential equations and nonlinear algebra requiring numerous iterations, lengthy calculation processes and multiple parameters. Due to the difficulties in computational efficiency and parameter identification, its application is somewhat restricted. Consequently, many researchers are continually searching for reasonable and effective simplification methods for the P2D, with the single-particle being the most commonly employed. The single-particle model, introduced for the first time by Haran et al. [99], assumes that the concentration of lithium ions in the liquid phase is uniformly distributed throughout the battery, and that the electric potential of the solid phase is consistent across the electrode. It overlooks the uneven distribution of the solid phase diffuse potential of lithium ions in the liquid phase, allowing the entire electrode to be represented by a single active particle. Building on the P2D model, it adopts simplifications such as fewer equations to solve,

fewer parameters and enhanced solving efficiency, which significantly reduces the calculation process. As a result, it has evolved into an electrochemical model suitable for real-time applications, and has been used by some researchers for real-time monitoring of lithium-ion concentrations in lithium-ion batteries. Its governing equations comprise Fick's law, which is a law detailing the diffusion occurring when solutions of different concentrations come into contact, and the Butler-Volmer kinetics equation, which describes the exponential relationship between the current density and the electrode potential, at both negative and positive electrodes [8]. These two are depicted in **Table 4 (3) and (7)**.

Nevertheless, the accuracy of the single-particle model is compromised due to the oversimplification of electrochemical processes, making it suitable only for low-rate charging and discharging conditions. To address its limitations, numerous scholars have proposed variations known as extended SP models. Luo W, Lyu C, et al. [100] incorporated the liquid phase diffusion process and the effect of heterogeneous reaction distribution into the SP model, leading to an extended one capable of supporting charge and discharge rates up to 4C. Similarly, Han X and Ouyang M, et al. [101] employed a series of first-order processes to approximate the solid-phase diffusion of lithium ions and modeled the concentration distribution of the liquid phase with a parabolic fit, proposing an extended SP suited for battery management systems. In conclusion, to summarize all the enhancements introduced with the extended models: in these versions, the electrode is still simplified to a single active particle and the electrochemical processes omitted in the original one are approximately addressed [86].

Following a brief introduction to the electrochemical model, the discussion now shifts to the coupling with the mechanical one. As previously mentioned in **Section 2.3**, this involves using input data from the electrochemical model to evaluate the stresses.

For a better visualization of the single-particle model and to summarize everything said so far, refer to **Figure 13**. Here, the electrolyte is not represented because it is considered in separator and porous electrode domains. Instead, the actual separator is typically not included because it has no significant influence on the simulation itself. This might be a bit confusing, but it is important to understand that whenever the 'separator' domain is mentioned, it actually refers to the electrolyte. In order to recap what has been discussed, the model simplifies the electrode by representing it as composed of a single particle. This approach naturally presents both advantages and disadvantages, which are detailed in **Table 3**. It is important to note that the entry in the drawback category 'active particle interaction' implies that the stresses are not accurately evaluated because, by considering only one particle, the influence of constraints from neighboring particles are neglected. Moreover, it can simulate the behavior of various types of cells, including pouch, prismatic and cylindrical, as its schematic does not closely mirror the actual form of a real cell. Indeed only the microscopic scale is considered, so consideration on the electrode thickness are not present.

Numerous studies were conducted on the single-particle type, Zhang et al. [65] present results of a set of simulation techniques for a LiMn_2O_4 , ranging from one-dimensional finite difference simulations of spherical particles, to fully three-dimensional 3D simulations of ellipsoidal particles, to systematically study the intercalation-induced stresses developed in particles of various shapes and sizes. Simulations of spherical particles show that larger particle sizes and larger discharge current densities give larger intercalation-induced stresses. Simulations of ellipsoidal particles show that large aspect ratios are preferred to reduce the intercalation-induced stresses. In total, these results suggest that it is desirable to synthesize electrode particles with smaller sizes and larger aspect ratios to reduce intercalation-induced stress during the cycling of lithium-ion batteries. Clerici et al. [16] showed the principles of diffusion induced stress theory are applied to predict concentration and stress field in the active material particles for three different state of charge levels. Coupled and uncoupled models are derived, depending on whether the effect of hydrostatic stress on concentration is considered or neglected. The analytical solution is a faster and simpler way to deal with the problem which otherwise should be solved in a numerical way with a finite difference method or a finite element model. Liu et al. [87] propose a novel binding protective structure for lithium-ion batteries and compare its performance during charge-discharge cycles with an unprotected structure, a core-shell structure and a hollow structure by analyzing their analytical solutions of radial and hoop stresses. Both analytical and numerical results demonstrate that the binding protective structure offers significant fracture-proof effectiveness and a high lithium-ion diffusion rate. It exhibits better ion permeability than the solid core-shell structure but has worse structural stability than the shell structure. A stress surge is observed at the binding interface, with an order of magnitude usually higher than that of the core-shell structure. The radial tensile stress at the interface may more easily induce interfacial debonding than superficial fractures. Chang et al. [88] propose a multiscale analysis of Si nanowire anode, tested for various sizes and shapes. Using a diffusion-induced stress model with Li concentration effects, such as softening of mechanical modulus and enhancement of Li diffusion. From the geometry context, the diffusion-induced stress model exhibits stress relaxation during the lithiation and optimal condition of the Si nanowire. Furthermore the results of the analyses of various sizes and charge rates of the Si nanowires demonstrate that the small diameter of nanowires and their slow charge rate are favorable for their safety operation. The findings also show that the ellipsoidal shape reduces the internal stress of Si nanowires. Kalnaus et al. [89] develop a work on Si particles fracture upon insertion of lithium in a Li-ion half-cell, treated within the continuum mechanics approach with brittle damage parameter. The results predict fracture upon the immediate first discharge and are in agreement with experimental acoustic emissions data obtained from charge/discharge cycling of a half cell with Si as anode active material. Considering particle size effect on developed chemical stresses suggests a critical size of a particle which would not fracture upon initial lithiation. Such critical size appears to be within the micrometer

scale. Zhu et al. [90] implemented the diffusion-driven approach and chemical potential-driven approach by developing ABAQUS user subroutines to perform the coupled diffusion-stress and crack analyses of NCM primary particles, with considering the effect of diffusion on material property. The results show that the crack initiates at the core of the particle and symmetrically propagates outward during the lithiation phase. In the delithiation phase, the internal crack gradually penetrates the particle accompanying with the formation of a new surface crack. The crack evolution assessment provides a comprehensive understanding of the failure mechanism on primary particle experiencing diffusion-induced-stresses.

Table 3: Advantages and drawbacks of the single-particle model.

Model Type	Advantages	Drawbacks
Single-particle	<ul style="list-style-type: none"> •Not computationally-intense •Perform well at low current •Every cell type can be modeled 	<ul style="list-style-type: none"> •Active particle interaction not properly described •Falls for high current •Only microscopic scale •Not precise as a 1D,2D,3D model

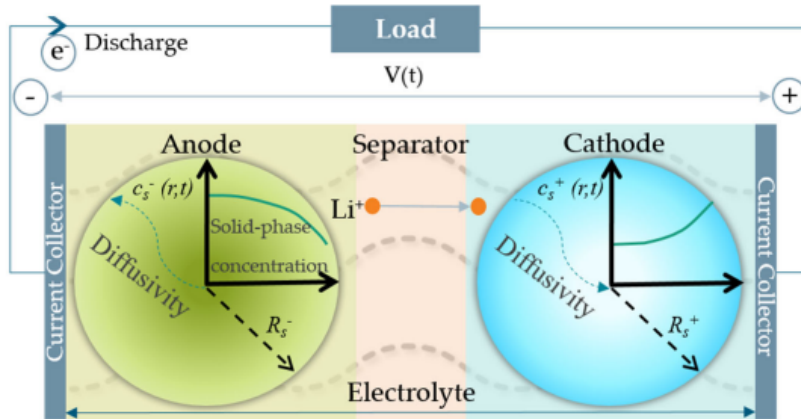


Figure 13: Single-particle model of a Li-ion cell [36].

2.3.2 Pseudo-two-dimensional model

In the initial section of this chapter, a brief explanation of the electrochemical P2D model, which can be called also 1D, will be introduced to understand its fundamental operating principles. Following this introductory part, there will be a discussion of the studies performed on this topic.

In 1993, Doyle et al. [61] introduced the P2D model for Li-ion batteries using a combination of the porous electrode theory and the concentrated solution theory. To this day the latter, depicted

in **Figure 14**, remains the most popular for Li-ion batteries. Going into details, the electrodes are considered as a porous matrix and their behavior is modeled with spherical particles surrounded by the electrolyte. The intercalation and the de-intercalation processes of the Li-ions are performed through the surface area of these particles. Also, the transfer processes are predominantly unidirectional. Its governing equations, showed **Table 5**, are:

- Fick's law of diffusion, which details the diffusion occurring when solutions of different concentrations come into contact, for spherical particles, to describe the solid-state Li-ions concentration, c_s , in the electrodes.
- Conservation of Li-ions equation to obtain the liquid-phase Li-ions concentration in the electrolyte, c_e .
- Ohm's law, which describes the movement of the electrons, in order to evaluate the solid-state potential, Φ_s , in the electrodes.
- Kirchhoff's and Ohm's laws, which deal with the movement of the electrons, to compute the liquid-phase potential, Φ_e , in the electrolyte.
- Butler-Volmer kinetics equation, which describes the exponential relationship between the current density and the electrode potential, to calculate the pore wall flux of Li-ions, J [8].

Numerous studies were conducted to test this model in different conditions. Martinez Rosas et al. [102] established a P2D model of LiMn_2O_4 battery and verified it under dynamic conditions. Zhang Q et al. [103] simulated the charge distribution of LiCoO_2 electrodes by P2D model, showing that for charge profiles with constant parameters, it predicts potential profiles in good agreement with experimental ones. While for discharging profiles with constant parameters, it has difficulties in predicting experimental data. Taslimi Taleghani et al. [104] proposed a model based on the radius of positive and negative particles and established a P2D model of 18650 LiFePO_4 battery. Following a brief introduction to the electrochemical model, the discussion now shifts to the coupling with the mechanical one. As previously mentioned in **Section 2.3**, this involves using input data from the electrochemical model to evaluate the stresses. In order to recap what has been discussed, the model simplifies the cell by representing it as a straight line composed of different segments having dimensions equal to the thickness of respective cell component: separator, cathode and anode. The electrolyte is not represented because it is considered in separator and porous electrode domain. Instead, the actual separator is typically not included because it has no significant influence on the simulation itself. This might be a bit confusing, but it is important to understand that whenever the 'separator' domain is mentioned, it actually refers to the electrolyte. This approach naturally presents advantages and disadvantages, which are detailed in **Table 5**. The

clear advantages over the single-particle model, **Section 2.3.1**, are that it considers both the microscopic scale of the active particles and the macroscopic scale of the entire electrode thickness. This approach allows for considerations not only about the particle itself but also about the entire domain considered. Nevertheless, it is not suitable for high currents even if it is more complicated than the single-particle model. Moreover, it can simulate the behavior of various types of cells, including pouch, prismatic and cylindrical, as its schematic does not closely mirror the actual form of a real cell.

Numerous studies were conducted regarding this model type. Renganathan et al. [40] develop a mathematical model of a dual porous insertion electrode cell sandwich comprised of lithium cobalt oxide and carbon, used to predict the influence of cell design parameters such as thickness, porosity and particle size of the electrodes on the magnitude of the diffusion-stress generation. The results show that the overall magnitude of stress decreased during the discharge process with a decrease in thickness, a decrease in particle size and an increase in porosity. The size of the particles in the electrode had a higher impact in reducing the stress generation than the thickness and the porosity in the simulations performed in this study. Han et al. [91] investigate the origin and evolution of the electrochemically induced stress of the graphite electrode by in situ optical experiments and simulations. The results showed that lithium intercalation leads to compressive stress, which presents a gradient distribution along the Li^+ diffusion path, and it exhibits a “piecewise” nonlinear growth trend with increasing lithiation time. In addition, as the potential decreases, the stress increases from slow to fast relative to the lithium-concentration increase, showing the characteristic of stages. Furthermore, it was found that the stress cause the slow diffusion in the late stage of lithiation, thus affecting the actual lithium-storage performance. Christensen [66] incorporate a rigorous mathematical model for diffusion-induced stress generation in spherical Li-ion active materials into a full-cell model with porous electrodes. The study shows that in conventional electrode materials with small volume expansion, pressure diffusion plays a limited role in determining the galvanostatic voltage response but becomes important in determining the stress response, whereas variability in the solid-phase diffusion coefficient can have a significant impact on both the voltage and stress responses. While they both play an important role in determining the voltage and stress response in large-volume-expansion materials, such as alloys and perhaps graphite at low utilization. Furthermore it was underlined that porous electrode effects, particularly in energy-type cells with thick electrodes, amplify the peak stresses encountered during charge and discharge and may result in nonuniform decrepitation through the depth of the electrode. Park et al. [92] develop a P2D Li-ion cell model to evaluate the stress generated within the active material particles of a battery due to the particle–particle and particle–binder interactions, and the influence of some crucial parameter on its evaluation. It is demonstrated that larger binder distributions, lower thicknesses, smaller Young modulus and radius reduce the maximum particle stress of graphite. Moreover,

smaller binder distributions and Young modulus along with larger thicknesses and radius reduce the maximum and average binder stress values. Furthermore, the interfaces between the particle–particle and particle–current collector are the typical maximum stress locations. Ali et al. [93] built a multiphysics–multiscale model to analyze the electrochemical and mechanical responses at both the particle and cell levels. The 1D Li-ion battery model is fully coupled with 2D representative volume element (RVE) model, where the particles are covered in binder layers and bridged through the binder. The simulation results show that when the binder constraint is incorporated, the particles achieve a lower surface state of charge during charging. Further, the cell charging time increases by 7.4% and the discharge capacity reduces by 1.4% for 1 C-rate charging/discharging. In addition, mechanical interaction creates inhomogeneous stress inside the particle, which results in particle fracture and particle–binder debonding. Gupta et al. [84] present a multiscale homogenization method that couples mechanics and electrochemistry at the particle, electrode and battery scales. The accuracy and efficiency of the method are demonstrated by comparisons to detailed finite element computations. Predictions of electrode layer stresses are also favorably compared to impedance measurements of electrode layers at different electrode positions. It is furthermore demonstrated that the effects of external battery loads like battery stacks, casings and external pressure can easily be captured by the model.

Table 4: P2D and single-particle model governing equations [8].

Model Type	Equation number and name	Governing equation
P2D/SP	(3) Fick's law	$\frac{\partial c_{s,k}(x,r,t)}{\partial t} = \frac{D_{s,k}}{r^2} \frac{\partial}{\partial r} \left(r^2 \frac{\partial c_{s,k}(x,r,t)}{\partial r} \right)$
P2D	(4) Conservation of Li-ions	$\epsilon_k \frac{\partial c_{e,k}(x,t)}{\partial t} = \frac{\partial}{\partial x} \left(D_{eff,k} \frac{\partial c_{e,k}(x,t)}{\partial x} \right) + a_k(1-t_+)J_k(x,t)$
P2D	(5) Ohm's law	$\sigma_{eff,k} \frac{\partial^2 \Phi_{s,k}(x,t)}{\partial x^2} = a_k F J_k(x,t)$
P2D	(6) Kirchhoff's and Ohm's laws	$-\sigma_{eff,k} \frac{\partial \Phi_{s,k}(x,t)}{\partial x} - k_{eff,k} \frac{\partial \Phi_{e,k}(x,t)}{\partial x} + \frac{2k_{eff,k}RT}{F} (1-t_+) \frac{\partial \ln(c_{e,k})}{\partial x} = I$
P2D/SP	(7) Butler-Volmer kinetics equation	$J_k(x,t) = K_k (c_{s,k}^{max} - c_{s,k}^{surf})^{0.5} (c_{s,k}^{surf})^{0.5} (c_{e,k})^{0.5} \left[\exp\left(\frac{0.5F\mu_{s,k}(x,t)}{RT}\right) - \exp\left(-\frac{0.5F\mu_{s,k}(x,t)}{RT}\right) \right]$

Table 5: Advantages and drawbacks of the P2D model.

Model Type	Advantages	Drawbacks
P2D	<ul style="list-style-type: none"> •Perform well at low current •Not computationally-intense •Every cell type can be modeled •Both microscopic and macroscopic scale 	<ul style="list-style-type: none"> •Falls for high current •Not precise as a 2D,3D model

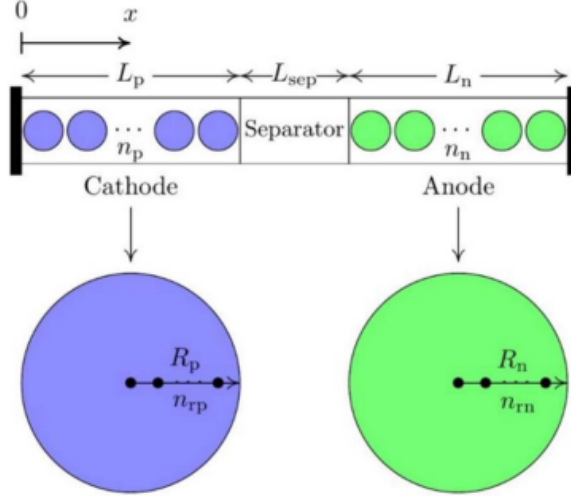


Figure 14: P2D model of a Li-ion cell [37].

2.3.3 Two-dimensional model

The working principle and governing equations of the 2D model are identical to those of the P2D described in **Section 2.3.2**. An instance of this model, which is not a general case but a specific representation since it can take various forms, is illustrated in **Figure 15**. All advantages and drawbacks are detailed in **Table 6**. One advantage over the P2D is the addition of a dimension, the height of the electrode, to better match the actual form of a real cell, effectively offering a side view of the electrode. This addition is beneficial compared to the previously mentioned cases, though it is not as accurate as a 3D that fully replicates the real shape of a cell. However, this can also be a limitation because the SP, P2D, and 2D models can replicate any cell type, whereas the 3D, being a true representation, should be limited to a specific type of cell. Moreover, it performs well even under high current, but its computational time exceeds that of an SP/P2D. In this case as well, both microscopic, concerning the active particles, and macroscopic, concerning the entire electrode thickness, analyses are conducted. Nonetheless, the literature typically lacks complete models that describe the entire cell; usually, they only depict the behavior of one electrode. This is a significant aspect crucial to the model developed in this work, as presented in **Section 3**.

Numerous studies were focused on the topic. Ji et al. [94] develop a multiscale model of porous electrodes based on the Gibbs free energy, in which the Li-ions diffusion, diffusion-induced stress (DIS) and polydispersities of electrode particle sizes are considered. Simulations show small particles exhibit higher charge/discharge degrees and more rapid charge/discharge rates than large particles at the same macroscopic state of charge (SOC)/depth of discharge (DOD). Furthermore it has been noticed that reduced sizes and size polydispersities of electrode particles are prone to alleviate these stresses and thus improve battery performance. Shi et al. [95] investigated a macro-scale 2D 1.5-cell model to evaluate stresses in the separator of a pouch cell. It was demonstrated that the

maximum stress in the separator always emerged at the inner side of it where it wrapped around the electrode edge when the lithium-ion battery was fully charged, and the rest of the separator was in a relatively low and stable stress state. Thermal effects were demonstrated to be significant, with the local maximum stress and strain in the separator actually decreased with rising temperature. Furthermore the results showed that the maximum Von Mises stress increased with increasing the thickness of the separator and the effective frictions between the latter and its adjacent electrodes. While under the same volume fractions of active materials, the particle radius had a negligible effect on the stress. Guo et al. [96] built a two-dimensional scanning electron microscopy image-dependent model of porous electrodes that accounts for the diffusion, DIS, and the size and shape polydispersity of electrode particles. Simulations show that small particles experienced less DIS than larger particles, primarily because of their reduced strain mismatch. In elliptical electrode particles, simple cracks appear at the endpoints of the major axis, while more complicated and severe cracks appear at the endpoints of the minor axis. Furthermore, small particles with a spherical geometry are most favorable for alleviating DIS.

Table 6: Advantages and drawbacks of the 2D model.

Model Type	Advantages	Drawbacks
2D	<ul style="list-style-type: none"> •Closer to a real-cell form than SP,P2D •Not computationally-intense as a 3D model •Perform well even at high current •Every cell type can be modeled •Both microscopic and macroscopic scale 	<ul style="list-style-type: none"> •Not real-cell form as a 3D •More computationally-intense than a SP/P2D •A complete model is not currently developed

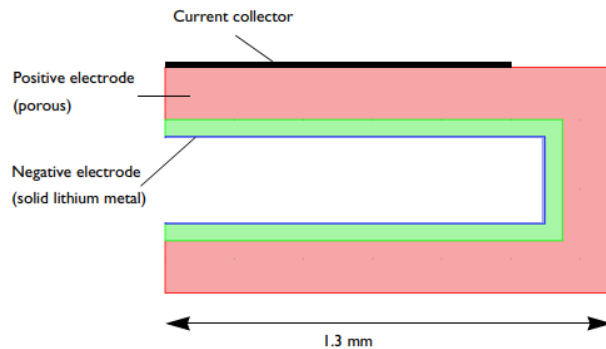


Figure 15: Example of a 2D model for a Li-ion cell [38].

2.3.4 Three-dimensional model

The working principle and governing equations of the 3D model are the same to those of the P2D described in **Section 2.3.2**. An instance of this model, which is not a general case but a specific representation since it can take various forms, is illustrated in **Figure 16**. Practically the model is a P2D developed in three dimensions. All advantages and drawbacks are detailed in **Table 7**. One advantage is that it can exactly match the actual form of a real cell. However, this can also be a drawback because it is limited to a specific type of cell. It performs well even under high current and it is very precise, but its computational time is the highest among the models. In this case as well, both microscopic, concerning the active electrode particles, and macroscopic, concerning the entire electrode thickness, analyses are conducted.

Numerous studies were focused on the topic. Shang et al. [39] derived an analytical solution of stress in the spherical electrode particle based on coupled thermal-diffusion induced stress model. The results show that more lithium ions are accumulated at the positive electrode during battery discharging. Moreover, the heat release rate is higher at the positive electrode than at the negative electrode and the temperature of the positive electrode particles is higher than that of the negative electrode, while for both the temperature near the current collector is highest. Furthermore, the tensile stress on the particle surface is the driving force for fracturing during the lithium intercalation and expansion of the electrode. The stress of the electrode near the current collector can easily reach its peak, and thus the electrode is more prone to fracture. Indeed, the elastic strain energy density of the electrode near the current collector is the highest as well as the material decay. Wu et al. [97] investigate the electrochemical properties and diffusion-induced-stresses in LiCoO_2 with realistic 3D microstructures. It has been found that the potential drops significantly with the increase of C rates and lithium-ion concentration distribution under high discharging rates shows strong inhomogeneity. Furthermore the maximum first principal stress under different C rates, which is more likely to occur at concave regions rather than convex regions, increases at the initial stage and then decreases. The maximum stress at 5C is 153 MPa, which is about 50% larger than the 1C case and 120% larger than the 0.5C case. Indeed for isolated LiCoO_2 particles, the fracture is more likely to occur on the surface rather than inside and failures have more probability of manifesting in large grains. Liu et al. [98] study the charge heterogeneity and mechanical degradation in the battery using a fully coupled electro-chemo-mechanics theory and computational 3D modeling at the cell level. The research points out that stress-regulated bulk ion diffusion is the major contribution of mechanical stresses. The gradient of stress in the composite promotes the homogeneous distribution of Li-ions and facilitates the rate performance of the cell. Indeed, the repetitive deformation of the active particles and the steady decrease of the interfacial strength cause mechanical failure, resulting in a dynamic and irreversible nature of Li-ions activity in the cell over cycles. The cyclic damage causes more charge heterogeneity, impedes charge transfer, increases Li-ions

retention within the active materials and causes a steady fade of capacity of batteries over cycles.

Table 7: Advantages and drawbacks of the 3D model.

Model Type	Advantages	Drawbacks
3D	<ul style="list-style-type: none"> •Real cell form •Perform well even at high current •Very precise •Both microscopic and macroscopic scale 	<ul style="list-style-type: none"> •Bound to a specific cell type •Computationally intense

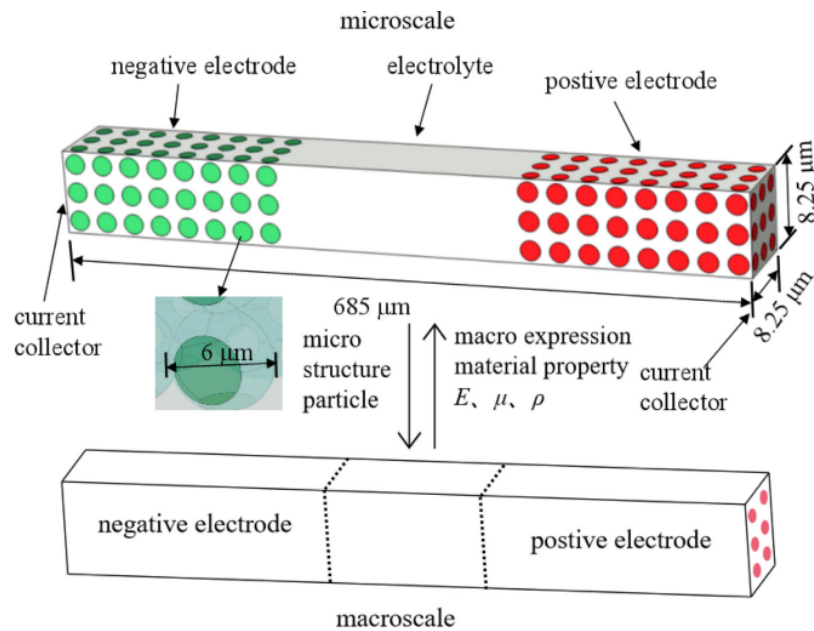


Figure 16: Example of a 3D model for a Li-ion cell [39].

2.4 Influence of key parameters on stress development

One of the objectives of this work, as precise in **Section 3.1** , is to consider the impact of certain key parameters on the development of stress. This aspect is crucial as it allows the identification of trends through model development that can help mitigate the problem. Consequently, this gives the readers some suggestions on the possibility of adopting specific electrode design optimal for stress-reduction. The factors that most significantly influence stress include:

- Charging and discharging rates.
- Thickness of the electrodes.

- Radius of the electrodes active particles.
- Porosity of the electrodes.
- Particle shapes.
- Young's modulus.
- Binder distribution.

For considering the influence of certain key parameters, reference will be made to the work performed by Renganathan et al. [40], which developed a mathematical model of a dual porous insertion electrode cell comprising lithium cobalt oxide and carbon. While the focus of their study was on the anode, similar trends can be observed for the cathode as well. However, it is important to note that the behavior of the cathode, not being as critical as the anode one, is not the focus of this thesis. The effects of discharging on the stress developed in the anode are depicted in **Figure 17**. Decreasing the discharging rate from 6C to C/2 results in a decrease in the maximum Von Mises stress from 40 MPa to around 8 MPa. This significant influence underscores the importance of avoiding excessively high discharging or charging rates, as they can be detrimental to the materials involved. **Figure 18** demonstrates the influence of active particle radius on the Von Mises stress in the anode at a discharging rate of 6C. Reducing the radius from 12.5 μm to 3 μm results in a drop in the maximum Von Mises stress from 40 MPa to 10 MPa, highlighting the importance of having electrodes with smaller active particle sizes to reduce stress. This influence, along with the discharging or charging rate, has the most impact on the stress development. **Figure 19** portrays the influence of anode porosity on the Von Mises stress within the anode itself, using a discharging rate of 6C. In this case, in contrast to what was done before, lowering the porosity from 0.6 to 0.3 provoke a significant growth in stress from 28 MPa to 50 MPa. This is because reducing porosity means less active material available to withstand stress, resulting in a more precarious situation. Lastly, it has been observed that an ellipsoidal shape generates a reduction in stress compared to a spherical one, and a smaller Young's modulus and reduced binder distribution also contribute to stress diminution [88] [92].

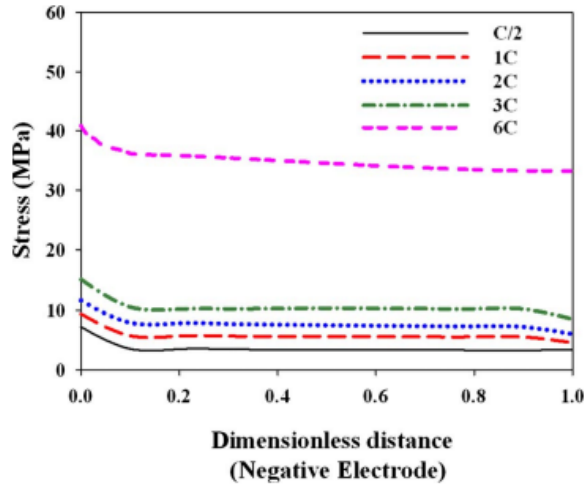


Figure 17: Von Mises stress at the surface of the particles along the thickness of the anode for different rates of discharge [40].

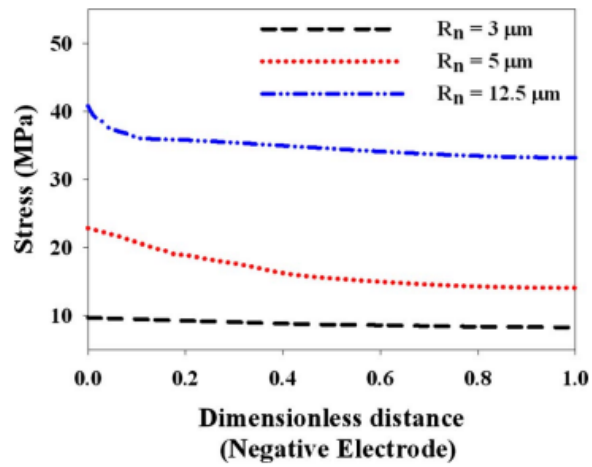


Figure 18: Von Mises stress at the surface of the particles along the thickness of the anode for various particle sizes [40].

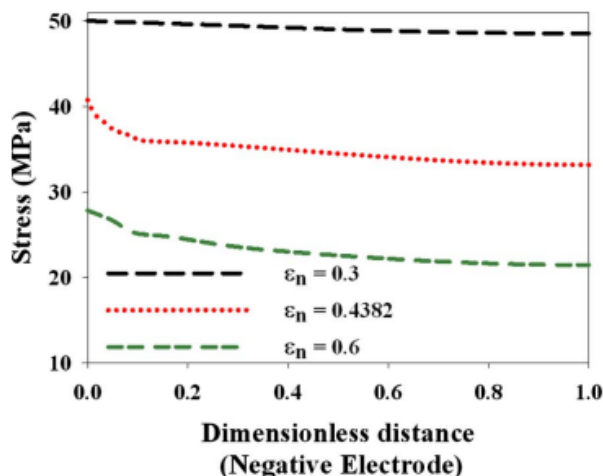


Figure 19: Von Mises stress at the surface of the particles along the thickness of the anode for various porosity values [40].

2.5 Experimental determination of diffusion-induced stress in Li-ion cell

As it will be outlined in **Section 4**, the results obtained by the model will be tested with laboratory experiments. Therefore, understanding the experimental approaches discussed in the literature is crucial to determine if the laboratory procedures align with established methods and have valid scientific grounding. This investigation will include reviewing the study conducted by Li et al. [41]. In this study, a transparent quartz cell was specifically engineered to allow in situ observation of the bending deformation of a bilayer electrode, utilizing a CCD video camera, as depicted in **Figure 20**. The experimental setup involved a commercially available graphite electrode, consisting of a composite of carbonaceous and polymeric materials, paired with LiFePO_4 serving as the positive electrode. To prevent short circuits, a woven Celgard 2400 separator was employed. Both types of electrodes were completely submerged in an electrolyte containing 1 M LiPF_6 . The assembled cell was left to rest in a glovebox for 12 hours before initiating the cycling tests to investigate the operational mechanism of the commercial graphite anode using a BKB6808 battery test system. The electrochemical cycling was performed under galvanostatic conditions with a constant current of $365 \mu\text{A}$, equivalent to a $C/10$ rate, over eight charge-discharge cycles. Images of the bending deformation were captured by the CCD camera every minute. Each electrode underwent eight charging and discharging cycles, each cycle lasting approximately 4 hours, totaling 64 hours of

testing. To evaluate the mechanical stresses involved, the following equations were used:

$$\varepsilon_0 = \frac{\Omega c (h_1^4 E_1(c) + 3h_c^2 h_1^2 E_c + 4h_c^3 h_1 E_c) E_1(c)}{3(h_1^4 E_1^2(c) + 4h_c h_1^3 E_c E_1(c) + 6h_c^2 h_1^2 E_c E_1(c) + 4h_c^3 h_1 E_c E_1(c) + h_c^4 E_c^2)} \quad (8)$$

$$\kappa = \frac{2\Omega c (h_c h_1^2 + h_c^2 h_1) E_c E_1(c)}{(h_1^4 E_1^2(c) + 4h_c h_1^3 E_c E_1(c) + 6h_c^2 h_1^2 E_c E_1(c) + 4h_c^3 h_1 E_c E_1(c) + h_c^4 E_c^2)} \quad (9)$$

$$E_1(c) = \frac{E_c \kappa h_c^4}{- (2\kappa h_1^3 h_c + 3\kappa h_1^2 h_c^2 + 2\kappa h_1 h_c^3 - \Omega c h_1^2 h_c - \Omega c h_1 h_c^2) + \sqrt{(2\kappa h_1^3 h_c + 3\kappa h_1^2 h_c^2 + 2\kappa h_1 h_c^3 - \Omega c h_1^2 h_c - \Omega c h_1 h_c^2)^2 - \kappa^2 h_1^4 h_c^4}} \quad (10)$$

$$\sigma_1 = E_1(c) (\varepsilon_0 + z\kappa) - \frac{1}{3} E_1(c) \Omega c \quad (11)$$

$$\sigma_c = E_c (\varepsilon_0 + z\kappa) \quad (12)$$

Here, h_1 and h_c represent the thicknesses of the active layer and the current collector. $E_1(c)$ and E_c denote the Young's modulus of the active layer and the current collector. Ω is the partial molar volume of the active material, z is the coordinate in the thickness direction (equal to zero at the interface between the negative electrode and the current collector), c is the lithium concentration in the active layer, assumed constant along the z -axis, and κ is the radius of curvature developing due to the charging and discharging cycles. From this radius and other input data, the stress in the active layer and current collector are calculated, denoted as σ_1 and σ_c .

Regarding the results evaluated, **Figure 21** displays the bending deformation, expressed as radius curvature, as a function of the normalized concentration of lithium ions. It is important to note that the radius of curvature, as defined by **Equation 9**, is a quantity varying only with time and not with spatial-coordinates. As observed, the curvature increases during the first phase of the cycle, indicating that the anode bends during the charging process, and then decreases attempting to return to its original position during the discharging phase. In both charging and discharging processes, the variation in curvature exhibits two distinct stages: an initial linear increase during the first three hours, followed by a decrease in slope during the last hour.

Meanwhile, **Figure 22** depicts the stress variations in the active layer along normalized concentrations at thicknesses of 90 μm . As outlined in **Equation 11**, the stress is a quantity that depends on the spatial-coordinate z , making it imperative to fix it for consideration of the outcomes. Analyzing these results, as lithium ions continuously migrate into the active material, the lithiated sections expand while the current collector and the non-lithiated sections remain relatively stationary. As a result, tensile stress is observed at the interface between the electrolyte and the active layer. Although it was noted that the stresses are not sufficient to cause cracking in the graphite particles,

they may still influence the spatial structure of the composite electrode.

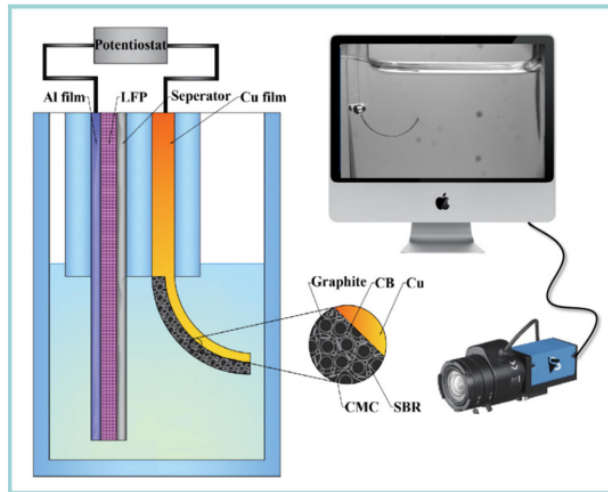


Figure 20: Schematic of the in situ measurement system, which consists of an electrochemical cell, CCD camera and a computer [41].

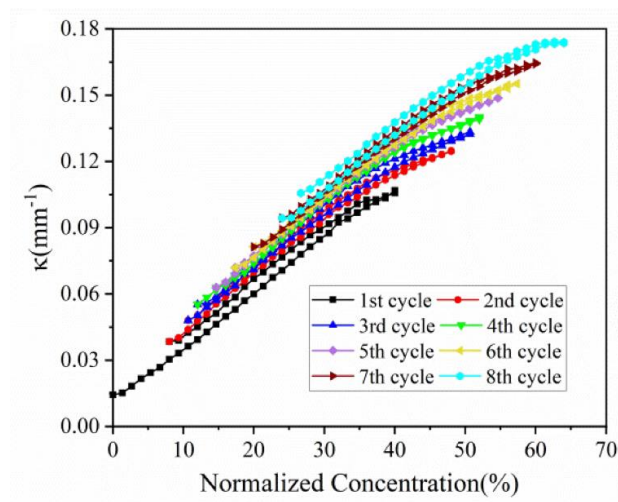


Figure 21: Curvature evolution of composite graphite electrodes in 8 cycles [41].

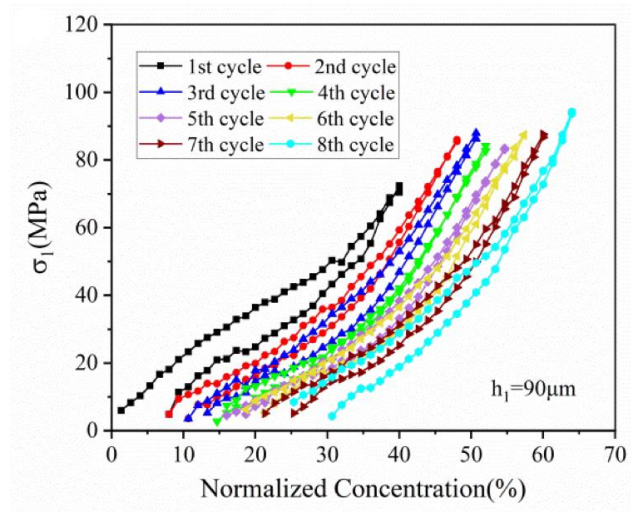


Figure 22: The evolution of stress in the active layer in the thickness of $90 \mu\text{m}$ [41].

3 Methodology

In this section, the objectives of the thesis and the software used for the model implementation will be presented. Additionally the model developed for this work, along with all the features and domains defined within the software, will be precisely explained. Each feature will be described in detail, covering the principles and equations it utilizes to provide the reader with a comprehensive overview of what has been established within the model and its underlying physics. Furthermore, all the input data required by the model will be presented in a dedicated sub-chapter, allowing the reader to easily reference it without needing to search through the thesis. It is important to note that all topics discussed here have a reference in the literature. For these references, please look at **Section 2** and also **Section 1**.

3.1 Objective of the thesis

Clearly outline the objectives of the work at the beginning of the methods section is crucial to clarify the aims of this study. The objectives are:

- Develop a comprehensive model: create a detailed electrochemical-mechanical battery cell model using COMSOL Multiphysics[®] to estimate stresses within the battery anode during the charging-discharging process. The stress evaluation includes not only tangential and radial stresses, but also considers the hydrostatic effect, which is rarely addressed in the literature.
- Test different anode materials: investigate the influence of various anode materials, including graphite and silicon on stress development. It is worth pointing out that regarding the effects of these materials, two different classes of simulations will be performed and validated. The first will use graphite as the anode material, while the second will use silicon.
- Understand the influence of key parameters: explore the effects of active electrode particle radius, anode thickness and applied c-rate on stress development during charging-discharging process.

The focus will be only on the static stresses developed in the anode, as they are the most critical for battery degradation.

3.2 Software employed: COMSOL Multiphysics

For the implementation of the model, COMSOL Multiphysics was selected as the software platform. COMSOL is a powerful finite element analysis, solver and simulation tool that utilizes advanced numerical methods for modeling and simulating physics-based problems. It supports

numerous multiphysics phenomena, that can be coupled to consider different aspects of a study, across various fields including electrical, mechanical, fluid flow and chemical applications.

Originating from MATLAB®-based codes at the Royal Institute of Technology (KTH) in Stockholm, Sweden, COMSOL has evolved into a globally recognized platform employed across numerous applications. It consists of three main components: the model geometry builder, mathematical solvers and an advanced module for post-processing and data visualization. It is well integrated with popular CAD software, allowing direct import of geometries into its solver interface.

Choosing this software for the research offers significant advantages, detailed as follows:

- **Speed and reliability:** COMSOL ODE solvers are built on the robust and efficient MATLAB framework. This reliability has been corroborated by other researchers, particularly in the field of lithium-ion battery modeling.
- **Flexibility:** the program excels in handling multi-domain models and interconnected physics, a necessity for the detailed lithium-ion battery model used in this research. Its configurable nature allows for quick and easy modifications of the research scope.
- **Simplicity:** its interactive interface facilitates a straightforward construction of complex models, eliminating the need for specialized coding. This reduces potential errors and accelerates the development process.

A key benefit of using COMSOL is that the model equations are all already implemented, which save considerable time and minimizes errors by eliminating manual coding. The software also allows us to discretize these equations with high precision.

For this thesis, all simulations were performed using COMSOL Multiphysics version 6.2a 64-bit, on an MSI® PC equipped with a 12th Gen Intel(R) Core(TM) i7-12650H processor at 2.30 GHz, 16 GB of RAM and SSD storage, running the Microsoft® Windows 11 Home operating system.

3.3 Description of the implemented electrochemical-mechanical battery cell model

The model presented in **Figure 23** is designed to effectively replicate the stresses occurring within a Li-ion cell. Giving to the model all input parameters detailed in **Section 3.7**, it will outputs the following quantities:

- Cell voltage and state of charge (SOC).
- Potentials of electrodes and electrolyte.
- Current densities of electrodes and electrolyte.

- Concentration of electrolyte salts.
- Heat generation during operation.
- Lithium-ion concentration.
- Radial, tangential, Von Mises and hydrostatic stress across each active particle in the anode and so also across the entire electrode thickness.

These outputs are crucial for assessing the correct evaluation of stresses within the battery, for this reason the methods of their evaluation will be explored in the following sub-sections. However, the primary focus of this study will be on the last point, which will be tested and validated through experimental methods.

As discussed in **Section 2**, there was previously a gap in the literature regarding a two-dimensional electrochemical-mechanical model for internal stresses analysis in batteries. This model fills that gap by enhancing precision over single-particle and P2D models while maintaining a good computational efficiency. In fact for this work even the most complex simulations completing in under ten minutes.

The model takes inspiration from a side view of a pouch cell but can also be interpreted as an expansion of the P2D model to another dimension, where particles are arranged not just horizontally on the same axis but also vertically, within a rectangular framework for each electrode and also for the electrolyte. This arrangement allows for a more comprehensive stress evaluation as it accounts for interactions between particles that are stacked or adjacent in multiple dimensions, closer to what happens in reality. Additionally, this design facilitates the creation of impactful two-dimensional graphical representations that depict the stress distribution across the entire geometry of the battery. Moreover, the model is able to reproduce the behavior of various types of cells, including pouch, prismatic and cylindrical, as its schematic does not closely mirror the actual form of a real cell. It also incorporates both microscopic (active particle) and macroscopic (entire electrode thickness) scales. Additionally, it is capable to capture the silicon anode behavior that is a material, seldom considered in the literature, of great interest due to its high capacity despite its susceptibility to stress-induced degradation. This capability could lead to insights and potential improvements for integrating high-capacity silicon within the battery anodes, individuating some potential trend that can reduce the stress-development. The model also addresses the effects of hydrostatic stress, a factor often overlooked in the literature but prevalent in real-world scenarios.

Overall, returning to **Figure 23**, the detailed elements from left to right are:

- Positive electrode: lithium metal. It is the interface surface at the leftmost beginning of the electrolyte.

- Separator (electrolyte): LiPF_6 . In this work, to remain consistent with COMSOL conventions, the term 'separator' will also be used as a synonym for electrolyte.
- Negative electrode: graphite or silicon.
- Negative current collector: copper.
- Negative tab: copper.

The decision to insert the tab was aimed at better managing the inlet current source, details of which will be further explained in **Section 3.5.5.3**. This choice will not interfere with reproducing the behavior of actual cells that do not feature a tab, as it does not influence its functioning.

The use of lithium metal will simplify the model by eliminating the porous electrode and introducing a standard surface electrode at the interface with the electrolyte, justified by the non-porous nature of lithium metal. Indeed, the representation as a surface is supported by the relative negligible role of the cathode lithium metal in influencing the overall behavior of the battery, by the fact that electrochemical reactions occur exclusively at the lithium metal surface and by its high electronic conductivity. Such a setup is typically referred to as a "half-cell" configuration, where the electrode of interest, the anode, is termed the working electrode, while the other one, the cathode, serving as the counter electrode assumed to maintain a fixed potential, here set to zero.

Consequently, the model at first with graphite anode and after with silicon, will be tested and validated with experimental results. In **Section 3.5**, every aspect of the model will be discussed, including the physics, equations and working principles of each component.

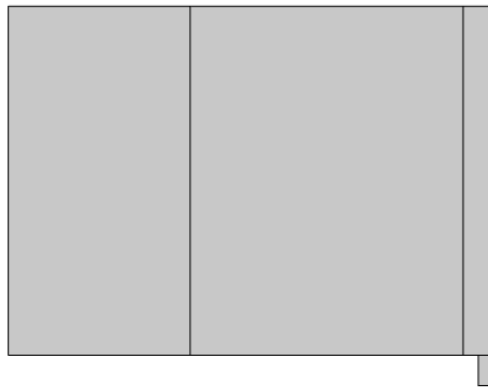


Figure 23: Electrochemical-mechanical model implemented.

3.4 Model constraints and boundary conditions

The assumptions and boundaries assumed are detailed in **Table 8**. The first assumption concerns the model itself. While it is quite precise, it still constitutes an approximation of the reality in which the cell is obviously in actual three-dimensions. Moreover, a real separator is not considered in the model as it does not influence its functionality, though in practice, it serves to prevent direct contact between the cathode and anode. Furthermore, the model only considers static stresses; however fatigue stresses also plays a role due to the battery undergoing numerous cycles. Despite this, static stresses has been demonstrated, as also highlighted in the literature (**Section 2**), to be the most impactful on battery degradation, making the omission of fatigue a reasonable simplification for this evaluation. Additionally, the active particles composing the electrodes are assumed to be spherical and uniform in size. While particles may vary in shape and size, treating them as equal offers a sufficiently accurate representation. The Young's modulus and Poisson ratio are considered constant, a common practice in the literature as seen in references [16] [87] and [65], to avoid over-complicating the model. The reference environment temperature is set at 298 K, which is the standard temperature used in laboratory experiments. The 'Composition of the electrolyte considered nearly constant' and 'Current-carrying ions are not significantly depleted' assumptions regarding the Primary current distribution type chosen for the model, which allow the use of the second Ohm's law to describe the current density inside the electrodes and electrolytes. This theory will be further explained in **Section 3.5.5**. Regarding the radial stress, the presented boundary is considered for solving the equation in **Section 3.5.5.2**. Concerning the double layer capacitance, it is a layer formed by two strata of electric charge with opposing polarity form at the electrode-electrolyte interface; one composed of electrons at the surface of the electrode and the other composed of lithium ions in the electrolyte. Although this double layer can be considered in certain studies, it does not influence the results of this model and is therefore omitted from this analysis.

Table 8: Assumptions and boundary conditions for the developed electrochemical-mechanical model.

2D model is used to represent a cell, but in reality the dimension are three.

There is not a real separator but only liquid electrolyte.

Only static stresses are considered.

The active material particles are assumed to be spherical and equal in size.

Young's modulus and Poisson's ratio are considered constant inside the materials.

The reference environment temperature is set to 298 K.

The composition of the electrolyte considered nearly constant.

Current-carrying ions are not significantly depleted.

Radial stress at the surface of the sphere is equal to zero.

Radial stress at the centre of the sphere is a finite number.

The double layer capacitance effect is not considered.

3.5 Understanding COMSOL domains

Figure 24 contains all the domains present in the model developed. Every aspect will be discussed in the following sub-chapters, including the physics, equations and working principles of each component.

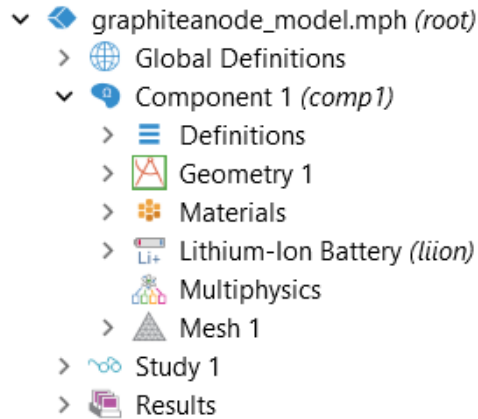


Figure 24: Comsol domains for the implemented model.

3.5.1 Global definitions domain

All the domains are depicted in **Figure 24**. The initial item in this list is the file name, which is designated as 'graphiteanode_model.mph (root)'. Following this, the first substantive domain, termed 'Global Definitions', is expanded in **Figure 25**. This section contains all necessary input

data for the model, presented in **Section 3.7**. It also includes critical parameters such as the volume expansion as a function of the degree of lithiation (normalized concentration), an essential input that will be further elucidated in **Section 3.5.5.2**, along with the reference environmental temperature.

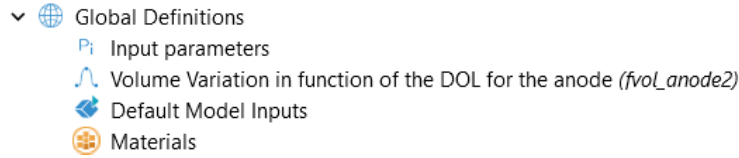


Figure 25: Global definition domain for the implemented model.

3.5.2 Definitions domain

Figure 26 expands the definition domain. Within this domain, certain variables, not defined by default in the software, are reported. The sole variable presented is the current applied, defined as follows:

$$I_{app} = I_{1C} \cdot C_{rate} \quad (13)$$

Practically, the applied current is defined as the product of the 1C current and the charging/discharging rate, also known as C-rate. This is extremely convenient because the current at a C-rate of one is automatically calculated by the given capacity. Thus, if it is necessary to modify the C-rate for different simulations, it will be sufficient to adjust the C-rate value in the input parameter, directly altering the current based on this variable. However, as also said before, this portion of setup is concise since all other equations required for the simulation are automatically available in COMSOL and, therefore, do not need be defined by the person developing the code.

Progressing further, the 'Selection' feature allows assigning specific definitions to each element within a geometry. This becomes crucial in the physics node where it is necessary to assign certain physics, such as porous electrodes or separators, to parts of the geometry. It also facilitates coupling multiple geometries under one selection, as is the case for the 'current collector selection' that merges the geometry of the current collector and the tab end. Each part of the geometry is assigned a specific selection, though specifics of these assignments are not detailed as they are not crucial for understanding the model development and would make the text too dense to read.

The 'Cell voltage probe' essentially serves as a method to automatically display selected variables, like the cell voltage, in the default graphs of the results. It is worth pointing out that this variable is typically calculated by default in COMSOL. 'Boundary system 1' clarifies which coordinates lie on the considered plane and which are orthogonal to it, reflecting the model 2D configuration. 'View 1' aids in understanding specifics regarding the visualization of the created geometry, such as whether to display axes, a grid, or utilize a scale, which in this instance is crucial as the dimension

on the y-axis is in centimeters while that on the x-axis is in micrometers.

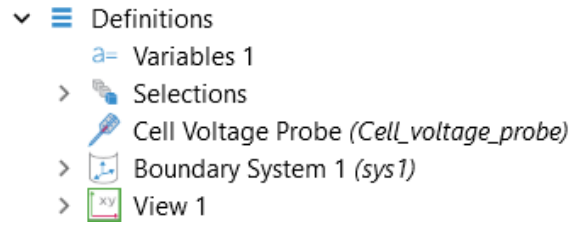


Figure 26: Definition domain for the implemented model.

3.5.3 Geometry domain

Figure 27 depicts the geometry domain. Within this domain, all the rectangles are constructed by providing the appropriate input data and positioning them accurately in space relative to the reference origin of the axes, as depicted in **Figure 23**. Each rectangle is constructed individually and subsequently merged using the 'form union' command. The specifics of the coordinates assigned to each rectangle are not detailed, as they are not critical for understanding the model development.

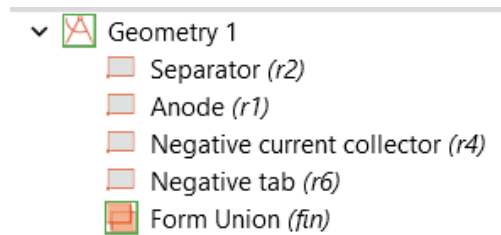


Figure 27: Geometry domain for the implemented model.

3.5.4 Materials domain

Figure 28 illustrate the materials used in the model domain, with graphite serving as the anode material. If silicon is considered it will replace the graphite. This section is dedicated to assigning specific materials to each component as outlined below:

- $LiPF_6$ as electrolyte.
- Graphite or silicon for the negative electrode.
- Copper for the negative current collector and tab.

This section integrates crucial input parameters from the COMSOL library and relevant literature. The use of the software library significantly simplifies the setup by reducing the need for extensive literature review for material properties. It is important to clarify that this section only includes the

intrinsic properties of the materials. Other parameters, such as porosity, the active material radius or some correction coefficient, which are indirectly related to the material properties are detailed in **Section 3.5.5.2** dealing with porous electrode domain. The parameters present in this sub-chapter are further presented in **Section 3.7**, where they are categorized based on the simulation considered. For detailed information on how they are utilized in equations and further explanations of those equations, please refer to **Section 3.5.5** discussing the physics of the model.

Table 9 provides the necessary input data for the current collector and tab. The only factors detailed here are the electrical conductivity, a measure of a material capacity to conduct electric current, which is utilized in the application of the second Ohm's law for the current collector domain and the Young's Modulus, crucial for the experimental stresses evaluation.

Table 10 outlines the input parameters for the electrolyte material. The first of these is the diffusion coefficient, which describes how the mass of a substance disperses over time across a surface, relevant for Fick's first law application. The second is the electrolyte conductivity, indicative of an electrolytic solution ability to conduct electric current mainly pertains to ion movement, which is applied in a modified version of Ohm's law for charge transport in the electrolyte. The third is the transport number, representing the fraction of the total current in an electrolyte by given atom, crucial for both modified Ohm's law and Fick's first law. The last is the activity dependence, reflecting how the chemical activity of a substance, which indicates its potential to undergo chemical reaction, varies with its molar concentration, playing a role in the modified version of Ohm's second law. Furthermore, temperature dependencies for these factors are also considered by introducing the following Arrhenius-type equation:

$$n(c, T) = n_c(c) \exp\left(\frac{E_{a,n}}{R} \left(\frac{1}{T_{\text{ref}}} - \frac{1}{T_2}\right)\right) \quad (14)$$

Here, n denotes a variable dependent on both concentration and temperature, $E_{a,n}$ represents the activation energy required to initiate a specific process, R is the universal gas constant and \exp represents $10^{(\text{argument})}$. In this formula the variable n is initially considered for its concentration dependence and subsequently adjusted for temperature influence considering an exponential. The temperatures applied in the calculations derive from **Equation 19**, T_2 , ensuring the values used in the formulas are consistently 319.15 K or 223.15 K depending on the actual temperature conditions. Additionally, **Figure 29** displays the diffusion coefficient, **Figure 30** illustrates the electrical conductivity, **Figure 31** shows the transport number and **Figure 32** depicts activity dependence all as solely dependent on lithium concentration.

Table 11 refers to the behavior of lithium metal. In this scenario, as it is not influencing the cell behavior, all data values are set to zero.

The values for the graphite electrode are outlined in **Table 12**. Similar to other materials, this

includes the electrical conductivity and the diffusion coefficient, with the latter subject to temperature dependencies by using the Arrhenius-type correlation. Additionally, the equilibrium potential is provided, which illustrates how the potential is linked to both concentration and temperature. The temperature influence in this context, as seen in **Equation 21**, is addressed through a derivative, differing from the Arrhenius approach. Also included is the equilibrium concentration that is utilized to define the lithium concentration based on the voltage level of the electrode. This is achieved using **Equation 25**, which implements the inverse of the previously defined equilibrium potential function. This means that given a voltage, it returns a normalized concentration, which is then multiplied by the maximum allowable lithium concentration to find the actual one. Furthermore, there are required data for SOC maximum and minimum limits. Additional crucial parameters, which will be more thoroughly addressed in **Section 3.5.5.2** concerning the porous electrode, include Young's modulus, a measure of a material ability to withstand changes in length under lengthwise tension or compression, Poisson ratio, the ratio of transverse contraction strain to longitudinal extension strain in the direction of stretching force, and volume expansion as a function of normalized concentration, which is the ratio between the actual concentration and the maximum possible one. Using this ratio is convenient as it accurately reflects the degree of lithiation. Specifically, if the ratio is equal to 0, it indicates that no lithium ions are hosted in the solid-phase, implying no lithiation. Conversely, if the ratio is equal to 1, it means that the solid-phase has reached its maximum hosting capacity, indicating full lithiation. The latter volume expansion is depicted in **Figure 35**, illustrating how graphite volume changes depending on the normalized lithium concentration. Furthermore, **Figure 33** and **Figure 34** respectively show the equilibrium concentration and the temperature derivative of the equilibrium concentration, both as functions of the normalized lithium concentration.

Table 13 presents the values for silicon, which are similar to those for graphite except that there is no temperature dependence of the properties. Similar to previous materials, **Figure 36** and **Figure 37** display the equilibrium potential and volume expansion as functions of the normalized lithium concentration. Notably, the volume expansion for silicon is significantly higher than that for graphite, 350% compared to nearly 13%. This is a crucial factor to consider when evaluating diffusion-induced stresses. To clarify, the schematics regarding the volume expansion of silicon were originally based on the number of Li-atoms, denoted as x , in Li_xSi varying from 0 to 4. However for modeling purposes, it is essential to associate silicon expansion in terms of the normalized lithium concentration. Therefore, a specific correlation has been established: the value of $x = 0$ in Li_xSi corresponds to the minimum normalized lithium concentration, equal to zero, while $x = 4$ aligns with the maximum normalized lithium concentration, equal to one. This correlation holds significant physical meaning as it directly relates the number of lithium atoms within Li_xSi to the lithiation level, facilitating a more accurate and meaningful interpretation of material behavior un-

der varying states of charge.






- ▼  Materials
 - >  Lithium Metal, Li (Negative, Li-ion Battery) (*mat1*)
 - >  LiPF6 in 3:7 EC:EMC (Liquid, Li-ion Battery) (*mat2*)
 - >  Graphite, LixC6 MCMB (Negative, Li-ion Battery) (*mat3*)
 - >  Copper (*mat4*)

Figure 28: Materials domain for the model with graphite anode.

Table 9: Copper input data taken from the COMSOL library and literature [9].

Property	Variable name	Value	Unit
Electrical conductivity	σ_{el}	$5.998 \cdot 10^7$	$\frac{S}{m}$
Young's modulus	E	117	GPa

Table 10: LiPF₆ input data taken from the COMSOL library and literature [10] [11].

Property	Variable name	Equation	Eq.no	Unit
Diffusion coefficient	D	$(D_c(c))exp\left(\frac{16500 \cdot (\frac{1}{T_{ref}} - \frac{1}{T_2})}{8.314}\right)$	(15)	$\frac{m^2}{s}$
Electrolyte conductivity	σ	$(\sigma_c(c))exp\left(\frac{4000 \cdot (\frac{1}{T_{ref}} - \frac{1}{T_2})}{8.314}\right)$	(16)	$\frac{S}{m}$
Transport number	t_+	$t_{+c}(c)$	(17)	-
Activity dependence	$\frac{\partial \ln(f)}{\partial \ln(c)}$	$(\frac{\partial \ln(f)}{\partial \ln(c)}_c(c))exp\left(\frac{-1000 \cdot (\frac{1}{T_{ref}} - \frac{1}{T_2})}{8.314}\right)$	(18)	-
Reference temperature	T_{ref}	298		K
Temperature for the equations	T_2	$min(393.15, max(T, 223.15))$	(19)	K
Actual temperature	T			K

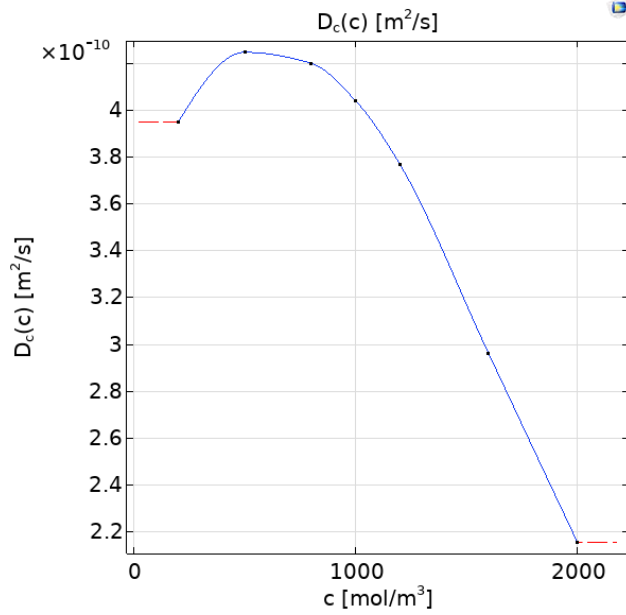


Figure 29: Diffusion coefficient depending only on the lithium concentration, $D_c(c)$, for LiPF₆.

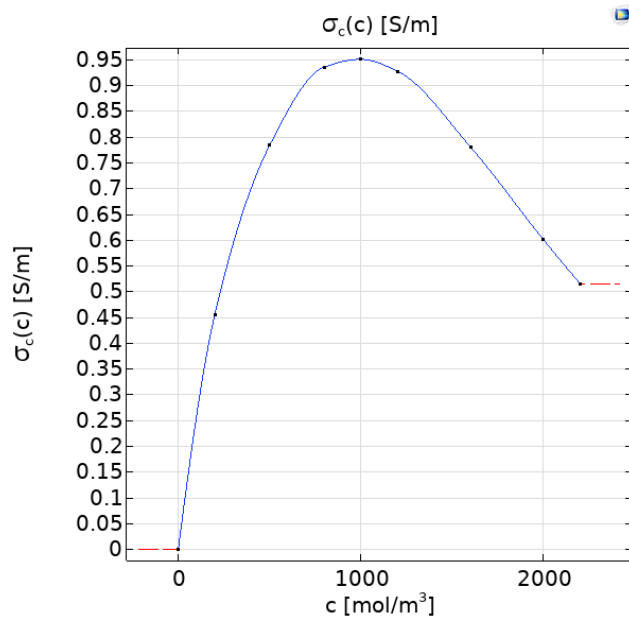


Figure 30: Electrical conductivity depending only on the lithium concentration, $\sigma_c(c)$, for LiPF₆.

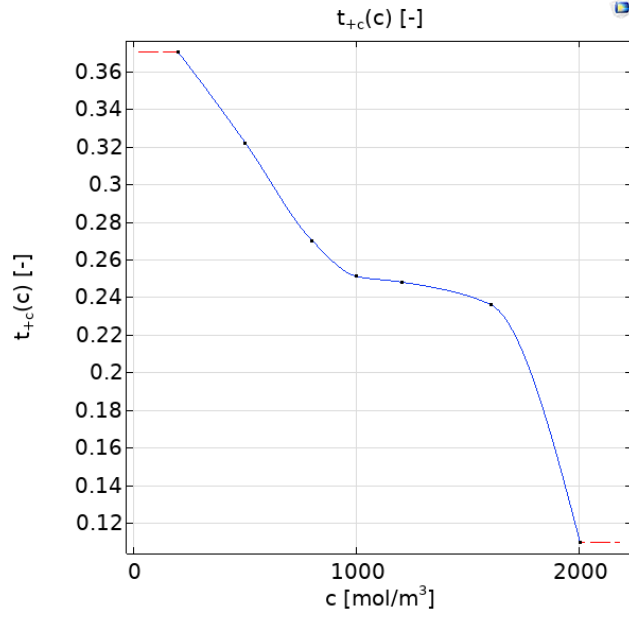


Figure 31: Transport number depending only on the lithium concentration, $t_{+c}(c)$, for LiPF₆.

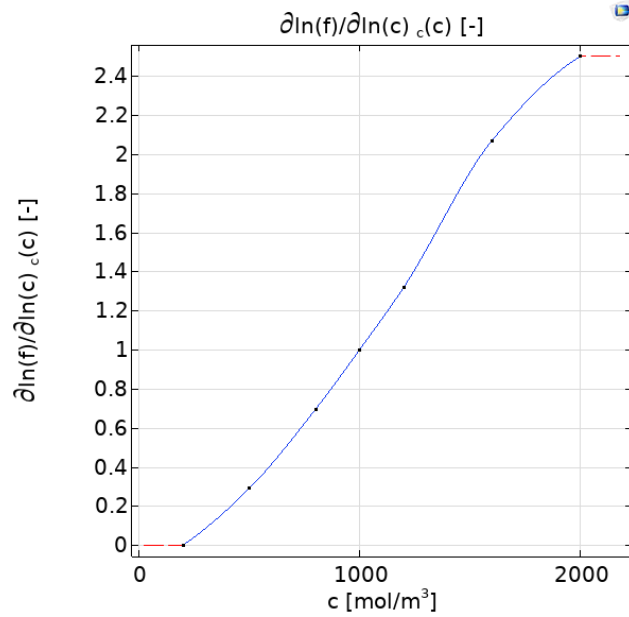


Figure 32: Activity dependence varying only with the lithium concentration, $\frac{\partial \ln(f)}{\partial \ln(c)}_c(c)$, for LiPF₆.

Table 11: Lithium metal input data taken from the COMSOL library.

Property	Variable name	Value	Unit
Lithium concentration	c	0	$\frac{\text{mol}}{\text{m}^3}$
Equilibrium potential	E_{eq}	0	V
Temperature derivative of equilibrium potential	$\frac{dE_{eq}}{dT}$	0	$\frac{\text{V}}{\text{K}}$

Table 12: Graphite input data taken from the COMSOL library and literature [12] [13] [14] [15] [16].

Property	Variable name	Equation	Eq.no	Unit
Electrical conductivity	σ_{el}	100		$\frac{\text{S}}{\text{m}}$
Diffusion coefficient	D	$(1.453 \cdot 10^{-13}) \exp\left(\frac{68025.7\left(\frac{1}{T_{ref}} - \frac{1}{T_2}\right)}{8.314}\right)$	(20)	$\frac{\text{m}^2}{\text{s}}$
Equilibrium potential	E_{eq}	$E_{eq,c}\left(\frac{c}{c_{max}}\right) + \frac{dE_{eq}}{dT} \cdot \left(\frac{c}{c_{max}}\right) \cdot (T - 298)$	(21)	V
Temperature derivative of equilibrium potential	$\frac{dE_{eq}}{dT}$	$\frac{dE_{eq}}{dT} \cdot \left(\frac{c}{c_{max}}\right)$	(22)	$\frac{\text{V}}{\text{K}}$
Maximum electrode SOC	SOC_{max}	$E_{eq,inv}(E_{max})$	(23)	%
Minimum electrode SOC	SOC_{min}	$E_{eq,inv}(E_{min})$	(24)	%
Equilibrium Li concentration	c_{eq}	$c_{max} E_{eq,inv}(E)$	(25)	$\frac{\text{mol}}{\text{m}^3}$
Maximum lithium concentration	c_{max}	31507		$\frac{\text{mol}}{\text{m}^3}$
Reference temperature	T_{ref}	318		K
Temperature for the equations	T_2	$\min(393.15, \max(T, 223.15))$	(19)	K
Actual temperature	T			K
Young's modulus	E	15		GPa
Poisson's ratio	ν	0.3		-

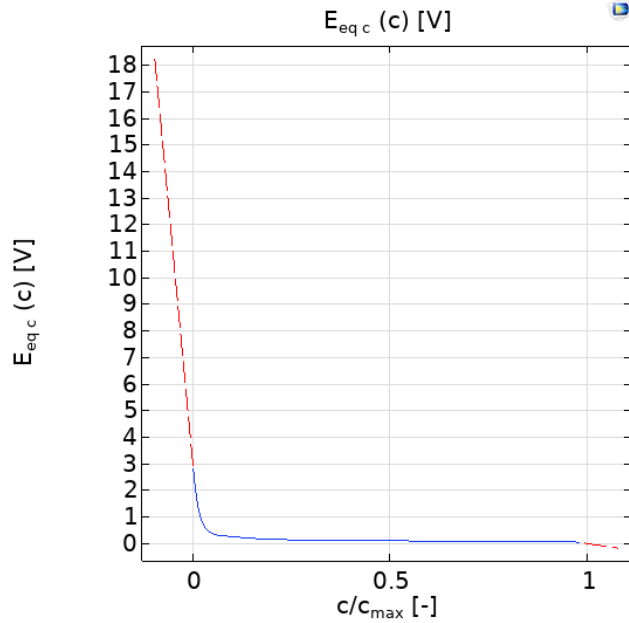


Figure 33: Equilibrium potential depending only on the normalized lithium concentration, $E_{eq,c}$, for graphite. $E_{eq,inv}$ which appears in **Equation 25** is the inverse of the function depicted in the figure.

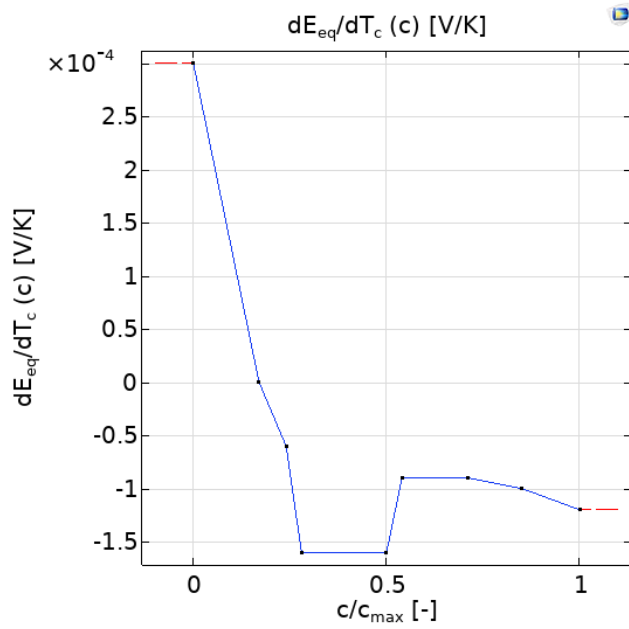


Figure 34: Derivative of the equilibrium potential with respect to the temperature depending only on the normalized lithium concentration, $\frac{dE_{eq}}{dT_c}$, for graphite.

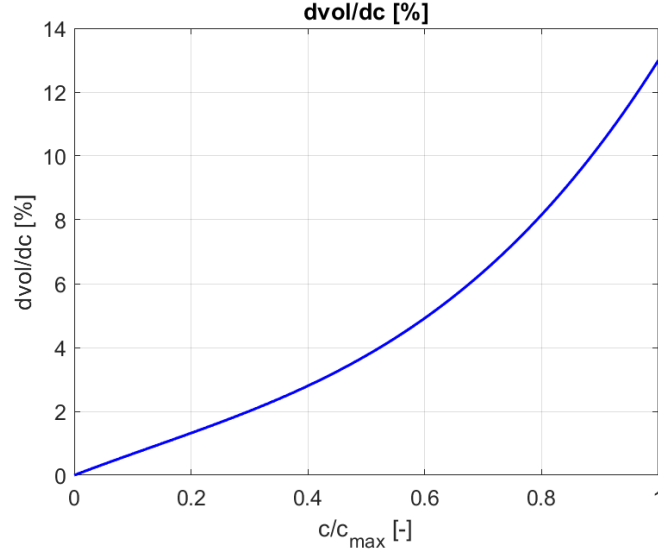


Figure 35: Volume variation in function of the normalized concentration for graphite, $\frac{dvol}{dc}(\frac{c}{c_{s,max}})$.

Table 13: Silicon input data taken from the COMSOL library [17] [18] [19] [20] [21] [22].

Property	Variable name	Equation	Eq.no	Unit
Electrical conductivity	σ_{el}	1000		$\frac{S}{m}$
Diffusion coefficient	D	$5 \cdot 10^{-14}$		$\frac{m^2}{s}$
Equilibrium potential	E_{eq}	$E_{eqc}(\frac{c}{c_{max}})$	(26)	V
Temperature derivative of equilibrium potential	$\frac{dE_{eq}}{dT}$	0		$\frac{V}{K}$
Maximum electrode SOC	SOC_{max}	$E_{eq,inv}(E_{max})$	(23)	%
Minimum electrode SOC	SOC_{min}	$E_{eq,inv}(E_{min})$	(24)	%
Equilibrium lithium concentration	c_{eq}	$c_{max}E_{eq,inv}(E)$	(25)	$\frac{mol}{m^3}$
Maximum lithium concentration	c_{max}	278000		$\frac{mol}{m^3}$
Young modulus	E	90		GPa
Poisson ratio	ν	0.29		-

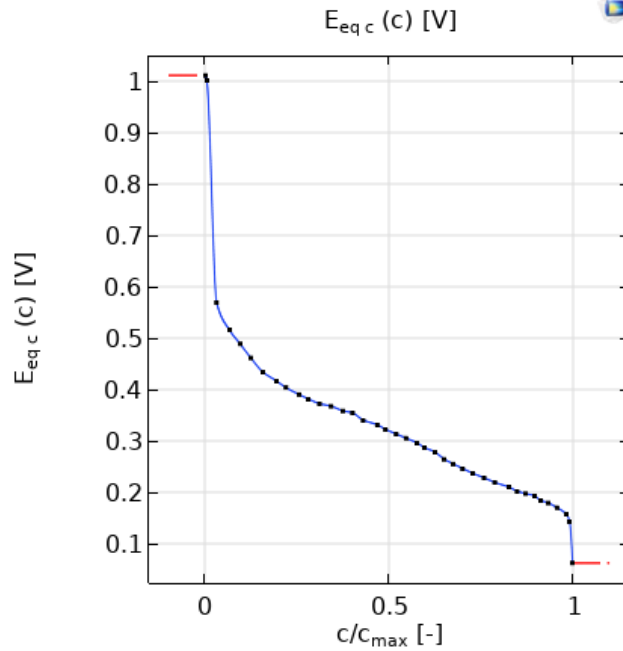


Figure 36: Equilibrium potential depending only on the normalized lithium concentration, $E_{eq,c}$, for silicon. $E_{eq,inv}$ which appears in **Equation 25** is the inverse of the function depicted in the figure.

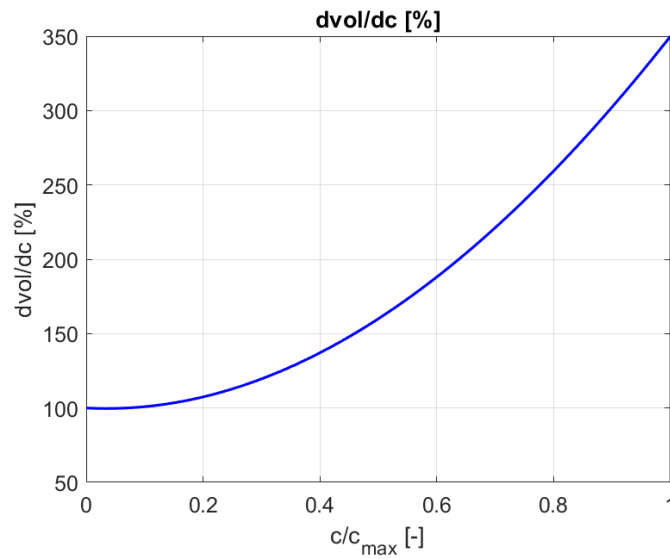


Figure 37: Volume variation in function of the normalized concentration for silicon, $\frac{dvol}{dc} \left(\frac{c_s}{c_{s,max}} \right)$.

3.5.5 Physics domain

The physics domain is the backbone of the model, providing tools for building detailed configurations of the electrodes and electrolyte in electrochemical cells, including a description of the electrochemical reactions and transport properties that influence the performance of batteries. **Fig-**

Figure 38 displays the physics domains for the model.

This section will first introduce all the physics domains, focusing primarily on the general domain known as 'Lithium-ion battery (liion)', which contains all other sub-domains. The latter is grounded in the works of Newman among others. Here, Ohm's law is utilized to describe charge transport in the electrodes, while for the electrolyte the theory of concentrated quiescent aprotic (1:1) electrolyte is employed to characterize charge and mass transport in its phase. An additional dimension is incorporated in the porous electrode domains to account for the transport of solid lithium in the solid electrode phase via Fick's law. Four dependent variables are considered and solved across different domains, including:

- Φ_l : electrolyte potential.
- Φ_s : electric potential in the electrodes.
- c_l : lithium salt concentration in the electrolyte.
- c_s : solid lithium concentration in the electrode particles.

The c_s variable is addressed in an added dimension that introduces a scale at the microscopic level, considering the radius of the active particles, and uses an internal discretization within this particle dimension not apparent in the standard model geometry. This variable is not automatically present in this section, but once a porous electrode domain is included, it is automatically added. The binary 1:1 liquid electrolyte option applies concentrated electrolyte theory to solve for the lithium salt concentration and the potential as dependent variables in the electrolyte phase. Additionally, convection can be considered as another mechanism for ion transport that accompanies heat transfer, but it is not selected here as it does not significantly impact the electrochemistry of the battery. This section also necessitates a width field to define the geometry width perpendicular to the cross-section. The value of this parameter is crucial for automatically calculating the total current from the current density vector. All the input data required for this domain are detailed in **Table 14**.

In the following sub-paragraphs will be explained all other physics domains, detailing their operating principles, governing equations and required parameters. It is worth pointing out that all the domains that will be introduced are based on the primary current distribution theory. It assumes linear relation of current density to the electric field and electrolyte current obeyed Ohm's law. Furthermore, the model has infinitely fast electrode kinetics, resulting in negligible potential drops over the electrode-electrolyte interfaces. These assumptions can be made if the composition of the electrolyte can be considered nearly constant and current-carrying ions are not significantly depleted. However, for the sake of completeness, it is worth mentioning that are present other type of current distribution. If the electrode reaction kinetics proceed at a finite rate, then the system has a

secondary current distribution. In the cases of more advanced nonlinear charge conservation equations being required and concentration-dependent electrode polarization, the system is described as obeying tertiary current distribution [24].

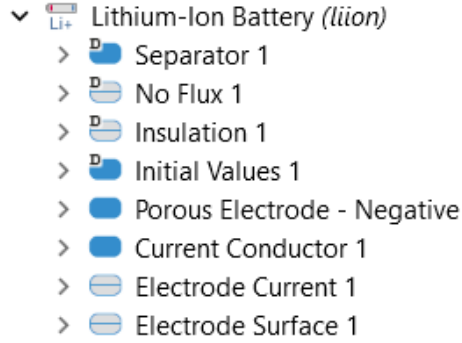


Figure 38: Physics domain for the developed model.

Table 14: Required input data for the 'Lithium-ion battery' domain.

Input data	Value	Unit
Out-of-plane width, d_y	3	mm

3.5.5.1 Separator domain

As previously described this domain contains the electrolyte, despite being labeled as "Separator." The separator material is not included in the simulation since its primary function is to prevent direct contact between the electrodes, which does not affect the model ability to mimic real cell behavior. This domain is crucial for defining the current conduction in the ion-conducting phase, based on concentrated solution theory. Here, the primary driving force for mass transfer, which characterizes ions transport within the electrolyte, is defined by the gradient in electrochemical potential, the electrical conductivity, the transference number and the diffusion coefficient. It is important to note that each of these properties depends on concentration. The equations provided below later detail these relationships:

$$\nabla \cdot \vec{J}_l = R_l \quad (27)$$

$$\nabla \cdot \vec{i}_l = Q_l \quad (28)$$

$$\vec{J}_l = -D_{l,eff} \nabla c_l + \frac{\vec{i}_l t_+}{F} \quad (29)$$

$$\vec{i}_l = -\sigma_{l,eff} \nabla \Phi_l + \left(\frac{2\sigma_{l,eff} RT}{F} \right) \left(1 + \frac{\partial \ln f}{\partial \ln c_l} \right) (1 - t_+) \nabla \ln c_l \quad (30)$$

$$D_{l,eff} = \varepsilon_l \cdot 1.5 \cdot D_l \quad (31)$$

$$\sigma_{l,eff} = \varepsilon_l \cdot 1.5 \cdot \sigma_l \quad (32)$$

Equation 27 represents the mass balance equation for the salt within the electrolyte. This equation can be elaborated upon in **Equation 29**, which aims to accurately describe the movement of ion particles in the electrolyte. The initial term, $-D_{l,eff} \nabla c_l$, demonstrates the application of Fick's First Law, while the subsequent term accounts for the influence of the current density across the electrolyte and the transport number in the diffusion process.

Equation 28 deals with the conservation of current. This is further developed in **Equation 30**, which describes how electric current is conducted within the electrolyte. Here, the first term, $-\sigma_{l,eff} \nabla \Phi_l$, refers to Ohm's Law, while the additional terms consider factors such as the electrolyte characteristics, including temperature, lithium concentration, activity dependence and transport number, all of which significantly impact current conduction.

Equation 31 and **Equation 32** adjust the diffusion coefficient and electrolyte conductivity by multiplying them by a factor that takes into account the electrolyte volume fraction, ε_l , and a corrective factor of 1.5, called Bruggeman correction factor. This adjustment can be needed because the electrolyte material may only partially occupy the separator domain; for instance, the separator could be a porous matrix containing the electrolyte. Indeed, this correction takes into account also the presence of the electrolyte in the pores of the porous electrode. However, in the case of the study, given that there is no physical separator in the experimental cell, this correction will consider only the Bruggeman coefficient [24].

To clarify all parameters present in the equations:

- \vec{J}_l : mass flux of Li-ions relative to the mass average velocity, measured in $\frac{kg}{m^2s}$.
- R_l : rate expression describing the production or consumption of Li-ions, measured in $\frac{kg}{m^3s}$.
- \vec{i}_l : current density of the electrolyte, measured in $\frac{A}{m^2}$.
- Q_l : current source within the electrolyte, measured in $\frac{A}{m^3}$.

- $D_{l,eff}$: effective electrolyte diffusion coefficient describing the rate at which a substance disperses over time across a surface, measured in $\frac{m^2}{s}$.
- c_l : concentration of lithium salt in the electrolyte, measured in $\frac{mol}{m^3}$.
- t_+ : transport number representing the fraction of total current carried by a given ion in the electrolyte, dimensionless.
- F : Faraday's constant, equal to $96485.3321 \frac{SA}{mol}$.
- $\sigma_{l,eff}$: effective electrolyte conductivity, indicating the electrolyte solution ability to conduct electric current, primarily through ion movement, measured in $\frac{S}{m}$.
- Φ_l : electrolyte potential, measured in Volts V.
- R : universal gas constant, $8.314 \frac{J}{molK}$.
- T : actual cell temperature, measured in Kelvin K.
- $\frac{\partial \ln f}{\partial \ln c_l}$: activity dependence coefficient reflecting how the chemical activity of a substance, indicating its potential to undergo chemical reactions, varies with its molar concentration, dimensionless.
- ε_l : electrolyte volume fraction, indicating the proportion of electrolyte present within the separator domain, dimensionless.
- 1.5: Bruggeman coefficient, used along with the electrolyte volume fraction to modify the values of electrolyte diffusion and electrolyte conductivity to account for the effective amount of electrolyte present in the separator domain.
- D_l : diffusion coefficient inherent to the electrolyte material, measured in $\frac{m^2}{s}$. It does not consider the presence of the electrolyte inside void spaces.
- σ_l : conductivity of the electrolyte material, measured in $\frac{S}{m}$. It does not consider the presence of the electrolyte inside void spaces.

Table 15 summarizes all the input data required for this domain. Values are not provided as they vary from simulation to simulation; for specific values, please refer to **Section 3.7**. Constants that do not change across simulations are the only numeric data listed here. It is important to note that some parameters appearing in the equations are not directly required as inputs in this domain, as they are sourced and specified directly in other domains later on. For a more detailed explanation of parameters specifically related to the electrolyte material, such as electrolyte conductivity, diffusion coefficient, transport number and activity dependence, please refer to **Section 3.5.4**.

Table 15: Required input data for the 'Separator' domain.

Input data	Value	Unit
Actual temperature, T		K
Faraday's constant, F	96485.3321	$\frac{sA}{mol}$
Universal constant of gas, R	8.314	$\frac{J}{molK}$
Electrolyte conductivity of the electrolyte material, σ_l		$\frac{S}{m}$
Diffusion coefficient of electrolyte material, D_l		$\frac{m^2}{s}$
Transport number, t_+		-
Activity dependence, $\frac{\partial \ln f}{\partial \ln c_l}$		-
Electrolyte volume fraction, ε_l		-
Bruggeman coefficient	1.5	-

3.5.5.2 Porous electrode domain along with diffusion-induced stresses evaluation

The domain in question applies only to the negative electrode due to the non-porous nature of the lithium metal cathode. This framework is derived from porous electrode theory, which provides a comprehensive macroscopic description of battery cycling behavior rooted in detailed microscopic physical models [105]. The focus here is on understanding the current density within both the electrolyte and electrode phases, as well as the diffusion processes of lithium ions between these two phases and the reactions occurring at their interface.

Originally formalized by Newman et al. [85], porous electrode theory addresses the material composition of the electrodes used in lithium-ion batteries. A porous electrode is a composite of porous reactive electronic conductors and mixtures of solid materials, which include both non-conducting reactive substances and electronic conductors. Besides the solid areas, the voids are filled with spaces containing the electrolytic solution that saturates the solid matrix. The reaction rates within a porous electrode may vary throughout its structure, influenced by the physical arrangement, conductivity of both the matrix and the electrolyte, and parameters that characterize its processes.

The goal of this model is to determine the concentrations of lithium ions within the electrode phase and the electrolyte phase, denoted as c_s and c_l , and the ion potentials in each phase, Φ_s and Φ_l , as shown in **Figure 39**. It should be noted that in the previously mentioned figure, the convention for individuating parameters associated with the solid-phase (electrode) involves the use of the suffix 1, whereas for the solution-phase (electrolyte), the suffix 2 is used. So, the complete electrode is treated as the superposition of two continua: one representing the solution and the other the solid matrix.

Proceeding with the discussion, both potentials are continuous functions across time and space co-

ordinates. To derive the variables related to the solid-phase, the model employs averaging several variables over a region of the electrode that is small relative to its overall dimensions but significantly larger compared to the pore structure. This operation, known as the macroscopic model, captures the general behavior of the electrode by considering averaged quantities. Additionally, it is assumed that each electrode is composed of spherical particles with a uniform radius, denoted as r_p . The description and behavior of these particles are defined as microscopic level. Additionally, also the solution-phase concentration of the lithium-ion is averaged across the pores, which helps to correlate the composition dependence of the diffusion coefficients, activity coefficients and the conductivity of the solution phase.

To properly describe this interface, the following equations are implemented:

$$\nabla \cdot \vec{J}_l = R_l \quad (33)$$

$$R_l = - \sum_m \frac{v_{Li+,m} i_{v,m}}{F} + R_{l,src} \quad (34)$$

$$\nabla \cdot \vec{i}_l = i_{v,total} + Q_l \quad (35)$$

$$\nabla \cdot \vec{i}_s = -i_{v,total} + Q_s \quad (36)$$

$$i_{v,total} = \sum_m i_{v,m} + i_{v,dl} \quad (37)$$

$$\vec{J}_l = -D_{l,eff} \nabla c_l + \frac{\vec{i}_l t_+}{F} \quad (29)$$

$$\vec{i}_l = -\sigma_{l,eff} \nabla \Phi_l + \left(\frac{2\sigma_{l,eff} RT}{F} \right) \left(1 + \frac{\partial \ln f}{\partial \ln c_l} \right) (1 - t_+) \nabla \ln c_l \quad (30)$$

$$\vec{i}_s = -\sigma_{s,eff} \nabla \Phi_s \quad (38)$$

$$D_{l,eff} = \varepsilon_l \cdot 1.5 \cdot D_l \quad (31)$$

$$\sigma_{l,eff} = \varepsilon_l \cdot 1.5 \cdot \sigma_l \quad (32)$$

$$\sigma_{s,eff} = \varepsilon_s \cdot 1.5 \cdot \sigma_s \quad (39)$$

$$\eta = E_{ct} - E_{eq} \quad (40)$$

$$E_{ct} = \Phi_s - \Phi_l \quad (41)$$

$$i_{v,m} = a_{v,m} i_{loc,m} \quad (42)$$

$$i_{loc,m} = i_{0,m} \left(\exp \left(\frac{\alpha_a F \eta}{RT} \right) - \exp \left(\frac{-\alpha_c F \eta}{RT} \right) \right) \quad (43)$$

$$i_{0,m} = i_{0,m,ref}(T) \left(\frac{c_s}{c_{s,ref}} \right)^{\alpha_c} \left(\frac{c_{s,max} - c_s}{c_{s,max} - c_{s,ref}} \right)^{\alpha_a} \left(\frac{c_l}{c_{l,ref}} \right)^{\alpha_a} \quad (44)$$

The mass balance equation for the lithium salt within the electrolyte present in the pores is represented in **Equation 33**. Here, the term R_l , which denotes the rate expression for the production

or consumption of Li-ions, has a more complex definition compared to that discussed in **Section 3.5.5.1**. As outlined in **Equation 34**, it comprises two components. The first accounts for lithium sourced from the reaction occurring between the electrolyte and the electrode, while the second, $R_{l,src}$, considers the contribution of specific additional reaction sources that impact the overall lithium sources.

This mass balance equation is further detailed in **Equation 29**, which accurately describes the ion movement within the electrolyte in the porous electrode domain. The initial term, $-D_{l,eff}\nabla c_l$, demonstrates the application of Fick's First Law, whereas the subsequent term reflects the influence of current density across the electrolyte and the transport number during the diffusion process.

Equation 35 and **Equation 36** address the conservation of current. Here too, an additional term appears compared to the same law seen in the separator domain. While Q denotes the current source within the electrode (Q_s) or electrolyte (Q_l) already included in the separator domain equation, here a new term referred to as the total current density of electrode-electrolyte reaction ($i_{v,total}$) is introduced. This last term, as described in **Equation 37**, comprises two components: the first relates to the reaction current between the electrode or electrolyte, and the second, $i_{v,dl}$, accounts for the non-Faradaic current due to the charge and discharge of the double layer. The latter is formed by two layers of electric charge with opposing polarity forming at the electrode-electrolyte interface. One is composed of electrons at the surface of the electrode, and the other is composed of lithium ions in the electrolyte. Although this double layer can be considered in certain studies, it does not influence the results of this model and is therefore omitted from this analysis.

The conservation of electric current for the electrolyte, as happens for the separator domain, is further elaborated in **Equation 30**, which elucidates how electric current is conducted within the electrolyte. The first term, $-\sigma_{l,eff}\nabla\Phi_l$, adheres to Ohm's Law, with additional terms reflecting factors such as the electrolyte characteristics, including temperature, lithium concentration, activity dependence and transport number, all of which significantly impact current conduction. Meanwhile, the conservation of current for the electrode is further developed in **Equation 38**, which is essentially the initial term of the previously mentioned equation for the electrolyte, Ohm's law.

Equation 31, **Equation 32**, and **Equation 39** adjust the electrolyte diffusion coefficient, electrolyte conductivity and electrical conductivity by incorporating factors accounting for the volume fraction of the electrode or electrolyte, ε_s or ε_l , and a corrective factor of 1.5, called Bruggeman correction factor. This adjustment is necessary because the electrode does not occupy the entire domain; instead, the void spaces are filled by the electrolyte.

The last five equations are pertinent to the electrode kinetics for a charge transfer reaction occurring at the interface between the pore electrolyte and the electrode matrix in a porous electrode. The objective of these equations is to describe the current of the charge transfer electrode-electrolyte reaction, which is crucial for developing the mass balance equation and conservation of current pre-

viously mentioned. Progressing logically, **Equation 42** relates the current density of the electrode-electrolyte reaction, $i_{loc,m}$ measured in $\frac{A}{m^2}$, to a current source of electrode-electrolyte reaction used in the mass balance and conservation of current equations, $i_{v,m}$ measured in $\frac{A}{m^3}$, presented in **Equation 37**. This is achieved by multiplying the former by $a_{v,m}$, which represent the specific surface area in $\frac{1}{m}$ of the electrode-electrolyte interface that is catalytically active for this reaction. Practically each m reaction is considered and all terms, belonging to different reactions, are summed in **Equation 34** and **Equation 37**. The focus then shifts to deriving an expression for this reaction current, $i_{loc,m}$. Initially, **Equation 40** and **Equation 41** evaluate the overpotential, which is the potential difference perceived by a redox couple against the equilibrium potential of the couple, providing the thermodynamic driving force for an electrochemical reaction through Faradaic charge transfer between the electrode and the electrolyte domains. The reaction current density is then expressed using a kinetic expression known as Lithium insertion, outlined in **Equation 43**. Here, the equation is divided into two terms: the first, $i_{0,m}$, is the reaction current density at zero overpotential, multiplied by parameters in an Arrhenius-type equation to account for the effects of overpotential and temperature. This equation is similar to the Butler-Volmer equation, but it is more detailed. At the end, **Equation 44** considers the dependency of $i_{0,m}$ on temperature and lithium concentration in the electrode and electrolyte.

It is also worth pointing out that, even though it is not present in these equations because it is used in an implicit equation in COMSOL for evaluating the lithium concentration in the solid-phase, the diffusion coefficient of the electrode, D_s , is a required data. To clarify all parameters present in the equations:

- \vec{J}_l : mass flux of Li-ions relative to the mass average velocity, measured in $\frac{kg}{m^2s}$.
- R_l : rate expression describing the production or consumption of Li-ions, measured in $\frac{kg}{m^3s}$.
- $\nu_{Li^+,m}$: stoichiometric coefficient of lithium ion insertion in the electrolyte for reaction m, equal to -1 .
- $i_{v,m}$: current source of electrode-electrolyte reaction for specific reaction m not considering the double layer capacitance, measured in $\frac{A}{m^3}$.
- $i_{v,dI}$: non-Faradaic current source due to the charge and discharge of the double layer capacitance, measured in $\frac{A}{m^3}$.
- F : Faraday's constant, equal to $96485.3321 \frac{sA}{mol}$.
- $R_{l,src}$: additional rate expression describing the production or consumption of Li-ions, measured in $\frac{kg}{m^3s}$.

- \vec{i}_l : current density of the electrolyte, measured in $\frac{A}{m^2}$.
- $i_{v,total}$: total current source of electrode-electrolyte reaction considering the double layer capacitance, measured in $\frac{A}{m^2}$.
- Q_l : current source within the electrolyte with the electrode-electrolyte reaction not considered, measured in $\frac{A}{m^3}$.
- \vec{i}_s : current density of the electrode, measured in $\frac{A}{m^2}$.
- Q_s : current source within the electrode with the electrode-electrolyte reaction not considered, measured in $\frac{A}{m^3}$.
- $D_{l,eff}$: effective electrolyte diffusion coefficient describing the rate at which a substance disperses over time across a surface, measured in $\frac{m^2}{s}$. It is assumed that the electrolyte is not present throughout the entire domain, but occupies a certain volume fraction of the total.
- c_l : concentration of lithium salt in the electrolyte, measured in $\frac{mol}{m^3}$.
- t_+ : transport number representing the fraction of total current carried by a given ion in the electrolyte, dimensionless.
- $\sigma_{l,eff}$: effective electrolyte conductivity, indicating the electrolyte solution ability to conduct electric current, primarily through ion movement, measured in $\frac{S}{m}$. It is assumed that the electrolyte is not present throughout the entire domain, but occupies a certain volume fraction of the total.
- Φ_l : electrolyte potential, measured in Volts V.
- Φ_s : electrode potential, measured in Volts V.
- R : universal gas constant, $8.314 \frac{J}{molK}$.
- T : actual cell temperature, measured in Kelvin K.
- $\frac{\partial \ln f}{\partial \ln c_l}$: activity dependence coefficient reflecting how the chemical activity of a substance, indicating its potential to undergo chemical reactions, varies with its molar concentration, dimensionless.
- $\sigma_{s,eff}$: effective electrical conductivity, indicating the electrode ability to conduct electric current, measured in $\frac{S}{m}$. It is assumed that the electrode is not present throughout the entire domain, but occupies a certain volume fraction of the total.

- ε_l : electrolyte volume fraction, indicating the proportion of electrolyte present within the void spaces of porous electrode, dimensionless.
- ε_s : electrode volume fraction, indicating the proportion of electrode present within porous electrode domain, dimensionless.
- 1.5: Bruggeman coefficient, used along with the electrolyte and electrode volume fraction to modify the values of electrolyte diffusion, electrolyte conductivity and electrical conductivity to account for the effective amount of electrolyte present in the separator domain.
- D_l : diffusion coefficient inherent to the electrolyte material, measured in $\frac{m^2}{s}$. It does not consider the presence of the electrolyte inside void spaces.
- σ_l : conductivity of the electrolyte material, measured in $\frac{S}{m}$. It does not consider the presence of the electrolyte inside void spaces.
- σ_s : conductivity of the electrode material, measured in $\frac{S}{m}$. It does not consider the presence of pores.
- η : overpotential, it indicates the difference perceived by a redox couple, measured against the equilibrium potential of the couple; it provides the thermodynamic driving force for an electrochemical reaction by faradaic charge transfer between the electrode and the electrolyte domains, measured in Volts V .
- E_{ct} : potential difference between the electrode and electrolyte potentials, measured in Volts V .
- E_{eq} : equilibrium potential, which illustrates how the potential is linked to both concentration and temperature in the electrode material, measured in Volts V . For a more detailed description of this quantity, please go to **Section 3.5.4**.
- $a_{v,m}$: specifies the area of the electrode-electrolyte interface that is catalytically active for the reaction m , measured in $\frac{1}{m}$.
- $i_{loc,m}$: current density of electrode-electrolyte reaction for specific reaction m excluding the double layer capacitance contribution, measured in $\frac{A}{m^2}$.
- $i_{0,m}$: current density of electrode-electrolyte reaction for specific reaction m considering an overpotential η equal to zero and excluding the double layer capacitance contribution, measured in $\frac{A}{m^2}$.

- α_a : anodic transfer coefficient, it impacts how much $i_{loc,m}$ will change upon a change in overpotential, equal to 0.5.
- α_c : cathodic transfer coefficient, it impacts how much $i_{loc,m}$ will change upon a change in overpotential, equal to 0.5.
- $i_{0,m,ref}$: current density of electrode-electrolyte reaction for specific reaction m . It is the value that assumes $i_{0,m}$ when the reference concentration of lithium-ion in the electrode and electrolyte, $c_{s,ref}$ and $c_{l,ref}$ are present, measured in $\frac{A}{m^2}$ and depending only on the temperature. In the simulation it is considered constant.
- c_s lithium ion concentration in the electrode, measured in $\frac{mol}{m^3}$.
- $c_{s,max}$: maximum lithium ion concentration in the electrode, measured in $\frac{mol}{m^3}$.
- $c_{l,ref}$: reference lithium-salt concentration in the electrolyte, equal to $1000 \frac{mol}{m^3}$.
- $c_{s,ref}$: reference lithium ion concentration in the electrode when the reference equilibrium potential is achieved, measured in $\frac{mol}{m^3}$. It is equal to $\frac{c_{s,max}}{2}$.
- D_s : electrode diffusion coefficient describing the rate at which a substance disperses over time across a surface, measured in $\frac{m^2}{s}$.

After addressing the governing equations, this section also plays a crucial role as it evaluates diffusion-induced stresses. Some of the parameters previously described, such as volume expansion as a function of the normalized concentration, Young's modulus and Poisson's ratio, which are already presented and mentioned in **Equation 3.5.4**, are required here.

Speaking about these stresses, the electrode host material can undergo significant volume changes during charging and discharging. If concentration gradients are present within the electrode particles, this can result in inhomogeneous elastic deformation, thereby inducing stresses. Since atomic diffusion in solids is significantly slower than elastic deformation, mechanical equilibrium is established much faster than diffusion equilibrium. Thus, mechanical equilibrium can be treated as a static equilibrium problem. In the analysis that follows, the electrode spherical particles are assumed to be isotropic linear elastic solids. An important input for the stress evaluation is the relative volume change depending on the concentration, $\frac{dvol}{dc}(\frac{c_s}{c_{s,max}})$, presented in **Figure 40** and **Figure 41** for graphite and silicon, respectively. To be precise, it is related to the normalized concentration, which is the ratio between the actual concentration and the maximum possible concentration. This is convenient as it accurately reflects the degree of lithiation. Specifically, if the ratio is equal to 0, it indicates that no lithium ions are hosted in the solid-phase, implying no lithiation. Conversely, if the ratio is equal to 1, it means that the solid-phase has reached its maximum hosting capacity,

indicating full lithiation.

The equations implemented are:

$$\sigma_r(r) = \frac{2E_a \left(\frac{dvol}{dc}{}_{avr} - \frac{dvol}{dc}{}_{avr,r}(c_s(r)) \right)}{n_{shape}(1 - v_a)} \quad (45)$$

$$\sigma_{surface,r} = surface(\sigma_r(r)) \quad (46)$$

$$\frac{dvol}{dc}{}_{avr} = \frac{1}{r_p^3} \int_0^{r_p} \frac{dvol}{dc}(c_s(r')) r'^2 dr' \quad (47)$$

$$\frac{dvol}{dc}{}_{avr,r}(c_s(r)) = \frac{1}{r^3} \int_0^r \frac{dvol}{dc}(c_s(r')) r'^2 dr' \quad (48)$$

$$\sigma_t(r) = \frac{E_a \left(2 \frac{dvol}{dc}{}_{n_{type}} + \frac{dvol}{dc}{}_{avr,r}(c_s(r)) - \frac{dvol}{dc}(c_s(r)) \right)}{n_{shape}(1 - v_a)} \quad (49)$$

$$\sigma_{surface,t} = surface(\sigma_t(r)) \quad (50)$$

$$\sigma_h(r) = \frac{\sigma_r(r) + 2\sigma_t(r)}{3} \quad (51)$$

$$\sigma_{surface,h} = surface(\sigma_h(r)) \quad (52)$$

$$\sigma_v(r) = |\sigma_r(r) - \sigma_t(r)| \quad (53)$$

$$\sigma_{surface,v} = surface(\sigma_v(r)) \quad (54)$$

With these equations, stresses are evaluated at the microscopic level; each variable from the previous equation is calculated for a specific active particle. Subsequently, all results are merged in COMSOL to consolidate the values for every active particle into a single matrix. This integration facilitates considerations not just at the microscopic level, but also at the macroscopic level, which encompasses the entire electrode thickness. Such macroscopic evaluation is accomplished by merging the surface stresses from each active particle. Being the electrode 2-dimensional in the model developed, it can be considered as composed of circles representing the active particles, each one characterized by the same quantity that can vary from one circle to another. So it is logical that considering the surface stresses for each active particle, it is possible to make consideration on the entire electrode thickness. Furthermore, it is important to note that these equations are specific to an active particle at a fixed time. As time or the active particle varies, the values obtained differ. The mentioned stresses are dependent solely on the radius, r , in this configuration, but there is an implicit dependence on the concentration as well. It was preferred to use only the radius dependence in the formulas for reflecting the nature of their evaluation, a spatial integral over a spherical particle.

Explaining the equations in detail, **Equation 45** displays the radial stress and **Equation 49** the tan-

gential stress. These stresses are evaluated for a spherical particle, calculated using variables such as the volume expansion in relation to the degree of lithiation, Poisson's ratio, Young's modulus and a coefficient that accounts for the shape of the particles, which in this case is spherical. The volume expansion related to lithiation is input in its normal form, as presented in **Figure 40** and **Figure 41**, then used as an average quantity to reflect the average occurrence within the particle, as shown in **Equation 47** and also as an average dependent on the radius r which varies with the particle radius, presented in **Equation 48**. It is crucial to mention that for radial stress σ_r , boundary conditions are applied: at the surface of the active particle, the stress is zero, while at the center of the particle, it is finite. For each stresses, there are surface functions that effectively extract its value at the surface of each active particle, which is important for macroscopic considerations. The surface quantities are obviously independent of the radius.

Equation 51 and **Equation 53** calculate the hydrostatic stress (essentially a mean stress), spread all over the surface being a pressure, and the Von Mises stress, which considers the combined effect of tangential and radial stresses in the particles. Due to the spherical symmetry, one principal stress is equal to σ_r , and the other two are equal to σ_t . For this reason this type of Von Mises and hydrostatic equations are obtained.

To clarify all parameters present in the equations:

- $\sigma_r(r)$: diffusion-induced radial stress inside the spherical active particle, measured in Pa .
- r : radius coordinate inside the sphere varying from zero to the radius of the active particle, measured in m .
- r_p : radius of the active particle, measured in m .
- n_{shape} coefficient used to describe the geometry of the active particle, equal to 3 for spherical ones.
- $\frac{dvol}{dc}(c(r))$: volume variation in function of the normalized concentration, expressed as a percentage.
- $\frac{dvol}{dc}_{avr}$: average volume variation in function of the normalized concentration, expressed as a percentage. It is constant at fixed time t inside the active particle i .
- $\frac{dvol}{dc}_{avr,r}(c(r))$: average volume variation in function of the normalized concentration and radius, expressed as a percentage. It is not constant at fixed time t inside the active particle i , but it depend on the radius coordinate within the sphere.
- E_a : Young's modulus of the anode material used, measured in Pa .
- ν_a : Poisson's ratio of the anode material used, adimensional.

- $\sigma_{surface,r}$: diffusion-induced radial stress at the surface of the spherical active particle, measured in Pa .
- $\sigma_t(r)$: diffusion-induced tangential stress inside the spherical active particle, measured in Pa .
- $\sigma_{surface,t}$: diffusion-induced tangential stress at the surface of the spherical active particle, measured in Pa .
- $\sigma_h(r)$: diffusion-induced hydrostatic stress inside the spherical active particle, measured in Pa .
- $\sigma_{surface,h}$: diffusion-induced hydrostatic stress at the surface of the spherical active particle, measured in Pa .
- $\sigma_v(r)$: diffusion-induced Von Mises stress inside the spherical active particle, measured in Pa .
- $\sigma_{surface,v}$: diffusion-induced Von Mises stress at the surface of the spherical active particle, measured in Pa .

To provide a summary of everything required for this domain, **Table 16** lists all the input data necessary. Values are not provided as they vary from simulation to simulation; for specific values, please refer to **Section 3.7**. Constants that do not change across simulations are the only numeric data listed here. It is important to note that some parameters appearing in the equations are not directly required as inputs in this domain, as they are already sourced and specified directly in other domains. For a more detailed explanation of parameters specifically related to the electrolyte and electrode material, please refer to **Section 3.5.4**.

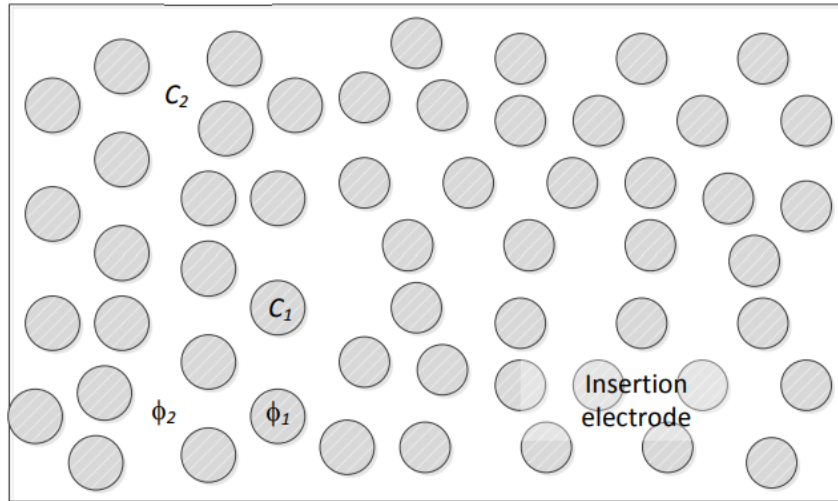


Figure 39: Porous electrode configuration along with parameters for potentials and concentrations [28].

Table 16: Required input data for the 'Porous electrode' domain.

Input data	Value	Unit
Actual temperature, T		K
Faraday's constant, F	96485.3321	$\frac{sA}{mol}$
Universal constant of gas, R	8.314	$\frac{J}{molK}$
Electrolyte conductivity of the electrolyte material, σ_l		$\frac{S}{m}$
Diffusion coefficient of electrolyte material, D_l		$\frac{m^2}{s}$
Transport number, t_+		-
Activity dependence, $\frac{\partial \ln f}{\partial \ln c_l}$		-
Electrical conductivity of the electrode material, σ_s		$\frac{S}{m}$
Electrode volume fraction, ε_s		-
Electrolyte volume fraction, ε_l		-
Bruggeman coefficient	1.5	-
Equilibrium lithium concentration, c_{eq}		$\frac{mol}{m^3}$
Maximum lithium concentration, c_{max}		$\frac{mol}{m^3}$
Diffusion coefficient of electrode material, D_s		$\frac{m^2}{s}$
Active particle radius, r_p		m
Young's modulus only for anode material, E_a		Pa
Poisson's ratio only for anode material, ν_a		-
Volume expansion in function of normalized concentration only for anode, $\frac{dvol}{dc}(c_s)$		%
Equilibrium potential, E_{eq}		V
Reference exchange current density, $i_{0,m,ref}$		$\frac{A}{m^2}$
Anodic transfer coefficient, α_a	0.5	-
Cathodic transfer coefficient, α_c	0.5	-
Electrolyte reference concentration, $c_{l,ref}$	1000	$\frac{mol}{m^3}$
Stoichiometric coefficient of lithium ion insertion in the electrolyte for reaction m, $\nu_{Li^+,m}$	-1	-
Stoichiometric coefficient of lithium ion insertion in the electrode for reaction m, $\nu_{Li^{\ominus},m}$	1	-
Temperature derivative of equilibrium potential, $\frac{dE_{eq}}{dc}$		$\frac{V}{K}$

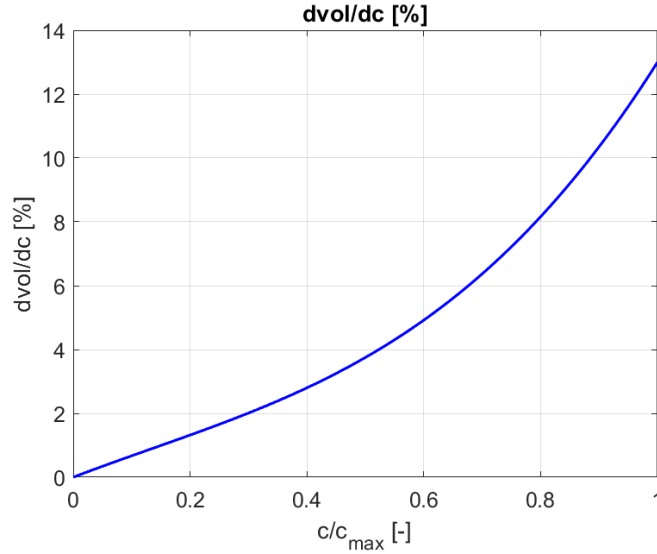


Figure 40: Volume variation in function of the normalized concentration for graphite, $\frac{dvol}{dc}(\frac{c_s}{c_{s,max}})$. (reproduction of **Figure 35**).

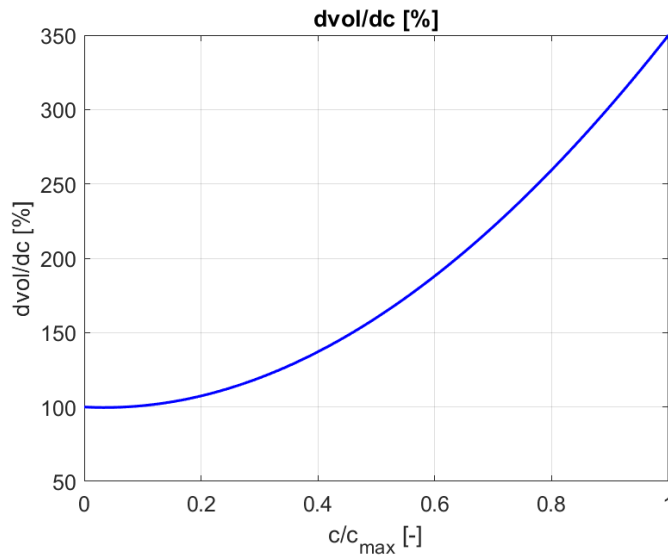


Figure 41: Volume variation in function of the normalized concentration for silicon, $\frac{dvol}{dc}(\frac{c_s}{c_{s,max}})$. (reproduction of **Figure 37**).

3.5.5.3 Electric ground, Electric current and Current conductor domains

The electric ground domain is established to set a reference potential of zero at a specific boundary of the cell. This is necessary whenever a current is applied and also extremely useful because, when measuring a voltage within the cell, it suffices to only measure the voltage at one terminal. This principle is also practical in real-world applications, as when using a voltmeter, it is simply needed

to connect one terminal to the point of interest and the other to the reference. The reference point is assigned a zero potential by ensuring that the following equation is satisfied at the boundary:

$$\Phi_{s,bnd1} = 0 \quad (55)$$

Where $\Phi_{s,bnd1}$ represents the potential at the selected boundary. In the model, this reference potential will be managed in the domain related to lithium-metal, as explained in **Section 3.5.5.5**. Obviously, setting a reference potential equal to zero will not compromise the cell behavior.

The electric current domain acts, as the name suggests, by imposing an electric current on the modelled cell. The sign of the current, which is directly applied to a boundary, is considered positive for charging and negative for discharging. It is crucial to note that 'boundary 1' refers to the one of the electric ground domain, while 'boundary 2' refers to the one of the electric current domain. The equation used for imposing this current is:

$$-\int_{\partial\Omega_{bnd2}} \vec{i}_s \cdot \vec{n}_{bnd2} dl_{bnd2} = I_{s,total} \quad (56)$$

Where:

- $\partial\Omega_{bnd2}$: infinitesimal surface of the boundary selected for the current application, measured in m^2 .
- \vec{i}_s : current density of the electrode, measured in $\frac{A}{m^2}$.
- \vec{n}_{bnd2} : outward pointing normal of the selected boundary, dimensionless.
- dl_{bnd2} : infinitesimal length of the selected boundary, measured in m .
- $I_{s,total}$: total current applied at the selected boundary, measured in A .

During the simulations, the 'Charging-discharging cycle' domain will also be used. Its principle is the same as that of the 'electric current' domain, with the only difference being that a cycle can be imposed. This requires both the charging and discharging currents, along with the respective upper and lower cut-off voltages. When these cut-off voltages are reached, the respective phase stops.

The current conductor domain is specialized to conduct current exclusively within the electron conducting phase, defining the current collector and the tab. Here, a lithium-ion concentration of zero is imposed in this domain, as lithium ions do not diffuse through it. The equations formulated for these purposes are:

$$\nabla \cdot \vec{i}_s = Q_s \quad (57)$$

$$\vec{i}_s = -\sigma_{s,cc} \nabla \Phi_s \quad (58)$$

- \vec{i}_s : current density of the electrode, measured in $\frac{A}{m^2}$.
- Q_s : current source within the electrode with the electrode-electrolyte reaction not considered, measured in $\frac{A}{m^3}$.
- $\sigma_{s,cc}$: conductivity of the current collector material, measured in $\frac{S}{m}$.
- Φ_s : potential at the electrode, measured in Volts V .

For an explanation of all quantities related to an electrode in this section, please refer to **Section 3.5.5.2**.

To provide a summary of everything required for this domains, **Table 17** lists all the input data necessary. Some parameters appearing in the equations are not directly required as inputs, as they are already sourced and specified directly in other domains. Additionally, it is beneficial to highlight a particularly useful expression for the applied current, which will be frequently utilized throughout the work:

$$I_{s,tot} = \pm I_{1C,cell} \cdot C - rate \quad (59)$$

In which $I_{1C,cell}$ represents the current required to fully charge (+) or discharge (-) the battery cell in one hour and the $C - rate$ is the the rate of time taken to charge or discharge a battery, adimensional. For example, a $C - rate$ equal to 2 will completely charge or discharge the cell in half an hour. The general formula used yo evaluate it is:

$$C - rate = \frac{1 \text{ hour}}{\text{time for totally charging or discharging the battery cell}} \quad (60)$$

Where the 'time for totally charging or discharging' is measured in h.

Table 17: Required input data for the 'Electric ground, Electrode current and Current conductor' domains.

Input data	Value	Unit
Total current applied, $I_{s,tot}$		A
Initial electric potential at boundary 2, $\Phi_{bnd2,init}$	1	V
Lithium ion concentration of current collector, c_{cc}	0	$\frac{mol}{m^3}$
Electrical conductivity of current collector, $\sigma_{neg,cc}$	$5.998 \cdot 10^7$	$\frac{S}{m}$

3.5.5.4 No flux, Insulation and Initial values domains.

The no flux domain applies boundary conditions to the area underlined in blue in **Figure 42**. As the name implies, these conditions prevent any mass flux across these boundaries, as dictated by

the following equation that must be ensured at the boundaries previously mentioned:

$$-\vec{n} \cdot \vec{J}_l = 0 \quad (61)$$

Where:

- \vec{n} : denotes the outward pointing normal of the selected boundary, dimensionless.
- \vec{J}_l : mass flux of Li-ions relative to the mass average velocity, measured in $\frac{kg}{m^2s}$.

The insulation domain introduces electric insulation conditions for the edges underlined in blue in **Figure 43**. In the latter, even though it is not highlighted in blue, electrical insulation is also present on the vertical edge at the far left, corresponding to the lithium-metal cathode. This occurs because a dedicated electric ground domain was not directly defined, so it does not appear in the electric insulation domain as blue but it is anyway present.

Returning to the insulation domain, as the term suggests, these conditions ensure that no current density passes through these boundaries. This is enforced by the following equations that must be observed at these locations:

$$-\vec{n} \cdot \vec{i}_l = 0 \quad (62)$$

$$-\vec{n} \cdot \vec{i}_s = 0 \quad (63)$$

Where:

- \vec{i}_l : current density of the electrolyte, measured in $\frac{A}{m^2}$.
- \vec{i}_s : current density of the electrode, measured in $\frac{A}{m^2}$.

The initial values domain specifies the initial concentration of lithium salt in the electrolyte, denoted as $c_{l,init}$, set equal to $1000 \frac{mol}{m^3}$.

To provide a summary of everything required for this domains, **Table 18** lists all the input data necessary. It is important to note that some parameters appearing in the equations are not directly required as inputs, as they are already sourced and specified directly in other domains.

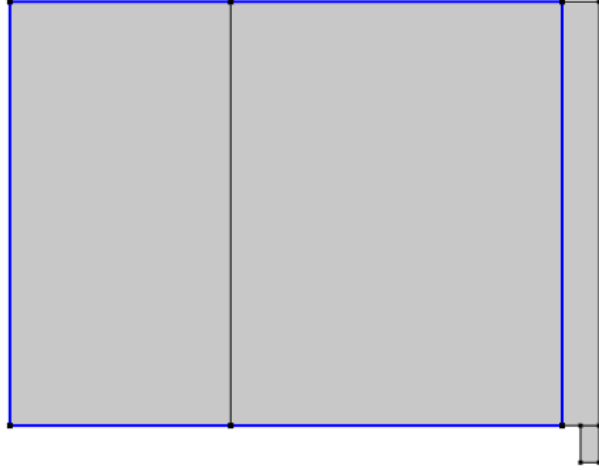


Figure 42: No mass flux condition across the blue boundaries for the developed model.

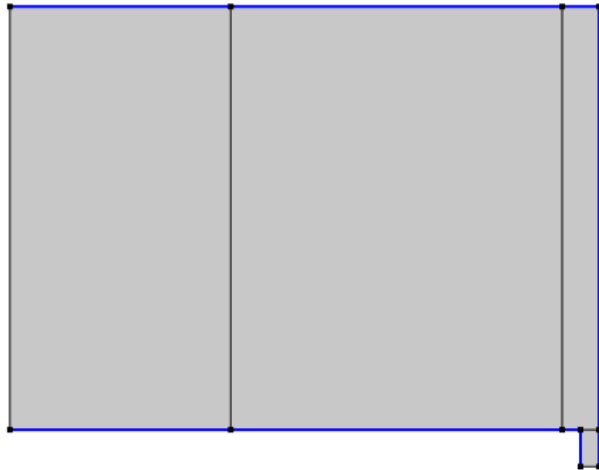


Figure 43: Electric insulation condition across the blue boundaries for the developed model.

Table 18: Required input data for the 'No flux, Isolation and Initial conditions' domains.

Input data	Value	Unit
Initial concentration of lithium salt in the electrolyte, $c_{l,init}$	1000	$\frac{mol}{m^3}$

3.5.5.5 Electrode surface domain.

As already outlined, the model lies in the elimination of the 'porous electrode' domain for the positive electrode replacing it with the 'electrode surface' domain for the cathode. This modification is justified by the non-porous nature of lithium metal. Indeed the representation as a surface is supported by the relatively negligible role of the cathode lithium metal in influencing the overall behavior of the battery, by the fact that electrochemical reactions occur exclusively at the lithium metal surface and by its high electronic conductivity. Consequently, the lithium concentration within the metal is assumed to be zero. Such a setup is typically referred to as a "half-cell" configuration, where the electrode of interest is termed the working electrode, while the other electrode, serving as the counter electrode, is assumed to maintain a fixed potential, here set to zero. This grounding the potential to zero effectively establishes a universal reference within the system, eliminating the need for a separate 'electric ground' domain, explained in **Section 3.5.5.3**. This procedure makes also clear the absence of the insulation blue line for the experimental model reported in **Section 3.5.5.4**.

The goal of the electrode surface domain is to accurately capture the interactions between the electrode and the electrolyte interface. The theoretical descriptions and equations utilized here bear similarities to those detailed in the porous electrode domain, explained in **Section 3.5.5.2**. To properly describe this interface, the following equations are implemented:

$$\vec{n} \cdot \vec{i}_l = i_{total} \quad (64)$$

$$i_{total} = \sum_m i_{loc,m} + i_{dl} \quad (65)$$

$$\vec{n} \cdot \vec{J}_l = - \sum_m \frac{\nu_{Li+,m} i_{loc,m}}{F} - \frac{\nu_{Li+} i_{dl}}{n_m F} \quad (66)$$

$$\eta = E_{ct} - E_{eq} \quad (40)$$

$$E_{ct} = \Phi_{s,ext} - \Phi_l \quad (67)$$

$$i_{loc,m} = i_{0,m} \left(\exp\left(\frac{\alpha_a F \eta}{RT}\right) - \exp\left(\frac{-\alpha_c F \eta}{RT}\right) \right) \quad (43)$$

$$i_{0,m} = i_{0,m,ref}(T) \left(\frac{c_l}{c_{l,ref}} \right)^{\alpha_a} \quad (68)$$

The conservation of electric current for the electrolyte is presented in **Equation 64**, which evaluates how electric current is conducted within the electrolyte. The total current can be further developed in **Equation 65** that is composed of two terms, the first taking into account the sum of the current density of electrode-electrolyte reaction for specific reaction m , while the second accounts non-Faradaic current density due to the charge and discharge of the double layer. This equation is the same as for the porous electrode domain, **Equation 37**, but instead of having a current source in

the right-side term, measured in $\frac{A}{m^3}$, it directly incorporates a current density in the right term, measured in $\frac{A}{m^2}$.

The mass balance equation for the lithium salt within the electrolyte is represented in **Equation 66**. Here, the term on the right comprises two components. The first accounts for the lithium sourced from the electrode-electrolyte reaction for specific reaction m , while the second accounts for the non-Faradaic lithium source due to the charge and discharge of the double layer. The latter is a stratum formed by two layers of electric charge with opposing polarity form at the electrode-electrolyte interface. One is composed of electrons at the surface of the electrode, and the other is composed of lithium ions in the electrolyte. Although this double layer can be considered in certain studies, it does not influence the results of this model and is therefore omitted from this analysis.

The last four equations are pertinent to the electrode kinetics for a charge transfer reaction occurring at the interface between the electrolyte and the electrode, at the surface. The objective of these equations is to describe the current of the charge transfer electrode-electrolyte reaction, which is crucial for developing the mass balance equation and conservation of the current previously mentioned. Progress logically, each m reaction is considered and all terms corresponding to different reactions are aggregated in **Equation 65**. The focus then shifts to deriving an expression for this reaction current, $i_{loc,m}$. Initially, **Equation 40** evaluates the overpotential, which is the potential difference perceived by a redox couple against the equilibrium potential of the couple, providing the thermodynamic driving force for an electrochemical reaction through Faradaic charge transfer between the electrode and the electrolyte domains. The reaction current density is then expressed using a kinetic expression specific to Lithium metal, outlined in **Equation 43**. Here, the equation is divided into two terms: the first, $i_{0,m}$, is the reaction current density at zero overpotential, multiplied by parameters in an Arrhenius-type equation to account for the effects of overpotential and temperature. This equation is similar to the Butler-Volmer equation, but it is more detailed. **Equation 68** considers the dependency of $i_{0,m}$ on temperature and lithium concentration only in the electrolyte and not also in the electrode, as has already been done in **Equation 44** for the porous electrode domain.

To clarify all parameters present in the equations:

- \vec{J}_l : mass flux of Li-ions relative to the mass average velocity, measured in $\frac{kg}{m^2s}$.
- $\nu_{Li+,m}$: stoichiometric coefficient of lithium ion insertion in the electrolyte for reaction m , equal to -1 .
- F : Faraday's constant, equal to $96485.3321 \frac{SA}{mol}$.
- \vec{i}_l : current density of the electrolyte, measured in $\frac{A}{m^2}$.
- c_l : concentration of lithium salt in the electrolyte, measured in $\frac{mol}{m^3}$.

- Φ_l : electrolyte potential, measured in volts V.
- $\Phi_{s,ext}$: fixed electrode potential, equal to 0 V.
- R : universal gas constant, $8.314 \frac{J}{molK}$.
- T : actual cell temperature, measured in Kelvin K.
- $i_{loc,m}$: current density of electrode-electrolyte reaction for specific reaction m excluding the double layer capacitance contribution, measured in $\frac{A}{m^2}$.
- η : overpotential, it indicates the difference perceived by a redox couple, measured against the equilibrium potential of the couple; it provides the thermodynamic driving force for an electrochemical reaction by faradaic charge transfer between the electrode and the electrolyte domains, measured in Volts V.
- E_{ct} : potential difference between the electrode and electrolyte potentials, measured in Volts V.
- E_{eq} : equilibrium potential, which illustrates how the potential is linked to both concentration and temperature in the electrode material, equal to 0 V.
- $i_{0,m}$: current density of electrode-electrolyte reaction for specific reaction m considering an overpotential η equal to zero and excluding the double layer capacitance contribution, measured in $\frac{A}{m^2}$.
- α_a : anodic transfer coefficient, it impacts how much $i_{loc,m}$ will change upon a change in overpotential, equal to 0.5.
- α_c : cathodic transfer coefficient, it impacts how much $i_{loc,m}$ will change upon a change in overpotential, equal to 0.5.
- $i_{0,m,ref}$: current density of electrode-electrolyte reaction for specific reaction m. It is the value that assumes $i_{0,m}$ when the reference concentration of lithium-ion in the electrolyte, $c_{l,ref}$ is present, measured in $\frac{A}{m^2}$ and depending only on the temperature. In the simulation is considered constant.
- $c_{l,ref}$ reference lithium-salt concentration in the electrolyte, equal to $1000 \frac{mol}{m^3}$.
- n_m : number of participating electrons per reaction, equal to 1.

Furthermore, with the 'electrode surface' domain it is not possible to have a separate domain for the SOC evaluation, as usually happen in COMSOL. Therefore, the SOC will be managed by considering the ratio between the lithium concentration and the maximum one at the anode, as clearly outlined in **Section 5**.

To provide a summary of everything required for this section, **Table 19** lists all the input data necessary. Constants that do not change across simulations are the only numeric data listed here. It is important to note that some parameters appearing in the equations are not directly required as inputs in this domain, as they are already sourced and specified directly in other domains.

Table 19: Required input data for the 'Electrode surface' domain.

Input data	Value	Unit
Actual temperature, T		K
Faraday's constant, F	96485.3321	$\frac{sA}{mol}$
Universal constant of gas, R	8.314	$\frac{J}{molK}$
Electrode potential, $\Phi_{s,ext}$	0	V
Equilibrium potential, E_{eq}	0	V
Concentration of lithium-ion in the electrode, $c_{s,ext}$	0	$\frac{mol}{m^3}$
Reference exchange current density, $i_{0,m,ref}$	100	$\frac{A}{m^2}$
Anodic transfer coefficient, α_a	0.5	—
Cathodic transfer coefficient, α_c	0.5	—
Electrolyte reference concentration, $c_{l,ref}$	1000	$\frac{mol}{m^3}$
Stoichiometric coefficient of lithium ion insertion in the electrolyte for reaction m, $\nu_{Li+,m}$	-1	—
Number of participating electrons per reaction, n_m	1	—

3.5.6 Mesh

The mesh functions to divide the domain of the problem into smaller regions or elements, where physical phenomena are numerically addressed within these discrete segments. The quality and density of the mesh greatly influence the accuracy of the simulation results. Typically, a finer mesh yields more accurate outcomes as it effectively captures the gradients and minor effects of physical processes. In fact, the stability and convergence of the solution are dependent on the quality of the mesh: a well-designed mesh ensures that the numerical solution steadily converges to the correct result as the mesh is refined, thus providing reliable and stable outcomes. However, a too fine mesh can lead to increased computational costs, provoking a significantly impact on the computational resources required, including memory and processing time.

In summary, an optimal mesh enhances the efficiency of simulations by minimizing computational demands while still maintaining the accuracy of the results.

The mesh used for all the simulations performed is illustrated in **Figure 44**. It is a free quad mesh, consisting entirely of quadrilateral elements with the following characteristic:

- Maximum element size: specify the maximum allowed element size. In this study it is chosen to be equal to $1.71 \cdot 10^{-4}$ m.
- Minimum element size: specify the minimum allowed element size. This value can be used to, for example, prevent the generation of many elements around small curved parts of the geometry. If some details of the geometry are smaller than the minimum element size, the mesh will contain elements of a smaller size in order to resolve the geometry. In this study it is chosen to be equal to $5.09 \cdot 10^{-9}$ m.
- Maximum element growth rate: determine the maximum rate at which the element size can grow from a region with small elements to a region with larger elements. The value must be greater or equal to one; for example, with a maximum element growth rate of 1.5, the element size can grow by at most 50% from one element to another. In this study it is chosen to be equal to 1.05.
- Curve factor: determine the size of boundary elements compared to the curvature of the geometric boundary (the ratio between the boundary element size and the curvature radius). The curvature radius multiplied by the curvature factor, which must be a positive scalar, gives the maximum allowed element size along the boundary. A smaller curvature factor gives a finer mesh along curved boundaries. In this study it is chosen to be equal to 0.2.
- Resolution of narrow regions: control the number of layers of elements that are created in narrow regions. The value must be a nonnegative scalar, a higher value gives a finer mesh in narrow regions. If the value of this parameter is less than one, the mesh generator might create elements that are anisotropic in size in narrow regions [23]. In this study it is chosen to be equal to 1.
- Scale factors: the z-direction scale is set to 100, while the x-direction scale is set to 1. This multiplicative factor is introduced to handle the significant difference between the cell length (x-direction), which is in the order of centimeters, and the thickness (z-direction), which is in the order of micrometers.

The mesh consists of 6410 domain elements and 475 boundary elements, The domain elements refer to the size of the elements into which the domain is discretized, while the boundary elements refer to the discretization of the model edges. The mesh is particularly fine because the dimensions

of the 2D model vary significantly.

It is also worth pointing out that other meshes have been tested with the model. Finer meshes were attempted, however, this resulted in the same level of accuracy but with higher computational costs. Consequently, the former type has been recognized as very efficient for problem resolution and has therefore been retained for use.

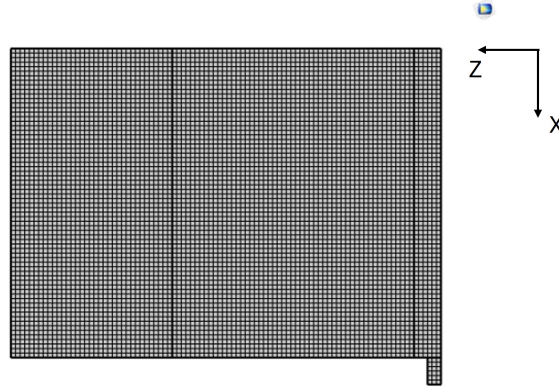


Figure 44: Applied mesh for the developed model.

3.5.7 Study domain

This domain constitutes the solver of the model, enabling the resolution of all physics equations detailed in **Section 3.5.5**. Going into the details, this domain contains a 'Current distribution with initialization' study step and a 'Time dependent' study step. In the first one, the simulation focuses on solving the initial conditions for the electrochemical model, particularly the potentials of the electrode and the electrolyte. This step also solves any global ordinary differential equations (ODEs) dependent variables that are critical to setting up the model correctly. The key aspect here is that this step calculates the initial conditions for these variables at a fixed point in time, setting up the starting scenario for the simulation. This does not mean that it calculates for a continuous range of time but rather initializes the state at a specific moment, usually at the start $t = 0$. Other variables that are not directly related to the potential calculations or ODEs, like concentrations in the electrodes or electrolyte, are not dynamically solved in this step by simply setting them to their predefined initial values.

The 'Time dependent' step comes after the initial conditions have been established and focuses on the dynamic evolution of all variables over time. Unlike the initialization step, which is fixed at a particular moment, it simulates how different variables change as the simulation progresses through time. In this phase, the model uses the initial values obtained from the 'Current distribution initialization' as the starting conditions and performs transient simulations. This means that the software computes the behavior of all variables, including those set to initial values in the first step, across a

specified time period, which could vary based on the duration setting for the simulation.

To summarize, the 'Current distribution with initialization' step is about solving for potentials and global ODE-dependent variables at a fixed initial time point, ensuring that the model starts from a consistent and correct state. The 'Time dependent' step is about letting the model run over a period of time, observing and analyzing how various variables evolve from the initial conditions provided by the first step.

The domain requires few inputs. Initially, in the 'Current distribution with initialization' step, it is essential to specify the chosen distribution current type, in this case, the Primary current distribution. This choice dictates the specific law governing the current density within the electrodes and electrolytes, set as the Second Ohm's Law. Secondly, the 'Time dependent' study required the specific simulation time.

3.6 Optimization of the model parameters tuning using a MATLAB code to fit experimental results

The developed model is electrochemical-mechanical and needs to be tested on both the electrochemical and mechanical sides. For details on how the experimental values, against which the model should be tested, are evaluated, please refer to **Section 4**.

In order to test the model electrochemically, the voltage against time curve obtained from the experimental results is compared. If the comparison matches and the error is low, the model is considered validated. To properly match the results, a tuning of the diffusion coefficient, the active material volume fraction and the reference exchange current density all belonging to the anode is performed, as these parameters have the most influence on the voltage against time curve. This first part of the testing does not require a dedicated MATLAB code, as manual adjustments are very effective. To this purpose, these parameters are slightly changed, always staying within the physical limits imposed by the literature. It is also worth mentioning that tuning the active material volume fraction is justified because the porosity of the anodes is not known a priori. For the effective values of the changed parameters, please refer to **Section 3.7**.

The testing of the mechanical model is more complex. To improve its efficiency and accuracy, a MATLAB code has been developed to optimize a function that plays a crucial role in stress development: the volume expansion as a function of the degree of lithiation. A portion of the code is presented in **Figure 45**, whose aim is to find the coefficients for the selected function that minimize the difference between the stress evaluated by the model and the one measured experimentally. Proceeding in order, 'lsqnonlin' is employed to solve nonlinear least-squares curve fitting problems. The objective is to minimize the sum of five terms, each representing the difference between the stress calculated by the model and the stress measured experimentally. Each term is squared and

'lsqnonlin' aims to find the best coefficients that minimize this sum and best approximate the experimental results. The initial guess for the volume expansion function coefficients, denoted by 'x0', is sourced from the literature, [23] for graphite and [19] for silicon, to emphasize the importance of previous studies and ensure that the resulting function remains close to established values. Additionally, constraints are applied through the variable 'nonlincon', guaranteeing that the function is always increasing and that its minimum and maximum values are consistent with those found in the previous studies. 'Optimoptions' is used to specify an error threshold that must be met, with the maximum number of iterations set to 2000. This limit is not excessively high, as the solution is typically reached quickly for the cases studied.

The resulting tuned functions are presented in **Figure 48** for graphite and **Figure 54** for silicon.

```
options = optimoptions('lsqnonlin', 'Display', 'iter', 'TolFun', 1e-10, ...  
    'TolX', 1e-10, 'MaxFunctionEvaluations', 2000, 'MaxIterations', 2000);  
solution = lsqnonlin(objective, x0, [], [], [], [], [], [], nonlincon, options);
```

Figure 45: Portion of the MATLAB code implemented for the mechanical-model tuning optimization.

3.7 Input data for simulations

In the following sub-section, all the input data required for the various simulations will be presented, allowing the reader to easily reference it without needing to search through the thesis. This part is preferred to be placed at the end of the methodology section since all the respective quantities have already been explained in the previous paragraphs. The first part of the data will refer to the generic simulation data, while the second part will be specific to the materials selected. The material data are also present in **Section 3.5.4**, where they are explained in greater detail.

3.7.1 Input data for simulation of graphite anode

Table 20: General data required for the simulation [23] [24] [25]. Input data graphite anode.

Property	Variable name	Value	Unit
Cell length	L_{cell}	11.5	mm
Tab length	L_{tab}	1	mm
Out-of-plane width	d_y	3	mm
Electrolyte thickness	h_l	60	μm
Anode thickness	h_{neg}	90	μm
Current collector thickness	h_{cc}	10	μm
Tab thickness	h_{tab}	5	μm
Electrode volume fraction in the anode	$\epsilon_{s,neg}$	0.7	[–]
Electrolyte volume fraction in the anode	$\epsilon_{l,neg}$	0.2	[–]
Electrolyte volume fraction in the separator	$\epsilon_{l,sep}$	1	[–]
Anode active particle radius	$r_{p,neg}$	22	μm
Reference exchange current density for the anode	$i_{o,m,ref,neg}$	0.98	$\frac{\text{A}}{\text{m}^2}$
Reference exchange current density for the cathode	$i_{o,m,ref,pos}$	100	$\frac{\text{A}}{\text{m}^2}$
Initial voltage	E_{ini}	2.5	V
Active material volume fraction for the anode	Ω	$1.46 \cdot 10^{-6}$	$\frac{\text{m}^3}{\text{mol}}$
Anodic transfer coefficient	α_a	0.5	[–]
Cathodic transfer coefficient	α_c	0.5	[–]
Electrolyte reference concentration	$c_{l,ref}$	1000	$\frac{\text{mol}}{\text{m}^3}$
Number of participating electrons	n_m	1	[–]
Stoichiometric coefficient for the electrolyte	ν_{Li^+}	–1	[–]
Stoichiometric coefficient for the electrode	$\nu_{Li\theta}$	1	[–]
Electrolyte Bruggeman coefficient	β_l	1.5	[–]
Electrode Bruggeman coefficient	β_s	1.5	[–]
Electrolyte reference concentration	$c_{l,ref}$	1000	$\frac{\text{mol}}{\text{m}^3}$
Initial concentration of lithium salt in the electrolyte	$c_{l,init}$	1000	$\frac{\text{mol}}{\text{m}^3}$
Battery capacity	C	0.54	mAh
Charging current applied	I_{charg}	0.12	mA
Discharging current applied	I_{disch}	–0.12	mA
Upper cut-off voltage	$E_{cut-off,upper}$	2.48	V
Lower cut-off voltage	$E_{cut-off,lower}$	0.03	V

Table 21: Graphite input data taken from the COMSOL library and literature [12] [13] [14] [15] [16]. Input data graphite anode.

Property	Variable name	Equation	Eq.no	Unit
Electrical conductivity	σ_{el}	100		$\frac{S}{m}$
Diffusion coefficient	D	$(1.453 \cdot 10^{-13}) \left(\frac{68025.7 \left(\frac{1}{T_{ref}} - \frac{1}{T_2} \right)}{8.314} \right)$	(20)	$\frac{m^2}{s}$
Equilibrium potential	E_{eq}	$E_{eq,c} \left(\frac{c}{c_{max}} \right) + \frac{dE_{eq}}{dT} \left(\frac{c}{c_{max}} \right) \cdot (T - 298)$	(21)	V
Temperature derivative of equilibrium potential	$\frac{dE_{eq}}{dT}$	$\frac{dE_{eq}}{dT} \left(\frac{c}{c_{max}} \right)$	(22)	$\frac{V}{K}$
Maximum electrode SOC	SOC_{max}	$E_{eq,inv}(E_{max})$	(23)	%
Minimum electrode SOC	SOC_{min}	$E_{eq,inv}(E_{min})$	(24)	%
Equilibrium Li concentration	c_{eq}	$c_{max} E_{eq,inv}(E)$	(25)	$\frac{mol}{m^3}$
Maximum lithium concentration	c_{max}	31507		$\frac{mol}{m^3}$
Reference temperature	T_{ref}	318		K
Temperature for the equations	T_2	$min(393.15, max(T, 223.15))$	(19)	K
Actual temperature	T			K
Young's modulus	E	15		GPa
Poisson's ratio	ν	0.3		-

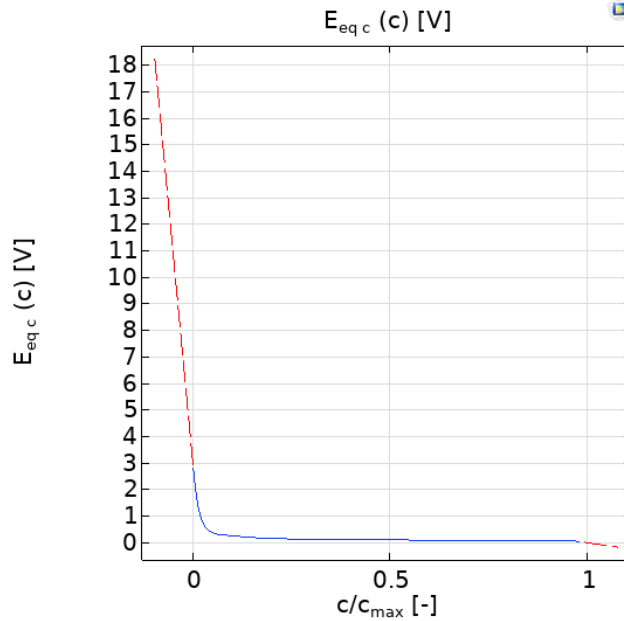


Figure 46: Equilibrium potential depending only on the normalized lithium concentration, $E_{eq,c}$, for graphite. $E_{eq,inv}$ which appears in **Equation 25** is the inverse of the function depicted in the figure. Input data graphite anode.

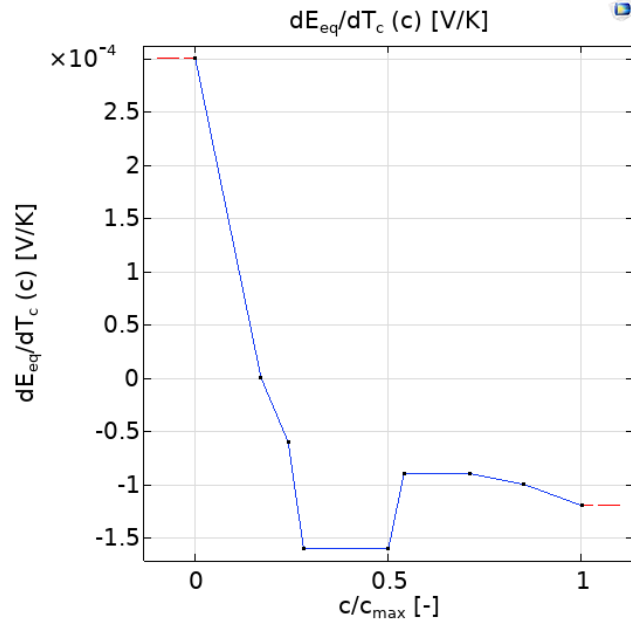


Figure 47: Derivative of the equilibrium potential with respect to the temperature depending only on the normalized lithium concentration, $\frac{dE_{eq}}{dT_c}$, for graphite. Input data graphite anode.

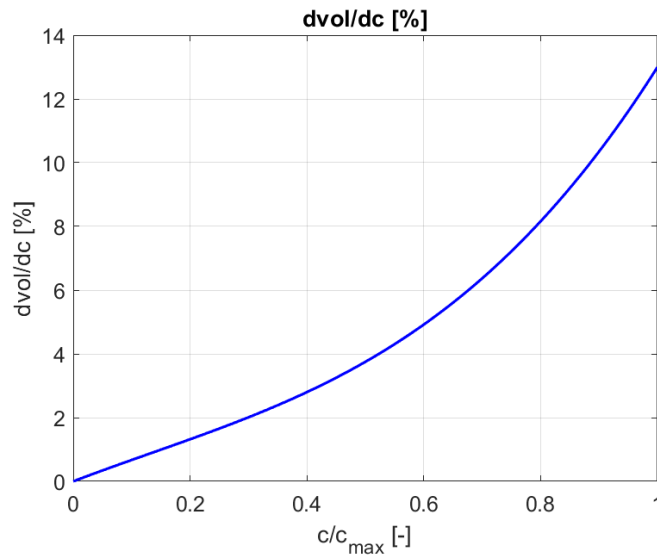


Figure 48: Volume variation in function of the normalized concentration for graphite, $\frac{dvol}{dc} \left(\frac{c_s}{c_{s,max}} \right)$. Input data graphite anode.

Table 22: Copper input data taken from the COMSOL library and literature [9]. Input data graphite anode.

Property	Variable name	Value	Unit
Electrical conductivity	σ_{el}	$5.998 \cdot 10^7$	$\frac{S}{m}$
Young's modulus	E	117	GPa

Table 23: LiPF₆ input data taken from the COMSOL library and literature [10] [11]. Input data graphite anode.

Property	Variable name	Equation	Eq.no	Unit
Diffusion coefficient	D	$(D_c(c))exp\left(\frac{16500 \cdot (\frac{1}{T_{ref}} - \frac{1}{T_2})}{8.314}\right)$	(15)	$\frac{m^2}{s}$
Electrolyte conductivity	σ	$(\sigma_c(c))exp\left(\frac{4000 \cdot (\frac{1}{T_{ref}} - \frac{1}{T_2})}{8.314}\right)$	(16)	$\frac{S}{m}$
Transport number	t_+	$t_{+c}(c)$	(17)	-
Activity dependence	$\frac{\partial \ln(f)}{\partial \ln(c)}$	$(\frac{\partial \ln(f)}{\partial \ln(c)}_c(c))exp\left(\frac{-1000 \cdot (\frac{1}{T_{ref}} - \frac{1}{T_2})}{8.314}\right)$	(18)	-
Reference temperature	T_{ref}	298		K
Temperature for the equations	T_2	$min(393.15, max(T, 223.15))$	(19)	K
Actual temperature	T			K

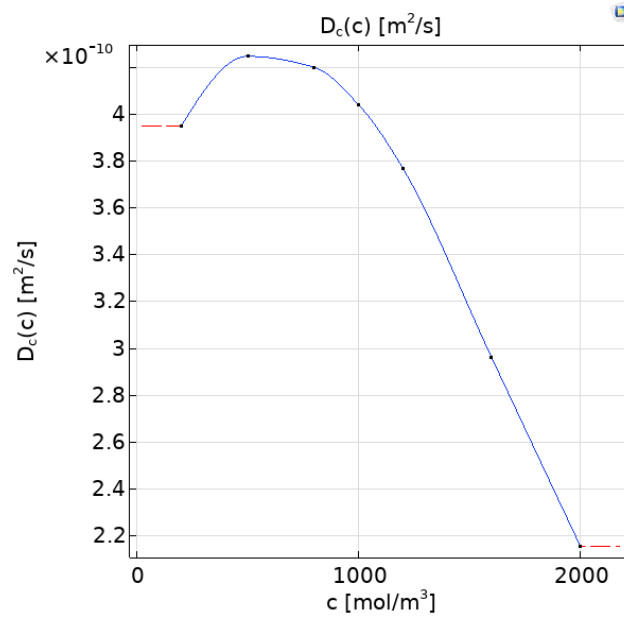


Figure 49: Diffusion coefficient depending only on the lithium concentration, $D_c(c)$, for LiPF₆. Input data graphite anode.

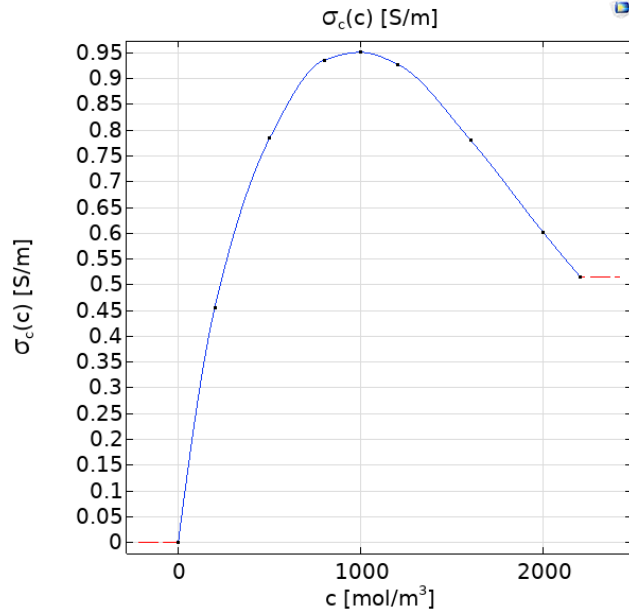


Figure 50: Electrical conductivity depending only on the lithium concentration, $\sigma_c(c)$, for LiPF₆. Input data graphite anode.

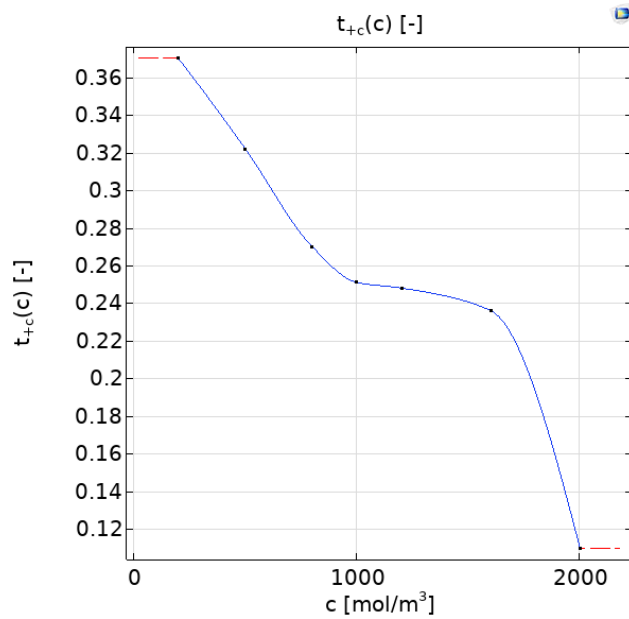


Figure 51: Transport number depending only on the lithium concentration, $t_{+c}(c)$, for LiPF₆. Input data graphite anode.

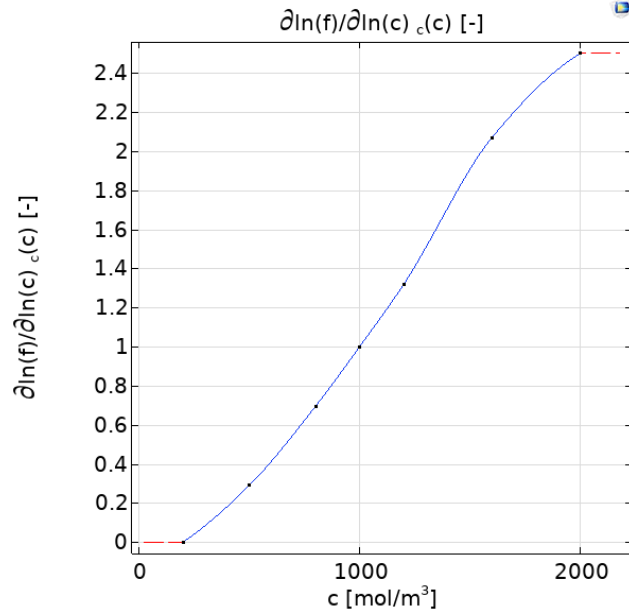


Figure 52: Activity dependence varying only with the lithium concentration, $\frac{\partial \ln(f)}{\partial \ln(c)}_c(c)$, for LiPF_6 . Input data graphite anode.

Table 24: Lithium metal input data taken from the COMSOL library. Input data graphite anode.

Property	Variable name	Value	Unit
Lithium concentration	c	0	$\frac{\text{mol}}{\text{m}^3}$
Equilibrium potential	E_{eq}	0	V
Temperature derivative of equilibrium potential	$\frac{dE_{eq}}{dT}$	0	$\frac{\text{V}}{\text{K}}$

3.7.2 Input data for simulation of silicon anode

Table 25: General data required for the simulation [23] [24] [21]. Input data silicon anode.

Property	Variable name	Value	Unit
Cell length	L_{cell}	11.5	mm
Tab length	L_{tab}	1	mm
Out-of-plane width	d_y	3	mm
Electrolyte thickness	h_l	60	μm
Anode thickness	h_{neg}	90	μm
Current collector thickness	h_{cc}	10	μm
Tab thickness	h_{tab}	5	μm
Electrode volume fraction in the anode	$\epsilon_{s,neg}$	0.4	[–]
Electrolyte volume fraction in the anode	$\epsilon_{l,neg}$	0.5	[–]
Electrolyte volume fraction in the separator	$\epsilon_{l,sep}$	1	[–]
Anode active particle radius	$r_{p,neg}$	22	μm
Exchange current density for the anode	$i_{o,m,neg}$	10^{-2}	$\frac{\text{A}}{\text{m}^2}$
Reference exchange current density for the cathode	$i_{o,m,ref,pos}$	100	$\frac{\text{A}}{\text{m}^2}$
Initial voltage	E_{ini}	1	V
Active material volume fraction for the anode	Ω	$1.45 \cdot 10^{-7}$	$\frac{\text{m}^3}{\text{mol}}$
Anodic transfer coefficient	α_a	0.5	[–]
Cathodic transfer coefficient	α_c	0.5	[–]
Electrolyte reference concentration	$c_{l,ref}$	1000	$\frac{\text{mol}}{\text{m}^3}$
Number of participating electrons	n_m	1	[–]
Stoichiometric coefficient for the electrolyte	ν_{Li^+}	–1	[–]
Stoichiometric coefficient for the electrode	$\nu_{Li\theta}$	1	[–]
Electrolyte Bruggeman coefficient	β_l	1.5	[–]
Electrode Bruggeman coefficient	β_s	1.5	[–]
Electrolyte reference concentration	$c_{l,ref}$	1000	$\frac{\text{mol}}{\text{m}^3}$
Initial concentration of lithium salt in the electrolyte	$c_{l,init}$	1000	$\frac{\text{mol}}{\text{m}^3}$
Battery capacity	C	2.184	mAh
Charging current applied	I_{charg}	0.17	mA
Discharging current applied	I_{disch}	–0.17	mA
Upper cut-off voltage	$E_{cut-off,upper}$	0.73	V
Lower cut-off voltage	$E_{cut-off,lower}$	0.02	V

Table 26: Silicon input data taken from the COMSOL library [17] [18] [19] [20] [21] [22]. Input data silicon anode.

Property	Variable name	Equation	Eq.no	Unit
Electrical conductivity	σ_{el}	1000		$\frac{S}{m}$
Diffusion coefficient	D	$5 \cdot 10^{-14}$		$\frac{m^2}{s}$
Equilibrium potential	E_{eq}	$E_{eq,c}(\frac{c}{c_{max}})$	(26)	V
Temperature derivative of equilibrium potential	$\frac{dE_{eq}}{dT}$	0		$\frac{V}{K}$
Maximum electrode SOC	SOC_{max}	$E_{eq,inv}(E_{max})$	(23)	%
Minimum electrode SOC	SOC_{min}	$E_{eq,inv}(E_{min})$	(24)	%
Equilibrium lithium concentration	c_{eq}	$c_{max}E_{eq,inv}(E)$	(25)	$\frac{mol}{m^3}$
Maximum lithium concentration	c_{max}	278000		$\frac{mol}{m^3}$
Young's modulus	E	90		GPa
Poisson's ratio	ν	0.29		-

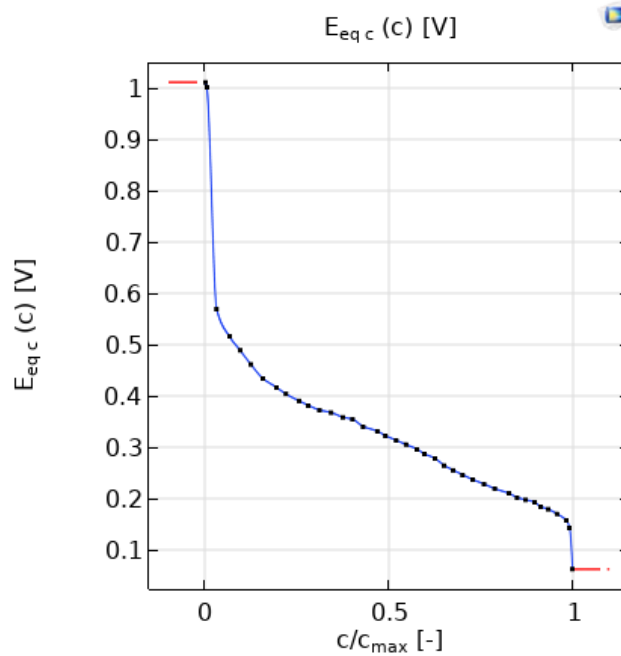


Figure 53: Equilibrium potential depending only on the normalized lithium concentration, $E_{eq,c}$, for silicon. $E_{eq,inv}$ which appears in **Equation 25** is the inverse of the function depicted in the figure. Input data silicon anode.

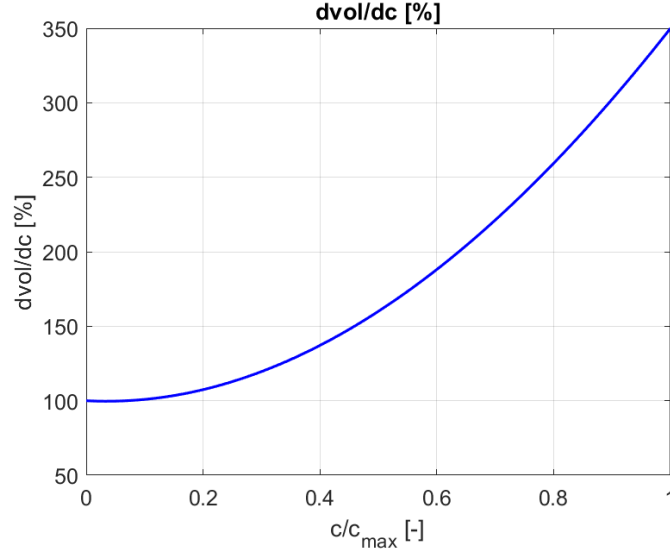


Figure 54: Volume variation in function of the normalized concentration for silicon, $\frac{dvol}{dc}(\frac{c_s}{c_{s,max}})$. Input data silicon anode.

Table 27: Copper input data taken from the COMSOL library and literature [9]. Input data silicon anode.

Property	Variable name	Value	Unit
Electrical conductivity	σ_{el}	$5.998 \cdot 10^7$	$\frac{S}{m}$
Young's modulus	E	117	GPa

Table 28: $LiPF_6$ input data taken from the COMSOL library and literature [10] [11]. Input data silicon anode.

Property	Variable name	Equation	Eq.no	Unit
Diffusion coefficient	D	$(D_c(c))exp\left(\frac{16500 \cdot (\frac{1}{T_{ref}} - \frac{1}{T_2})}{8.314}\right)$	(15)	$\frac{m^2}{s}$
Electrolyte conductivity	σ	$(\sigma_c(c))exp\left(\frac{4000 \cdot (\frac{1}{T_{ref}} - \frac{1}{T_2})}{8.314}\right)$	(16)	$\frac{S}{m}$
Transport number	t_+	$t_{+c}(c)$	(17)	-
Activity dependence	$\frac{\partial \ln(f)}{\partial \ln(c)}$	$(\frac{\partial \ln(f)}{\partial \ln(c)}_c(c))exp\left(\frac{-1000 \cdot (\frac{1}{T_{ref}} - \frac{1}{T_2})}{8.314}\right)$	(18)	-
Reference temperature	T_{ref}	298		K
Temperature for the equations	T_2	$min(393.15, max(T, 223.15))$	(19)	K
Actual temperature	T			K

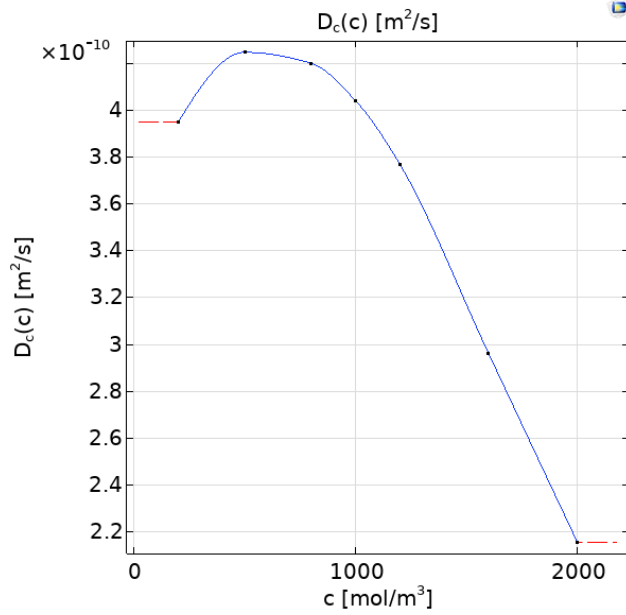


Figure 55: Diffusion coefficient depending only on the lithium concentration, $D_c(c)$, for LiPF_6 . Input data silicon anode.

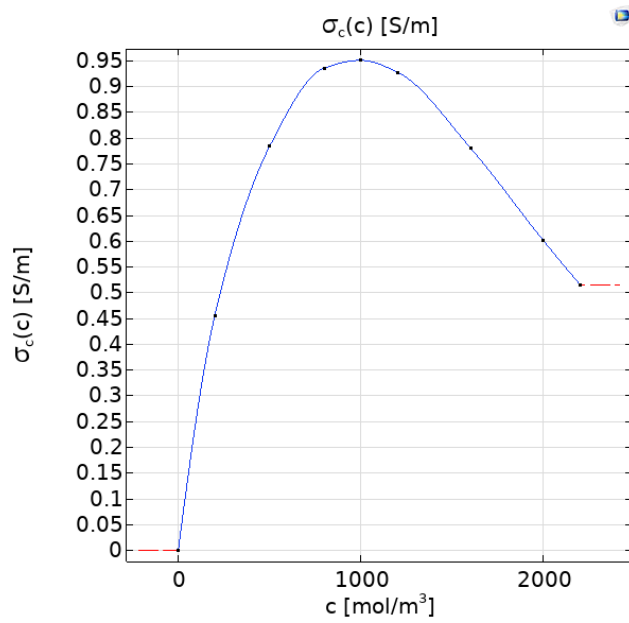


Figure 56: Electrical conductivity depending only on the lithium concentration, $\sigma_c(c)$, for LiPF_6 . Input data silicon anode.

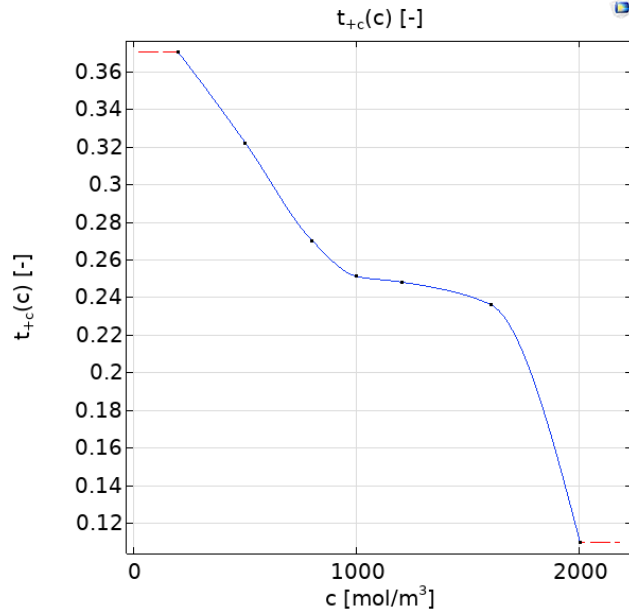


Figure 57: Transport number depending only on the lithium concentration, $t_{+c}(c)$, for LiPF₆. Input data silicon anode.

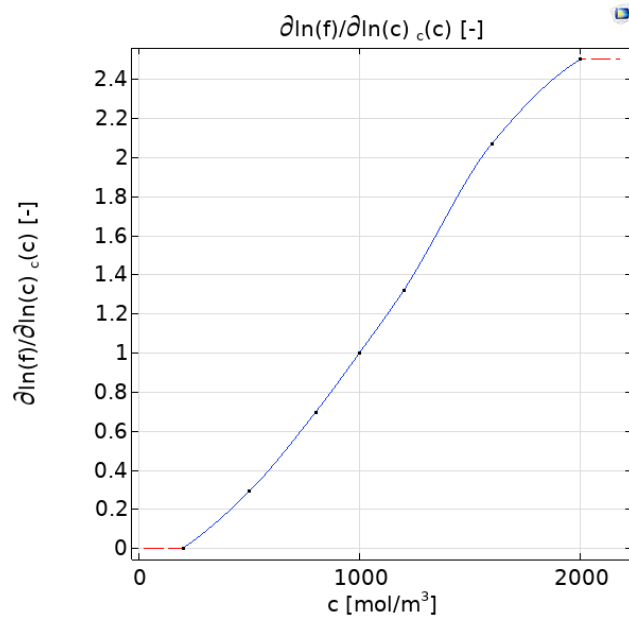


Figure 58: Activity dependence varying only with the lithium concentration, $\frac{\partial \ln(f)}{\partial \ln(c)}_c(c)$, for LiPF₆. Input data silicon anode.

Table 29: Lithium metal input data taken from the COMSOL library. Input data silicon anode.

Property	Variable name	Value	Unit
Lithium concentration	c	0	$\frac{\text{mol}}{\text{m}^3}$
Equilibrium potential	E_{eq}	0	V
Temperature derivative of equilibrium potential	$\frac{dE_{eq}}{dT}$	0	$\frac{V}{K}$

4 Experiments conducted at the laboratory

This part deals with the construction of experimental cells and the measurement of the stress generated from their cycling. These cells serve as real-world scenarios to gather results for testing the fidelity of the model. It is important to note that two different experimental cells were prepared, all characterized by lithium metal-cathode, $LiPF_6$ -electrolyte and copper current collector for the anode. However, the anode material will differ: one cell will contain graphite while the other silicon. For a more detailed description of the materials used and the rationale behind their selection, please refer to **Section 3.3**.

4.1 Mixture preparation

The mixture preparation involves composing the anode material, which will be layered on a copper substrate serving as the current collector. As previously mentioned, two different anode material mixtures will be prepared for two different simulations. The first utilizes graphite as the active material, while the second silicon. These mixtures cannot consist solely of active material particles; binders are incorporated to bind the active material particles together and enhance performance, as explained in **Section 2**, related to the literature review.

For the graphite anode, at first deionized water is added to a beaker to ensure the solution that is going to be formed is not too dense. Deionized water is chosen for its high purity compared to distilled or tap water. Two binders are then added: Styrene-Butadiene Rubber, SBR, and Carboxymethyl cellulose, CMC. Entering into the details of the binders choices, SBR is commonly used because of its excellent flexibility, good aging stability and high tensile strength; while CMC is used as a thickener for SBR to adjust the viscosity. Next, in a separate beaker, carbon black and graphite are added. Carbon black was added to enhance the electrical conductivity, mechanical support and stability to the active components in the electrodes. This mixture is then placed on a vortex mixer, depicted in **Figure 59**, with intermediate speed selected to ensure proper blending between the active material and carbon black. Simultaneously, the beaker containing water, SBR and CMC is transferred to a hot plate, presented in **Figure 60**, that heats up the mixture ensuring the proper dissolution of the binders in water. The hot plate, which also acts as a mixer due to its rotating feature, is set to a speed of 1000 rpm and a temperature of 230°C for one minute for initial heating, then reduced to 80°C otherwise the binders will melt. The rotation is achieved using three magnets inside the beaker moved by a magnetic field beyond the hot plate, where to prevent the beaker movement, a clamp is used. Subsequently, the graphite with carbon black mixture is gradually added to the beaker containing water, SBR and CMC, while it is heated up and rotating to ensure everything is adequately blended. The process involves adding a small amount at a time

and waiting until it is well mixed, if the active material particles are not visible at the surface, more is added. Once completed, the anode material is allowed to cool down for a day with a cover to prevent the evaporation of water and its components.

For the silicon anode, the procedure is the same, with the only difference being that, in addition to the two binders already used (CMC and SBR), Polyacrylic acid (PAA) is also added. The latter is characterized by high polar solvent solubility⁹, improved cycling performance, improved power characteristics, low-temperature performance, less expansion and strong adhesive properties [106]. It is important to underline that all the elements are weighed using a precise scientific balance, as presented in **Figure 61**.

To summarize the procedure done, all the elements present and their percentages are reported in **Table 30** for graphite anode and **Table 31** for silicon one.

Regarding the differences between these two mixtures, aside from the different binders used, another distinction is that while graphite particles were already present, the silicon particles were created by fragmenting a silicon chunk. After fragmentation, the correct particle size was ensured by passing the particles through a sieve available in the laboratory. Another difference lies in the percentage of carbon black, which is higher for silicon because the latter is less conductive than graphite. Additionally, the quantity of deionized water is not listed in the tables because it is used solely as a solvent. It is added as needed to adjust the viscosity of the mixture, but it does not directly affect the mixture composition rules.

Table 30: Mixture composition for graphite anode.

Material	Percentage with respect to 2g
Styrene-Butadiene Rubber, SBR	2.25%
Carboxymethyl cellulose, CMC	2.25%
Carbon black	1%
Silicon with 22 μ m spherical particle radius	94.5%

⁹This means that PAA can dissolve readily in highly polar solvents, such as water.

Table 31: Mixture composition for silicon anode.

Material	Percentage with respect to 2g
Polyacrylic acid, PAA	3%
Styrene-Butadiene Rubber, SBR	2%
Carboxymethyl cellulose, CMC	1%
Carbon black	3%
Silicon with $22\mu m$ spherical particle radius	91%



Figure 59: FOUR E'S scientific vortex mixer.



Figure 60: Thermo scientific CIMAREC hot plate.



Figure 61: Electronic balance SLSC series.

4.2 Application of the anode mixture on the current collector

After the mixture is created, as explained in **Section 4.1**, it is cooled and then poured on the current collector, which has been chosen to be copper. This is a very delicate action that is performed using the machine presented in **Figure 62**. The copper is first cleaned with acetone and dried before being firmly secured on the surface with some tape. Now, the mixture is spread on it and, by using a four paths precision film applicator shown in **Figure 63**, it is dragged ensuring the desired thickness for coating the anode. Afterwards Polyacrylic acid, PAA, is applied at the back of the current collector, to ensure insulation. At the end, it is dried on the hot plate, and then placed in the vacuum drying oven, depicted in **Figure 64**, for one day to completely dry while the inside temperature is set to 80 °C . The vacuum is created by setting the pressure inside to 0.06 MPa.

Finally, **Table 32** and **Table 33** summarize the different thicknesses for each type of anode created, which is the most important data evaluated in this section.

Table 32: Thickness employed for graphite anode and for its current collector.

Component	Thickness	Unit
Graphite anode	90	μm
Copper current collector	10	μm

Table 33: Thickness employed for silicon anode and for its current collector.

Component	Thickness	Unit
Silicon anode	90	μm
Copper current collector	10	μm

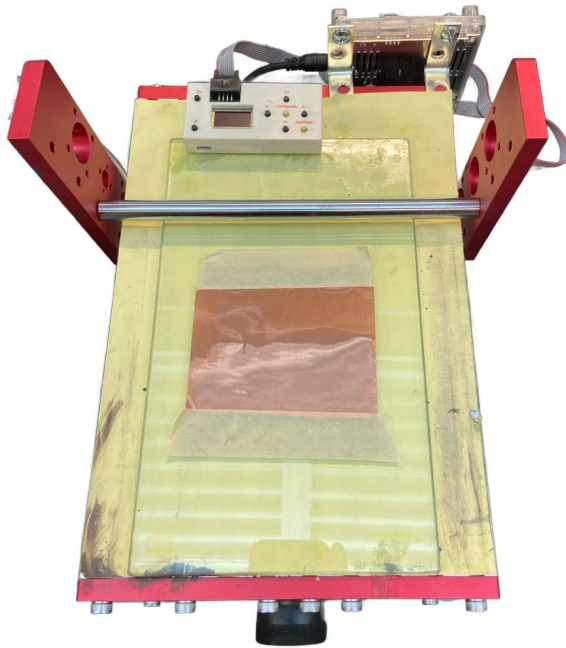


Figure 62: Base used for the application of anode mixture on the current collector.



Figure 63: Four paths precision film applicator used for choosing the anode thickness.



Figure 64: Vacuum drying oven DZF-6020.

4.3 Experimental cell assembly

The experimental half-cell, composed of the cathode, electrolyte, anode and negative current collector, was put in a Teflon box to ensure of an isolated and non reactive pure environment with air sealed condition.

First, the environment to contain the cell is built. Using the CAD software CATIA[®], the CAD models of the geometry to be obtained is created, as presented in **Figure 65** and **Figure 66**. Both components were fabricated using the CNC milling machine, shown in **Figure 67**, which receives an algorithm from the CATIA CAD to execute specific movements and create the desired geometry. The geometries were built separately and then assembled together. The first one, the box, is made of Teflon and the second one, the insert, is made of ultra-high molecular weight polyethylene, which are excellent insulator and resistant to nearly all battery electrolytes.

Specifically, **Figure 65** shows the box. The dimensions are not specified as they are not directly related to the problem, with only the maximum diameter provided to give an idea of the size. The two circumferential cavities are designed for O-ring to ensure isolation and the circular holes are created to secure the quartz window, that was placed on top to allow observation of the cell deflection during the charging-discharging process.

The insert, displayed in **Figure 66**, was holding the anode and cathode. The anode and cathode were screwed into the indicated surfaces inside the argon filled glovebox, presented in **Figure 68**. The latter is crucial because it contains very low humidity and is filled with Argon inside it, avoiding any possible reaction of the atmosphere with the lithium metal and the electrolyte. While the

cathode was completely fixed to its surface, only a portion of the anode was fixed, allowing the other part to deflect during the charging/discharging process, like a cantilever. The purpose is to measure this deflection and evaluate the resulting stress. Even here only the most important dimensions are presented, in order to provide an idea of the size of the crucial attachment surfaces. To summarize the built cells were made of:

- Lithium metal as cathode.
- $LiPF_6$ electrolyte.
- Graphite or silicon coating as anode.
- Copper current collector.

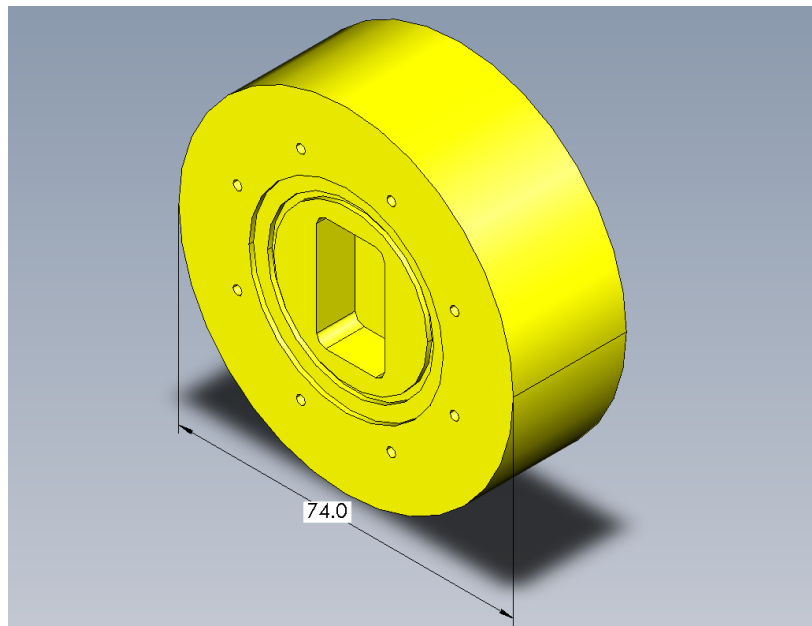


Figure 65: CATIA CAD model of the Teflon box containing the cell.

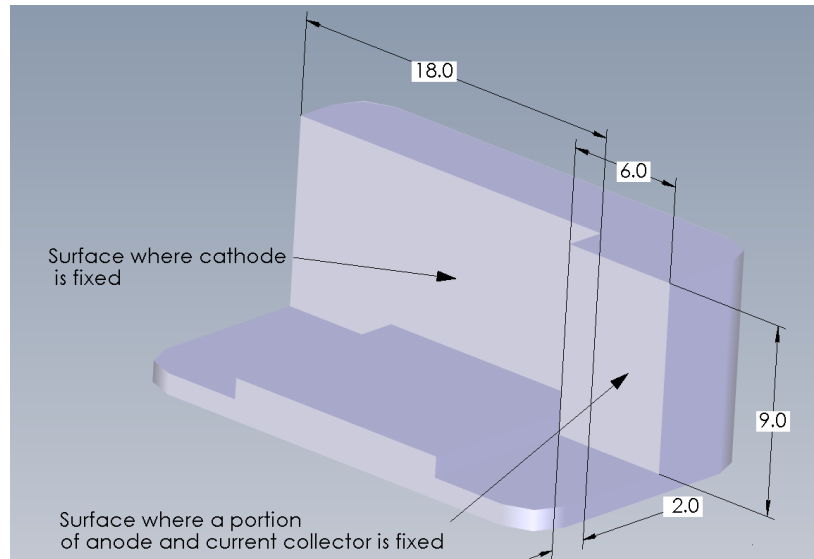


Figure 66: CATIA CAD model of the Ultra-high molecular weight polyethylene insert used to fix the cell, contained within the Teflon box.

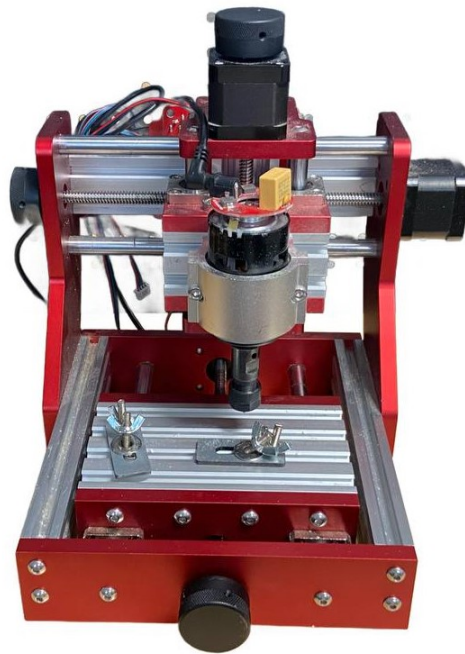


Figure 67: CNC milling machine.



Figure 68: Glovebox.

4.4 Evaluation of cell deflection and stress under charging-discharging cycle

After the cell remains inside the glovebox for 18 hours, it is taken out and prepared for testing. The completed cell is shown in **Figure 69**. **Figure 70** illustrates the setup for stress evaluation. In this setup, a digital microscope is positioned to capture time laps images for deflection analysis. The anode and cathode are connected to the red and black connectors for the application of the charging-discharging cycle.

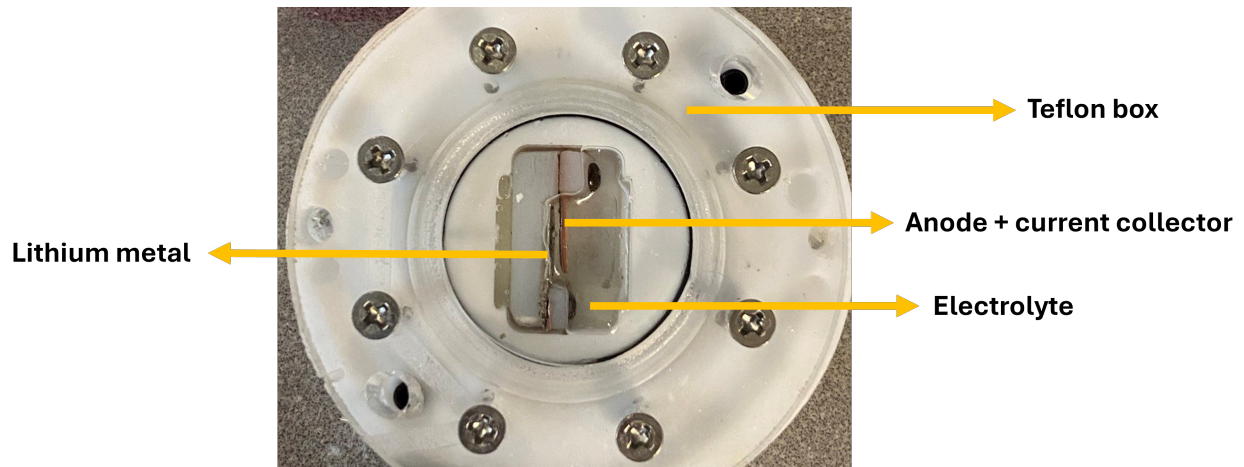


Figure 69: Description of the built experimental-cell.



Figure 70: Deflection evaluation setup equipped with a digital microscope.

The terminals are directly connected to the Battery analyzer (LANDT), shown in **Figure 71**. This system ensures high-precision testing of the battery, utilizing various programs for data acquisition and processing. The applied cycle is created and controlled by the LANDT program, as illustrated in **Figure 72** for graphite and **Figure 73** for silicon. Each cycle features a charge-discharge process, but while the graphite cycle uses a current of $\frac{C}{4.5}$, equal to 0.12 mA, the silicon one uses a current of $\frac{C}{12.85}$, equal to 0.17 mA. The C-rate for graphite is higher than that for silicon, due to the lower diffusion coefficient of lithium in silicon necessitates a smaller c-rate being the electrochemical reactions slower. For graphite, the charging cycle continues until the voltage reaches 0.03 V, while discharging continues until it reaches 2.8 V. For silicon, charging stops when the voltage drops below 0.02 V, and discharging stops at 0.73 V. In both cases, when the respective voltage threshold is reached, the phase ends and the next one begins. Additionally, a time marker labeled "Record: 01:00" indicates that voltage data were recorded every minute. On the right side of the both the figures, the 'Global Config' section, as the name suggests, contains global configuration settings for the imposed cycle. For this work the necessary variables are the nominal capacity (used for current calculation, as current is determined by the C-rate) and the maximum and minimum safety voltages. These safety voltages ensure that the simulation stops if either of the safety thresholds

is reached. They differ from the phase voltage thresholds, which transition the cycle to the next phase if met. Therefore, the safety values were set below the phase voltage thresholds to avoid an abrupt interruption. It is worth noting that in this work, to be in accordance with the criteria utilized, "charge" refers to the process in which lithium ions are intercalated in the anode, while "discharge" refers to the opposite process, regardless of whether the voltage decreases or increases.

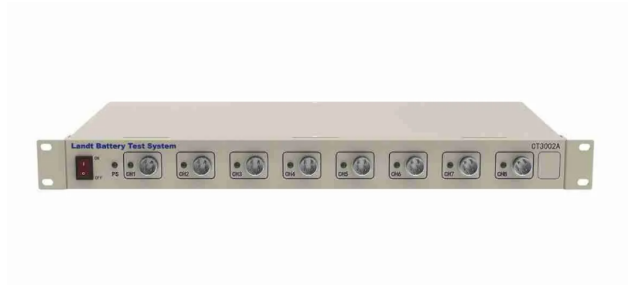


Figure 71: Eight channel battery analyzer.

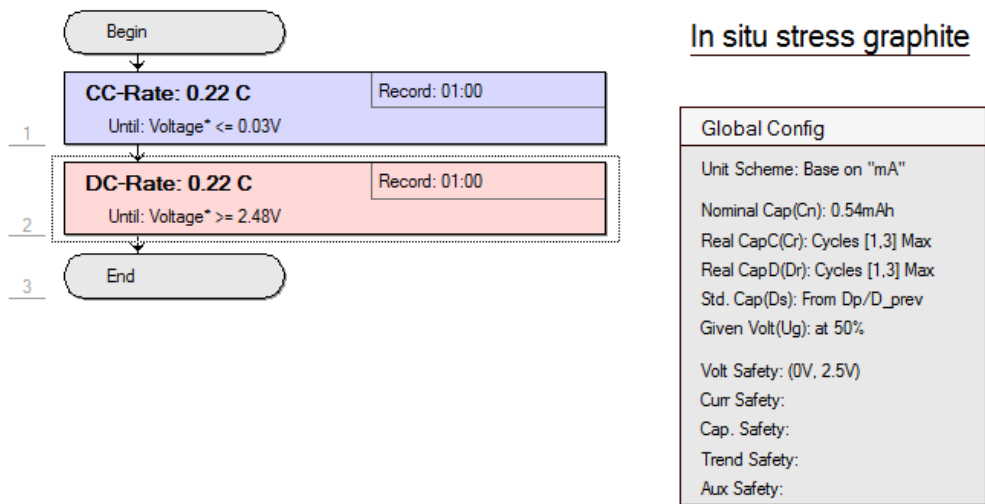


Figure 72: Charging-discharging cycle applied to the graphite anode using the LANDT Battery Analyzer program.

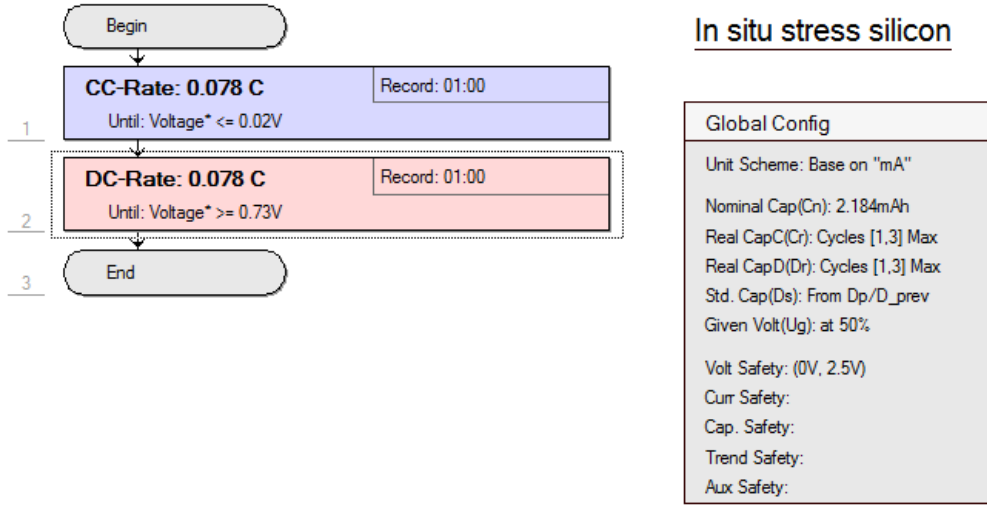


Figure 73: Charging-discharging cycle applied to the silicon anode using the LANDT Battery Analyzer program.

During the cycle, as lithium ions enter the anode during charging, there is an increase in deflection. Naturally, the opposite occurs during discharging. The deflection at the free end, that is the maximum one for each time instant, is captured by the previously mentioned microscope by taking pictures. To better understand what happens during the cycle, it is possible to refer to **Figure 74**, where the electrode is treated as a cantilever beam. When lithium ions are intercalated into it, there is a positive deflection, while during de-intercalation, which occurs during discharging, the deflection is reduced. Due to this correspondence, the deflection is defined as the difference in the z-direction between the deformed beam and its rest position, which is horizontal. It is worth noting that the x direction corresponds to the anode length, while the z direction corresponds to the thickness.

To complete the equivalence to a cantilever beam, the intercalation and de-intercalation processes can be treated as a cantilever beam under a uniformly distributed load. Therefore, a relationship can be established between the deflection and the curvature, as demonstrated in the study by Yang et al. [107]. Specifically, the curvature related to deflection can be evaluated as follows:

$$\kappa = \frac{4 \cdot \text{deflection}}{(\text{Anode length})^2} \quad (69)$$

Now, to relate the evaluated deformation to the stress developed, the following formulas are used, based on the work of Li et al. [41]. The convention utilized with these equations is shown in **Figure 76** where, as before, the z-direction indicates the thickness and the x-direction represents the length of the anode itself. Obviously, even if not present in the figure, for lithium-ion extraction the convention remains the same but the deformation decreases. The used formulas, evaluating

stress based on curvature and hence the deformation, are as follows:

$$\varepsilon_0 = \frac{\Omega c (h_1^4 E_1 + 3h_c^2 h_1^2 E_c + 4h_c^3 h_1 E_c) E_1}{3(h_1^4 E_1^2 + 4h_c h_1^3 E_c E_1 + 6h_c^2 h_1^2 E_c E_1 + 4h_c^3 h_1 E_c E_1 + h_c^4 E_c^2)} \quad (70)$$

$$\sigma_1 = E_1 (\varepsilon_0 + z\kappa) - \frac{1}{3} E_1 \Omega c \quad (71)$$

Where:

- Ω is the partial molar volume of the active material, measured in $\frac{m^3}{mol}$.
- c is the lithium-ion concentration, derived from the electrochemical model after testing, measured in $\frac{mol}{m^3}$.
- h_1 is the anode thickness, measured in micrometers.
- E_1 is the Young's modulus of the active material, measured in *MPa*.
- h_c is the current collector thickness, measured in micrometers.
- E_c is the Young's modulus of the current collector, measured in *MPa*.
- ε_0 is the in-plane strain, dimensionless.
- z is the distance of the evaluated part from the current collector interface, measured in micrometers.
- σ_1 is the diffusion-induced stress in the anode, measured in *MPa*.

It is important to note that the model developed is an electrochemical-mechanical model. When the model accurately reproduces the electrochemical behavior and it is tested to verify if it replicates the voltage versus time cycle imposed in the experiment, the concentration data can be used to evaluate stress experimentally. Furthermore, it is crucial to specify that the chosen value of z is equal to the anode thickness. This ensures that the stress is focused on the electrolyte interface, which is the area experiencing the highest stress during the cycle. As can be seen, changes in the x-direction do not influence this focus. For consistency, testing the COMSOL model will also concentrate on the active particles positioned at this distance. In fact, the anodes consist of numerous active material particles, and the model can evaluate stress development for each one. **Figure 75** illustrates the specific one chosen for the model, to be consistent with the experimental evaluation. However, the results will also include considerations across the entire electrode surface.

Here, the specific values used for the calculation are not reported, as they are all presented in **Section 3.7**.

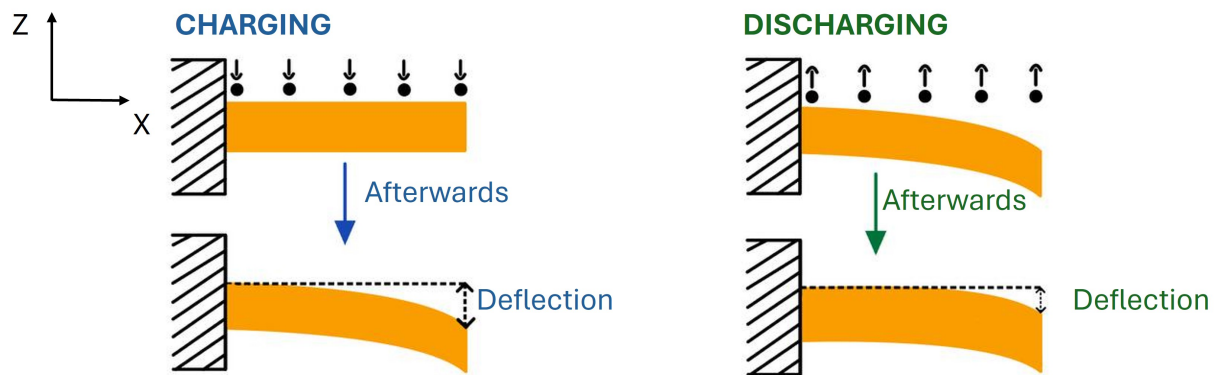


Figure 74: Deflection of the cantilever anode during lithiation, in blue, and delithiation, in green.

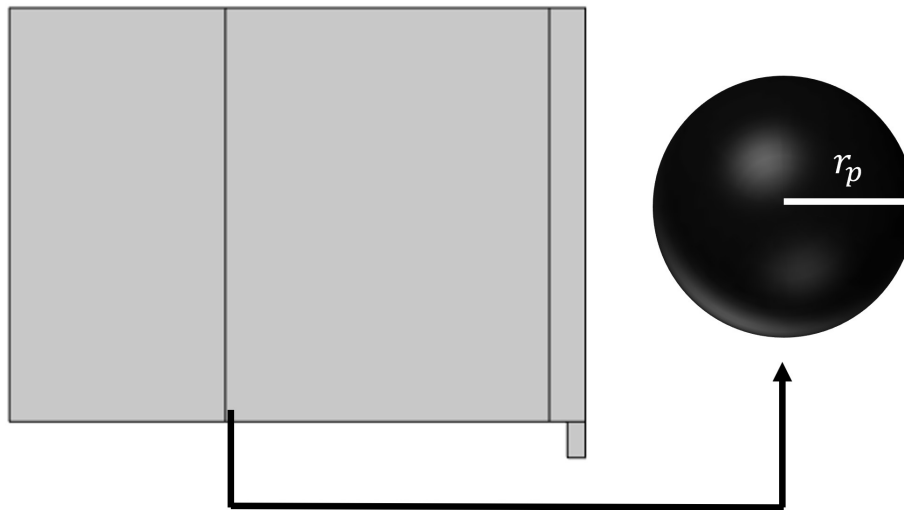


Figure 75: Selection of anode active particle position for the model intra-particle results.

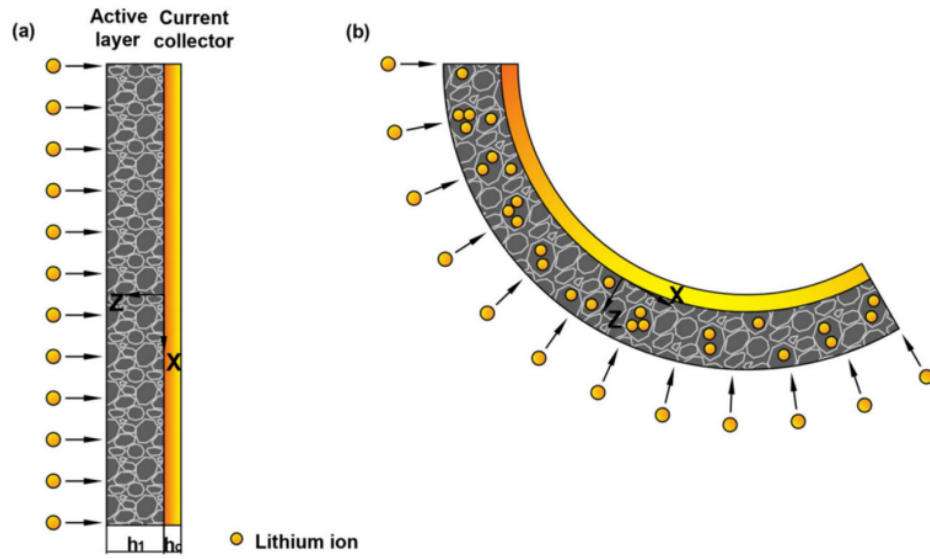


Figure 76: Convention utilized for the experimental stress evaluation. (a) indicates the initial state of the anode, while (b) a deformed state with lithium ions insertion. For the extraction of lithium ions the convention is still the same, but the deflection obviously decreases [41].

5 Results and discussions

In this section, the results for both silicon and graphite anodes, obtained from experimental data and the developed model, will be evaluated. This part is divided into paragraphs discussing the results for the graphite anode, the silicon anode and a comparison of them.

5.1 Graphite anode

This paragraph regarding the graphite anode is divided into three subsections. The first, as the name suggests, compares the results obtained experimentally with those obtained by the model to test its validity. The following, using the tested results, goes beyond the experimental considerations and makes a deeper analysis of the stresses development that can only be done using the model features. The last one performs a parametric analysis. Using the same data for which the model is appropriately tested, the influence of variations in active particle size, anode thickness and charging rate applied on the development of stress is studied to understand a possible trend that could reduce them.

5.1.1 Model validation

As also explained in **Section 4.4**, the graphite cell built in the laboratory is tested with a charging-discharging cycle at a current of $\frac{C}{4.5}$; specifically, the absolute value of the current applied is 0.12 mA. It is worth noting that in this work, to be in accordance with the criteria utilized, "charge" refers to the process in which lithium ions are intercalated in the graphite, while "discharge" refers to the opposite process, regardless of whether the voltage decreases or increases.

Figure 77 shows the voltage vs. time during the cycle. The cell is fully charged until 242 minutes and then fully discharged from 242 minutes to 523 minutes. The experimental results are shown in orange dashed line, while the model results are shown in solid blue line. As can be seen the model, thanks to appropriate parameter tuning, accurately reproduces the experimental results, with their behavior matching within an error of 3%. It is worth pointing out that this voltage characteristic is also influenced by the fact that the built cell is tested during the first cycle, and so it is affected by the SEI layer formation. This is done because, after the first cycle, as will be seen, stress starts from an initial deformation state rather than the initial position itself.

In conclusion, the electrochemical behavior of the model is tested and it is confirmed that it can reproduce the electrochemical reactions in the cell. As already explained, the model is an electrochemical-mechanical one, so now the mechanical aspect also needs to be verified.

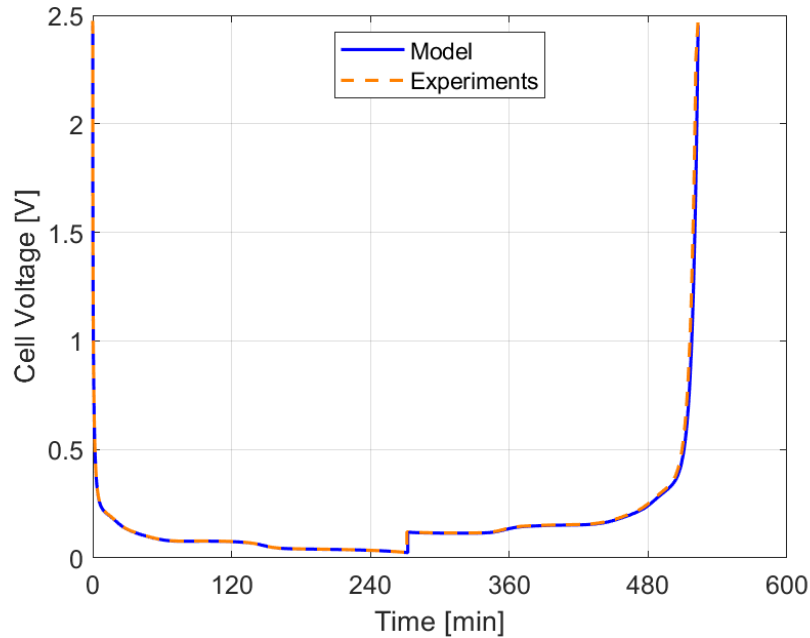


Figure 77: Voltage-time profile of the graphite anode cell during the charging-discharging cycle.

In order to test the mechanical-model, it is necessary to track the concentration of lithium ions within the cell at each time instant. These data can be directly obtained from the electrochemical model, as this feature has already been validated.

Figure 78 explains an important concept for evaluating the results, as already discussed in **Section 4.4**. Graphite anode consists of numerous particles of active material and the model can evaluate the lithium concentration and stresses development for each of them. Therefore, most of the results presented in this work, except for the one relative to the entire anode surface, refer to the specific active particle highlighted at the electrolyte-anode interface, as it is the one characterized by the highest stress developed. It is important to note that when referring to these particles, the x-axis of the graph represents the quantity $\frac{r}{R}$, where 0 denotes the center of the particle and 1 denotes the surface. To maintain clarity, each figure caption will indicate whether it refers to this specific particle or not, for both the model and experimental results. For a better understanding of how the microscopic level of particle and macroscopic level of electrode thickness, are treated, please refer to **Section 3.5.5.2**.

Figure 79 shows the lithium concentration for the selected particle during the charging phase at various time instants, and so at various SOC. The value of the SOC is calculated multiplying by 100 the normalized concentration at the surface of the active particle. It has been decided to adopt this definition to align with the observation that maximum concentration values during charging and minimum values during discharging occur at the particle surface, corresponding to 0% and 100% SOC, respectively. For this reason in this work, whenever an increase in SOC is mentioned,

it directly relates to the lithium insertion phase. Conversely, a decrease in SOC refers to the lithium extraction phase. Continuing with the charging phase, the normalized lithium concentration starts from zero, reflecting that it is the first cycle applied to the cell, and increases steadily. By the end of charging, it reaches its peak due to lithium intercalation. As it can be noticed, concentration values at the particle center are consistently lower than those at the surface, reflecting the ongoing insertion and migration of lithium ions.

Figure 80 depicts the discharging phase that follows the charging one explained before. Here, the lithium concentration decreases as lithium ions are extracted from the particle, reaching at the end of the process a minimum value of zero. Furthermore, it is evident that concentration values at the particle center are consistently higher than those at the surface due to the extraction of lithium ions. Speaking about both processes, the increase or decrease in lithium ions during charging or discharging is uniform due to the fact that the diffusion coefficient is obviously the same. Indeed, it is important to note that these values represent the total lithium ions that can be fully extracted and inserted into the particle during the cycle. This excludes any lithium ions that may remain irreversibly trapped after completing the full cycle, which significantly influences residual stress, as it will be discussed later.

Moreover the effective concentration values, rather than normalized ones, will be used to assess stress development both experimentally and in the model itself.

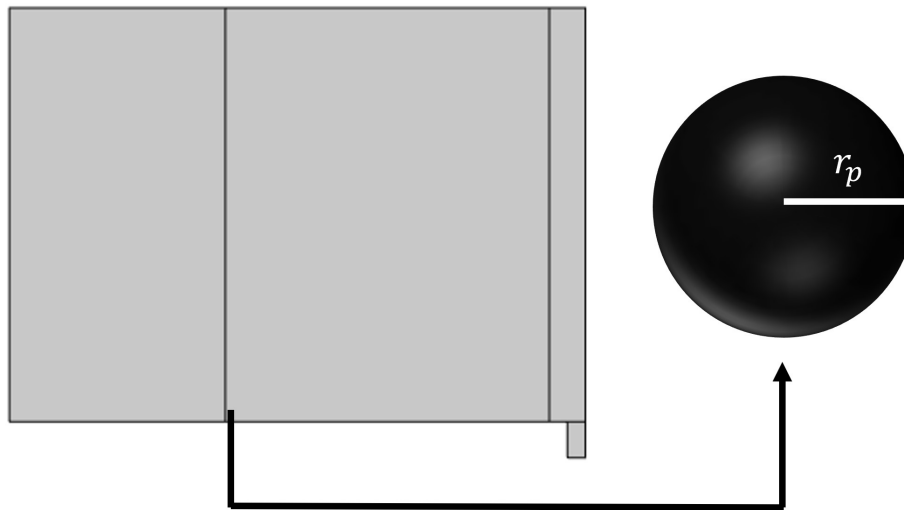


Figure 78: Selection of active particle position for intra-particle results, graphite anode.

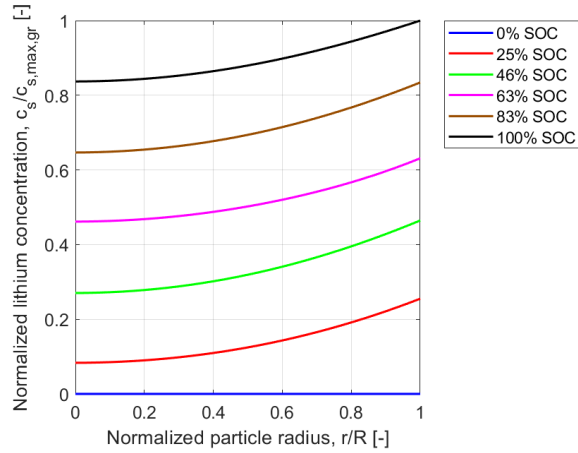


Figure 79: Normalized lithium ions concentration variation in the selected active particle during the charging phase of the cycle, graphite anode.

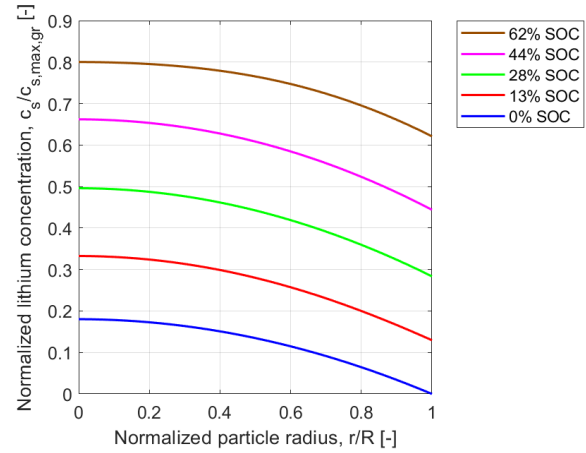


Figure 80: Normalized lithium ions concentration variation in the selected active particle during the discharging phase of the cycle, graphite anode.

After the electrochemical model has been tested and the concentration values evaluated, the mechanical model results are now presented.

Figure 81 illustrates the free-end deflection relative to the initial position of the graphite anode during the cycle. During charging, deflection increases as lithium ions are inserted into the graphite electrode, causing expansion. Being a cantilever, the electrode is free to deflect on its unattached side. Deflection remains nearly constant until 156.9 minutes. From 163.2 to 217.6 minutes, there is an increase in slope, followed by a decrease as pores for lithium ions shuttling become further taken up and embedding paths becomes winding as well, which blocks and mitigate the further lithiation and so deformation towards the end, where it reaches a peak of 5.39 mm.

During discharge the trend reverses, as the ions are extracted from the anode, the induced volume contraction leads to a deflection reduction. Initially, there is a steep slope in deflection reduction within the first 50 minutes of discharge, followed by a slower decrease. Notably, at the cycle end, the electrode does not return to its initial position, retaining a small deflection of 0.87 mm due to the residual lithium ions that cannot be extracted from the particle.

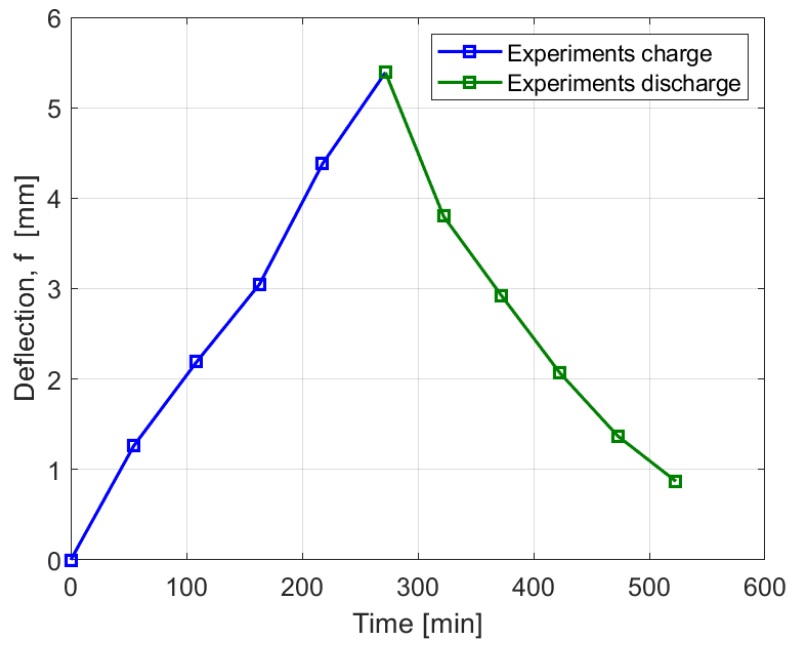
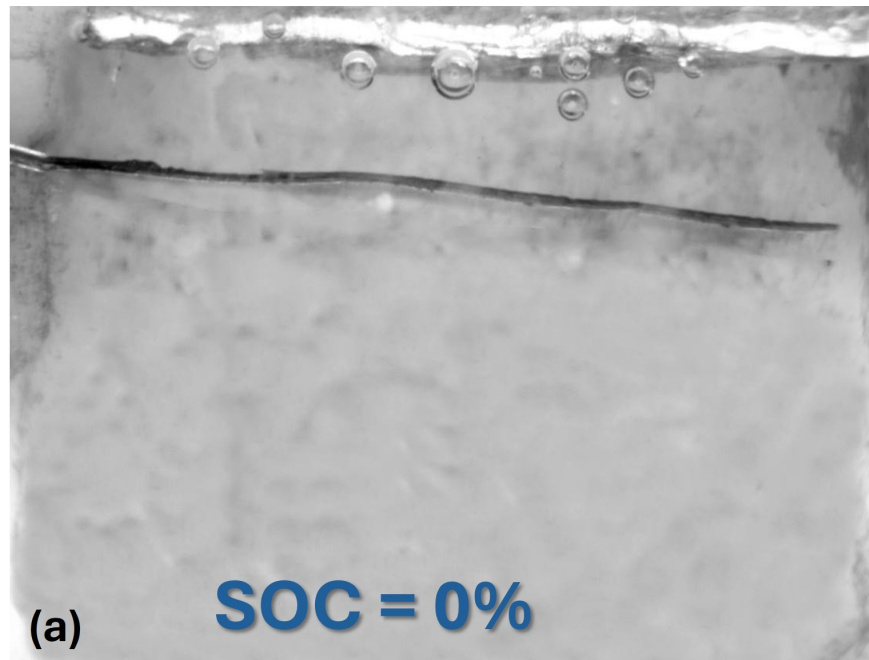


Figure 81: Deflection of graphite cantilever anode during the charging-discharging cycle.



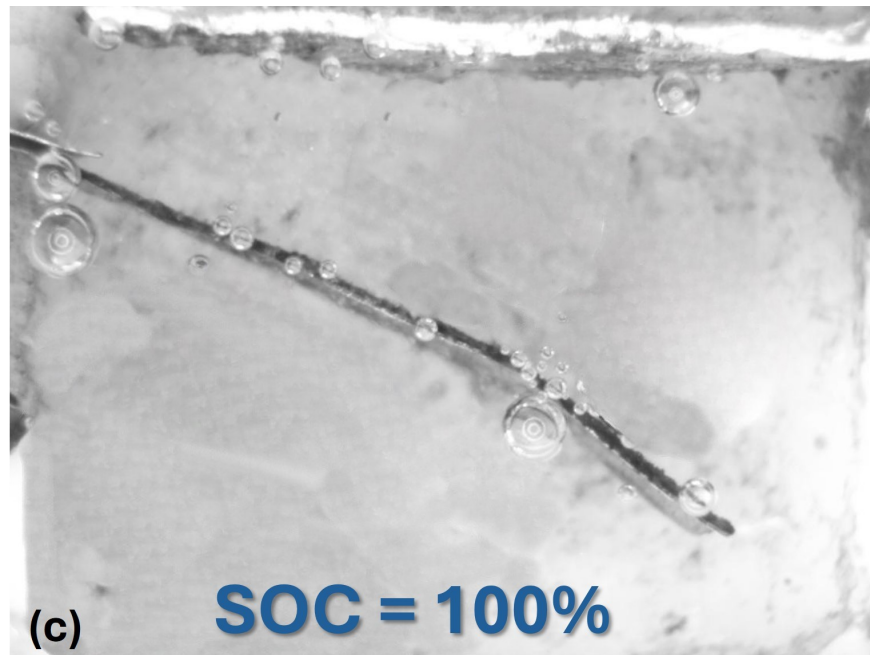
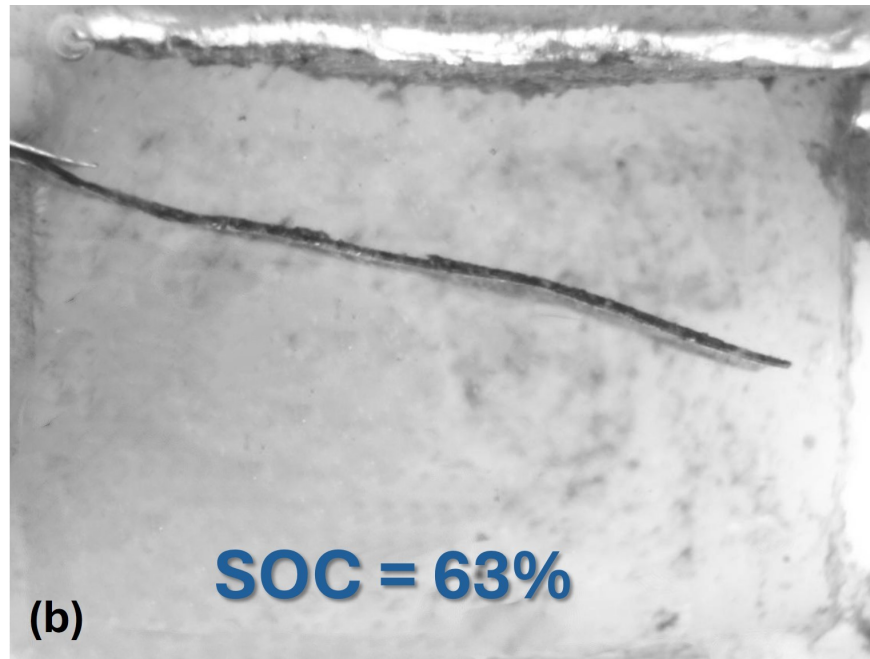


Figure 82: Images taken by the digital microscope capturing the graphite anode deflection, throughout the experiments, for different SOC during the cycle, focusing on the charging phase. (a), (b) and (c) represent the deflection at SOC equal to 0%, 63% and 100%, respectively.

Figure 83 presents the stress evaluations from both experimental data, highlighted with dashed lines, and the model ones, presented in solid lines. Von Mises stress was chosen for the selected active particle because it correlates directly with deformation generated from the bending of the

cantilever electrode. It is surface Von Mises stress since the measured deflection occurs at the surface level, not within the particle itself. Detailed particle-level considerations will be addressed in **Section 5.1.2**.

As can be seen, the model results closely align with the experimental ones. Stress, arise from factors such as current collector presence and non-uniformities in the lithiated structure, increase progressively as lithium ions intercalate. Entering into details, their increment is gradual initially, with a notable slope increase between 163.2 and 217.6 minutes and after a decrease , paralleling the deflection trend. At the end of charging, the maximum value reaches 53.69 MPa.

During discharge, stress decreases as lithium ions de-intercalate, initially with a steeper slope within the first 50 minutes of discharging, followed by a gentler decrease. At cycle end, as with deflection, it does not return to zero but stabilizes at 8.33 MPa. This residual is attributed to lithium ions that cannot be fully de-intercalated.

The conducted experiments indicate that the maximum stress reached does not cause particle fragmentation or destruction, as the electrode remains intact throughout the cycle. Establishing a tensile strength under such conditions is challenging. However literature, specifically Li et al. [41], reports stress levels up to 100 MPa for similar electrode compositions without observing fragmentation, but identifies it as a threshold. Thus, the observed values are well below critical limits, though values exceeding this threshold could cause fracture.

Figure 84 represents the relative error between experimental data and model results, below 2%, with a notable decrease in the middle of the cycle, indicating a high reliability of the implemented model.

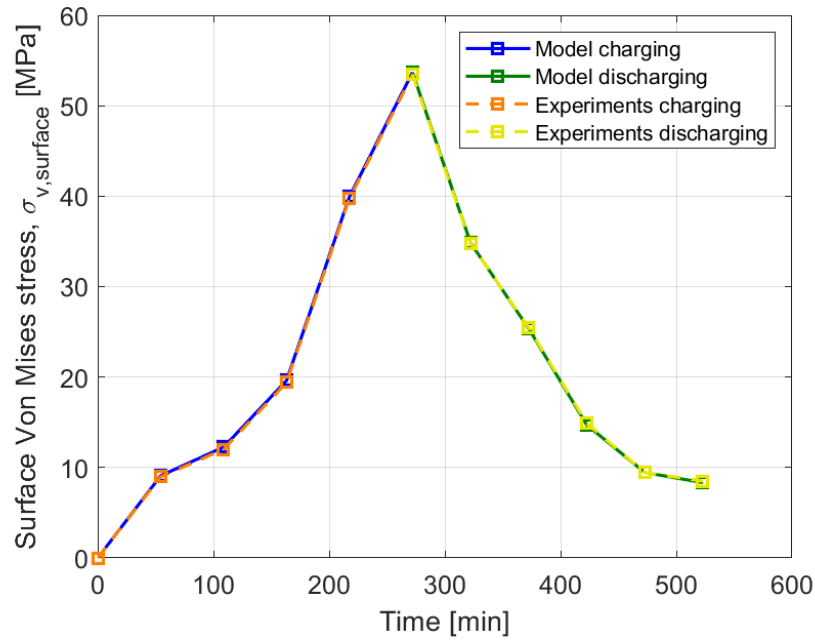


Figure 83: Surface Von Mises stress comparison between experimental and model data during the charging-discharging cycle for the selected active particle, graphite anode.

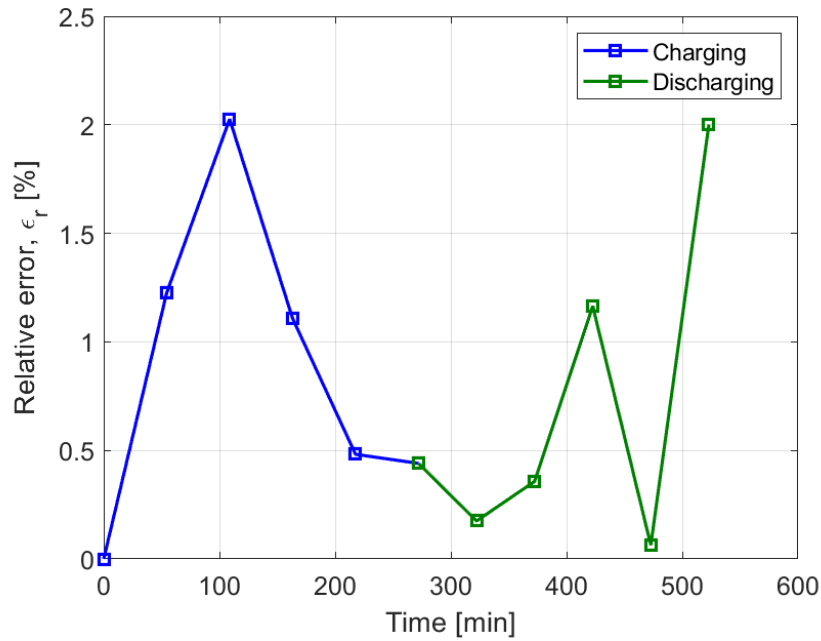


Figure 84: Relative error of the surface Von Mises stress between experimental and model data during the charging-discharging cycle for the selected active particle, graphite anode.

5.1.2 Extended model results

As previously mentioned, this section aims to provide an in-depth understanding of the various stresses developed within the cell by utilizing the full capabilities of the model. It is important to note that the results presented here are the same as those tested experimentally, confirming their reliability. This detailed analysis will cover all the generated stresses; the focus will be not only on the Von Mises one, but it will also include considerations for both the selected particle and the entire electrode thickness.

Figure 85 shows the radial stress in the selected active particle as a function of its position within the particle at different SOC, during the charging phase. The initial value is zero and with the concentration of lithium ions increasing, and so also the SOC, it is encountered a rise in the radial stress magnitude. The slope of the curves at the particle centre increases slowly until 63% SOC, after which it rises more rapidly, particularly between 63% and 83% and then from 83% to 100%, reaching the peak stress value of 48.65 MPa. The stress is always maximum at the center and zero at the surface due to the constraints imposed for model resolution. Its sign is positive because of this constraint, indicating that there is no neighboring particle on the surface in the radial position that would prevent the selected one from expanding. Consequently, the developed stress is tensile, as the particle tends to expand due to lithiation.

Figure 86 shows the radial stress during the discharging phase of the cycle. The initial value at the particle center is -38.93 MPa. As lithium ions are extracted, the radial stress curve slope at the particle centre decreases. The most significant decrease occurs between 44% and 28% SOC. The stress is negative because, with the radial stress at the surface being zero and no neighboring particle constraints, the developed stress is compressive, as the particle tends to contract during delithiation.

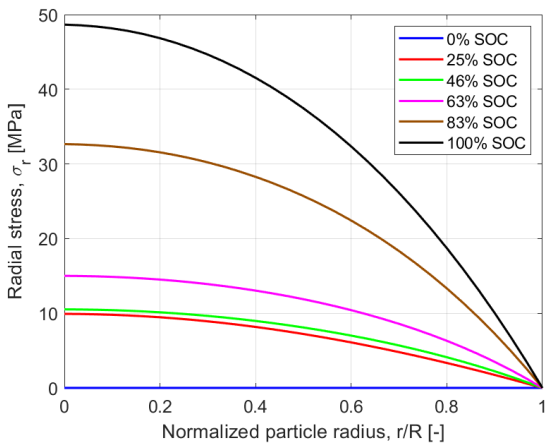


Figure 85: Radial stress in the selected active particle during the charging phase of the cycle, graphite anode.

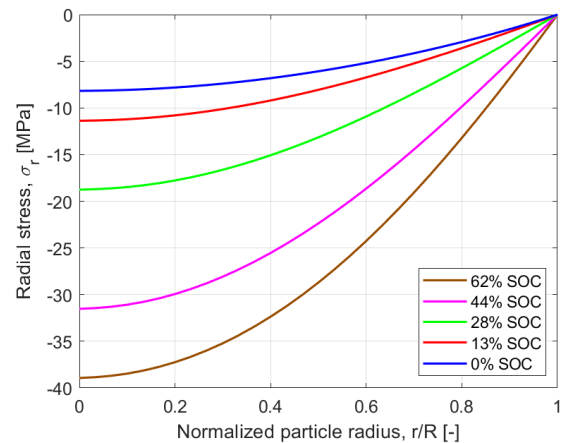


Figure 86: Radial stress in the selected active particle during the discharging phase of the cycle, graphite anode.

Figure 87 presents the tangential stress in the selected active particle as a function of its position within the particle at different SOC values, during the charging phase of the cycle. It is notable that the sign of stress changes for all SOC values. The stress is maximum at the center, reaches zero at $\frac{r}{R}$ around 0.7, and achieves its minimum value, changing its sign to negative, at the surface. The initial value is zero and as the SOC increases the tangential stress rises to a maximum value of 48.65 MPa, equal to the radial stress, and a minimum of -53.69 MPa, which absolute value corresponds to the maximum surface Von Mises stress shown in **Figure 83**. Speaking about the trend of the curves, the stress increases more significantly between 63% and 83%, and 83%-100% at the center, while at the surface it increases¹⁰ more between 63% and 83%. Unlike the radial one, the sign of the tangential stress is not always the same. Without the constraint that the surface stress must be zero, the particles at the surface are constrained by neighboring ones. When lithium ions intercalate, they tend to expand, but this expansion is restricted by the neighboring entities resulting in compressive stress. Near the center, where there is no constraint from neighboring particles, the stress remains positive, reflecting the graphite tendency to expand as lithium is inserted.

Figure 88 presents the tangential stress in the selected active particle during the discharging phase of the cycle. The trend is the opposite of the charging phase. Near the surface, the extraction of lithium ions causes the active particle to contract, but this contraction is constrained by neighboring particles inducing tensile stress. Near the center, where there is no constraint, the stress is negative. The values, for both centre and surface, decrease in magnitude with de-lithiation with a more or less uniform decrease across different SOC values, except for a smaller one in the final phase of discharging. Here, the maximum value is 34.94 MPa, matching the respective surface Von Mises stress in **Figure 83**, and the minimum is -38.93 MPa. As in the charging phase, at around $\frac{r}{R}$ equal to 0.7 all tangential stresses are zero.

¹⁰remember that the sign is negative.

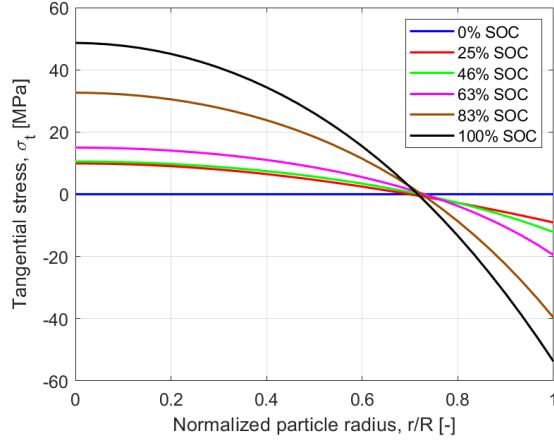


Figure 87: Tangential stress in the selected active particle during the charging phase of the cycle, graphite anode.

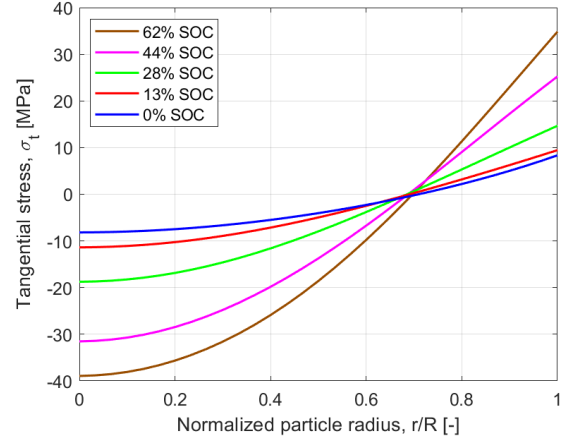


Figure 88: Tangential stress in the selected active particle during the discharging phase of the cycle, graphite anode.

Figure 89 and **Figure 90** show the behavior of the hydrostatic stress for the selected active particle, depending on the position inside it for different SOC, during the charging and discharging phases of the cycle. This stress arises due to pressure changes as a function of lithium diffusion and are distributed throughout the particle. It is important to note that it is not related to the deformation but can influence the concentration level within the particle. Tensile hydrostatic stress allows for storing a greater amount of lithium ions compared to a model that does not account for it, while compressive hydrostatic stress results in a reduction of storable lithium ions.

Analyzing the trend for both charge and discharge, it has the same behavior as the tangential stress but shifted on the x-axis due to the presence of radial stress, with almost all functions reaching zero when $\frac{r}{R}$ is around 0.8. During charging, the stress increases more significantly between 63% and 83% SOC, and between 83% and 100% SOC at the center of the particle, while it increases more between 63% and 83% SOC at the surface. The maximum and minimum values are reached at 100% SOC, as for the tangential stress, at the center and the surface, respectively. For the discharging phase the values, for both centre and surface, decrease in magnitude with de-lithiation with a more or less uniform decrease across different SOC, except for a smaller one in the final phase of discharging. Here, the maximum stress is present at the surface, while the minimum at the centre. In both the cases, the stress at the center is equal to the tangential or radial stress, while the value at the surface is the same as the tangential stress multiplied by $\frac{2}{3}$.

In order to summarize, the maximum and minimum values for the charging phase are 48.65 MPa and -35.8 MPa, and for the discharging phase, they are 23.22 MPa and -38.93 MPa.

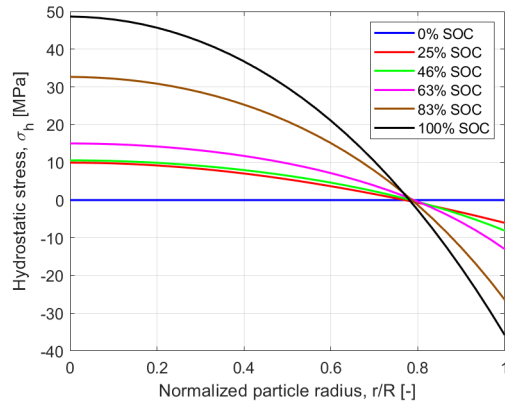


Figure 89: Hydrostatic stress in the selected active particle during the charging phase of the cycle, graphite anode.

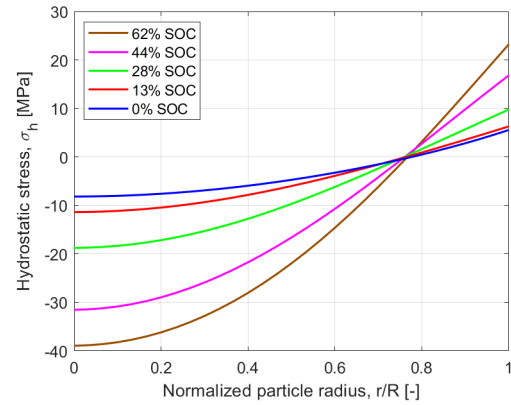


Figure 90: Hydrostatic stress in the selected active particle during the discharging phase of the cycle, graphite anode.

Figure 91 and **Figure 92** show the behavior of the Von Mises stress for the selected active particle, depending on the position inside it for different SOC levels, during the charging and discharging phases of the cycle. As already explained, this stress is crucial because it is responsible for the deformation, taking into account the presence of both radial and tangential stresses. By definition, it is always positive and the trend is an increase with increasing lithium concentration. Therefore during charging, the stress increases over time as SOC increases, and during discharging, the stress decreases over time as SOC decreases. It is important to note that the values at the surface of the particle are the same as those reported and discussed in **Figure 83**. Entering into details, during charging, the curve slope at the surface increases more in the last phase of the charging period, especially between 46% and 63% SOC, reaching a maximum value of 53.69 MPa. The curve slope at the surface decreasing trend during discharging is more pronounced until 28% SOC, after which it attenuates. Here, the maximum value is obviously reached at the beginning of the discharge, equal to 34.84 MPa. In both cases, the maximum magnitudes for each SOC level are reached at the surface of the particles, while by definition, the minimum stress is reached at the center, always equal to zero.

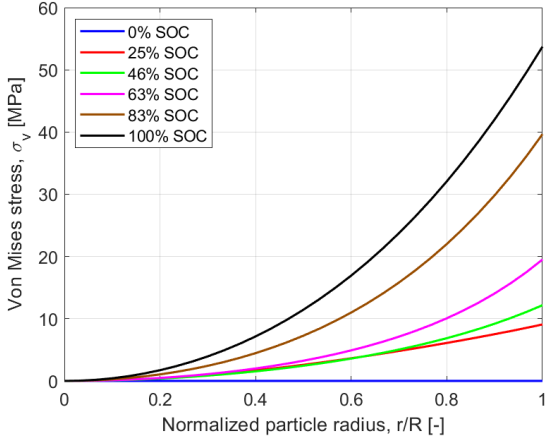


Figure 91: Von Mises stress in the selected active particle during the charging phase of the cycle, graphite anode.

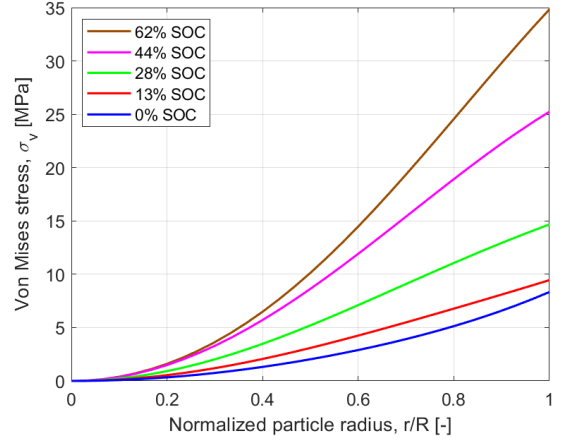


Figure 92: Von Mises stress in the selected active particle during the discharging phase of the cycle, graphite anode.

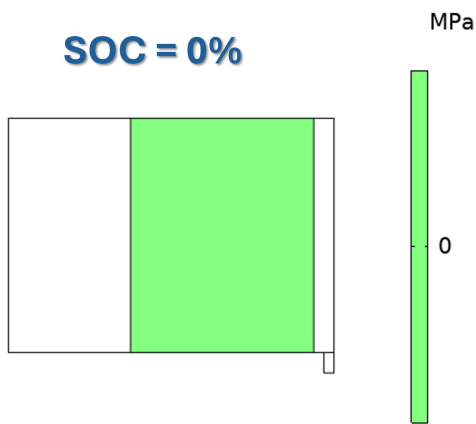
Figure 93 shows the surface Von Mises stress evolution across the entire electrode thickness, highlighting the anode in color, throughout the charging-discharging cycle at various SOC levels. The charging phase is represented by SOC text in blue, while the discharging phase is indicated in green. As can be seen, the values reported close to the separator are the same as those presented in **Figure 83**, because the active particle considered is in that zone.

Focusing on the charging phase, it is evident that the higher stresses are always closer to the separator and then decrease as they approach the current collector. This is because, during charging, the Li-ions intercalate coming from the cathode via the electrolyte, resulting in a higher concentration close to the electrolyte and a lower concentration as moving towards the current collector. Whenever this change in concentration is more marked, the difference in stress is more evident. This is particularly noticeable at 83% SOC, where the maximum stress is around 40 MPa and the minimum is around 27 MPa, registering a 13 MPa difference that is the biggest among all, showing a decrease of 32.5% with respect to the maximum value.

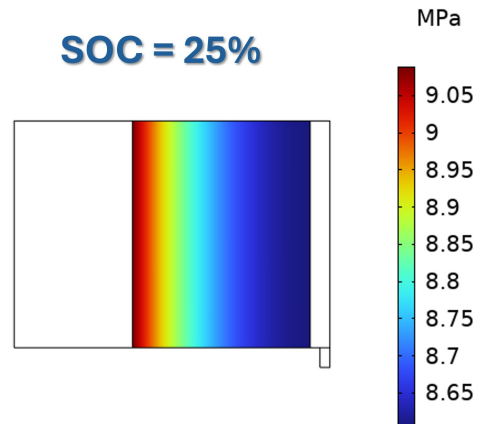
During discharge, the opposite happens. The lithium ions leave the anode through the electrolyte to go to the cathode. In this case, the lithium ions leave faster from the part of the anode close to the electrolyte and slower from the part close to the current collector. This behavior is strictly correlated to stress development. While in the first phase of the charging, the higher stress is always close to the electrolyte because the faster depletion of lithium ions cannot compensate for the higher concentration there, at 0% SOC, the expected situation is reached. Consequently, the lithium ion concentration is higher in the part close to the current collector and lower close to the electrolyte interface, leading to a lower stress close to the electrolyte accordingly. For the discharging phase, the most evident difference is at 62% SOC, where the maximum stress is around 35 MPa and the minimum is 24 MPa, with a difference of 11 MPa, representing a decrease of 31.42% with respect

to the maximum value.

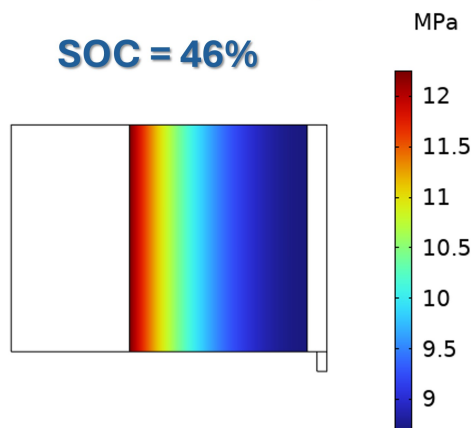
(a) Surface Von Mises stress, $\sigma_{v,surface}$



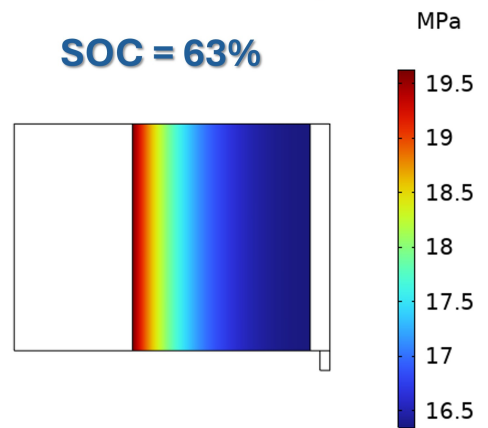
(b) Surface Von Mises stress, $\sigma_{v,surface}$



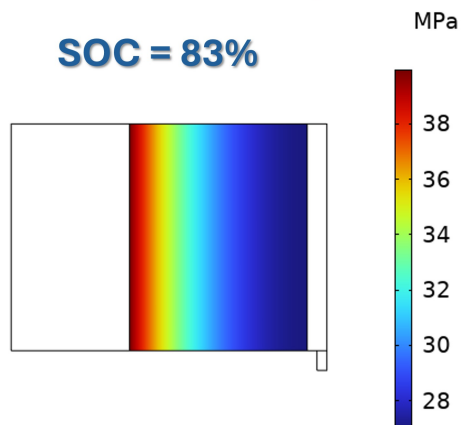
(c) Surface Von Mises stress, $\sigma_{v,surface}$



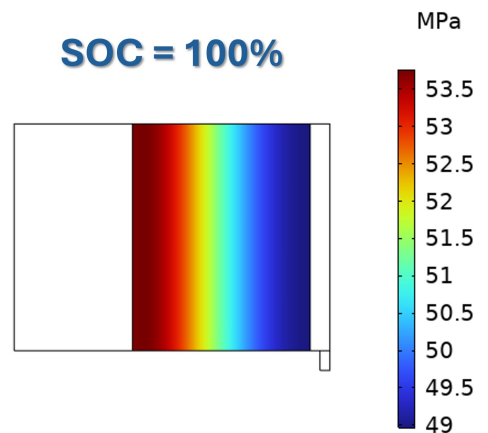
(d) Surface Von Mises stress, $\sigma_{v,surface}$



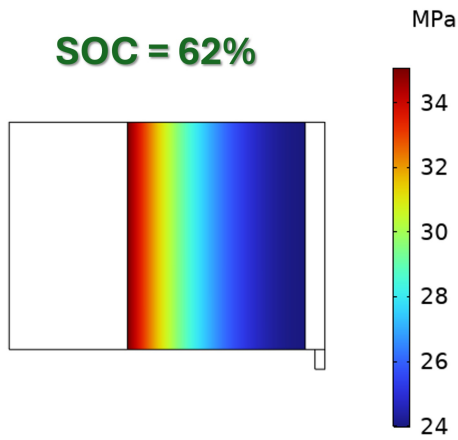
(e) Surface Von Mises stress, $\sigma_{v,surface}$



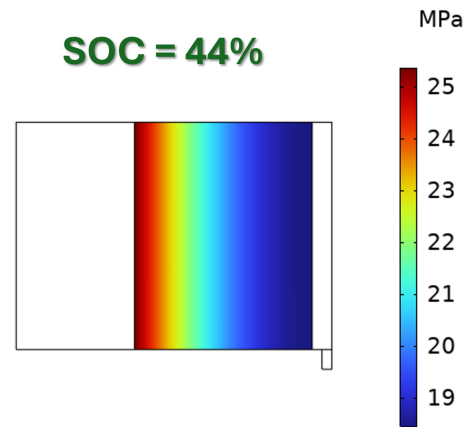
(f) Surface Von Mises stress, $\sigma_{v,surface}$



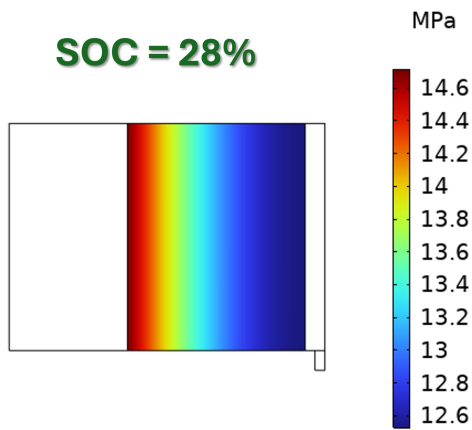
(g) Surface Von Mises stress, $\sigma_{v,surface}$



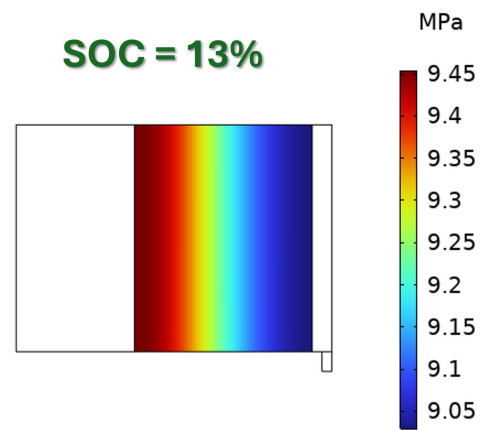
(h) Surface Von Mises stress, $\sigma_{v,surface}$



(i) Surface Von Mises stress, $\sigma_{v,surface}$



(j) Surface Von Mises stress, $\sigma_{v,surface}$



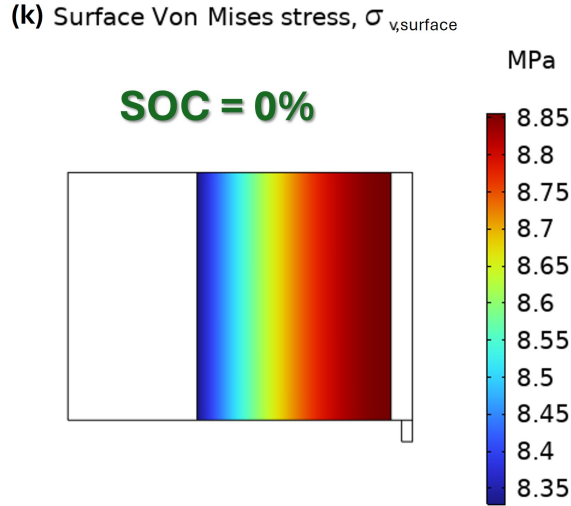


Figure 93: Surface Von Mises stress evolution across the graphite anode thickness, highlighting the anode in color, throughout the charging-discharging cycle at various SOCs. The charging phase is represented by the SOC text in blue ((a), (b), (c), (d), (e) and (f)), while the discharging phase is indicated in green ((g), (h), (i), (j) and (k)).

5.1.3 Parametric analyses

This paragraph aims to understand the influence of certain parameters on the surface Von Mises stress of a specific active particle. For details on the active particle, please refer to **Figure 78**. The parameters studied are:

- Active particle radius.
- Anode thickness.
- Charging rate applied.

To understand the influence of these factors, the focus has been placed solely on the charging cycle. This cycle is crucial as the stress starts from zero and reaches its maximum value, representing the most critical case. It is important to note that while studying the influence of a particular element, all other not-affecting parameters used in the simulation remain constant to isolate the effect of the one being studied. Each parameter is varied by a constant quantity to ensure a fair comparison between different values. To maintain consistency across all simulations, the same lower cut-off voltage is used, stopping the simulation once this voltage is reached as done for the baseline data.

Figure 94 shows the influence of the active particle radius on stress development. As seen, all the lines have almost the same slope for the same SOC interval, and the clear trend is that increasing the particle radius leads to an increase in stress. In a real-case scenario, if there is a choice between technologies with different active particle radii that both work efficiently, it is better to choose the

one with a smaller radius for stress minimization. For instance, when the radius increases from $22\ \mu\text{m}$ to $26\ \mu\text{m}$, the maximum stress rises from $53.69\ \text{MPa}$ to $69.38\ \text{MPa}$, an increase of 29.2% . Conversely, when the radius decreases from 22 to $18\ \mu\text{m}$, the stress decreases from $53.69\ \text{MPa}$ to $36.38\ \text{MPa}$, a reduction of 32.24% . This indicates that the reduction or increase trend is similar, with a slightly more pronounced effect when the particle size is decreased.

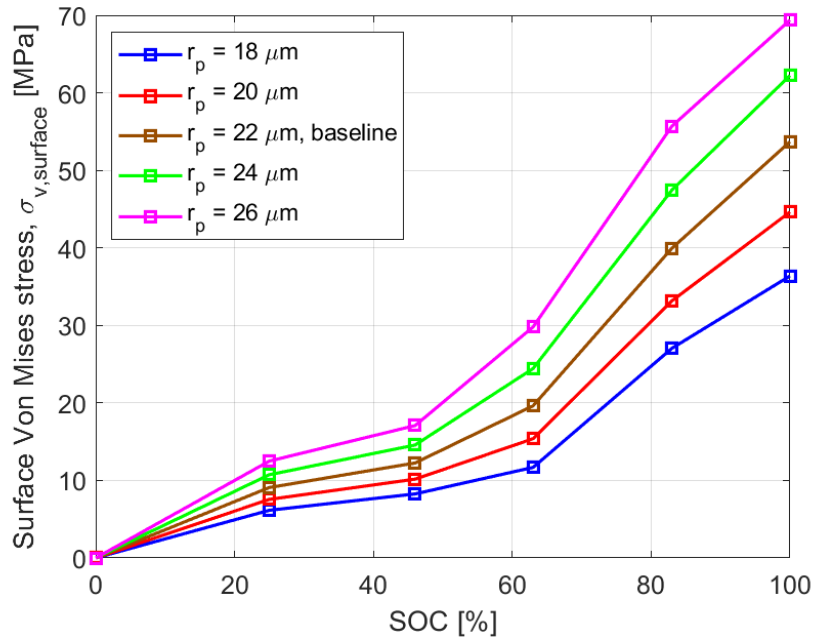


Figure 94: Impact of the active particle radius on surface Von Mises stress during the charging phase of the cycle for the selected active particle, graphite anode.

Figure 95 shows the influence of different anode thicknesses, called L_{neg} , on stress development. Unlike the particle size, the slopes of the different lines for the same SOC interval vary significantly. This variation is because the electrode thickness is directly related to the electrode capacity, causing the stress span to be less wide than in previous cases. However, a trend can still be observed: increasing the electrode thickness results in lower stress. In a real-case scenario, if there is a choice between technologies with different anode thicknesses that both work efficiently, it is better to choose the one with a larger one to minimize stress. Specifically, when the thickness decreases from $90\ \mu\text{m}$ to $60\ \mu\text{m}$, the stress increases from $53.69\ \text{MPa}$ to $60.34\ \text{MPa}$, an increase of 12.39% . Conversely, when the thickness increases from $90\ \mu\text{m}$ to $120\ \mu\text{m}$, the stress decreases from $53.69\ \text{MPa}$ to $40.74\ \text{MPa}$, a reduction of 24.12% . Thus, the influence of increasing the thickness L_{neg} is more pronounced than its decrease.

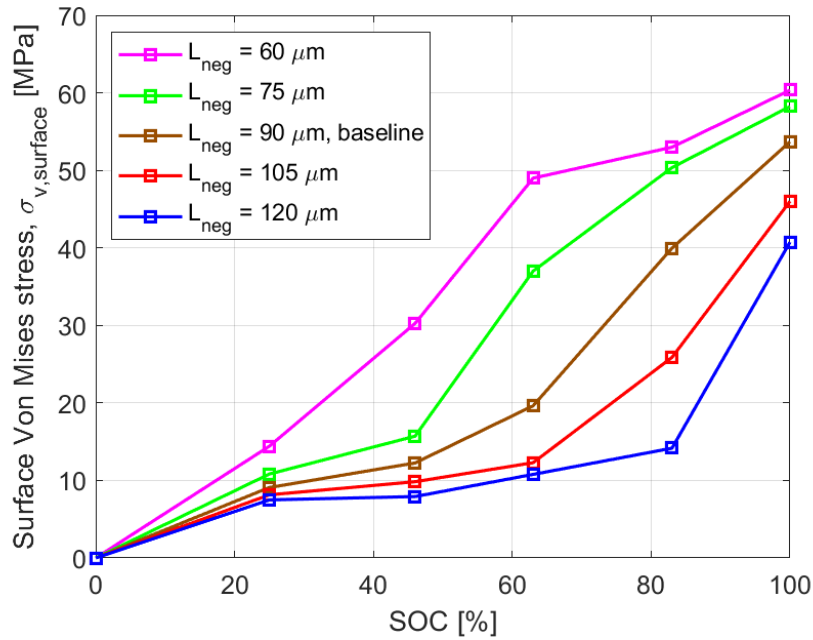


Figure 95: Impact of the graphite anode thickness on surface Von Mises stress during the charging phase of the cycle for the selected active particle.

Figure 96 shows the influence of the charging rate applied on stress development. Here the slopes of the different lines for the same SOC interval are almost the same, as seen with the active particle, with a slight variation for the highest parameter value. It is clear that decreasing the charging rate, by applying a smaller current, is beneficial for reducing stress. Specifically, when it increases from $\frac{1}{4.5}$ to $\frac{1}{2.5}$, the stress rises from 53.69 MPa to 91.11 MPa, an increase of 69.7%, the most significant influence among all the parameters studied. This further confirms the importance of avoiding high currents, as they can directly cause high stress. Conversely, if the selected factor decreases from $\frac{1}{4.5}$ to $\frac{1}{6.5}$, resulting in a lower current, the stress decreases from 53.69 MPa to 36.92 MPa, a reduction of 31.23%. Although the increase due to higher current is more substantial than the decrease due to lower current, this reduction is still one of the highest among all the cases studied. It is worth emphasizing the importance of these conclusions because, unlike the active particle size and anode thickness, which must be defined before cell construction, the current can be adjusted during usage making these considerations very important.

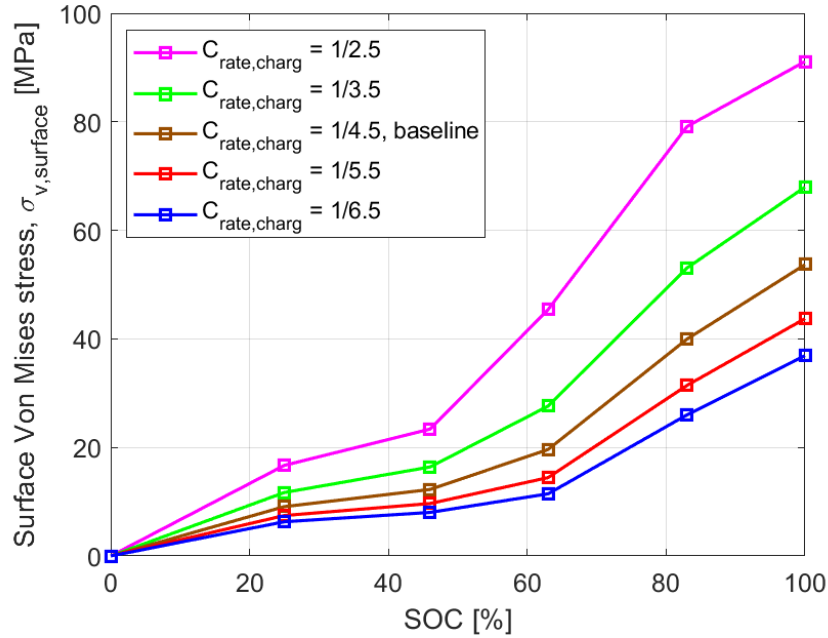


Figure 96: Impact of the charging rate on surface Von Mises stress during the charging phase of the cycle for the selected active particle, graphite anode.

Figure 97 is a summary of all the parametric studies evaluated, focusing on what happens with the relative variation with respect to the baseline value at 100% SOC, where the stresses are highest. The x-axis reports an identification number: 1 refers to the active particle radius sweep, 2 to the anode thickness sweep, and 3 to the charging rate sweep. The y-axis shows the percentage variation, calculated as:

$$\text{Variation} = \frac{\text{Data}_{\text{sweep}100\text{SOC},\text{max}/\text{min}} - \text{Data}_{100\text{SOC},\text{baseline}}}{\text{Data}_{100\text{SOC},\text{baseline}}} \cdot 100 \quad (72)$$

The variation is evaluated at two points for each parametric study: the maximum increase, positive, and the maximum decrease, negative. These points are then connected by straight lines to show the total variation span of the sweep. It is evident that the parameter most responsible for a stress increase is the growth in charging rate, leading to a 69.7% rise. This is followed by the active particle radius sweep and the anode thickness sweep. Regarding the positive effects that can reduce stress, decreasing the particle size can cause the biggest reduction of 32.24%, followed by decreasing the discharging current and decreasing the electrode thickness. Furthermore, the largest span of variation is due to the charging rate, followed by the active particle radius and lastly the anode thickness, which has the smallest span and is not as detrimental when increased.

In conclusion, high charging rates should be avoided and smaller particle sizes should be used to

reduce, to a bigger extent, the developed stress.

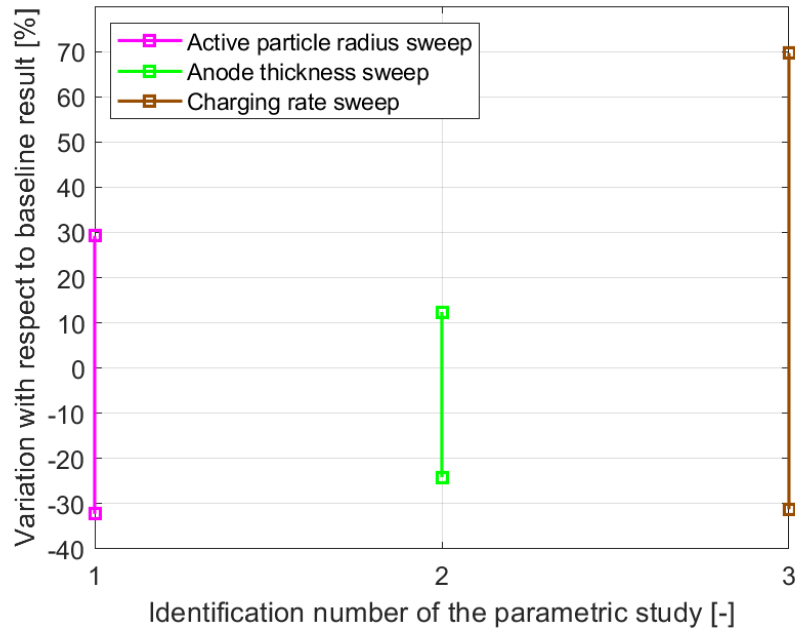


Figure 97: Comparison of different surface Von Mises stress variations at 100% SOC for the parametric studies performed. On the x-axis, the number 1 refers to the active particle radius sweep, the number 2 to the anode thickness sweep and the number 3 to the charging rate sweep. Graphite anode.

5.2 Silicon anode

This paragraph regarding the silicon anode is divided into three subsections. The first, as the name suggests, compares the results obtained experimentally with those obtained by the model to test its validity. The following, using the tested results, goes beyond the experimental considerations and makes a deeper analysis on the stresses development that can only be done using the model features. The last one performs a parametric analysis. Using the same data for which the model is appropriately tested, the influence of variations in active particle size, anode thickness and charging rate applied to the development of stress is studied to understand a possible trend that could reduce them.

5.2.1 Model validation

As also explained in **Section 4.4**, the silicon cell built in the laboratory is tested with a charging-discharging cycle at a current of $\frac{C}{12.85}$; specifically, the absolute value of the current applied is 0.17 mA. The c-rate involved is considerably lower than the one of graphite, since silicon has a lower diffusion coefficient that requires a low current, being the occurring electrochemical reactions slower.

It is worth noting that in this work, to be in accordance with the criteria utilized, "charge" refers to the process in which lithium ions are intercalated in the silicon, while "discharge" refers to the opposite process, regardless of whether the voltage decreases or increases.

Figure 98 shows the voltage vs. time during the cycle. The cell is fully charged until 771 minutes and then fully discharged from 771 minutes to 1410 minutes. The experimental results are shown in orange dashed line, while the model results are shown in solid blue line. As can be seen the model, thanks to appropriate parameter tuning, accurately reproduces the experimental results, with their behavior matching within an error of 2%. It is worth pointing out that this voltage characteristic is also influenced by the fact that the built cell is tested during the first cycle, and so it is affected by the SEI layer formation. This is done because, after the first cycle, as will be seen, stress starts from an initial deformation state rather than the initial position itself.

In conclusion, the electrochemical behavior of the model is tested and it is confirmed that it can reproduce the electrochemical reactions in the cell. As already explained, the model is an electrochemical-mechanical one, so now the mechanical aspect also needs to be verified.

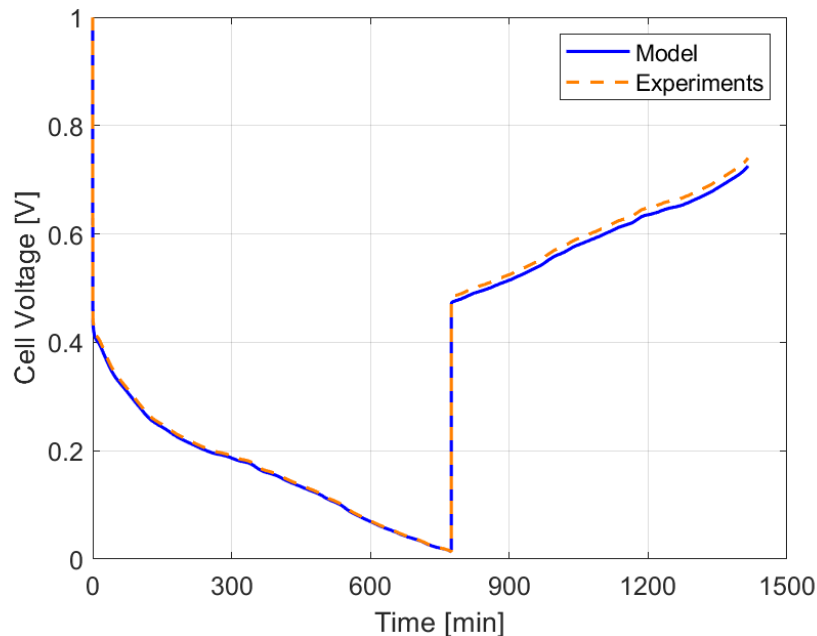


Figure 98: Voltage-time profile of the silicon anode cell during the charging-discharging cycle.

In order to test the mechanical-model, it is necessary to track the concentration of lithium ions within the cell at each time instant. These data can be directly obtained from the electrochemical model, as this feature has already been validated.

Figure 99 explains an important concept for evaluating the results, as already discussed in **Section 4.4**. Silicon anode consists of numerous particles of active material and the model can evaluate the

lithium concentration and stresses development for each of them. Therefore, most of the results presented in this work, except for the one relative to the entire anode surface, refer to the specific active particle highlighted at the electrolyte-anode interface, as it is the one characterized by the highest stress developed. It is important to note that when referring to these particles, the x-axis of the graph represents the quantity $\frac{r}{R}$, where 0 denotes the center and 1 denotes the surface. To maintain clarity, each figure caption will indicate whether it refers to this specific particle or not, for both the model and experimental results. For a better understanding of how the microscopic level of particle and macroscopic level of electrode thickness, are treated, please refer to **Section 3.5.5.2**.

Figure 100 shows the lithium concentration for the selected particle during the charging phase at various time instants, and so at various SOC. The value of the SOC is calculated multiplying by 100 the normalized concentration at the surface of the active particle. It has been decided to adopt this definition to align with the observation that maximum concentration values during charging and minimum values during discharging occur at the particle surface, corresponding to 0% and 100% SOC, respectively. For this reason in this work, whenever an increase in SOC is mentioned, it directly relates to the lithium insertion phase. Conversely, a decrease in SOC refers to the lithium extraction phase. During the charging phase, the normalized lithium concentration starts from zero, as the cell is tested in its first cycle. The concentration increases almost uniformly, due to the intercalation of lithium ions, until it reaches its maximum value at the end of the charging phase. Furthermore, it can be underlined that the values at the center of the particle are always smaller than those at the surface due to the insertion of lithium ions and their continued migration.

Figure 101 depicts the discharging phase that follows the charging one explained before. Here, the lithium concentration decreases as lithium ions are extracted from the particle, reaching at the end of the process a minimum value of zero. Furthermore, it is evident that concentration values at the center are consistently higher than those at the surface due to the extraction of lithium ions.

Speaking about both processes, the increase or decrease in lithium ions during charging or discharging is uniform due to the fact that the diffusion coefficient is obviously the same. Indeed, it is important to note that these values represent the total lithium ions that can be fully extracted and inserted into the particle during the cycle. This excludes any lithium ions that may remain irreversibly trapped after completing the full cycle, which significantly influences residual stress, as it will be discussed later. Moreover the effective concentration values, rather than normalized ones, will be used to assess stress development both experimentally and in the model itself.

In order to compare these results with respect to what happened for the graphite in **Figure 79** and **Figure 80**, it is evident that the difference in concentration between the center and the surface is less pronounced in silicon. This is due to silicon lower diffusion coefficient and, consequently, its lower reaction velocity.

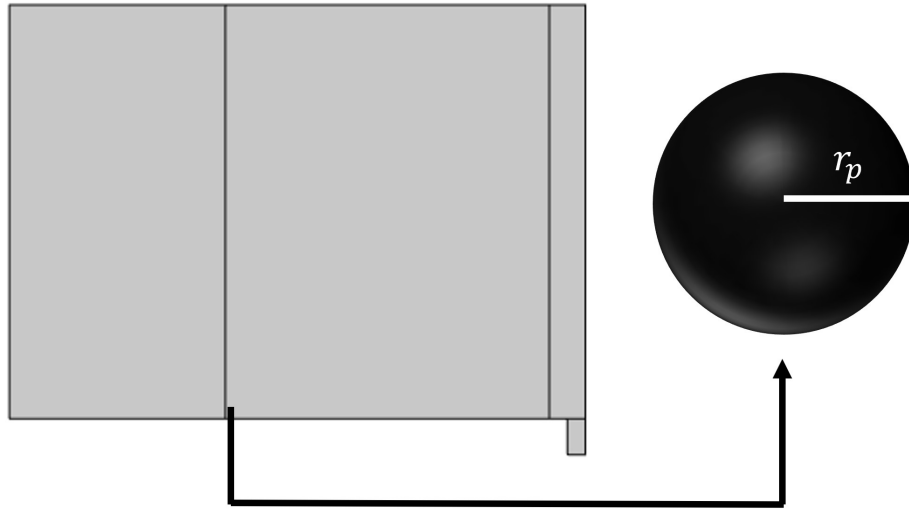


Figure 99: Selection of active particle position for intra-particle results, silicon anode.

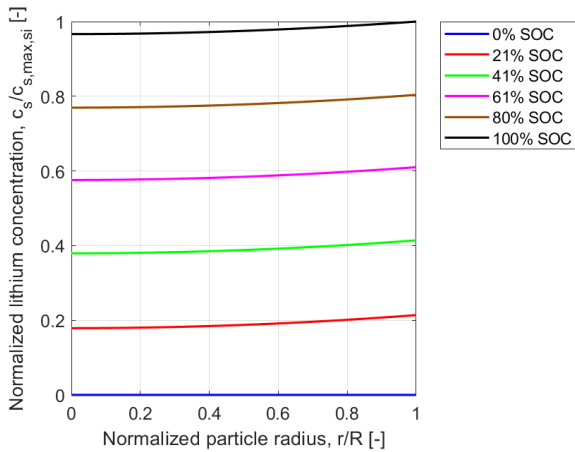


Figure 100: Normalized lithium ions concentration variation in the selected active particle during the charging phase of the cycle, silicon anode.

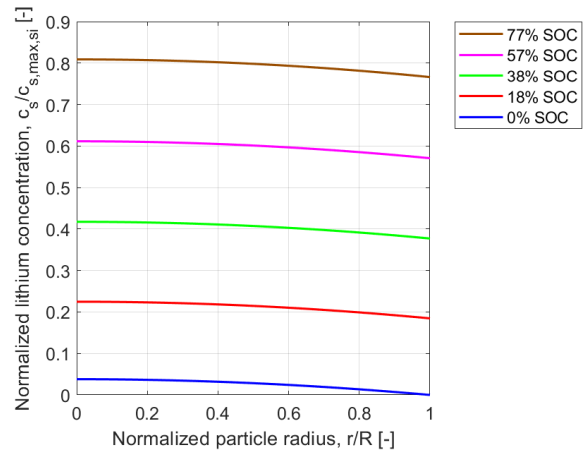


Figure 101: Normalized lithium ions concentration variation in the selected active particle during the discharging phase of the cycle, silicon anode.

After the electrochemical model has been tested and the concentration values evaluated, the mechanical model results are now presented.

Figure 102 illustrates the free-end deflection relative to the initial position of the silicon anode

during the charging-discharging cycle. During charging, deflection increases as lithium ions are inserted into the silicon electrode, causing expansion. As a cantilever, the electrode is free to deflect on its unattached side. The deflection is more evident in the first phase of the charging, but after 309 minutes, there is an attenuation caused by the fact that pores for lithium ions shuttling becomes further taken up and embedding paths becomes winding as well, which blocks and mitigate the further lithiation and so deformation towards the end, where it reaches a peak of 7.9 mm.

During discharge, except for the first part where the slope is low and the reduction in deflection is slower, after 899 minutes the deflection reduction has almost the same slope. Notably, at the cycle end, the electrode does not return to its initial position, retaining a small deflection of 1.06 mm due to the residual lithium ions that cannot be extracted from the particle.

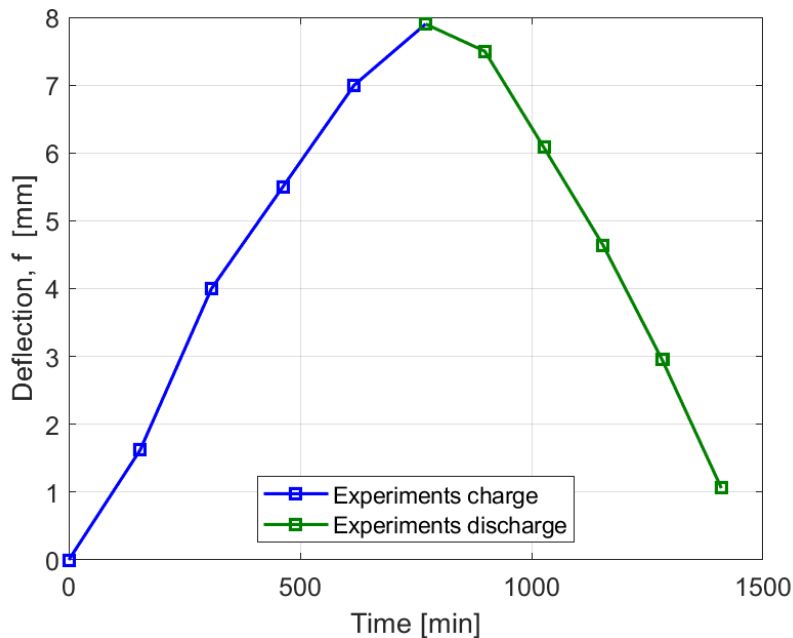
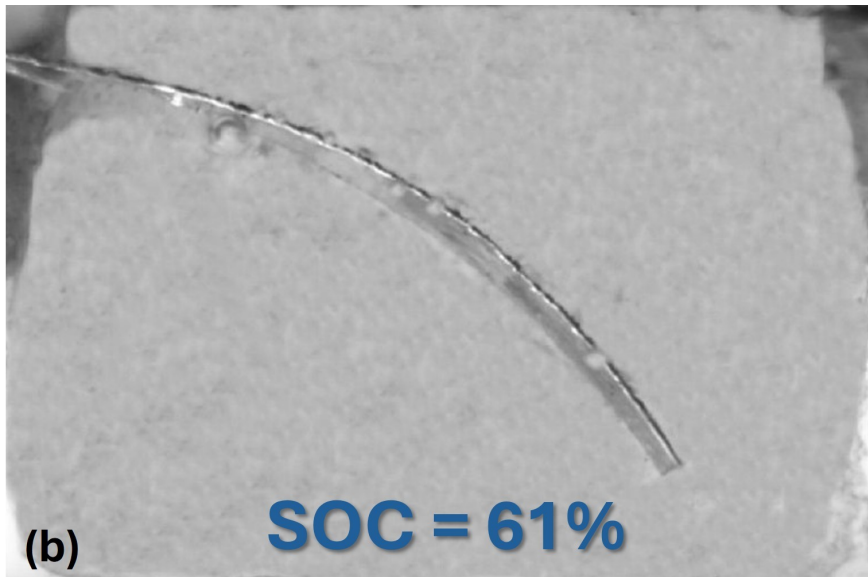
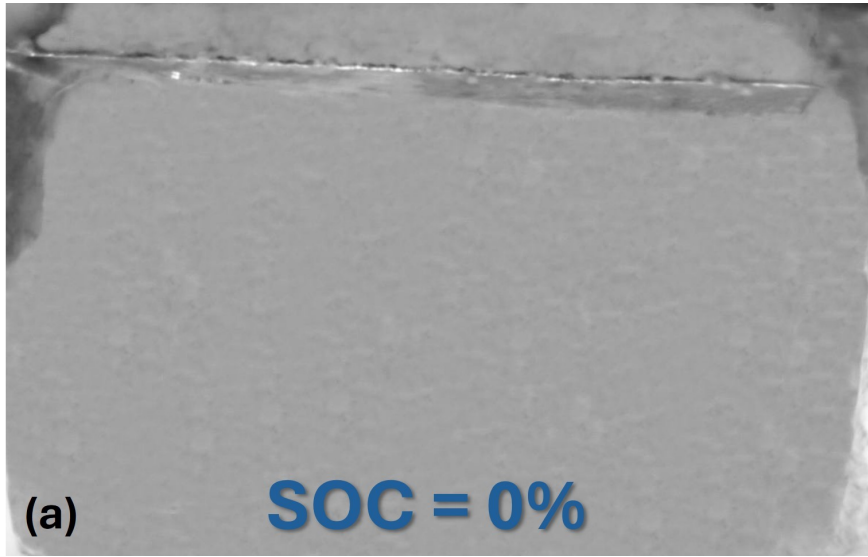


Figure 102: Deflection of silicon cantilever anode during the charging-discharging cycle.



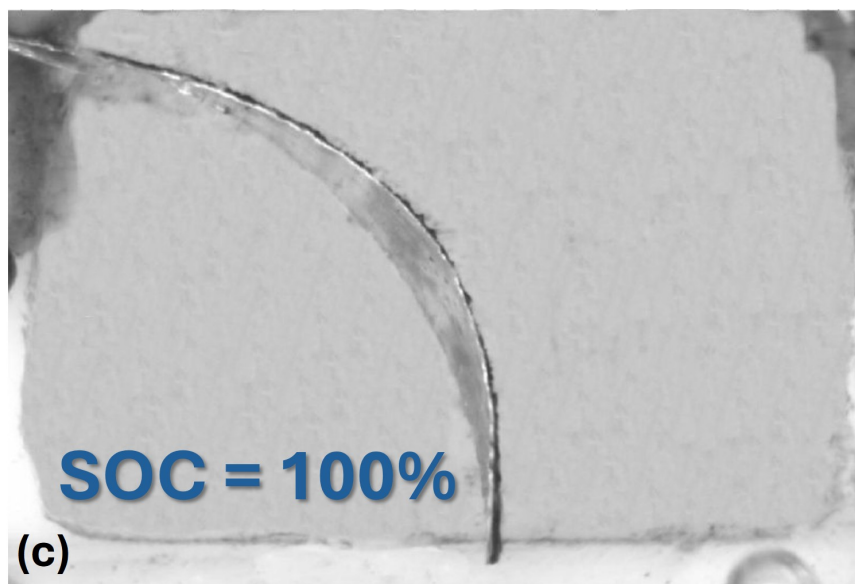


Figure 103: Images taken by the digital microscope capturing the silicon anode deflection, throughout the experiments, for different SOC during the cycle, focusing on the charging phase. (a), (b) and (c) represent the deflection at SOC equal to 0%, 61% and 100%, respectively.

Figure 104 presents the stress evaluations from both experimental data, highlighted with dashed lines, and the model ones, presented in solid lines. Von Mises stress was chosen for the selected active particle because it correlates directly with deformation generated from the bending of the cantilever electrode. It is surface Von Mises stress since the measured deflection occurs at the surface level, not within the particle itself. Detailed particle-level considerations will be addressed in **Section 5.2.2**.

As can be seen, the model results closely align with the experimental ones. Stress, arise from factors such as current collector presence and non-uniformities in the lithiated structure, increase progressively as lithium ions intercalate. Entering into details, the stress rapidly increases in the first part of charging, but after 309 minutes there is an attenuation. At the end of the charging, the maximum stress reaches 1.5 GPa. The trend during discharge is the opposite; as the lithium ions de-intercalate the surface Von Mises stress decreases, initially with a very slow slope and after 899 minutes the decrease is almost at a constant slope. At the end, as seen with the deflection, the stress is not exactly zero but is equal to 0.19 GPa. This is because some lithium ions cannot be de-intercalated.

The conducted experiments indicate that the maximum stress reached does not cause particle fragmentation or destruction, as the electrode remains intact throughout the cycle. Establishing a tensile strength under such conditions is challenging. However literature, specifically Yu et al. [108], reports stress levels up to 2.5 GPa for similar electrode compositions without observing fragmentation, but it can be identified as a threshold. Thus, the observed values are well below critical limits,

though values exceeding this threshold could cause a fracture.

Indeed, **Figure 105** shows the relative error between the experimental data and the model result. As can be seen the error is always very small being less than 5%, with increased precision during the discharging cycle. This confirms the good reliability of the model.

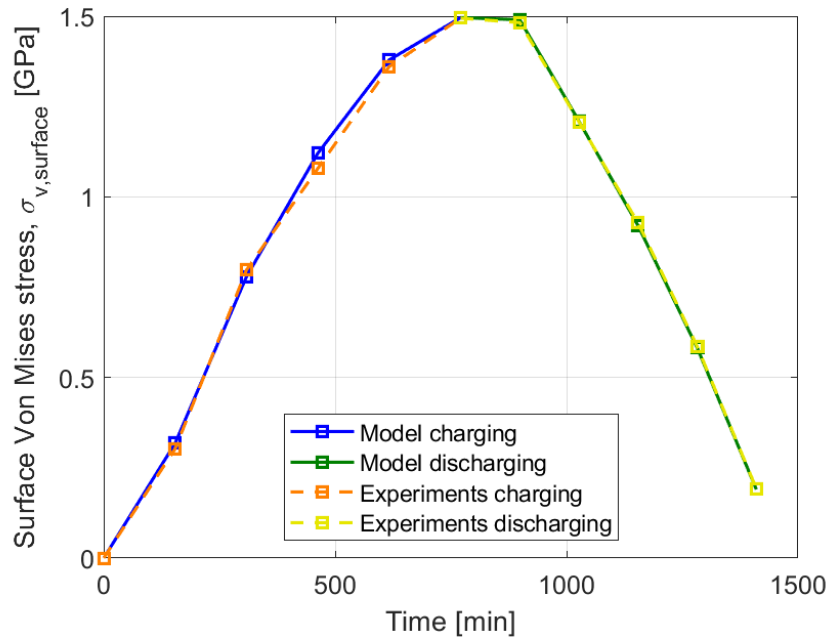


Figure 104: Surface Von Mises stress comparison between experimental and model data during the charging-discharging cycle for the selected active particle, silicon anode.

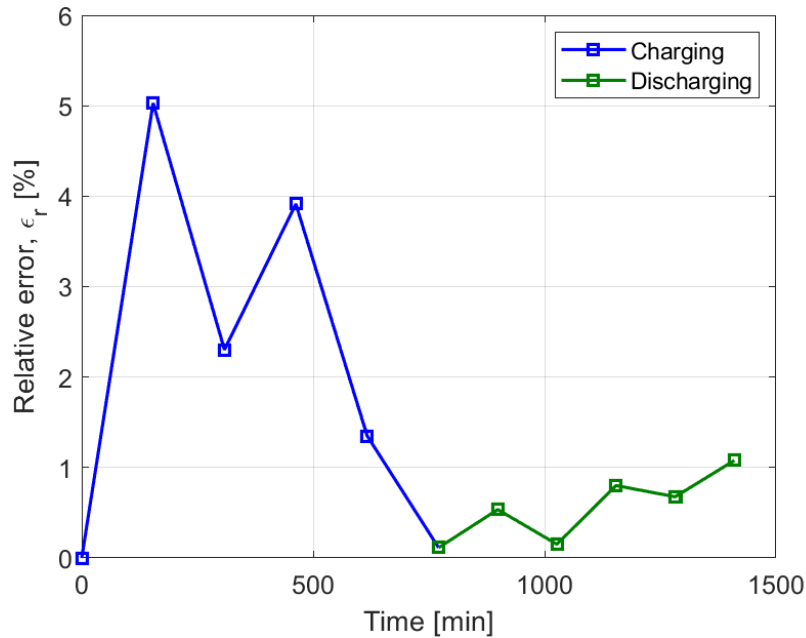


Figure 105: Relative error of the surface Von Mises stress between experimental and model data during the charging-discharging cycle for the selected active particle, silicon anode.

5.2.2 Extended model results

As previously mentioned, this section aims to provide an in-depth understanding of the various stresses developed within the cell by utilizing the full capabilities of the model. It is important to note that the results presented here are the same as those tested experimentally, confirming their reliability. This detailed analysis will cover all the generated stresses, the focus will be not only on the Von Mises one, but it will include considerations for both the selected particle and the entire electrode thickness.

Figure 106 shows the radial stress in the selected active particle as a function of its position within the particle at different SOCs, during the charging phase. The initial value is zero and with the concentration of lithium ions increasing, and so also the SOC, it is encountered a rise in the radial stress magnitude. The slope of the curves at the particle centre increases almost constantly until between 80% and 100% where the slope increase is lower, reaching the peak stress value of 1.53 GPa. The stress is always maximum at the center and zero at the surface due to the constraints imposed for model resolution. Its sign is positive because of this constraint, indicating that there is no neighboring particle on the surface in the radial position that would prevent the selected one from expanding. Consequently, the developed stress is tensile, as the particle tends to expand due to lithiation.

Figure 107 shows the radial stress during the discharging phase of the cycle. The initial value at the

particle center is -1.51 GPa. As lithium ions are extracted, the radial stress curve slope at the centre decreases uniformly. The stress is negative because, with the radial stress at the surface being zero and no neighboring particle constraints, the developed stress is compressive, as the particle tends to contract during delithiation.

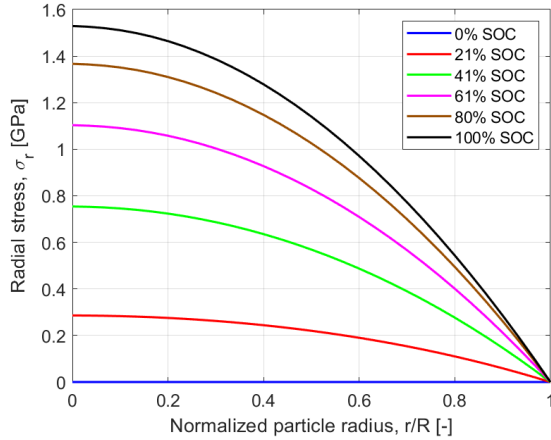


Figure 106: Radial stress in the selected active particle during the charging phase of the cycle, silicon anode.

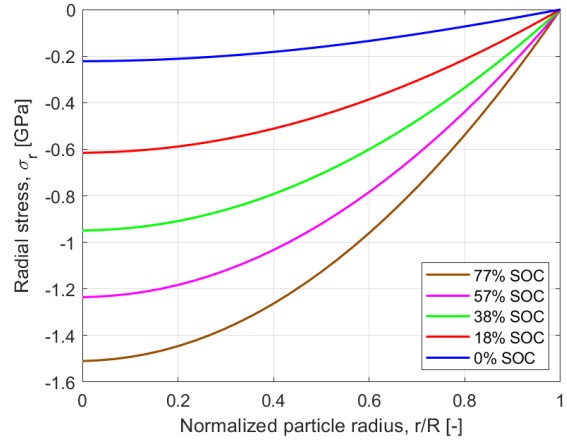


Figure 107: Radial stress in the selected active particle during the discharging phase of the cycle, silicon anode.

Figure 108 presents the tangential stress in the selected active particle as a function of its position within the particle at different SOC values, during the charging phase of the cycle. It is notable that the sign of stress changes for all SOC values. The stress is maximum at the center, reaches zero at $\frac{r}{R}$ equal to 0.7, and achieves its minimum value, changing its sign to negative, at the particle surface. The initial value is zero and as the SOC increases the tangential stress rises to a maximum value of 1.53 GPa, equal to the radial stress, and a minimum of -1.5 GPa, which absolute value corresponds to the maximum surface Von Mises stress shown in **Figure 104**. Speaking about the trend of the curves, the stress increases almost constantly in modulus until between 80% and 100% where the growth is lower for both the center and the surface of the particle. Unlike the radial one, the sign of the tangential stress is not always the same. Without the constraint that the surface stress must be zero, the particles at the surface are constrained by neighboring ones. When lithium ions intercalate, they tend to expand, but this expansion is restricted by the neighboring entities resulting in compressive stress. Near the center, where there is no constraint from neighboring particles, the stress remains positive, reflecting the silicon tendency to expand as lithium is inserted.

Figure 109 presents the tangential stress in the selected active particle during the discharging phase of the cycle. The trend is the opposite of the charging phase. Near the surface, the extraction of lithium ions causes the active particle to contract, but this contraction is constrained by neighboring ones inducing tensile stress. Near the center, where there is no constraint, the stress is negative.

The values, for both centre and surface, decrease in magnitude with de-lithiation with a uniform decrease across different SOC. Here, the maximum value is 1.49 GPa, matching the respective surface Von Mises stress in **Figure 104**, and the minimum is -1.5 GPa. As in the charging phase, at around $\frac{r}{R}$ equal to 0.7 all tangential stresses are zero.

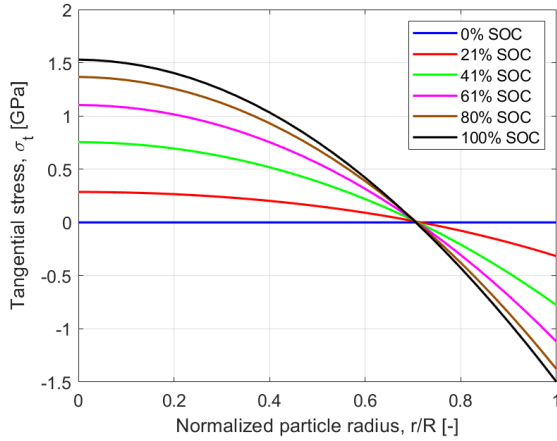


Figure 108: Tangential stress in the selected active particle during the charging phase of the cycle, silicon anode.

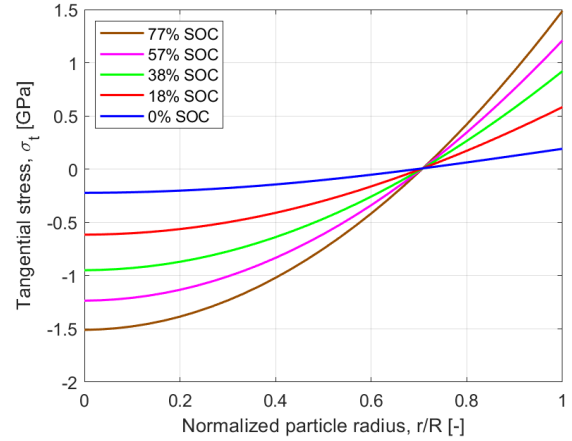


Figure 109: Tangential stress in the selected active particle during the discharging phase of the cycle, silicon anode.

Figure 110 and **Figure 111** show the behavior of the hydrostatic stress for the selected active particle, depending on the position inside it for different SOC, during the charging and discharging phases of the cycle. This stress arise due to pressure changes as a function of lithium diffusion and are distributed throughout the particle. It is important to note it is not related to the deformation but can influence the concentration level within the particle. Tensile hydrostatic stress allows for storing a greater amount of lithium ions compared to a model that does not account for it, while compressive hydrostatic stress results in a reduction of storable lithium ions.

Analyzing the trend for both charge and discharge, it has the same behavior as the tangential stress but shifted on the x-axis due to the presence of radial stress, with almost all functions reaching zero when $\frac{r}{R}$ is around 0.8. During charging, the stress increases almost constantly in modulus until between 80% and 100% where the growth is lower for both the center and the surface of the particle. The maximum and minimum values are reached at 100% SOC, as for the tangential stress, at the center and the surface, respectively. For the discharging phase the values, for both centre and surface, decrease in magnitude with de-lithiation with a uniform trend across different SOC. Here, the maximum stress is present at the surface, while the minimum is at the centre. In both cases, the stress at the center is equal to the tangential or radial stress, while the value at the surface is the same as the tangential stress multiplied by $\frac{2}{3}$.

In order to summarize, the maximum and minimum values for the charging phase are 1.53 GPa and

-1 GPa, and for the discharging phase, they are 1 GPa and -1.51 GPa.

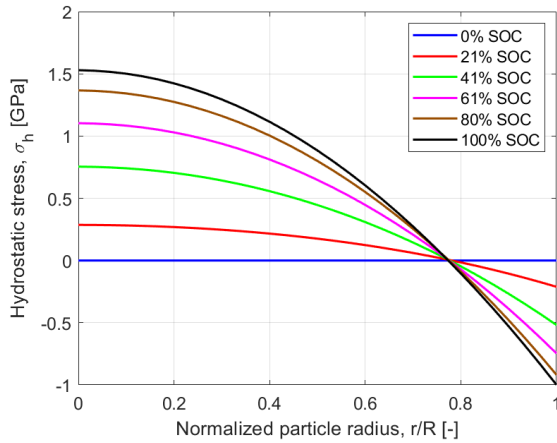


Figure 110: Hydrostatic stress in the selected active particle during the charging phase of the cycle, silicon anode.

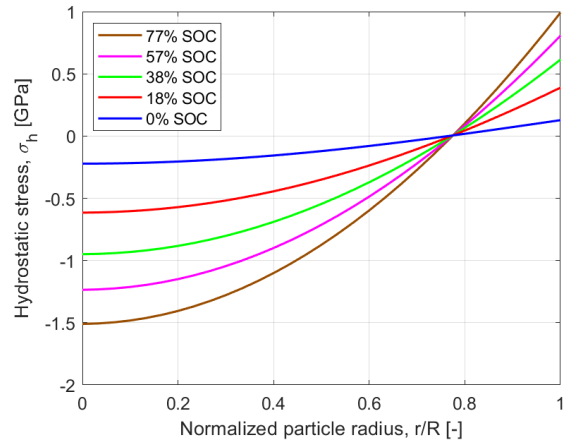


Figure 111: Hydrostatic stress in the selected active particle during the discharging phase of the cycle, silicon anode.

Figure 112 and **Figure 113** show the behavior of the Von Mises stress for the selected active particle, depending on the position inside it for different SOC levels, during the charging and discharging phases of the cycle. As already explained, this stress is crucial because it is responsible for the deformation, taking into account the presence of both radial and tangential stresses. By definition, it is always positive and the trend is an increase with increasing lithium concentration. Therefore during charging, the stress increases over time as SOC increases, and during discharging, the stress decreases over time as SOC decreases. It is important to note that the values at the surface of the particle are the same as those reported and discussed in **Figure 104**. Entering into details, during charging, the curve slope at the surface increases almost constantly in modulus until between 80% and 100% where the growth is lower, reaching a maximum value of 1.5 GPa. The curve slope at the surface decreases uniformly. Here, the maximum value is obviously reached at the beginning of the discharge, equal to 1.49 GPa. In both cases, the maximum magnitudes for each SOC level are reached at the surface of the particles, while by definition, the minimum stress is reached at the center, always equal to zero.

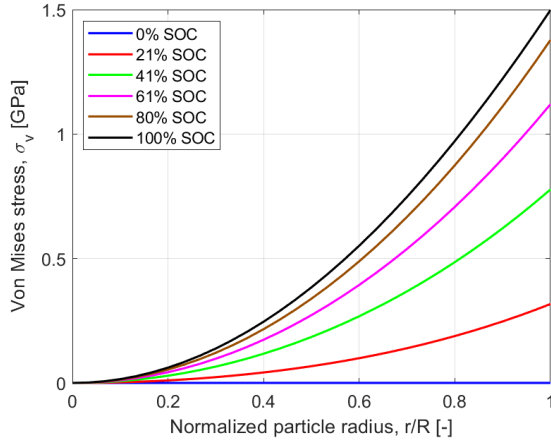


Figure 112: Von Mises stress in the selected active particle during the charging phase of the cycle, silicon anode.

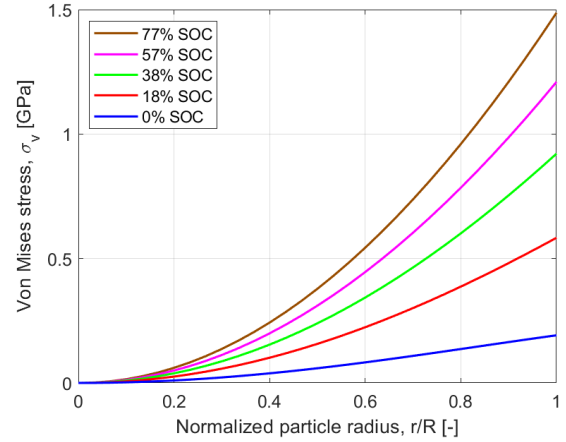


Figure 113: Von Mises stress in the selected active particle during the discharging phase of the cycle, silicon anode.

Figure 114 shows the surface Von Mises stress evolution across the entire silicon anode thickness, highlighted in color, throughout the charging-discharging cycle at various SOC levels. The charging phase is represented by SOC text in blue, while the discharging phase is indicated in green. As can be seen, the values reported close to the separator are the same as those presented in **Figure 104**, because the active particle considered is in that zone.

Focusing on the charging phase, higher stresses are always presented closer to the separator, decreasing as moving toward the current collector. This is because, during charging, the lithium ions intercalating from the cathode via the electrolyte remain in higher concentrations close to the electrolyte and in lower concentrations closer to the current collector. Whenever this change in concentration on the surface from the electrolyte to the current collector is more marked, the difference in stress is more evident. For example, at 41% SOC during the charging phase, the maximum stress is around 0.78 GPa and the minimum stress is around 0.72 GPa, registering a 0.05 GPa difference, which is a decrease of 6.41% with respect to the maximum value.

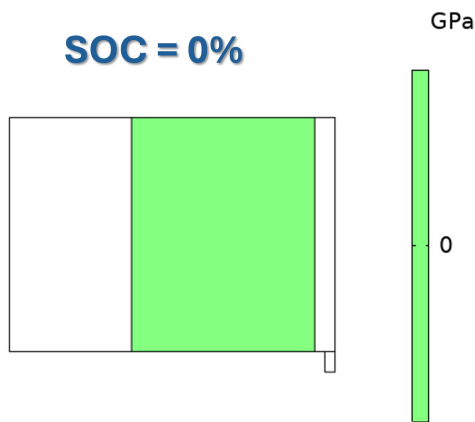
Compared to the graphs related to graphite shown in **Figure 93**, it is evident that there is a much smaller difference in stress across the electrode thickness for silicon. This is due to silicon lower diffusion coefficient, which makes the concentration of lithium ions practically constant on the surface of the electrode, not leading to a significant differences.

During discharge, the opposite happens. The lithium ions leave the anode through the electrolyte to go to the cathode. In this case, the lithium ions leave faster from the part of the anode close to the electrolyte and slower from the part close to the current collector. This behavior is closely related to stress development. While in the first phase of the charging the higher stress is always close to the electrolyte because the faster departure of lithium ions cannot compensate for the higher concentration here, starting from 38% SOC, the expected situation is reached. The lithium ion concentration

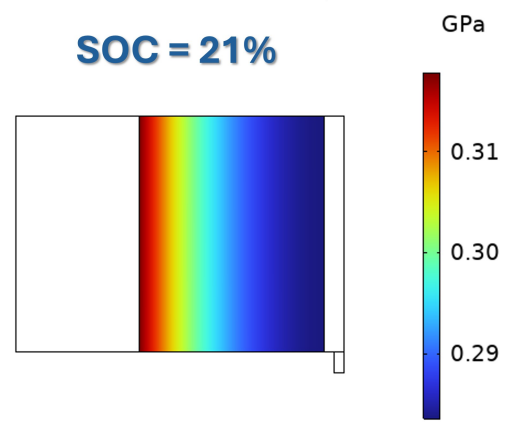
becomes higher in the part close to the current collector and lower close to the electrolyte, leading to lower stress here. During discharge, the most evident difference is at 77% SOC, where the maximum stress is around 1.49 GPa and the minimum stress is 1.34 GPa, with a difference of 0.15 GPa, representing a decrease of 10.1% with respect to the maximum value: the largest difference observed in the entire cycle.

Compared to the graphite case shown in **Figure 93**, during discharge, the inversion of the maximum stress happens earlier in the discharge cycle for silicon, at 38% SOC, while for graphite, it occurs only in the last part at 0% SOC.

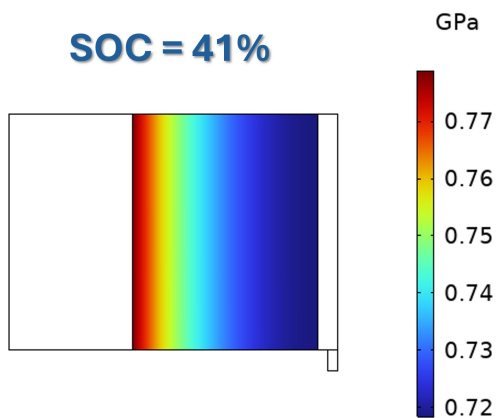
(a) Surface Von Mises stress, $\sigma_{v,surface}$



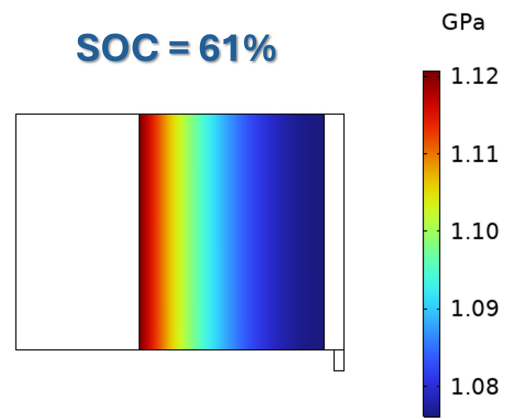
(b) Surface Von Mises stress, $\sigma_{v,surface}$



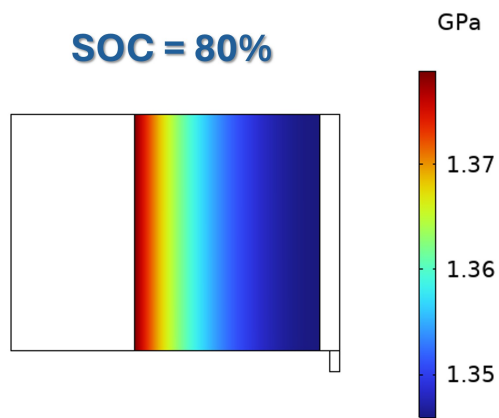
(c) Surface Von Mises stress, $\sigma_{v,surface}$



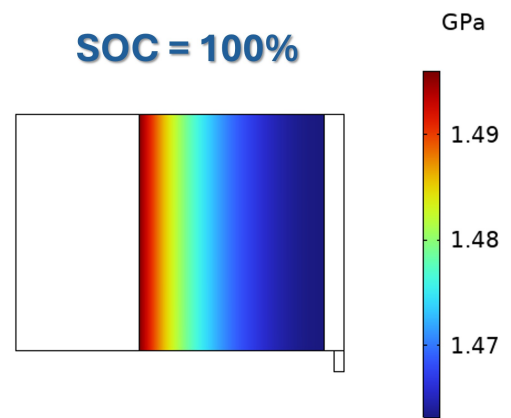
(d) Surface Von Mises stress, $\sigma_{v,surface}$



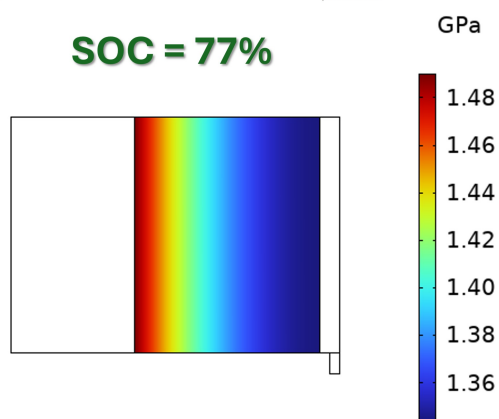
(e) Surface Von Mises stress, $\sigma_{v,surface}$



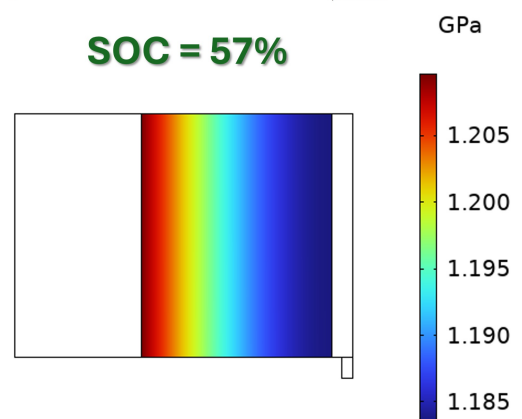
(f) Surface Von Mises stress, $\sigma_{v,surface}$



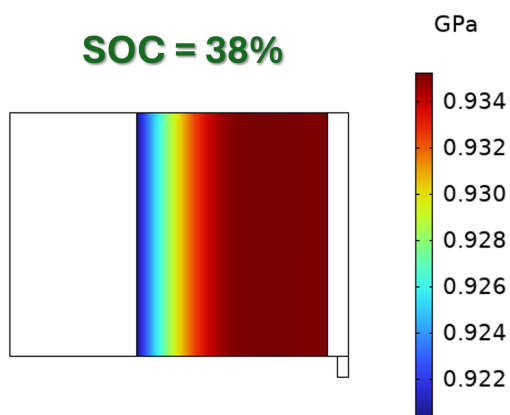
(g) Surface Von Mises stress, $\sigma_{v,surface}$



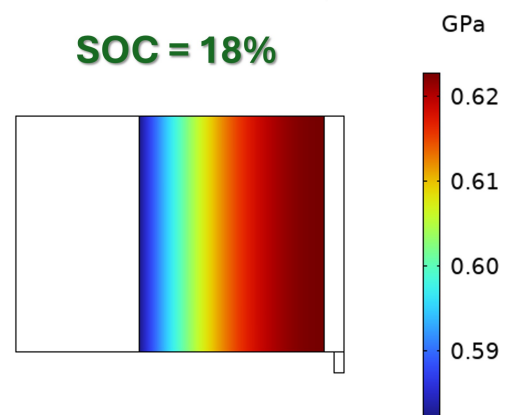
(h) Surface Von Mises stress, $\sigma_{v,surface}$



(i) Surface Von Mises stress, $\sigma_{v,surface}$



(j) Surface Von Mises stress, $\sigma_{v,surface}$



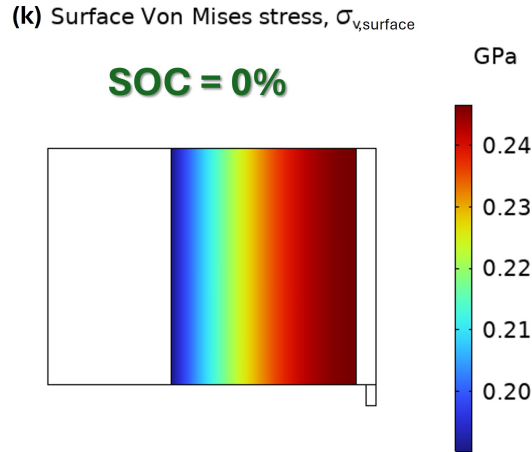


Figure 114: Surface Von Mises stress evolution across the entire silicon anode thickness, highlighting in color, throughout the charging-discharging cycle at various SOCs. The charging phase is represented by the SOC text in blue ((a), (b), (c), (d), (e) and (f)), while the discharging phase is indicated in green ((g), (h), (i), (j) and (k)).

5.2.3 Parametric analyses

This paragraph aims to understand the influence of certain parameters on the surface Von Mises stress of a specific active particle. For details on the active particle, please refer to **Figure 99**. The parameters studied are:

- Active particle radius.
- Anode thickness.
- Charging rate applied.

To understand the influence of these factors, the focus has been placed solely on the charging cycle. This cycle is crucial as the stress starts from zero and reaches its maximum value, representing the most critical case. It is important to note that while studying the influence of a particular element, all other not-affecting parameters used in the simulation remain constant to isolate the effect of the one being studied. Each parameter is varied by a constant quantity to ensure a fair comparison between different values. To maintain consistency across all simulations, the same lower cut-off voltage is used, stopping the simulation once this voltage is reached as done for the baseline data.

Figure 115 shows the influence of the active particle radius on stress development. As seen, all the lines have almost the same slope for the same SOC interval, and the clear trend is that increasing the particle radius leads to an increase in stress. In a real-case scenario, if there is a choice between technologies with different active particle radii that both work efficiently, it is better to choose the one with a smaller radius for stress minimization. For instance, when the radius increases from

22 μm to 26 μm , the maximum stress rises from 1.5 GPa to 2.17 GPa, an increase of 44.7%. Conversely, when the radius decreases from 22 to 18 μm , the stress decreases from 1.5 GPa to 1.01 GPa, a decrease of 32.7%. This indicates that the reduction or increase trend is similar, with a slightly more pronounced effect when the particle size is increased.

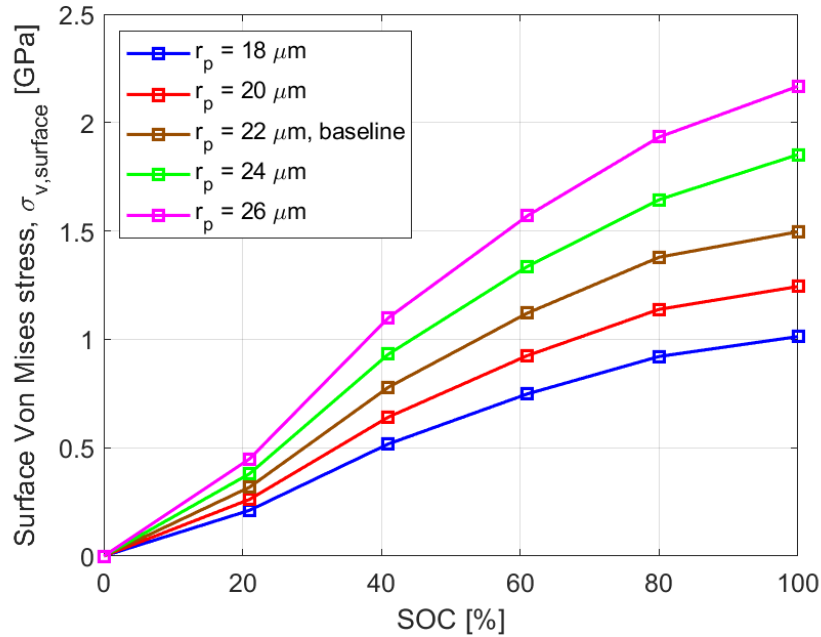


Figure 115: Impact of the active particle radius on surface Von Mises stress during the charging phase of the cycle for the selected active particle, silicon anode.

Figure 116 shows the influence of different anode thicknesses, called L_{neg} , on stress development. Here, unlike what is seen for particle size, the slope of the different lines for the same SOC interval is not always the same, varying especially with the L_{neg} of 75 μm . However, the slope difference is much less evident than in the graphite case shown in **Figure 95**. Furthermore, here a higher stress span is evident due to the higher porosity of the silicon anode compared to graphite. In order to summarize these results, a trend can be extracted: the increase in electrode thickness reduces the stress. In a real-case scenario, if there is a choice between technologies with different anode thicknesses that both work efficiently, it is better to choose the one with a higher thickness for stress purposes. Going into detail, when the thickness decreases from 90 μm to 60 μm , the stress increases from 1.5 GPa to 2.23 GPa, constituting a 48.7% increase. Conversely, when the thickness increases from 90 μm to 120 μm , the stress decreases from 1.5 GPa to 1.16 GPa, representing a decrease of 22.7%. Thus, the influence of increasing the width is more marked than that of decreasing it.

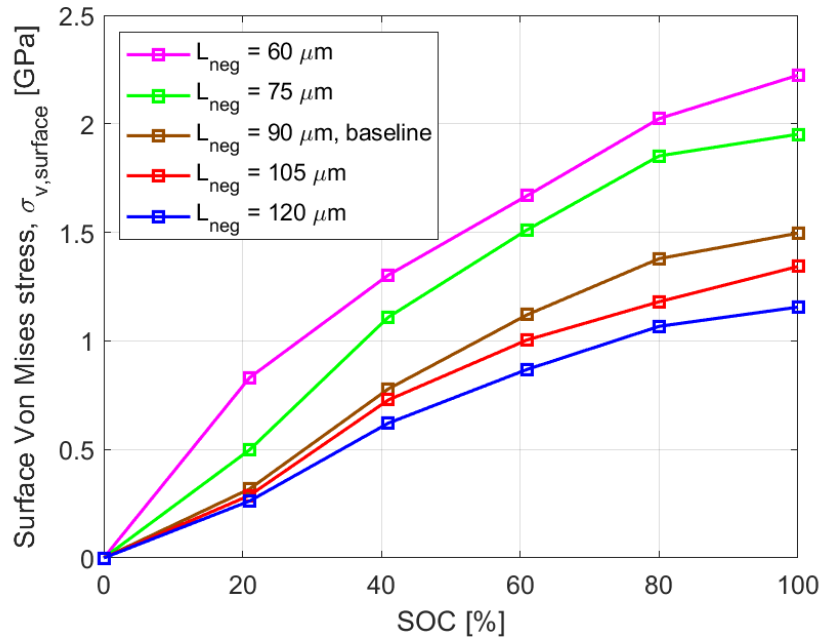


Figure 116: Impact of the silicon anode thickness on surface Von Mises stress during the charging phase of the cycle for the selected active particle.

Figure 117 shows the influence of the charging rate applied on stress development. Here the slopes of the different lines for the same SOC interval are almost the same, as seen with the active particle, with a slight variation for the highest parameter value. It is clear that decreasing the charging rate, by applying a smaller current, is beneficial for reducing stress. Specifically, when it increases from $\frac{1}{12.85}$ to $\frac{1}{7}$, the stress rises from 1.5 GPa to 2.48 GPa, an increase of 65.3%, the most significant influence among all the parameters studied. This further confirms the importance of avoiding high currents, as they can directly cause high stress. Conversely, if the selected factor decreases from $\frac{1}{12.85}$ to $\frac{1}{6.5}$, resulting in a lower current, the stress decreases from 1.5 GPa to 1 GPa, a negative change of 33.3%. Although the increase due to higher current is more substantial than the decrease due to lower current, this reduction is still the highest, making this parameter the most effective for the stress, in both positive and negative ways. It is worth emphasizing the importance of these conclusions because, unlike the active particle size and anode thickness, which must be defined before cell construction, the current can be adjusted during usage, making these considerations very important.

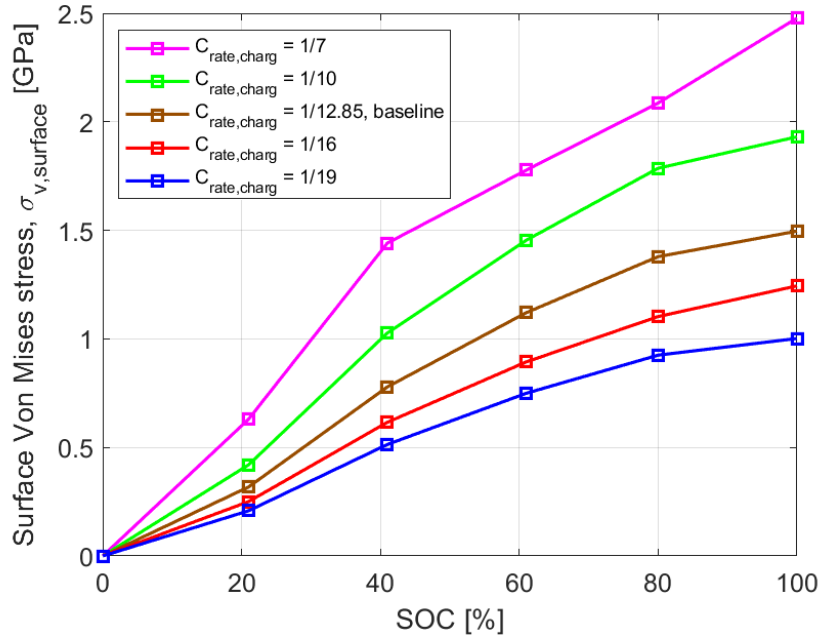


Figure 117: Impact of the intensity of the charging rate on surface Von Mises stress during the charging phase of the cycle for the selected active particle, silicon anode.

Figure 118 is a summary of all the parametric studies evaluated, focusing on what happens with the relative variation with respect to the baseline value at 100% SOC, where the stresses are highest. The x-axis reports an identification number: 1 refers to the active particle radius sweep, 2 to the anode thickness sweep, and 3 to the charging rate sweep. The y-axis shows the percentage variation, calculated as:

$$Variation = \frac{Data_{sweep100SOC,max/min} - Data_{100SOC,baseline}}{Data_{100SOC,baseline}} \cdot 100 \quad (73)$$

The variation is evaluated at two points for each parametric study: the maximum increase, positive, and the maximum decrease, negative. These points are then connected by straight lines to show the total variation span of the sweep. It is evident that the parameter most responsible for a stress increase is the growth in charging rate, leading to a 65.3% rise. This is followed by the anode thickness sweep and the active particle radius sweep. Regarding the positive effects that can reduce stress, the decrease of charging rate can cause the biggest negative variation of 33.3%, followed by a decrease in the active particle radius and the anode thickness. Furthermore, the largest span of variation is due to the charging rate, followed by the active particle radius, and lastly the anode thickness, which has the smallest span.

In conclusion, high charging rates should be avoided while lower ones should be used to reduce, to a bigger extend, the developed stress.

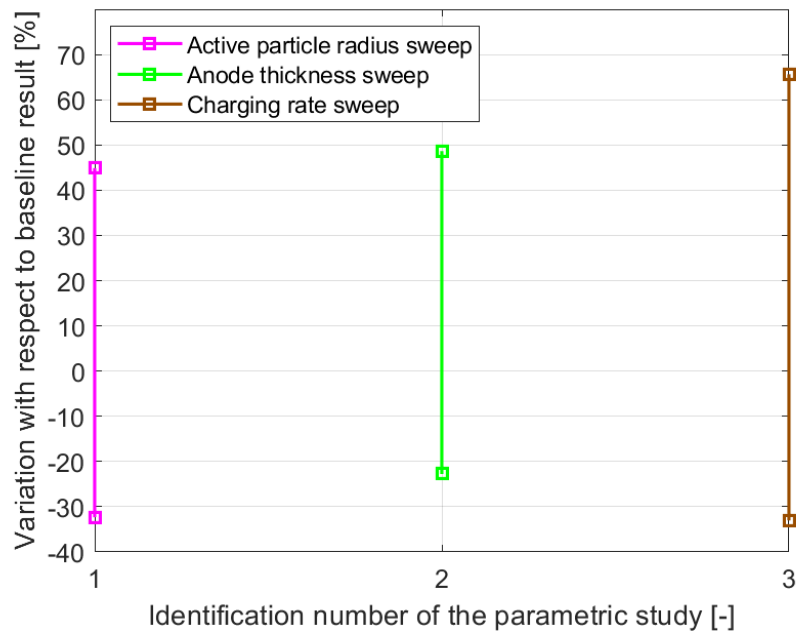


Figure 118: Comparison of different surface Von Mises stress variations at 100% SOC for the parametric studies performed. On the x-axis, the number 1 refers to the active particle radius sweep, the number 2 to the anode thickness sweep and the number 3 to the charging rate sweep. Silicon anode.

5.3 Comparison between graphite and silicon anodes

As the name of the paragraph suggests, it is related to a comparison of the results for graphite and silicon to see the differences in their behavior. It is important to point out that this paragraph is a comparison; for more detailed descriptions, please refer to **Section 5.1** for the graphite anode and **Section 5.2** for the silicon one.

Figure 119 and **Figure 120** display the deflection of the cantilever anodes during the cycles, for graphite and silicon respectively. The first noticeable difference is that the deflection of graphite is lower than that of silicon, as expected due to the higher volume expansion in relation to the degree of lithiation of silicon. Comparing the maximum deflection, graphite has a maximum one of 5.39 mm while silicon has 7.9 mm. Consequently, the remaining deflection after the cycle is higher for silicon: 1.06 mm compared to 0.87 mm for graphite. Regarding its increase over time during charging, both are characterized by a smaller slope in the last phases because the pores for lithium ions shuttling become further taken up and embedding paths becomes winding as well, which blocks and mitigate the further lithiation and so deformation towards the end. However, while for silicon there is an almost constant slope followed by a decrease, graphite shows an increase in slope between 163.2 and 217.6 minutes. During discharging, the trend is slightly different: for graphite, the deflection decrease is more pronounced in the first phase and becomes less pronounced

afterward, while for silicon, the first part is not so pronounced, however after 899 minutes the reduction increases, having almost the same slope until the end of the cycle.

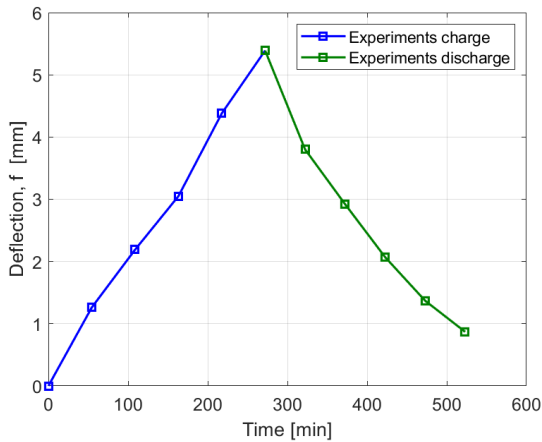


Figure 119: Deflection of graphite cantilever anode during the charging-discharging cycle. It is a reproduction of **Figure 81**.

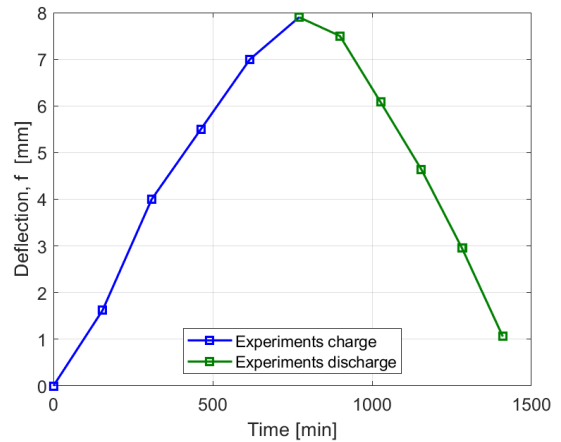


Figure 120: Deflection of silicon cantilever anode during the charging-discharging cycle. It is a reproduction of **Figure 102**.

Figure 121 and **Figure 122** show the surface Von Mises stress developed for the graphite and silicon anodes, both experimentally and by model. As is evident, the model in both cases is able to reproduce the real behavior. Naturally, corresponding to the larger silicon deflection, the stresses are also higher, with the maximum stress for graphite being 53.69 MPa while for silicon it is 1.5 GPa. At the end of the cycle, the residual stress is 8.33 MPa for graphite and 0.19 GPa for silicon. This big difference is also amplified by the fact that Young's modulus of silicon is much larger than the one of graphite. Regarding the stress increase over time during charging, both are characterized by a decrease in slope in the last phases because the pores for lithium ions shuttling become further taken up and embedding paths becomes winding as well, which blocks and mitigate the further lithiation and so deformation towards the end. However, for silicon, there is an almost constant slope followed by a decrease, whereas graphite shows an increase in slope between 163.2 and 217.6 minutes, miming what happens for the deflection. During discharging, the trend is slightly different: for graphite, the decrease is more pronounced in the first phase and becomes less pronounced afterward, while for silicon, the first part is not so pronounced, but after 899 minutes the reduction has almost the same slope, miming the deflection as well.

Figure 123 and **Figure 124** show the relative error between the experimental data and the model. As is clear, the errors are very low in both cases: for graphite it is lower than almost 2%, while for silicon it is lower than 5%. These are very good values that confirm the reliability of the model. Entering into the details for silicon, the discharge is more accurate than the charge itself.

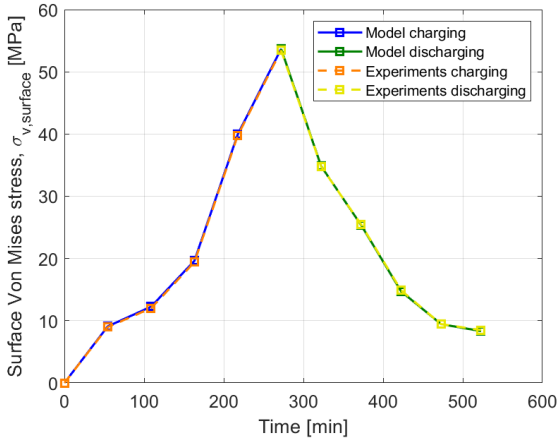


Figure 121: Surface Von Mises stress comparison between experimental and model data during the charging-discharging cycle for the selected active particle, graphite anode. It is a reproduction of **Figure 83**.

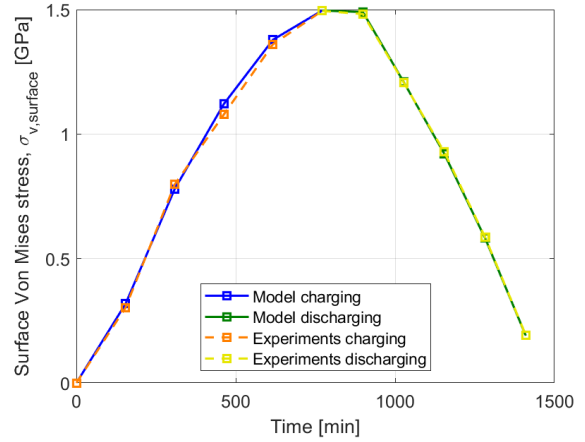


Figure 122: Surface Von Mises stress comparison between experimental and model data during the charging-discharging cycle for the selected active particle, silicon anode. It is a reproduction of **Figure 104**.

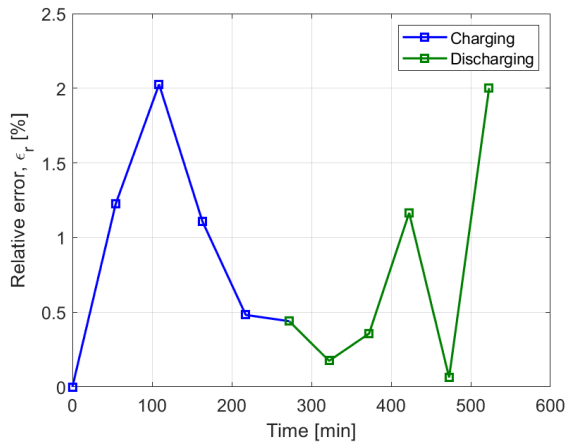


Figure 123: Relative error of the surface Von Mises stress between experimental and model data during the charging-discharging cycle for the selected active particle, graphite anode. It is a reproduction of **Figure 84**.

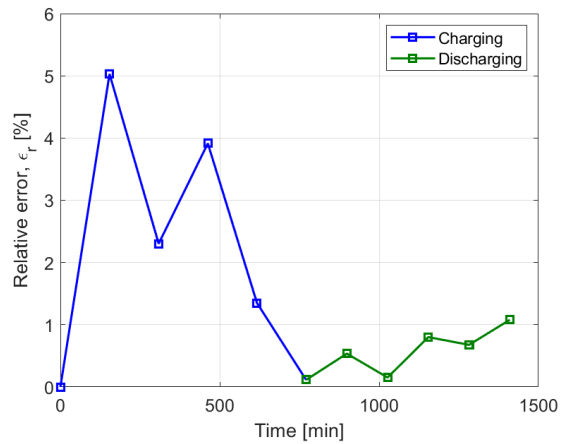


Figure 124: Relative error of the surface Von Mises stress between experimental and model data during the charging-discharging cycle for the selected active particle, silicon anode. It is a reproduction of **Figure 105**.

Figure 125 and **Figure 126** display the surface von Mises stress, across the entire electrode thickness, characterized by the biggest difference between the stress at the electrolyte interface and the ones at the current collector boundary. The individuated SOC values are 83% during charging for graphite and 77% during discharging for silicon. While the trend of the surface stress for different SOC values is well analyzed in **Figure 93** for graphite and **Figure 114** for silicon, the comparison of these two graphs highlights an important difference between the materials involved. Going in order, it is

evident that the difference in stress for silicon is much smaller, ranging from a maximum of 1.49 GPa to a minimum of 1.34 GPa, registering an interval of 0.15 GPa which is a 10.1% decrease from the maximum value. For graphite, the stress ranges from a maximum of 40 MPa to a minimum of around 27 MPa, showing a difference of 13 MPa which is a 32.5% decrease from the maximum value. This discrepancy in the percentage decrease is the result of the lower diffusion coefficient of silicon compared to graphite, resulting in a more uniform lithium concentration along the surface and consequently more uniform stress.

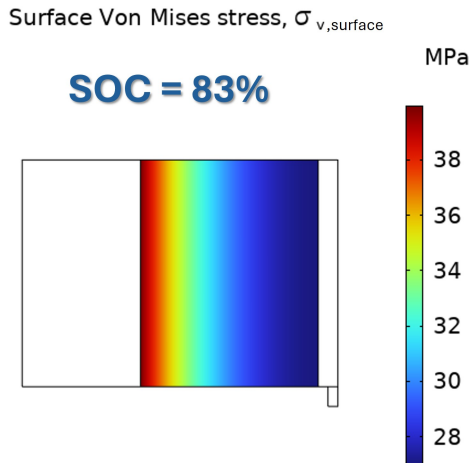


Figure 125: Surface Von Mises stress evolution across the entire thickness of the graphite anode at 83% SOC during charging, highlighting the maximum difference in stress values between the side close to electrolyte and the one close to current collector.

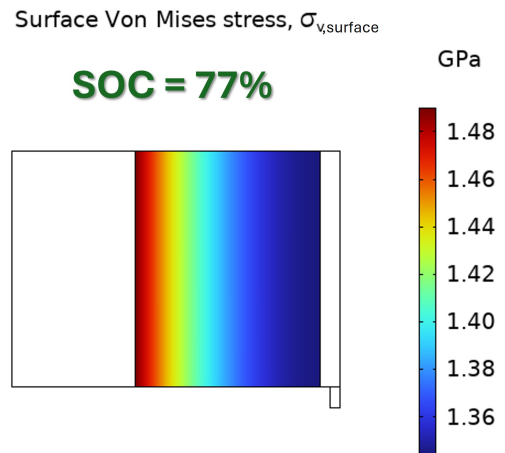


Figure 126: Surface Von Mises stress evolution across the entire thickness of the silicon anode at 77% SOC during discharging, highlighting the maximum difference in stress values between the side close to electrolyte and the one close to current collector.

Figure 127 and **Figure 128** show a summary of the different parametric studies conducted on graphite and silicon. It is important to note that on the x-axis, the number 1 refers to the active particle radius sweep, number 2 to the anode thickness sweep and number 3 to the charging rate sweep. For specific details regarding the individual effects, refer to **Section 5.1.3** for graphite and **Section 5.2.3** for silicon.

In both cases, it is evident that the parameter most responsible for increasing the surface Von Mises stress is the increase in the charging rate, leading to a 69.7% growth for graphite and a 65.3% for silicon. Thus, the rise is almost the same but has a slightly bigger influence on graphite. For graphite, this is followed by the active particle sweep and then the anode thickness sweep, that is the one having the smallest influence on the stress increase by far. While for silicon the trend is different, with the anode thickness rise being more detrimental than the active particle one by small percentage values. Regarding the positive effects that can reduce stress, the most beneficial for

graphite is lowering the particle size, which can cause a 32.24% reduction. For silicon, the most beneficial factor is still the charging rate, which, if reduced can lead to a 33.3% negative variation, higher than the maximum one for graphite. Furthermore, the difference between the total spans of anode thickness and active particle is less pronounced for silicon compared to graphite, where the anode thickness is significantly lower probably due to the lowest porosity of the graphite case. To summarize, for graphite, the most detrimental factor for increasing stress is a high charging rate, and the most beneficial is having a lower particle radius. For silicon, the highest charging rate is the most dangerous, and the lowest rate provides the most benefit. Comparing the entire interval, in both cases the charging change has the widest impact, followed by the active particle and then the electrode thickness.

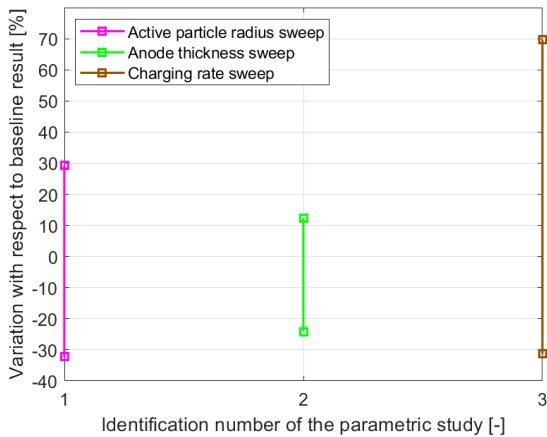


Figure 127: Comparison of different surface Von Mises stress variations at 100% SOC for the parametric studies performed. On the x-axis, the number 1 refers to the active particle radius sweep, the number 2 to the anode thickness sweep and the number 3 to the charging rate sweep. Graphite anode. It is a reproduction of **Figure 97**.

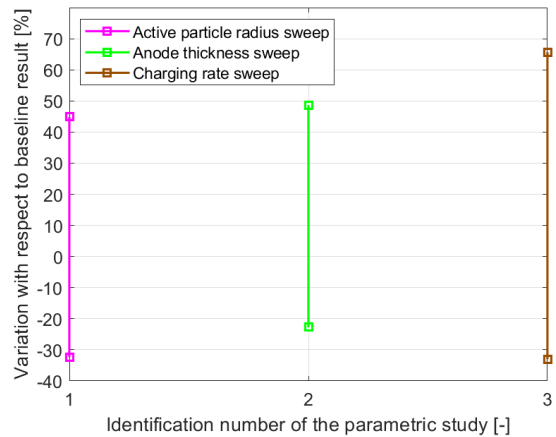


Figure 128: Comparison of different surface Von Mises stress variations at 100% SOC for the parametric studies performed. On the x-axis, the number 1 refers to the active particle radius sweep, the number 2 to the anode thickness sweep and the number 3 to the charging rate sweep. Silicon anode. It is a reproduction of **Figure 118**.

6 Conclusion and future works

In conclusion, the developed electrochemical-mechanical battery model is able to accurately reproduce the experimental cell behavior. Specifically, the voltage vs. time curve is reproduced within an error margin of 3% for the graphite anode cell and 2% for the silicon one. Regarding the mechanical model, it precisely replicates the experimental results, staying within an error margin below 2% for the graphite anode and 5% for the silicon. These low errors demonstrate the model high fidelity in reproducing real cell behavior. Going into details, the surface Von Mises stress in the active particle near the electrolyte interface during the charging and discharging cycle is compared between analytical and experimental results, as it represents the maximum stress experienced by the anode. The maximum stress during charging for graphite is 53.69 MPa, while for silicon it is 1.5 GPa. While, at the end of the cycle, the residual stress is 8.33 MPa for graphite and 0.19 GPa for silicon. This significant difference is due to the higher deflection and volume expansion of silicon, which can reach up to 350% compared to 13% for graphite, and due to the silicon higher Young's modulus. The stress increases over time during charging, but both materials exhibit a decrease in slope in the later phases due to the pores for lithium-ion shuttling becoming occupied and the embedding paths becoming winding, which blocks and mitigates further lithiation and deformation towards the end. While, during discharging, a stress decrease is experienced. Experimental results show that these stresses did not cause fragmentation of the electrode but caused permanent deformation as the yield stress was exceeded in both cases and some lithium ions remained trapped inside the anode.

The model not only reproduces the surface Von Mises stress inside a specific active particle but also evaluates radial, tangential, hydrostatic and Von Mises stress inside each active particle in the anode. This allows for considerations of the entire electrode thickness, recognizing a trend where, during the charging phase the maximum surface Von Mises stress is always at the electrolyte interface. However, during the last phase of discharging, it is inverted with the maximum stress at the current collector interface for both graphite and silicon anodes.

A parametric study was also performed to understand the influence of active particle radius, anode thickness and charging rate on the surface Von Mises stress developed. For graphite, the most detrimental factor for increasing stress is a high charging rate, leading to a 69.7% increase, while the most beneficial is having a lower particle radius, inducing a 32.24% decrease. For silicon, the highest charging rate is the most dangerous, generating a 65.3% increase, while the lowest rate is the most beneficial, provoking a negative variation of 33.3%. Comparing the entire interval, in both cases, the charging rate has the widest impact, followed by the active particle radius and then the electrode thickness.

To trace the final thought about the developed model, being very precise, it can be applied in the

industry for stresses-related applications. For any type of battery of interest, it requires completing the data relevant to the case under examination and the stresses can be accurately reproduced. This proves to be valuable for determining the optimal combination of active particle radius, thickness and charging rate to limit the effects of stresses in the anode. The focus is evidently on the anode, regardless of the type of cathode involved. Even if the cathode is porous, like NMC, as long as the data for the anode are appropriately filled and it is studied under the same voltage span, the model remains reliable. This is because the latter does not influence the stresses when the voltage and lithium-ion concentration are kept constant. In terms of material behavior, the deflection and stresses observed in graphite are minimal compared to silicon, which highlights why this material is widely used in industry. Conversely, the ones in silicon are significantly higher, and although no fractures were observed during experiments, stresses could become critical when using different combinations of thickness and binders in practical applications. This confirms the challenges of using silicon as the sole anode material for battery development. However, a solution that combines silicon and graphite could be promising, as it merges the high specific capacity of silicon, which is essential for long-lasting batteries, with the lower volume expansion of graphite, which helps mitigate the detrimental expansion of silicon.

Regarding future works, it will be interesting to consider fatigue stresses. While static stresses are the most detrimental to battery degradation, fatigue stresses can also induce the formation of cracks, which, due to the long cycling life of Li-ion batteries, can constitute a problem for battery operation.

References

- [1] V. B. Shenoy, P. Johari, and Y. Qi, “Elastic softening of amorphous and crystalline li–si phases with increasing li concentration: a first-principles study,” *Journal of Power Sources*, vol. 195, no. 19, pp. 6825–6830, 2010.
- [2] B. Boukamp, G. Lesh, and R. Huggins, “All-solid lithium electrodes with mixed-conductor matrix,” *Journal of the Electrochemical Society*, vol. 128, no. 4, p. 725, 1981.
- [3] Y. Qi, H. Guo, L. G. Hector, and A. Timmons, “Threefold increase in the young’s modulus of graphite negative electrode during lithium intercalation,” *Journal of The Electrochemical Society*, vol. 157, no. 5, p. A558, 2010.
- [4] P. J. Bouwman, “Lithium intercalation in preferentially oriented submicron licoo2 films,” *Netherland: University of Twente*, 2002.
- [5] H. Wang, Y.-I. Jang, B. Huang, D. R. Sadoway, and Y.-M. Chiang, “Tem study of electrochemical cycling-induced damage and disorder in licoo2 cathodes for rechargeable lithium batteries,” *Journal of the Electrochemical Society*, vol. 146, no. 2, p. 473, 1999.
- [6] D. Wang, X. Wu, Z. Wang, and L. Chen, “Cracking causing cyclic instability of lifepo4 cathode material,” *Journal of Power Sources*, vol. 140, no. 1, pp. 125–128, 2005.
- [7] M. Thackeray, “Structural considerations of layered and spinel lithiated oxides for lithium ion batteries,” *Journal of the Electrochemical Society*, vol. 142, no. 8, p. 2558, 1995.
- [8] A. Jokar, B. Rajabloo, M. Désilets, and M. Lacroix, “Review of simplified pseudo-two-dimensional models of lithium-ion batteries,” *Journal of Power Sources*, vol. 327, pp. 44–55, 2016.
- [9] D. Li and Y. Wang, “In-situ measurements of mechanical property and stress evolution of commercial graphite electrode,” *Materials & Design*, vol. 194, p. 108887, 2020.
- [10] T. G. Zavalis, M. Behm, and G. Lindbergh, “Investigation of short-circuit scenarios in a lithium-ion battery cell,” *Journal of the electrochemical Society*, vol. 159, no. 6, p. A848, 2012.
- [11] A. Nyman, M. Behm, and G. Lindbergh, “Electrochemical characterisation and modelling of the mass transport phenomena in lipf6–ec–emc electrolyte,” *Electrochimica Acta*, vol. 53, no. 22, pp. 6356–6365, 2008.

- [12] K. E. Thomas and J. Newman, "Heats of mixing and of entropy in porous insertion electrodes," *Journal of power sources*, vol. 119, pp. 844–849, 2003.
- [13] K. Kumaresan, G. Sikha, and R. E. White, "Thermal model for a li-ion cell," *Journal of the Electrochemical Society*, vol. 155, no. 2, p. A164, 2007.
- [14] D. K. Karthikeyan, G. Sikha, and R. E. White, "Thermodynamic model development for lithium intercalation electrodes," *Journal of Power Sources*, vol. 185, no. 2, pp. 1398–1407, 2008.
- [15] V. Srinivasan and J. Newman, "Design and optimization of a natural graphite/iron phosphate lithium-ion cell," *Journal of the Electrochemical Society*, vol. 151, no. 10, p. A1530, 2004.
- [16] D. Clerici, F. Mocera, and A. Somà, "Analytical solution for coupled diffusion induced stress model for lithium-ion battery," *Energies*, vol. 13, no. 7, p. 1717, 2020.
- [17] V. A. Sethuraman, V. Srinivasan, and J. Newman, "Analysis of electrochemical lithiation and delithiation kinetics in silicon," *Journal of the Electrochemical Society*, vol. 160, no. 2, p. A394, 2012.
- [18] R. Chandrasekaran and T. F. Fuller, "Analysis of the lithium-ion insertion silicon composite electrode/separator/lithium foil cell," *Journal of The Electrochemical Society*, vol. 158, no. 8, p. A859, 2011.
- [19] F. Yang, Y. Li, and K. Zhang, "A multiplicative finite strain deformation for diffusion-induced stress: An incremental approach," *International Journal of Engineering Science*, vol. 187, p. 103841, 2023.
- [20] F. Fan, S. Huang, H. Yang, M. Raju, D. Datta, V. B. Shenoy, A. C. Van Duin, S. Zhang, and T. Zhu, "Mechanical properties of amorphous lixi alloys: a reactive force field study," *Modelling and Simulation in Materials Science and Engineering*, vol. 21, no. 7, p. 074002, 2013.
- [21] M. Wang, X. Xiao, and X. Huang, "A multiphysics microstructure-resolved model for silicon anode lithium-ion batteries," *Journal of Power Sources*, vol. 348, pp. 66–79, 2017.
- [22] A. Saidi, A. Tanguy, M. Fourmeau, G. Molnár, A. Boucherif, and D. Machon, "Coupling between mechanical stresses and lithium penetration in a lithium ion battery," *Mechanics of Materials*, vol. 177, p. 104532, 2023.
- [23] COMSOL, "Comsol reference manual," *Comsol Documentation*, 2023.

- [24] COMSOL, “Battery design module user’s guide,” *Comsol Documentation*, 2023.
- [25] H. Jiang, Y. He, X. Li, Z. Jin, H. Yu, and D. Li, “Effect of the charge rate on the mechanical response of composite graphite electrodes: in situ experiment and mathematical analysis,” *Physical Chemistry Chemical Physics*, vol. 26, no. 2, pp. 1245–1254, 2024.
- [26] A. Mukhopadhyay and B. W. Sheldon, “Deformation and stress in electrode materials for li-ion batteries,” *Progress in Materials Science*, vol. 63, pp. 58–116, 2014.
- [27] S. Sepasi, *Adaptive state of charge estimation for battery packs*. PhD thesis, 12 2014.
- [28] S. Chepyala, *Simulation of Li-Ion Coin Cells Using COMSOL Multiphysics*. PhD thesis, The Florida State University, 2017.
- [29] R. M. Salgado, F. Danzi, J. E. Oliveira, A. El-Azab, P. P. Camanho, and M. H. Braga, “The latest trends in electric vehicles batteries,” *Molecules*, vol. 26, no. 11, p. 3188, 2021.
- [30] Q. Hu, “Hybrid tin based nanostructures wrapped with graphene as efficient anode material for lithium ion batteries,” Master’s thesis, University of Waterloo, 2015.
- [31] J. Y. Huang, L. Zhong, C. M. Wang, J. P. Sullivan, W. Xu, L. Q. Zhang, S. X. Mao, N. S. Hudak, X. H. Liu, A. Subramanian, *et al.*, “In situ observation of the electrochemical lithiation of a single SnO_2 nanowire electrode,” *Science*, vol. 330, no. 6010, pp. 1515–1520, 2010.
- [32] K. Kanamura, H. Naito, T. Yao, and Z.-i. Takehara, “Structural change of the LiMn_2O_4 spinel structure induced by extraction of lithium,” *Journal of Materials Chemistry*, vol. 6, no. 1, pp. 33–36, 1996.
- [33] H.-H. Ryu, K.-J. Park, C. S. Yoon, and Y.-K. Sun, “Capacity fading of ni-rich $\text{Li}[\text{Ni}_x\text{Co}_y\text{Mn}_{1-x-y}]\text{O}_2$ (0.6 x 0.95) cathodes for high-energy-density lithium-ion batteries: bulk or surface degradation?,” *Chemistry of materials*, vol. 30, no. 3, pp. 1155–1163, 2018.
- [34] H. Gabrisch, J. Wilcox, and M. Doeff, “Tem study of fracturing in spherical and plate-like LiFePO_4 particles,” *Electrochemical and Solid-State Letters*, vol. 11, no. 3, p. A25, 2008.
- [35] H. Jung, M. Park, Y.-G. Yoon, G.-B. Kim, and S.-K. Joo, “Amorphous silicon anode for lithium-ion rechargeable batteries,” *Journal of power sources*, vol. 115, no. 2, pp. 346–351, 2003.
- [36] S. Singh, Y. E. Ebongue, S. Rezaei, and K. P. Birke, “Hybrid modeling of lithium-ion battery: Physics-informed neural network for battery state estimation,” *Batteries*, vol. 9, no. 6, p. 301, 2023.

- [37] W. Ai, L. Kraft, J. Sturm, A. Jossen, and B. Wu, "Electrochemical thermal-mechanical modelling of stress inhomogeneity in lithium-ion pouch cells," *Journal of The Electrochemical Society*, vol. 167, no. 1, p. 013512, 2020.
- [38] COMSOL-Multiphysics, "2d lithium-ion battery," *Battery Design Module Application Library*, 2023.
- [39] X. Shang, Q. Liu, and Z. Zhang, "Analytical solution for thermal-diffusion induced stress model and numerical simulation of battery structure during charging-discharging process," *Arabian Journal of Chemistry*, vol. 16, no. 10, p. 105127, 2023.
- [40] S. Renganathan, G. Sikha, S. Santhanagopalan, and R. E. White, "Theoretical analysis of stresses in a lithium ion cell," *Journal of the Electrochemical Society*, vol. 157, no. 2, p. A155, 2009.
- [41] D. Li, G. Zhu, H. Liu, and Y. Wang, "Diffusion-induced stress in commercial graphite electrodes during multiple cycles measured by an in situ method," *Micromachines*, vol. 13, no. 1, p. 142, 2022.
- [42] J.-M. Tarascon and M. Armand, "Issues and challenges facing rechargeable lithium batteries," *nature*, vol. 414, no. 6861, pp. 359–367, 2001.
- [43] J. O. Besenhard, *Handbook of battery materials*. John Wiley & Sons, 2008.
- [44] V. Ravello, "E-powertrain components course materials," *Politecnico di Torino*, 2023.
- [45] A. Mukhopadhyay, A. Tokranov, K. Sena, X. Xiao, and B. W. Sheldon, "Thin film graphite electrodes with low stress generation during li-intercalation," *Carbon*, vol. 49, no. 8, pp. 2742–2749, 2011.
- [46] U. Kasavajjula, C. Wang, and A. J. Appleby, "Nano-and bulk-silicon-based insertion anodes for lithium-ion secondary cells," *Journal of power sources*, vol. 163, no. 2, pp. 1003–1039, 2007.
- [47] B. Kang and G. Ceder, "Battery materials for ultrafast charging and discharging," *Nature*, vol. 458, no. 7235, pp. 190–193, 2009.
- [48] B. Scrosati, "Recent advances in lithium ion battery materials," *Electrochimica Acta*, vol. 45, no. 15-16, pp. 2461–2466, 2000.
- [49] J. Hassoun, S. Panero, P. Reale, and B. Scrosati, "A new, safe, high-rate and high-energy polymer lithium-ion battery," *Advanced Materials*, vol. 21, no. 47, pp. 4807–4810, 2009.

- [50] W. R. Bennett, "Considerations for estimating electrode performance in li-ion cells," in *2012 IEEE Energytech*, pp. 1–5, IEEE, 2012.
- [51] W. Wang, Y. Wang, L. Yuan, C. You, J. Wu, L. Liu, J. Ye, Y. Wu, and L. Fu, "Recent advances in modification strategies of silicon-based lithium-ion batteries," *Nano Research*, vol. 16, no. 3, pp. 3781–3803, 2023.
- [52] B. E. Murdock, K. E. Toghill, and N. Tapia-Ruiz, "A perspective on the sustainability of cathode materials used in lithium-ion batteries," *Advanced Energy Materials*, vol. 11, no. 39, p. 2102028, 2021.
- [53] J. Dahn, U. von Sacken, and C. Michal, "Structure and electrochemistry of $\text{Li}_{1\pm}\text{NiO}_2$ and a new Li_2NiO_2 phase with the $\text{Ni}(\text{OH})_2$ structure," *Solid State Ionics*, vol. 44, no. 1-2, pp. 87–97, 1990.
- [54] F. Capitaine, P. Gravereau, and C. Delmas, "A new variety of LiMnO_2 with a layered structure," *Solid State Ionics*, vol. 89, no. 3-4, pp. 197–202, 1996.
- [55] A. Madsen, *Lithium iron sulphide as a positive electrode material for rechargeable lithium batteries*. PhD thesis, University of Southampton, 2013.
- [56] O. J. Gross and J. Swoyer, "The next step in low cost lithium ion polymer systems," in *Seventeenth Annual Battery Conference on Applications and Advances. Proceedings of Conference (Cat. No. 02TH8576)*, pp. 135–139, IEEE, 2002.
- [57] Y. Mekonnen, A. Sundararajan, and A. I. Sarwat, "A review of cathode and anode materials for lithium-ion batteries," *SoutheastCon 2016*, pp. 1–6, 2016.
- [58] H. Dasari, *Predicting the Effects of Capacity Fade and Thermal Behavior of Silicon Anodes in Lithium-Ion Batteries*. PhD thesis.
- [59] T. Zheng, J. Reimers, and J. Dahn, "Effect of turbostratic disorder in graphitic carbon hosts on the intercalation of lithium," *Physical Review B*, vol. 51, no. 2, p. 734, 1995.
- [60] J. Besenhard, J. Yang, and M. Winter, "Will advanced lithium-alloy anodes have a chance in lithium-ion batteries?," *Journal of Power Sources*, vol. 68, no. 1, pp. 87–90, 1997.
- [61] M. Endo, C. Kim, K. Nishimura, T. Fujino, and K. Miyashita, "Recent development of carbon materials for li ion batteries," *Carbon*, vol. 38, no. 2, pp. 183–197, 2000.
- [62] B. W. Sheldon, S. K. Soni, X. Xiao, and Y. Qi, "Stress contributions to solution thermodynamics in li-si alloys," *Electrochemical and Solid-State Letters*, vol. 15, no. 1, p. A9, 2011.

- [63] V. A. Sethuraman, M. J. Chon, M. Shimshak, V. Srinivasan, and P. R. Guduru, “In situ measurements of stress evolution in silicon thin films during electrochemical lithiation and delithiation,” *Journal of Power Sources*, vol. 195, no. 15, pp. 5062–5066, 2010.
- [64] W. H. Woodford, Y.-M. Chiang, and W. C. Carter, ““electrochemical shock” of intercalation electrodes: a fracture mechanics analysis,” *Journal of the Electrochemical Society*, vol. 157, no. 10, p. A1052, 2010.
- [65] X. Zhang, W. Shyy, and A. M. Sastry, “Numerical simulation of intercalation-induced stress in li-ion battery electrode particles,” *Journal of the Electrochemical Society*, vol. 154, no. 10, p. A910, 2007.
- [66] J. Christensen, “Modeling diffusion-induced stress in li-ion cells with porous electrodes,” *Journal of the Electrochemical Society*, vol. 157, no. 3, p. A366, 2010.
- [67] A. McAlister, “The al- li (aluminum- lithium) system,” *Bulletin of alloy phase diagrams*, vol. 3, no. 2, pp. 177–183, 1982.
- [68] A. Mukhopadhyay, F. Guo, A. Tokranov, X. Xiao, R. H. Hurt, and B. W. Sheldon, “Engineering of graphene layer orientation to attain high rate capability and anisotropic properties in li-ion battery electrodes,” *Advanced Functional Materials*, vol. 23, no. 19, pp. 2397–2404, 2013.
- [69] C. Tian, F. Lin, and M. M. Doeff, “Electrochemical characteristics of layered transition metal oxide cathode materials for lithium ion batteries: surface, bulk behavior, and thermal properties,” *Accounts of chemical research*, vol. 51, no. 1, pp. 89–96, 2017.
- [70] H. Liu, Y. Wu, E. Rahm, R. Holze, and H. Wu, “Cathode materials for lithium ion batteries prepared by sol-gel methods,” *Journal of Solid State Electrochemistry*, vol. 8, pp. 450–466, 2004.
- [71] J. Christensen and J. Newman, “A mathematical model of stress generation and fracture in lithium manganese oxide,” *Journal of The Electrochemical Society*, vol. 153, no. 6, p. A1019, 2006.
- [72] H.-Y. S. Huang and Y.-X. Wang, “Dislocation based stress developments in lithium-ion batteries,” *Journal of the Electrochemical Society*, vol. 159, no. 6, p. A815, 2012.
- [73] A. Purwanto, C. S. Yudha, U. Ubaidillah, H. Widiyandari, T. Ogi, and H. Haerudin, “Nca cathode material: Synthesis methods and performance enhancement efforts,” *Materials Research Express*, vol. 5, no. 12, p. 122001, 2018.

- [74] Y. Hu, X. Zhao, and Z. Suo, "Averting cracks caused by insertion reaction in lithium-ion batteries," *Journal of Materials Research*, vol. 25, no. 6, pp. 1007–1010, 2010.
- [75] K. Aifantis and J. Dempsey, "Stable crack growth in nanostructured li-batteries," *Journal of power sources*, vol. 143, no. 1-2, pp. 203–211, 2005.
- [76] X. Xiao, P. Liu, M. Verbrugge, H. Haftbaradaran, and H. Gao, "Improved cycling stability of silicon thin film electrodes through patterning for high energy density lithium batteries," *Journal of Power Sources*, vol. 196, no. 3, pp. 1409–1416, 2011.
- [77] D. Zane, A. Antonini, and M. Pasquali, "A morphological study of sei film on graphite electrodes," *Journal of power sources*, vol. 97, pp. 146–150, 2001.
- [78] S. K. Soni, B. W. Sheldon, X. Xiao, M. W. Verbrugge, A. Dongjoon, H. Haftbaradaran, and G. Huajian, "Stress mitigation during the lithiation of patterned amorphous si islands," *Journal of the Electrochemical Society*, vol. 159, no. 1, p. A38, 2011.
- [79] S. K. Soni, B. W. Sheldon, X. Xiao, A. F. Bower, and M. W. Verbrugge, "Diffusion mediated lithiation stresses in si thin film electrodes," *Journal of the Electrochemical Society*, vol. 159, no. 9, p. A1520, 2012.
- [80] K. Zhao, G. A. Tritsarlis, M. Pharr, W. L. Wang, O. Okeke, Z. Suo, J. J. Vlassak, and E. Kaxiras, "Reactive flow in silicon electrodes assisted by the insertion of lithium," *Nano letters*, vol. 12, no. 8, pp. 4397–4403, 2012.
- [81] A. Tokranov, B. Sheldon, P. Lu, X. Xiao, and A. Mukhopadhyay, "The origin of stress in the solid electrolyte interphase on carbon electrodes for li ion batteries," *Journal of The Electrochemical Society*, vol. 161, no. 1, p. A58, 2013.
- [82] A. Mukhopadhyay, A. Tokranov, X. Xiao, and B. W. Sheldon, "Stress development due to surface processes in graphite electrodes for li-ion batteries: A first report," *Electrochimica Acta*, vol. 66, pp. 28–37, 2012.
- [83] A. Van der Ven, M. Aydinol, G. Ceder, G. Kresse, and J. Hafner, "First-principles investigation of phase stability in $li_x coo_2$," *Physical Review B*, vol. 58, no. 6, p. 2975, 1998.
- [84] P. Gupta and P. Gudmundson, "A multi-scale model for simulation of electrochemically induced stresses on scales of active particles, electrode layers, and battery level in lithium-ion batteries," *Journal of Power Sources*, vol. 511, p. 230465, 2021.
- [85] J. Newman and W. Tiedemann, "Porous-electrode theory with battery applications," *AIChE Journal*, vol. 21, no. 1, pp. 25–41, 1975.

- [86] J. Zhou, B. Xing, and C. Wang, “A review of lithium ion batteries electrochemical models for electric vehicles,” in *E3S web of conferences*, vol. 185, p. 04001, EDP Sciences, 2020.
- [87] Q. Liu, J. Wang, and B. Hu, “Progressive damage analysis for spherical electrode particles with different protective structures for a lithium-ion battery,” *ACS omega*, vol. 8, no. 8, pp. 7492–7506, 2023.
- [88] S. Chang, J. Moon, and M. Cho, “Stress-diffusion coupled multiscale analysis of si anode for li-ion battery,” *Journal of Mechanical Science and Technology*, vol. 29, pp. 4807–4816, 2015.
- [89] S. Kalnaus, K. Rhodes, and C. Daniel, “A study of lithium ion intercalation induced fracture of silicon particles used as anode material in li-ion battery,” *Journal of Power Sources*, vol. 196, no. 19, pp. 8116–8124, 2011.
- [90] X. Zhu, Y. Chen, H. Chen, and W. Luan, “The diffusion induced stress and cracking behaviour of primary particle for li-ion battery electrode,” *International Journal of Mechanical Sciences*, vol. 178, p. 105608, 2020.
- [91] B. Han, B. Shi, H. Xie, and Y. Kang, “Evolution of electrochemically induced stress and its effect on the lithium-storage performance of graphite electrode,” *Science China Technological Sciences*, vol. 66, no. 6, pp. 1784–1796, 2023.
- [92] J. H. Park, J. E. Choi, and S. Y. Kim, “Stress analysis of graphite anode under various binder conditions in a multiparticle model through multiscale simulation and experimental verification,” *Energy Technology*, p. 2300898, 2024.
- [93] Y. Ali, I. Shah, T. A. Khan, and N. Iqbal, “A multiphysics-multiscale model for particle–binder interactions in electrode of lithium-ion batteries,” *Energies*, vol. 16, no. 15, p. 5823, 2023.
- [94] L. Ji, Z. Guo, and Y. Wu, “Computational and experimental observation of li-ion concentration distribution and diffusion-induced stress in porous battery electrodes,” *Energy Technology*, vol. 5, no. 9, pp. 1702–1711, 2017.
- [95] D. Shi, X. Xiao, X. Huang, and H. Kia, “Modeling stresses in the separator of a pouch lithium-ion cell,” *Journal of Power Sources*, vol. 196, no. 19, pp. 8129–8139, 2011.
- [96] Z. Guo, L. Ji, and L. Chen, “Analytical solutions and numerical simulations of diffusion-induced stresses and concentration distributions in porous electrodes with particles of different size and shape,” *Journal of Materials Science*, vol. 52, pp. 13606–13625, 2017.

- [97] L. Wu, Y. Wen, and J. Zhang, “Three-dimensional finite element study on li diffusion induced stress in fib-sem reconstructed licoo2 half cell,” *Electrochimica Acta*, vol. 222, pp. 814–820, 2016.
- [98] P. Liu, R. Xu, Y. Liu, F. Lin, and K. Zhao, “Computational modeling of heterogeneity of stress, charge, and cyclic damage in composite electrodes of li-ion batteries,” *Journal of The Electrochemical Society*, vol. 167, no. 4, p. 040527, 2020.
- [99] B. S. Haran, B. N. Popov, and R. E. White, “Determination of the hydrogen diffusion coefficient in metal hydrides by impedance spectroscopy,” *Journal of Power Sources*, vol. 75, no. 1, pp. 56–63, 1998.
- [100] W. Luo, C. Lyu, L. Wang, and L. Zhang, “A new extension of physics-based single particle model for higher charge–discharge rates,” *Journal of Power Sources*, vol. 241, pp. 295–310, 2013.
- [101] X. Han, M. Ouyang, L. Lu, and J. Li, “Simplification of physics-based electrochemical model for lithium ion battery on electric vehicle. part ii: Pseudo-two-dimensional model simplification and state of charge estimation,” *Journal of Power Sources*, vol. 278, pp. 814–825, 2015.
- [102] E. Martínez-Rosas, R. Vasquez-Medrano, and A. Flores-Tlacuahuac, “Modeling and simulation of lithium-ion batteries,” *Computers & Chemical Engineering*, vol. 35, no. 9, pp. 1937–1948, 2011.
- [103] Q. Zhang, Q. Guo, and R. E. White, “Semi-empirical modeling of charge and discharge profiles for a licoo2 electrode,” *Journal of power sources*, vol. 165, no. 1, pp. 427–435, 2007.
- [104] S. Taslimi Taleghani, B. Marcos, and G. Lantagne, “Modeling and simulation of a commercial graphite–lifepo 4 cell in a full range of c-rates,” *Journal of Applied Electrochemistry*, vol. 48, pp. 1389–1400, 2018.
- [105] R. B. Smith and M. Z. Bazant, “Multiphase porous electrode theory,” *Journal of The Electrochemical Society*, vol. 164, no. 11, p. E3291, 2017.
- [106] T. R. Martin, R. T. Pekarek, J. E. Coyle, M. C. Schulze, and N. R. Neale, “Understanding why poly (acrylic acid) works: decarbonylation and cross-linking provide an ionically conductive passivation layer in silicon anodes,” *Journal of Materials Chemistry A*, vol. 9, no. 38, pp. 21929–21938, 2021.

- [107] J. Yang, J. Chen, and M. Cheng, “In-situ nanomechanical characterization of electrochemical cycles in lithium ion batteries,” in *2013 Transducers & Eurosensors XXVII: The 17th International Conference on Solid-State Sensors, Actuators and Microsystems (TRANSDUCERS & EUROSENSORS XXVII)*, pp. 438–441, IEEE, 2013.
- [108] C. Yu, X. Li, T. Ma, J. Rong, R. Zhang, J. Shaffer, Y. An, Q. Liu, B. Wei, and H. Jiang, “Silicon thin films as anodes for high-performance lithium-ion batteries with effective stress relaxation,” *Advanced Energy Materials*, vol. 2, no. 1, pp. 68–73, 2012.

Vita auctoris

NAME: Filippo D'Ugo

PLACE OF BIRTH: Pescara, Italy

YEAR OF BIRTH: 2000

EDUCATION: Bachelor of Applied Science in Mechanical Engineering,
Politecnico di Torino, 2022

Master of Applied Science in Automotive Engineering,
University of Windsor, 2024

Master of Applied Science in Automotive Engineering,
Politecnico di Torino, 2024